Oxide Perovskites for Photoelectrochemical Water Splitting

Freeman, Emma

Award date:
2020

Awarding institution:
University of Bath

Oxide Perovskites for Photoelectrochemical Water Splitting

Submitted by

Emma Melita Freeman

For the degree of Doctor of Philosophy

University of Bath

Centre for Doctoral Training in Catalysis

Department of Chemical Engineering

February 2020

Copyright notice

Restrictions on use and licensing

Declaration of any previous submission of the work

The material presented here for examination for the award of a higher degree by research has not been incorporated into a submission for another degree.

Declaration of authorship

I am the author of this thesis, and the work described therein was carried out by myself personally, except where explicit reference is made regarding the contribution of others.

Chapter 3
Min Su Park completed the synthesis of the PVC-*g*-POEM block co-polymer at Yonsei University, which was used as a templating agent for LFO photocathodes.

Chapter 5
Hayley Pickering synthesised and characterised $PrFeO_3$ nanoparticles and Sophie Thomas fabricated and characterised $PrFeO_3$ photocathodes prepared through a doctor blading method, under my supervision.

Chapter 6

Research ideas and concepts associated with the fabrication of metal-insulator-semiconductor junctions were developed by Dr. Ibrahim Ahmet and Prof. Roel van de Krol at the Helmholtz Center Berlin for Materials and Energy. Dr. Ibrahim Ahmet fabricated $BiVO_4$ films.

Candidate's signature

Acknowledgements

Special thanks go to my supervisor Dr Salvador Eslava for his continued knowledge, support and patience which has directed and helped me progress throughout my PhD. His input has been extremely valuable and much appreciated. Additional thanks go to my co-supervisor Prof. David Fermin for all his additional help and guidance. Also, to everyone in the Eslava group for their assistance, especially Jifang, Shawn, Miriam, Ria and Santosh who have made research much more enjoyable.

Thank you to all the members of the Materials and Characterisation facility at the University of Bath who have assisted me in acquiring micrographs, especially Dr. Philip Fletcher and Ursula Potter. Thanks also to all the technical staff in the Chemical Engineering department whose help has been invaluable. An important thank you goes to the CDT in Catalysis and the EPSRC for funding which has allowed me this opportunity to conduct this research as part of my PhD. Thank you to the Helmholtz Center Berlin for Materials and Energy for allowing me to complete a research placement, with a special thanks to Prof. Roel van de Krol and Dr. Ibbi Ahmet for hosting me, I had a fantastic and wunderbar time.

Finally, thank you to my family, my parents Laura and David, my twin Katherine, my brother James and my Yorkshire Terriers Rocky and Pippin, for their continued support throughout my studies. Also, to my friends Alex, Jimmy, Alba, Jon and Lauren who have helped me a great deal and made me laugh along the way.

Table of Contents

Abstract

Renewable and sustainable alternatives to fossil fuels are needed to limit the impact of global warming and to meet increasing energy demands. Electricity generation through solar energy storage using metal oxide semiconductors as photoelectrodes within photoelectrochemical (PEC) cells is one such alternative. For example, PEC water reduction can be completed in order to produce H_2 which can then be used as a fuel or within fuel cell devices. Finding suitable semiconductors can be challenging with persistent and common limitations arising such as high rates of electron-hole recombination, poor light absorption and poor stability. For example, some metal oxides are restricted due to wide band gaps and hence inactivity in the visible light region, which encompasses about 40 % of the solar light spectrum. Additionally, with reference to photocathodes, there are common issues arising from instability (e.g. Cu_2O and Cu_2S), thus it is advantageous to investigate alternative materials that have smaller band gaps and are highly stable.

Hence, perovskite oxides (ABO_3) such as lanthanum iron oxide ($LaFeO_3$) and praseodymium iron oxide ($PrFeO_3$) have been investigated here, due to their benefits of visible light absorption, abundancy and good stability. The effects of film fabrication method on film quality and ultimate performance had been rarely discussed. In this work, various film fabrication methods have been explored for $LaFeO_3$ photocathodes, including doctor blading, spray pyrolysis of precursors and spin coating with polymer templates. The best overall PEC performance was found for $LaFeO_3$ films prepared through a sacrificial templating method using a non-ionic surfactant, polyoxyethylene octyl phenyl ether (Triton X-100). A photocurrent density of -161±6 μA cm^{-2} at +0.43 V_{RHE} was recorded, with an impressive onset potential of +1.4 V_{RHE} for cathodic photocurrent, with increased electrochemically active surface area and charge separation compared to other methods. This is a substantial increase on many literature values and is comparable to the highest achieved photocurrent reported. $PrFeO_3$ photocathodes prepared through spray pyrolysis were also examined, which achieved a photocurrent density of -130±0.6 μA cm^{-2} at +0.43 V_{RHE} with an onset potential of +1.4 V_{RHE} for cathodic photocurrent. This is believed to be the first demonstration of $PrFeO_3$ photocathodes.

Dissemination of Thesis

Peer-reviewed articles:

Strategies for deposition of $LaFeO_3$ photocathodes: improving the photocurrent with a polymer template; Emma Freeman, Santosh Kumar, Veronica Celorrio, Min Su Park, Jong Hak Kim, David J. Fermin and Salvador Eslava, Sustainable Energy and Fuels, 2020, **4**, 884-894.

$PrFeO_3$ photocathodes prepared through spray pyrolysis; Emma Freeman, Santosh Kumar, Sophie R. Thomas, Hayley Pickering, David J. Fermin and Salvador Eslava, ChemElectroChem, 2020, **7**, 1-9

Electricity generation from moss with light-driven microbial fuel cells; Pablo Ampudia Castresana, Sara Monasterio Martinez, Emma Freeman, Salvador Eslava and Mirella Di Lorenzo, Electrochimica Acta, 2019, **298**, 934-942.

All-inorganic $CsPbBr_3$ nanocrystals: gram-scale mechanochemical synthesis and selective photocatalytic CO_2 reduction to methane; Santosh Kumar, Miriam Regue, Mark Isaacs, Emma Freeman and Salvador Eslava, ACS Appl. Energy Mater. 2020, DOI: 10.1021/acsaem.0c00195

Presentations of work:

Emma Freeman, Veronica Celorrio, David J. Fermin and Salvador Eslava, poster presentation, UK Solar Fuels Symposium, University of Newcastle, 27th Jan 2017.

Emma Freeman, Veronica Celorrio, David J. Fermin and Salvador Eslava, poster presentation, Photochemistry Symposium, University of York, 16-17th March 2017.

Emma Freeman, Veronica Celorrio, David J. Fermin and Salvador Eslava, poster presentation, Solar Fuels Network and SuperSolar Symposium, Imperial College London, 26th April 2017.

Emma Freeman, Veronica Celorrio, David J. Fermin and Salvador Eslava, poster presentation, CSCT Summer Showcase: Sustainable Chemical Technologies for a Circular Economy, University of Bath, 11th July 2017.

Emma Freeman, Min Su Park, Jong Hak Kim, Veronica Celorrio, David J. Fermin and Salvador Eslava, poster presentation, Materials Research Society (MRS) conference, Boston, USA, 26th November to 1st January 2017.

Emma Freeman, Min Su Park, Jong Hak Kim, Veronica Celorrio, David J. Fermin and Salvador Eslava, poster presentation, Speaking of Science, Cardiff University, 3rd May 2018.

Emma Freeman, Min Su Park, Jong Hak Kim, Veronica Celorrio, David J. Fermin and Salvador Eslava, poster presentation and poster prize winner, Great Western Electrochemistry Meeting, 16th July 2018.

Emma Freeman, Min Su Park, Jong Hak Kim, Veronica Celorrio, David J. Fermin and Salvador Eslava, oral presentation, UK&I Semiconductor Photochemistry meeting, Gran Canaria, 10th September 2018.

Emma Freeman, Min Su Park, Jong Hak Kim, Veronica Celorrio, David J. Fermin and Salvador Eslava, poster presentation, International Bunsen-Discussion-Meeting, Taormina, Italy, 1st April to 5th April 2019.

List of abbreviations

ALD: Atomic layer deposition

BET: Branauer, Emmett and Teller

ECSA: Electrochemically active surface area

EIS: Electrochemical impedance spectroscopy

FE-SEM: Field-emission scanning electron microscopy

FTO-ABS: Fluorine-doped tin oxide coated aluminoborosilicate glass

GC: Gas chromatograph

GPC: Growth rate per cycle

HER: Hydrogen evolution reaction

HR-TEM: High-resolution transmission electron microscopy

IPCE: Incident photon-to-current conversion efficiency

LFO: Lanthanum iron oxide

LSV: Linear sweep voltammetry

MIS: Metal-insulator-semiconductor junction

NHE: Normal hydrogen electrode

OER: Oxygen evolution reaction

ORR: Oxygen reduction reaction

PEC: Photoelectrochemical

PFO: Praseodymium iron oxide

PV: Photovoltaic

PVC-*g*-POEM: poly(vinyl chloride)-*g*-poly(oxyethylene methacrylate)

RHE: Reversible hydrogen electrode

UV-Vis: Ultraviolet-visible light spectroscopy

XPS: X-ray photoelectron spectroscopy

XRD: X-ray diffraction

Chapter 1

1 Introduction

1.1 Energy crisis

With growing world population there has been increasing negative impacts of human activity on the Earth's atmosphere. Processes such as deforestation, agricultural practises, burning fossil fuels, urban development and industrial processes have led to an enhanced global warming effect through the releasing of greenhouse gases. Atmospheric CO_2 has increased by 31 % since 1895, whilst other greenhouse gases such as methane and nitrous oxide have increased by 151 % and 17 % respectively.[1] It is vital that the research community and the general population understand the negative effects of greenhouse gases, and are aware of what actions that need to be taken to limit their detrimental impact. Globally, the Paris Agreement was established and signed in 2016 as part of the United Nations Framework Convention on Climate Change (UNFCCC). This outlines climate change targets such as limiting the increase of global temperature to well below 2 °C at a preferred level of 1.5 °C. With an additional strategy to reduce CO_2 emissions by 20 %, increase renewable energy market share to 20 % and have a 20 % increase in energy efficiency.[2] In the UK, the Climate Change Act (2008) works to commit the UK government to reduce greenhouse gas emissions by at least 80 % of 1990 levels by 2050.[3]

Burning fossil fuels is one of the major contributors to CO_2 emissions, and is a finite resource for our energy demands, hence alternative and renewable sources of energy are desperately needed. Such alternatives include wind farms[4], nuclear power[5], tidal power[6] and solar energy.[7] Table 1 shows that the sun can provide much more power than other sources of renewable energy, and also beneficially requiring a smaller proportion of the Earth's surface. In addition, the Sun's power can provide the world's energy demands for a year within one hour, and so if this energy was utilised more effectively then it could provide a sufficient alternative to fossil fuels. A study into the world's energy consumption by the International Energy Agency (IEA) shows that in 2050, solar array installations will supply approximately 45 % of the world's energy demand, demonstrating the feasibility and popularity of solar energy alternatives.[8]

Table 1: Estimated global power generation capacities. Adapted from ref.[9] with permission from Springer.

Energy source	Power (TW)	Remarks
Wind	4	Represents 10-15 % of global technical potential for on- and off-shore installations.
Hydroelectric	1-2	Remaining untapped potential is 0.5 TW.
Tidal	<2	
Geothermal	12	Only a small fraction can be exploited.
Biomass	10	Requires 10 % of Earth's land surface to be covered with switchgrass.
Nuclear	10	Required construction of a 1-GW_{peak} power plant every 35 h for the next 40 years. Finite uranium supplies imply need for fast breeder of thorium reactors.
Solar	<20	Required 0.16 % of the earth's surface to be covered with 10 % efficient solar cells. Total solar power reaching the Earth's surface is 120,000 TW.

One such way to utilise solar energy for electricity generation or energy storage, is through photoelectrochemical (PEC) processes which can include the generation of hydrogen through PEC water splitting. Hydrogen is receiving increased attention as it has a vast abundance within water and a wide range of organic compounds, and on oxidising releases just water and oxygen, which are non-toxic and environmentally friendly. However current production methods for H_2 include, partial oxidation, coal gasification, biomass pyrolysis and steam methane reforming. Natural gas accounts for 48 % of current global production of H_2 with oil, coal and electrolysis providing 30, 18 and 4 % respectively.[10] Steam reforming has shown to yield the highest hydrogen concentration compared with partial oxidation and autothermal reforming.[11]

Equation 1 $$CH_4 + H_2O \leftrightarrow CO + 3H_2$$

Equation 2 $$CO + H_2O \leftrightarrow CO_2 + H_2$$

Equation 3: Methane steam reforming $$CH_4 + 2H_2O \leftrightarrow CO_2 + 4H_2$$

The reforming processes involves the use of fossil fuels, such as methane, and emit CO_2 (Equation 3) and so are not currently a sustainably viable route for hydrogen production. Hence, solar energy can be utilised in order to satisfy this need for more renewable and less harmful H_2 generation alternatives. Photocatalytic water splitting involves the use of a photoactive semiconductor which absorbs photons of greater

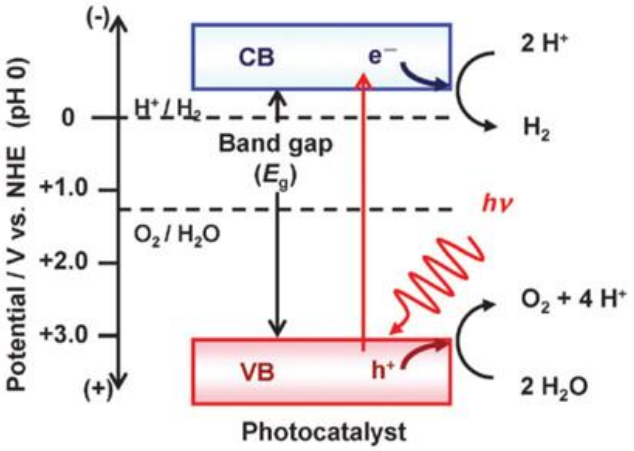

Figure 1-1: Photocatalytic water splitting using a photocatalyst with appropriate band gap energy. Adapted from ref.[12] with permission from the Royal Society of Chemistry.

energy than the band gap energy of the material, which promotes an electron from the valence band into the conduction band, creating electron-hole pairs. These photogenerated electrons in the conduction band, and holes in the valence band can then reduce H^+ ions into H_2 and oxidise H_2O to O_2 and H^+ ions respectively.[10] This is demonstrated in brief based on a one-step excitation in
Figure 1-1, that includes the potential energy levels required for water oxidation and reduction. This is currently a small-scale route for alternative H_2 production, that could be utilised for lab-scale reactions where small proportions of H_2 are required or for energy storage applications. For overall photocatalytic water splitting from powders, it has been calculated that a solar-to-hydrogen efficiency (STH) of 5-10 % is needed for it to be a commercially viable route for hydrogen production.[13] However, current photocatalysts such as doped $SrTiO_3$ and $BiVO_4$ powders achieve just 1 % STH, showing that further work is required to make this process more viable.[14] It can be noted that not all papers report or calculate STH, making it difficult to attain how close materials are to achieving this required efficiency.

Ultimately, when larger scale photocatalytic water reduction is achieved, this sustainable way of obtaining hydrogen can be potentially used within fuel cells for example. Within hydrogen fuel cells, H_2 enters at the anode and is oxidised to produce electricity, with just water and oxygen being formed during this process.[15] Using hydrogen within fuel cells is therefore of high potential due to its relative ease to

produce electricity, and its environmentally friendly nature. Additionally, their versatility means that they can be used in applications such as in cars[16] or in buildings.[17] In addition, photoelectrochemical water splitting can also be achieved to produce H_2, which benefits from the avoidance of dispersion effects that can cause problems within photocatalytic investigations. Hence, a further focused investigation into PEC processes and energy commitments can be explored.

1.2 Photoelectrochemical water splitting

Water can be electrolysed into its components O_2 and H_2 in the presence of a cathode, an anode and the application of an external potential. With respect to thermodynamics, the application of at least +1.23 V is required to electrolyse water under standard conditions, with a Gibbs free energy (ΔG) of 238 KJ mol^{-1}. These redox half reactions that occur at the anode and cathode to evolve O_2 and H_2 incur kinetic barriers associated with bond making and breaking. These barriers manifest themselves in the form of overpotentials at each electrode, in so increasing the voltage required to pass the given current density through the electrode/solution interface, relative to the voltage required to split water. An additional voltage is also required to overcome ohmic resistance exhibited in the aqueous electrolyte. The overall overpotential of the system is the sum of the kinetic overpotentials for the hydrogen evolution and oxygen evolution reactions, the concentration potential (depletion of reactant concentration relative to product), and the potentials required to overcome ohmic resistance.[18]

PEC cells can be used for water splitting reactions through the use of a photoelectrode and a metal counter electrode as demonstrated in Figure 1-2. The working electrode consists of a semiconductor which is able to convert incident photons to electron-hole pairs, which are separated from each other with an internal electric field. The photogenerated charge can then travel towards the conductive back contact of the working electrode, and then travel through an external circuit to a metal counter electrode. A commonly used configuration is that of a 3-electrode system that incorporates a reference electrode, such as a hydrogen electrode (RHE) or a silver/silver chloride reference electrode (Ag/AgCl). A potential is applied to the working electrode using a potentiostat with respect to the reference electrode of known

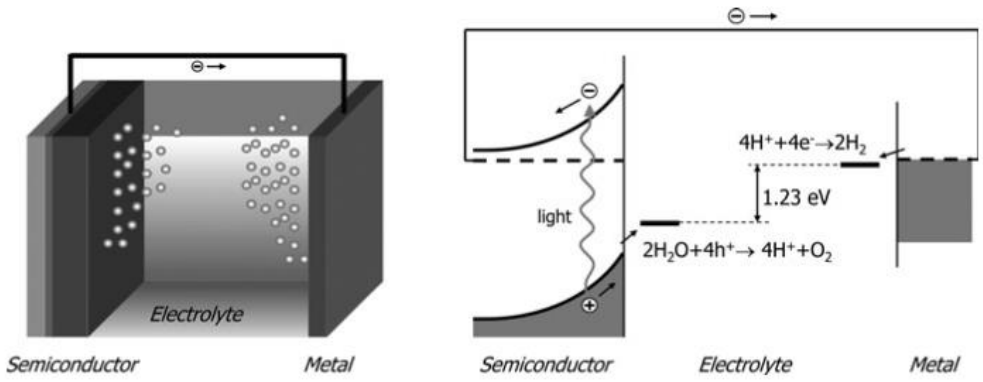

Figure 1-2: PEC cell consisting of a semiconductor photoanode and a metal cathode (left) with corresponding energy diagram (right). Reproduced from Ref.[9] with permission from Springer.

potential. On application of this bias, current flows either away or towards the working electrode depending on the type of semiconductor used. For an n-type semiconductor, photoexcited electrons (e^-) flow through the external circuit to the counter electrode which are the majority charge carriers, and photogenerated holes (h^+) travel to the semiconductor/electrolyte interface to oxidise water to oxygen. For a p-type semiconductor, photoexcited electrons in the conductance band reduce H^+ ions to H_2 in the electrolyte, with holes travelling to the back contact to combine with electrons flowing from the counter electrode. Here, the holes are the majority charge carrier with H_2 being evolved at the working electrode and oxygen from the counter

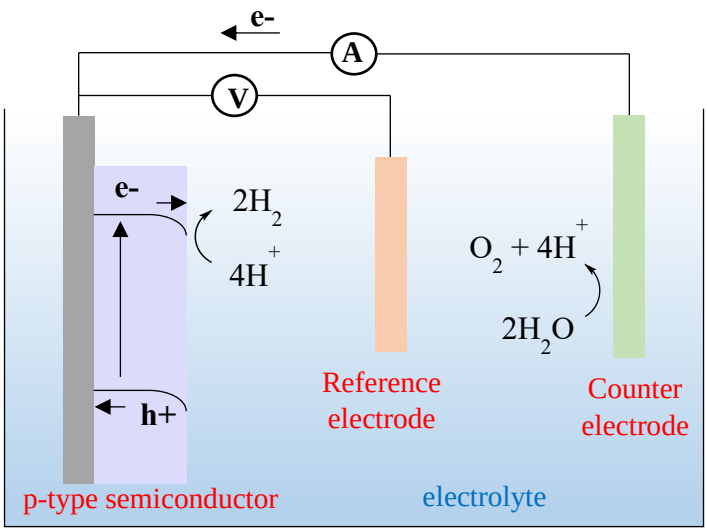

Figure 1-3: Diagram of 3-electrode PEC cell with a p-type semiconductor photocathode (own work).

electrode.[9] This common 3-electrode set-up is demonstrated in Figure 1-3 for a p-type semiconductor working electrode.

To fabricate the working electrode for a PEC system, an appropriate substrate with a conductive back contact for the semiconductor to be coated on is required, to allow for charge transport in the cell. The substrate needs to be both optically transparent as well as sufficently conductive. Transparent conductive electrodes are able to transmit light and conduct electrical current and so are of increasing importance in the area of photovoltaics. In particular, transparent conductive oxides (TCOs) have been studied for over 100 years, with early invesitgations being made into CdO, Cu_2O and PbO in 1907.[19,20] Today, tin oxide (SnO_2) is a popular TCO, with its wide gap it exhibits high optical transparency with the ability, on doping, to extensively enhance electrical conductivity.[21] Indium tin oxide (ITO) is one such doped tin oxide displaying a high electrical conductivity.[22] However, ITO thin films are limited due to the expense of indium and their toxicity.[23] Hence, it is wise to use non indium contianing doped-SnO_2 such as fluorine doped tin oxide (FTO), which displays good visible transparency due to its wide band gap whilst retaining a low electrical resistivity.[21]

When considering the overall process for PEC water splitting within any fabricated device, it is important to take into account the reduction and oxidation potentials for water, especially with reference to pH of the electrolyte. The Nernst equation can be used to observe the relationship between redox potentials and pH, as shown in Equation 4 and Equation 5.

$$E_{red} = E^{\circ}_{red} - \frac{RT}{4F} ln\left(\frac{\left[P_{H_2}\right]^2}{[H^+]^4}\right) = E^{\circ}_{red} - 2.3\frac{RT}{F}\left(log(P_{H_2})^{1/2} + pH\right)$$

Equation 4: Nernst equation to calculate water reduction potential.

$$E_{ox} = E^{\circ}_{ox} + \frac{RT}{4F} ln\left(P_{O_2}[H^+]^4\right) = E^{\circ}_{ox} + 2.3\frac{RT}{F}\left(log(P_{O_2}) - pH\right)$$

Equation 5: Nernst equation to calculate water oxidation potential.

When consdiering the pH dependance for the determination of potential, we can show that for alkaline conditions with pH 14 the water reduction and oxidation potentials can be demonstrated as:

$$Cathode: 4H_2O + 4e^- \rightarrow 2H_2 + 4OH^- \qquad E^\circ_{red} = -0.83\, V_{NHE}$$

$$Anode: 2H_2O + O_2 \rightarrow 4OH^- + 4h^+ \qquad E^\circ_{ox} = +0.40\, V_{NHE}$$

Equation 6: Water redox reactions in alkaline solution (pH 14).

The same can also be calculated for acidic conditions where pH = 0:

$$Cathode: 4H^+ + 4e^- \rightarrow 2H_2 \quad E^\circ_{red} = 0\, V_{NHE}$$

$$Anode: 2H_2O + 4h^+ \rightarrow O_2 + 4H^+ \; E^\circ_{ox} = +1.23\, V_{NHE}$$

Equation 7: Water redox reactions in acidic solution (pH 0).

In addtion, to allow for ease of comparisions between different PEC cell conditions, it is common to convert redox potentials to the reversible hydrogen electrode (RHE) as this measured potential does not change with pH. If experimentally a Ag/AgCl reference electrode is used, then the equivalent redox potentials can be converted to an RHE scale if the pH of electrolyte is known, using the following equation:

$$E_{RHE} = E_{Ag/AgCl} + 0.059 \times pH + E^0{}_{Ag/AgCl}$$

Equation 8: Modified Nernst equation for potential conversion.[24]

where E_{RHE} and $E_{Ag/AgCl}$ are the chosen reduction or oxidation potentials with respect to the reversible hydrogen electrode and the Ag/AgCl electrode respectively. $E^0{}_{Ag/AgCl}$ refers to the standard reference potential for Ag/AgCl (0.1976 at 25 °C). For example Depending on whether the working electrode is an anode or a cathode, the potential of reduction/oxidation at a given pH of electrolyte for a particular reference electrode can be determined.[24]

As well as the discussed 2 or 3-electrode PEC cell arrangements, they can also form part of more complex devices to enhance performance. For example, a PEC/PEC tandem cell can be created where there is an integration of a photoanode and photocathode that enables both electrodes to exhibit a beneficial photoresponse. This can allow for increased light absorption and charge generation.[25] In addition, another arrangement can be employed where PEC cells are coupled with photovoltaic (PV)

devices to create PEC/PV tandem cells. In this case, the PV cell can generate the applied bias needed between the photoelectrode and the counter electrode, hence the voltage required for water splitting is generated from a renewable energy resource.[26] Ultimately, for commercial use it would be required for large area PEC devices to be fabricated in order to up-scale water splitting to allow it to become more relevant. This has been investigated recently using a PEC/PV tandem device, incorporating a stand-alone a cobalt phosphate coated tungsten doped $BiVO_4$ (CoPi/W:$BiVO_4$) anode and series-connected silicon solar cells. This PEC/PV device was fabricated with an impressive area of 50 cm^2, however it was found that PEC performance was drastically diminished on scale-up from much smaller devices due to ohmic losses on the FTO substrate. Here, the main limitations to performance were found to be that of high resistivity of FTO and limited ionic conductivity of the electrolyte, demonstrating the issues associated with PEC device scale-up.[27]

When considering the realisation of larger scale PEC devices to produce hydrogen, there has to be a focus on achieving a lower cost per kg of hydrogen than current methods. The US department of energy calculated the cost of H_2 production for a 10 tonne per day production scale for various PEC systems to be at \$1.6-\$10.4 kg^{-1} of H_2, which is within the target threshold cost of \$2-\$4 kg^{-1} of H_2. This demonstrates that PEC water splitting can be a viable route for hydrogen production in the future if material performance requirements are met. A feasibility study has been carried out for photocatalytic and photoelectrochemical solar hydrogen generation, where solar-to-hydrogen efficiency (STH) is used to determine device performance (Equation 9).[28]

$$STH = \frac{j\ (mA\ cm^{-2})\ x\ 1.23\ V}{P\ (mW\ cm^{-2})}$$

Equation 9: Solar-to-hydrogen conversion efficiency calculation.

Here they calculated the upper limits of achievable efficiencies of materials subjected to solar AM 1.5 G illumination using maximum theoretical photocurrent for a given band gap, assuming a 100 % Faradaic conversion efficiency. Where these maximum theoretical photocurrents assumed all photons are absorbed and are converted to current.[29] Figure 1-4 shows the maximum theoretical limits for STH efficiency for a band gap of 2.26 eV is 11.2 % for a single absorber system. Hence ,when investigating

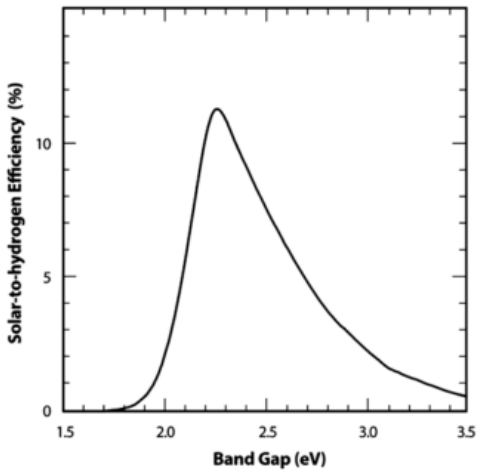

Figure 1-4: Maximum theoretical solar-to-hydrogen efficiency for a single absorber material as a function of band gap. Adapted from ref.[28]

appropriate materials for commercial PEC devices, STH efficiencies of close to 10 % are needed if they are to be used for cost effective solar hydrogen production.

1.3 Metal oxide semiconductors

The first demonstration of the use of semiconductors for the electrochemical photolysis of water was exhibited by Fujishima and Honda in 1972. They showed that using an illuminated TiO_2 and dark Pt electrode that stoichiometric amounts of H_2 and O_2 could be yielded.[30] This resulted in a vast increase in interest into the area of heterogeneous photocatalysts, with TiO_2 at the spear head. TiO_2 is photocatalytically active and has been demonstrated to be suitable in applications not only in water splitting[31], but in self-cleaning glass[32] and water purification systems[33]. In general, for a semiconductor to be a suitable photoelectrode, it has to meet certain criteria in areas such as, light absorption, charge separation and diffusion to electrode surface, and charge injection into an electrolyte to oxidise or reduce water. Metal oxides are becoming popular candidates for this due to their suitable band edge positions, chemical stability, low cost and tuneable band gaps (Figure 1-5). The band gap of the material dictates how it will behave under illumination of light with respect to absorption. Metal oxides such as TiO_2, ZnO and $SrTiO_2$ have wide band gaps that provide a suitable band edge position for water electrolysis potentials but are not optimal for visible light absorption.[34]

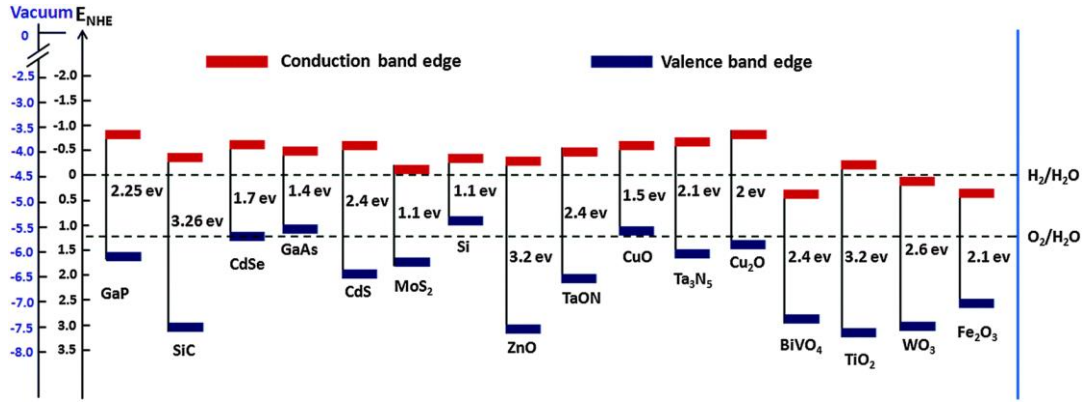

Figure 1-5: Band edge potentials for various semiconductor materials. Reproduced from Ref.[35] *with permisison from The Royal Society of Chemistry.*

When metal oxide semiconductors are used within PEC devices, an important factor to consider is that of the semiconductor/electrolyte interface (SEI) on light illumination. This interaction at the interface determines electron-hole separation kinetics. At the SEI the redox level (E_{redox}) of the electrolyte is lower than the fermi level (E_f) of the semiconductor. This results in a change in the electrochemical potential across the junction, due to electrons crossing the interface from the semiconductor to the electrolyte. This continues until an equilibrium is reached ($E_f = E_{redox}$) and bend bending occurs within the semiconductor towards the fermi level. This created space charge layer (SCL) is attributed to the accumulation of electrons or holes at the surface.[36] This allows for a Schottky junction to be formed, which is an important element when considering charge separation as it allows charge to travel in just one direction. A demonstration of this can be seen in Figure 1-6, showing the

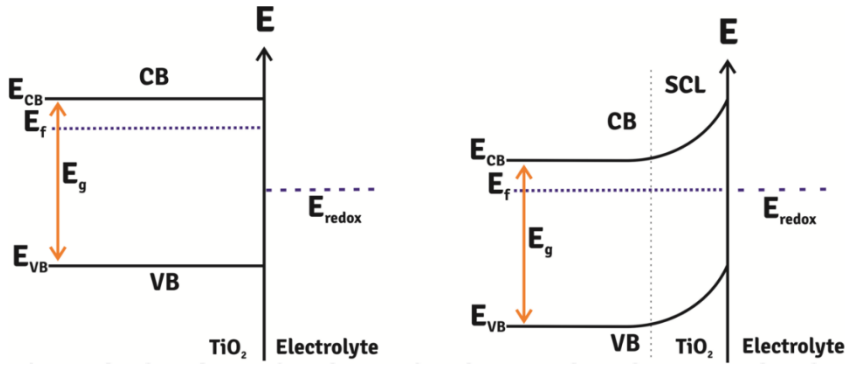

Figure 1-6: Energy band diagram for an n-type semiconductor (TiO_2) before equilibration of E_f and E_{redox} at the SEI (left), and after with the appearance of band bending within the SCL. Reproduced from Ref.[36]

energy band diagram of TiO_2 before and after equilibration on contact with an electrolyte on light illumination.

Various metal oxides can be used as either n-type photoanodes or p-type photocathodes. As mentioned previously, TiO_2 is the most widely studied semiconductor for water splitting and has a band gap of 3.2 eV which, when converted to wavelength using Planck's equation, follows that it absorbs light in the region of 387 nm, which lies within the ultra-violet region of the light spectrum. Ideally, an efficient photocatalyst would be able to absorb light in the visible light region, as this forms a large part of the solar light spectrum. There are also intrinsic limitations in wide band gap semiconductors. For example, titania has a hole diffusion length of 10 nm that would give rise to increased chances of electron-hole recombination.[34] As well as titania, Fe_2O_3 has become an extremely popular photoanode for water splitting. Hematite (α-Fe_2O_3) has been studied extensively due to advantages such as abundance, high photochemical stability, non-toxicity and narrow band gap (1.9-2.2 eV). Limitations of hematite however include poor carrier collection, light absorption and sluggish oxygen evolution reaction kinetics.[35] It has been reported for a hematite photoanode doped with platinum, that a photocurrent density of +4.32 mA cm^{-2} at +1.23 V_{RHE} has been achieved.[37]

Additionally, tungsten oxide has also become popular due to its suitable band gap and its activity for water splitting. On preparing WO_3 films through atomic layer deposition (ALD) with a stabilised Mn oxygen evolution catalyst, energy conversion efficiencies of 1.1 % (at +0.8 V_{RHE}) and high stability in neutral solutions was found. But WO_3 can still suffer with weak absorption in the visible light region.[38] $BiVO_4$ (BVO) has also been demonstrated as an appropriate n-type semiconductor for water splitting, achieving a quantum yield of 1.6 %.[39] BVO is showing promise for water oxidation but is reported to be limited by slow kinetics and poor charge separation, that has been somewhat alleviated by the addition of Co-Pi which allowed for a photocurrent of +1.7 mA cm^{-2} at +1.23 V_{RHE} to be achieved.[40] There is abundant research detailing the activity of photoanodes for PEC processes, hence further focus should be directed in finding stable p-type materials, that can replace expensive Pt electrodes and are able to exhibit beneficial photoresponses.

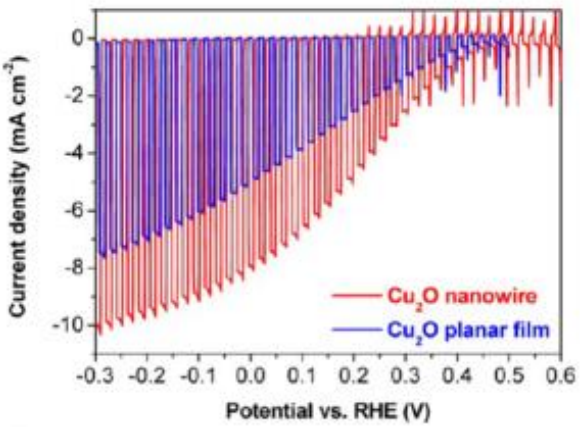

Figure 1-7: J-V curves under chopped simulated sunlight for protected Cu_2O nanowires compared to planar Cu_2O films. Adapted from Ref.[41]

Cu_2O is a p-type semiconductor that has been shown to be active for water reduction and has a favourable energy band position, with a band gap of 2 eV. However, it is limited due to poor stability in aqueous solutions due to the redox potentials for monovalent copper oxide lying within the band gap.[42] Due to this, protection layers are required, for example TiO_2 has been used as an overlayer and achieved a photocurrent density of -7.6 mA cm^{-2}, with a theoretically achievable photocurrent of -14.7 mA cm^{-2}.[42] Also, on fabrication of a $Cu_2O/Ga_2O_3/TiO_2/RuO_x$ photocathode, a photocurrent of -6 mA cm^{-2} at +0.5 V_{NHE} was recorded.[43] Impressively, on application of conformal TiO_2 layers and RuO_x co-catalysts onto Cu_2O nanowires, a photocurrent of -10 mA cm^{-2} was exhibited, with stable operation over 10 hours and with a photocurrent onset +0.48 V_{RHE}, showing benefits over planar films (Figure 1-7).[41]

There has been a more recent publication that has created an impressive benchmark for a high performance p-type semiconductor, outperforming Cu_2O. Sb_2Se_3 has been used as a photocathode with a TiO_2 layer and RuO_x catalyst, and has demonstrated a record photocurrent of close to 30 mA cm^{-2} at 0 V_{RHE} with close to 100 % IPCE (Figure 1-8). This exceeds that achieved for any other p-type photocathode. These Sb_2Se_3 electrodes were prepared through a close space sublimation process (CSS), a form of physical vapour deposition. It displays a band gap of 1.2 eV, and as well as being low cost, shows high charge mobility and high photostability unlike Cu_2O. A tandem device was then created with $BiVO_4$ as the photoanode to achieve unassisted overall water splitting with an STH efficiency of 1.5 % and high stability over 10 h. However,

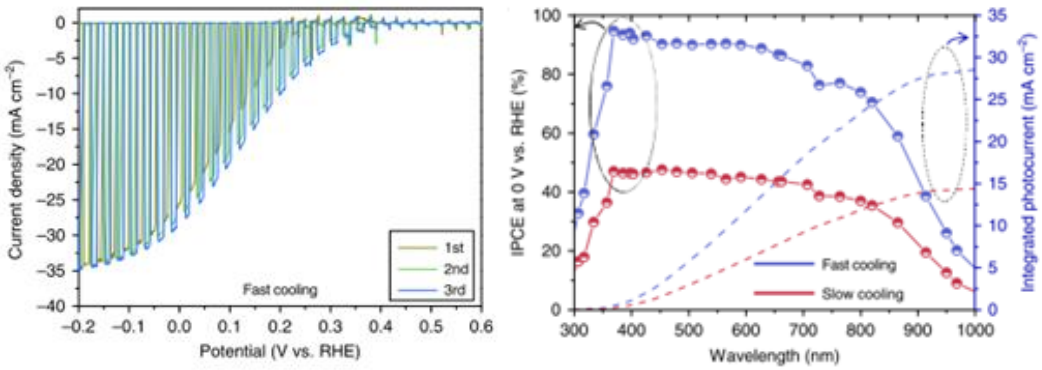

Figure 1-8: PEC performance of RuOx/TiO_2/Sb_2Se_3/Au/FTO photocathodes with calculated IPCE values. Adapted from Ref.[44]

due to this small band gap of Sb_2Se_3, there are limitations in light absorption and hence ultimate restrictions in solar-to-hydrogen conversion efficiencies as seen in Figure 1-4. In addition to this, as mentioned previously, an STH efficiency of approximately 10 % is required to allow PEC processes to become commercially viable, highlighting further work needed.

These photocathodes have been prepared through a chemical bath deposition method and exhibited a photocurrent density of -7.0 mA cm^{-2} at -0.3 V_{RHE} with an onset potential of +0.48 V_{RHE}. This was achieved through the addition of a CdS buffer layer, TiO_2 protection layer and RuO_x HER catalyst.[45] Cupric oxide (CuO) films have also been successfully investigated for PEC water reduction. CuO consists of an optical band gap of 1.5 eV and has a greater optical absorption and theoretical maximum photocurrent (-35 mA cm^{-2}) than Cu_2O, but poor crystallinity and photostability limits the activity of CuO. Thin films of CuO have been deposited onto FTO-coated glass and demonstrated a photocurrent density of -2.5 mA cm^{-2}.[46] In addition to this, Cu_2O/CuO have been fabricated in order to increase stability and showed increases in photocurrent when compared to Cu_2O and CuO alone.[47,48] Despite these relatively large photocurrents obtained for these discussed p-type semiconductors, they continually require the application of protection layers to maintain high photocurrents, which is problematic due to any failure in these coatings leading to fast electrode corrosion. In addition, these p-type photocathodes (e.g Cu_2O) exhibit relatively low cathodic onset potentials of +0.48 V_{RHE}, demonstrating a lack of activity over a large potential range.[41] More recent work however has demonstrated more positive onset

potentials of +1.0 V_{RHE} for Cu_2O, but required extensive modification.[49] Hence, it is much more beneficial to investigate inherently more stable metal oxides, that do not require extensive protection and have improved photocurrent onset potential. Further materials that have gained much popularity in recent years are perovskite compounds, which have shown photocatalytic activity with many showing good stability.

1.4 Perovskite semiconductors

Perovskites are a group of mineral compounds that initially referred to calcium titanate ($CaTiO_3$), but by definition has broadened to a class of compounds that have the same crystal structure as $CaTiO_3$. The general formula of perovskite compounds is ABX_3, where A and B are two cations of different sizes, and X is an anion that bonds to A and B. The ideal structure has a cubic symmetry, where the B cation is 6-fold coordinated and the A cation is 12-fold coordinated, surrounded by an octahedron of the X anions. There is a wide variety of compositions of perovskites in which the A cation is usually larger than the B cation, whereby the overall properties of the compound is determined by the cations. Common structures include halide perovskites where X is F, Cl, Br, or I, and perovskite oxides with have the general formula ABO_3 (Figure 1-9).[50] Perovskites have more favourable band gap positions than other materials, hence many are active in the visible light region and additionally have high structural flexibility, making them promising candidates for PEC processes.

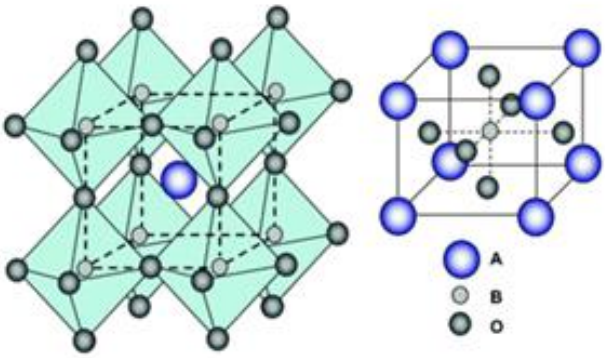

Figure 1-9: ABO_3 perovskite structure (left) and corner sharing BO_6 with B-site cation in the centre of the cell (right). Adapted from Ref.[51] with permission from the Royal Society of Chemistry.

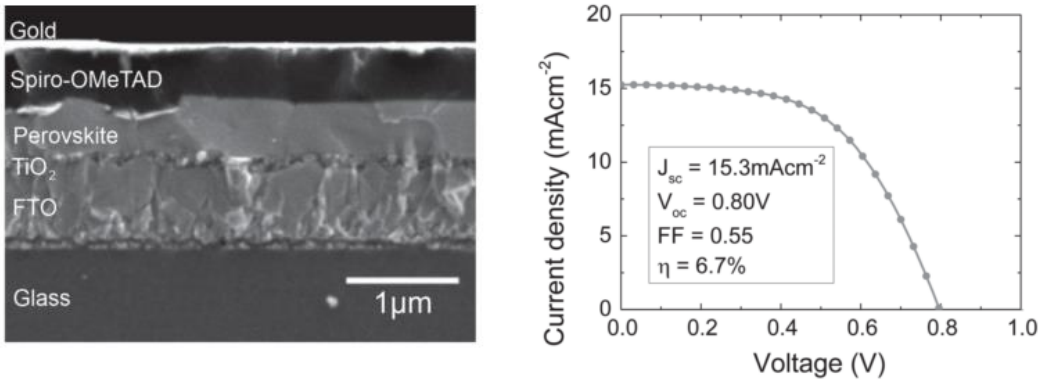

Figure 1-10: Cross-section SEM of planar heterojunction perovskite solar cell (left) and average current-voltage characteristics measured under AM 1.5 sunlight (right). Adapted from Ref.[52]

Perovskites have shown to be active in various photocatalytic processes such as that in photovoltaics, degradation of organic dyes and in water splitting reactions. Perovskite structures based on organolead trihalide compounds have been well studied and shown to be very effective in hybrid solid-state solar cells. Efficiencies have been reported as high as 12.3 %.[53] In particular, $CH_3NH_3PbI_{3-x}Cl_x$ has been widely demonstrated to be effective as part of a thin film architecture within solar cells. It can act as the intrinsic absorber and electron transporter within a perovskite solar cell, and has been fabricated at low temperatures with efficiencies of 11.4 % shown in Figure 1-10. There is a high dependency on morphology of these perovskite films on achieving high surface coverages.[52] Organo-inorganic lead halide perovskites are highly efficient in applications such as solar cells, but are limited through issues of stability, especially in the presence of water, and the toxicity of the use of lead compounds.[54] Making them largely inappropriate for water splitting reactions.

However, more recent work has made progress in making halide-based perovskites more stable in the presence of water, in order to increase their viability for water splitting applications. It has been demonstrated that a fusible InBiSn alloy can be used to protect $CH_3NH_3PbI_3$ from water which allowed for a photocurrent of -9.8 mA cm^{-2} at 0 V_{RHE} (retaining 80 % of photocurrent after 1 hour) to be achieved.[55] Gao et al also used InBiSn to protect $CsPbBr_3$, where a photocurrent of -1.2 mA cm^{-2} at 0 V_{RHE} was recorded, in which 94 % remained after constant illumination over 1 hour.[56] Additional work by Poli et al also achieved high water stability for $CsPbBr_3$, through

using a commercial thermal graphite sheet and a mesoporous carbon layer for protection.[57] Despite these advances it is clear that halide-based perovskites are not ideal candidates for water splitting reactions, due to the need for protection layers and the use of toxic Pb, as well as the difficulties associated with lead halide perovskite synthesis.

Perovskites that are more stable and suitable for PEC water splitting applications are that of perovskite oxides (ABO_3). The crystal structure of these involve a BO_6 octahedra and 12 oxygen coordinated A cations, resulting in a cubic lattice. Depending on the ionic radii and electronegativity of the A and B site cations, tilting of the octahedral takes place which can yield different perovskite crystal geometries. Several perovskite oxides have sufficiently cathodic conduction bands for hydrogen evolution, with the A and B site cations providing a broader scope for design and potential altering of band structure and photophysical properties.[58] This further demonstrates the advantages of using perovskite compounds due to this inherent structural flexibility.

There are many groups of perovskite oxides that have shown activity for water splitting. Titanate based perovskites for instance have been studied for their photocatalytic activity, and most commonly have a band gap value of more than 3.0 eV, that show good photocatalytic properties under UV light. They also have a more negative conduction band than TiO_2 and so are more suitable for hydrogen evolution. Additionally, they have good photostability and corrosion resistance in aqueous solutions.[58] Doping of titanates allows for beneficial band gap shifts into the visible light region. Rh-doped $SrTiO_3$ prepared thin films functions as a photocathode for PEC water reduction under visible light, achieving 0.18 % incident photon-to-electron conversion efficiency (IPCE).[59] Other titanate perovskites such as Rh-doped $BaTiO_3$[60] and Cu-doped $CaTiO_3$ are also catalytically active.[61] Tantalate perovskites, similarly to titanates, have shown to be efficient for overall water splitting, but also require the use of dopants to achieve visible light activity. Bi-doped $NaTaO_3$ has shown to significantly affect activity for hydrogen evolution, with the Na/Ta ratio being close to unity allowing for the band gap to be narrowed to 2.64 eV.[62]

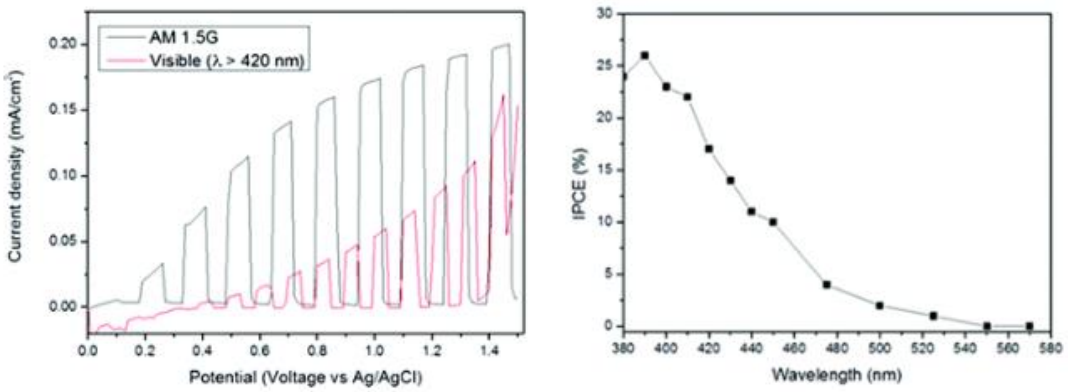

Figure 1-11: J-V curves under chopped simulated sunlight and visible light (left) and IPCE spectrum measured at +1.2 V_{RHE} for $BiFeO_3$ photoanodes. Adapted from Ref.[63]

Another group of perovskite oxides that have become increasingly popular are that of ferrite perovskites. The main advantage of these ferrite perovskites is that the majority possess band gaps encompassing the visible light region, avoiding the need of dopants to provide visible light activity. Iron oxide containing compounds such as hematite have previously shown problems such as poor light absorption, low charge separation efficiency and short excited state lifetimes.[35] Ferrite-based perovskites on the other hand have displayed good photoactivity for water splitting, perhaps going some way into providing a useful alternative to binary iron oxides.[58] $BiFeO_3$ (BFO) for example has a band gap of 2.3 eV, and on doping with Gd an increase in activity for the photocatalytic degradation of rhodamine B was seen.[64] Additionally, on Ca doping of BFO nanofibers, improvements for the degradation of Congo Red dye was also shown.[65] BFO has been studied as both a photocathode and photoanode, with respect to water reduction, it has displayed a photocurrent of -4 µA cm^{-2} at 0 V_{RHE} that increased to -70 µA cm^{-2} on addition of Ag.[66] Other work achieved higher photocurrents of -60 µA cm^{-2} for bare BFO.[67] Studied as a photoanode it has displayed activity of +170 µA cm^{-2} at +1 V_{RHE} with an IPCE of 23 % at 400 nm as shown in Figure 1-11.[63] BFO clearly demonstrates both p and n-type conductivity, which is thought to be due to the strain induced by the large Bi^{3+} ions that can have strong influences on electronic structure.[68] Due to this, it could be beneficial to consider ferrite perovskites that contain smaller A-site cations, such as $LaFeO_3$.

$LaFeO_3$ (LFO) has been studied for a wide range of photocatalytic processes. It has been shown to be active for the photocatalytic degradation of rhodamine B (RhB) and

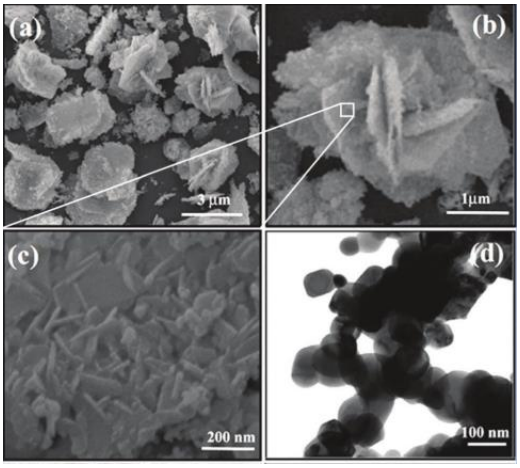

Figure 1-12: (a-c) SEM micrographs of the $LaFeO_3$ floral nanostructures and (d) TEM micrograph. Reproduced from ref.[69]

methylene blue (MB), with a beneficial effect found in having floral like nanostructures over bulk $LaFeO_3$ (Figure 1-12).[69] It has also been shown to outperform P-25 TiO_2 in photocatalytic degradation of Rhodamine B when synthesised using a sol-gel method.[70] Additionally, it has also been studied for its activity for hydrogen evolution from water, where on loading with a Pt co-catalyst, showed an impressive yield of 3315 μmol h^{-1} g^{-1}, with a calculated band gap of 2.07 eV.[71] This exceeds the hydrogen evolved from other perovskite oxides, such as Rh-$SrTiO_3$ and $PrFeO_3$ with Pt co-catalyst loadings, which achieved hydrogen evolutions of 962 and 2847 μmol h^{-1} g^{-1} respectively.[72,73] More understudied ferrite perovskites such as $YFeO_3$ and $PrFeO_3$ have also shown activity for water reduction.[73,74] Due to this activity for PEC processes, including hydrogen evolution, coupled with its visible light activity and the general advantages of using perovskite oxides, a closer look at the catalytic potential of $LaFeO_3$ is of interest. In addition, the exploration of little-known materials such as $PrFeO_3$ could be of benefit. Overall, on looking at these various metal oxide semiconductors for photocatalytic applications, with a closer look at perovskites, there appears to be a selection of common limitations, including electron-hole recombination, limited stability and poor light harvesting. It is therefore useful to explore in more detail the various techniques that have been commonly implemented to alleviate these issues.

1.5 Improving photocatalytic activity in semiconductors

1.5.1 Dopants

One of the major limitations with some semiconductors is that of wide band gaps, inferring the inability to absorb light in the visible light region. When utilising solar energy, it is important for photocatalysts to absorb as much of the available light as possible. Hence, techniques such as doping can narrow band gaps and modify electronic properties through introducing impurities with energy states within the band structure of a material. This can vastly improve, for example, the electrical conductivity of TiO_2.[34] Titania has been studied extensively in order to increase its ability to absorb light in the visible light region. Techniques employed include metal-ion doping such as Pt and Cr[75] and non-metal doping.[76] In example, nitrogen and indium co-modified titania prepared through a sol-gel method was found to improve photocatalytic activity for the degradation of 4-chlorophenol. The surface-state energy levels of the introduced species on the TiO_2 surface were located close to the valance and conduction bands, potentially leading to greater visible light absorption.[77]

Metal ion doping can also have positive effects on overall activity, as well as effecting the crystal structure of a catalyst. Al^{3+} has been doped into methyl ammonium lead iodide perovskite films for solar cells, through combining of aluminium acetylacetone with $MAPbI_3$ precursors. It was found that the electronic qualities of the $MAPbI_3$ films were extensively enhanced by low level doping of Al^{3+}. In the presence of metal ion doping, there was reduced microstrain in the perovskite crystal, suggesting a reduction in crystal defects. An increase in luminescent properties and reduced electronic disorder were also seen, demonstrating the value of metal ion doping.[78] Dopants can also be used in way of metal ion replacement within a catalyst structure. Transition metals such as Mn, Co and Cu have been doped into $LaFeO_3$ at a loading of 10 %, resulting in metal replacement of the iron atoms within the perovskite structure. This was then tested for PEC water oxidation under visible light, with Cu doping ($LaFe_{0.9}Cu_{0.1}O_3$) being found to be the most effective, achieving a photocurrent of +0.99 mA cm^{-2}, 3 times higher than that of pure $LaFeO_3$.[79] It has also been shown that metal ion doping can decrease distortion of the BO_6 octahedra structure within perovskite oxide materials ($LaCu_{0.5}$ $Rh_{0.5}O_3$ and $LaMn_{0.5}Rh_{0.5}O_3$). This can ease

crystal structure strain and hence go onto improve catalytic efficiency.[80] Substitutional doping of La^{3+} with K^{+} has also been done with $LaFeO_3$ which was found to increase charge transport properties and decrease electron-hole recombination, and was shown to increase photocurrent by more than double to -268 μA cm^{-2} at 0.6 V_{RHE}.[81]

1.5.2 Co-catalysts

Co-catalysts can also be introduced to semiconductors to enhance activity of either the oxygen evolution reaction (OER) or hydrogen evolution reaction (HER), these co-catalysts are usually small metal nanoparticles. The contact between the semiconductor and the metal co-catalyst creates an electric field that separates electrons and holes more easily, which can help prevent recombination. If the metal's work function (ϕ_m) is larger than that of the semiconductor (ϕ_s) then the electrons will transfer from the semiconductor to the metal until an equilibrium is reached, whereby both fermi levels are at the same energy level. Hence, a depletion layer is formed in the semiconductor as there is a lower concentration of electrons at the interface with the metal, compared to the bulk of the semiconductor. A repulsion between the depletion layer and the negatively charged metal surface now exists, resulting in band bending and therefore a Schottky contact is formed (Figure 1-13).[82] Hence, the presence of metal co-catalysts can assist in charge transport to the electrolyte and in increasing the activity of the semiconductor for PEC processes.

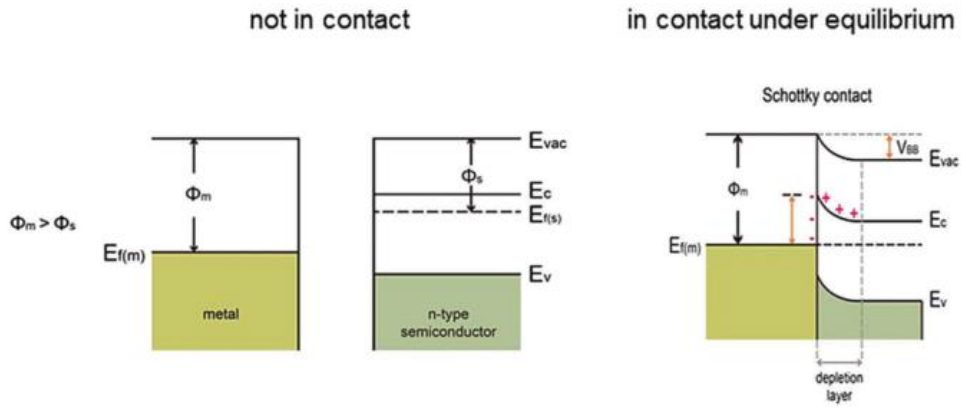

Figure 1-13: Schematic of the energy band model of a Schottky junction between a semiconductor and metal co-catalyst before and after contact. Adapted from Ref.[82] *with permission from the Royal Society of Chemistry.*

Co-catalysts can be deposited through two main techniques, photodeposition and impregnation.[83] Pt has been used extensively to assist in H^+ reduction in materials such as TiO_2[84], Cu_2O[42] and $LaFeO_3$[85] amongst many others. IrO_2 can also be used as a co-catalyst to assist in the O_2 generation during water oxidation.[86] Further investigations have involved the beneficial effects of using core shell co-catalysts. Bai et al developed an atomically controlled Pd@Pt core shell co-catalyst combined with anatase TiO_2, that allowed for an increase of water splitting efficiency by a factor of 322 when compared to bare TiO_2. Electron trapping by the Schottky junction can be promoted through the charge polarization taking place at the interface of Pd and Pt, which prolongs carrier lifetime through facilitating charge separation.[87] Moreover, as discussed previously RuO_x has been used as a hydrogen evolution catalyst on Cu_2O, that both catalyses HER and can also improve stability.[43,41]

1.5.3 Heterojunctions and composites

Another widely used technique to improve activity in a PEC system is to introduce an additional semiconductor, metal or molecule that can lead to the formation of a heterojunction structure between them, known also as composite materials. These systems can allow for reduced electron-hole recombination rates which can in turn increase overall efficiency. These structures can enhance photocatalytic activity through the migration of excited electrons from one semiconductor to another, the second in which would commonly have a higher efficiency than that of the first. There are 3 main types of heterojunction based on the position of the valence and conduction band of each semiconductor as shown in Figure 1-14. Type 1 usually does not contribute to increases in activity of the system due to both electrons and holes moving to one semiconductor, resulting in an accumulation. Type 2 allows for increased charge separation efficiency, longer lifetime of charge carriers and decreased rates of recombination. This is achieved through semiconductor 2 having a lower conduction and valence band than semiconductor 1, allowing for electron and hole transfer between the two in opposite directions. Type 3 consists of one of the semiconductors having both the conduction and valence band lower than the other. Here, an electron mediator is required to connect the two semiconductors.[83]

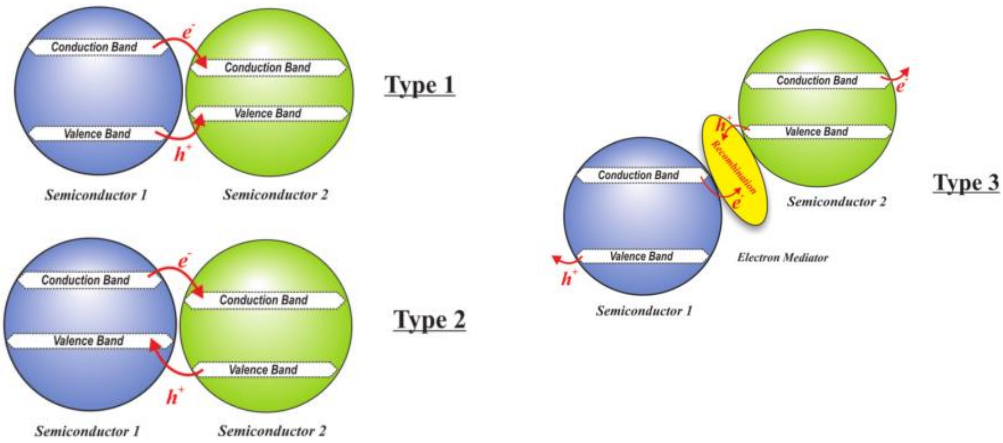

Figure 1-14: Three types of heterojunction formed between two different semiconductors. Adapted from Ref.[83] *with permission from The Royal Society of Chemistry.*

Many successful heterojunctions have been reported in the literature. For example, a Fe_2O_3/SnO_2 nanostructured heterojunction has been fabricated, which demonstrated a 34 % photocurrent increase when compared to Fe_2O_3 alone, due to longer electron lifetime provided by the heterojunction.[88] Moreover a 20 % increase in photocurrent was achieved on creation of a WO_3/Fe_2O_3 composite when compared to control hematite films.[89] Additionally, on creation of a $WO_3/BiVO_4$ heterojunction, increases in both photoconversion efficiency and photocorrosion stability were found, compared to tungsten oxide alone.[90] It is clear that the fabrication of heterojunctions can have a significant impact on the electronic properties of a semiconductor, which can lead to vast increases in overall photocatalytic activity.

Another material that has been studied is graphene, a type of carbon nanomaterial with outstanding conductivity and electron mobility properties with a high specific surface area. Graphene can help facilitate charge separation and migration within a photocatalytic system, and can be used to assist in applications such as water splitting and CO_2 reduction.[91] Additionally to graphene, reduced graphene oxide (rGO) and graphene oxide (GO) have been used as mixed composite materials to enhance catalytic activity. It has been shown that incorporating hematite nanoparticles on the surface of rGO nanosheets results in increases in photocurrent and reduces the rate of charge recombination. Transient absorption and time-domain tetrahertz spectroscopy

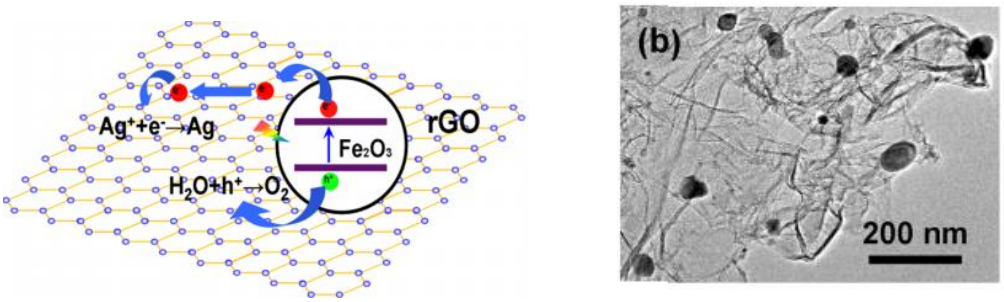

Figure 1-15: Schematic of charge transfer in α-Fe_2O_3/rGO composite (left) and TEM micrograph of the composite (right).Adapted from Ref.[92]

have shown that the photogenerated electrons have transferred from hematite to rGO, resulting in the reduction of charge recombination (Figure 1-15).[92] Other materials such as $LaFeO_3$[93], TiO_2[94] and Cu_2O[95] have all shown to benefit from the use of rGO as a composite/template for various photocatalytic applications. Graphene based composites could be limited however due to the high levels of light absorption by graphene containing materials, which could reduce the level of exposed light to the photocatalyst, decreasing efficiency.

1.5.4 Passivation layers

The incorporation of passivation/blocking layers have also been employed, especially in the areas of perovskite solid state solar cells, in order to promote charge separation. The role of an electron transport layer (ETL) is to form an electron-selective contact with, for example a perovskite (light absorbing) layer, to improve extraction efficiency of electrons. This also prevents the migration of holes to the counter electrode, hence reducing charge recombination.[96] There are a selection of materials that have been investigated for their ability to behave as effective transport layers, such as ZnO that can be used as an ETL within film architectures to help charge separation and transport.[56] Hole transport layers (HTL) can be additionally used and are especially beneficial for photocathodes. For example, NiO can be deposited onto the glass substrate prior to the p-type semiconductor, to assist in hole transport to the back contact and has benefits of high hole mobility and good stability. This has been demonstrated for Cu_2O photocathodes, and was shown to enhance performance through improving charge carrier transport at the back contact due to extracting

photogenerated holes from Cu_2O.[97]

Another technique is to apply blocking layers onto metal oxides to prevent detrimental charge transport to the electrolyte. It has been previously seen with $LaFeO_3$ photocathodes that there is a competition for holes with water oxidation at the electrolyte[98], hence a TiO_2 hole blocking layer has been successfully implemented to vastly enhance PEC responses for HER.[99] Additional work into WO_3 photoanodes has shown that an interfacial blocking layer can be created using an initially deposited mesoporous polymer templated WO_3 layer, with subsequent hydrothermal growth of WO_3. This allowed for the reduction of interfacial charge recombination at the FTO surface due to the mesoporous layer blocking electrons and holes from recombining at exposed areas of FTO.[100] It is clear that the application of charge transport or blocking layers can be extremely beneficial in enhancing charge separation, through directing charge carrier transport. This can be especially relevant in cases where charge recombination or competitive PEC processes are typically problematic.

1.5.5 Surface modification

The nanostructure of catalytic materials is of great interest and importance to catalytic efficiency, and so modification of resulting surface structures of metal oxide semiconductors can be beneficial. During synthesis, surface structure of a desired material can be altered in order to display desired surface morphology, such as larger surface areas and better substrate coverage. For example, the preparation of Cu_2O nanowires were superior in performance to that of planar Cu_2O due to increased surface area that allows for greater light absorption, and increased ease of charge transport, highlighting the benefits of morphology considerations.[41] As well as choice of preparation method dictating advantageous nano structuring, various techniques have been studied such as polymer templating to manipulate surface structure. For example, polyethylene glycol has been used to template titania to achieve a nanospider morphology (Figure 1-16) with large homogeneity, with an efficient application to photocatalytic degradation of methylene blue. On templating, a photocurrent density was two times larger than a thin film with no templating.[101] This shows how vital the surface structure of metal oxides have on the overall efficiency of the system, and hence should always be considered when fabricating electrodes. Additionally, α-

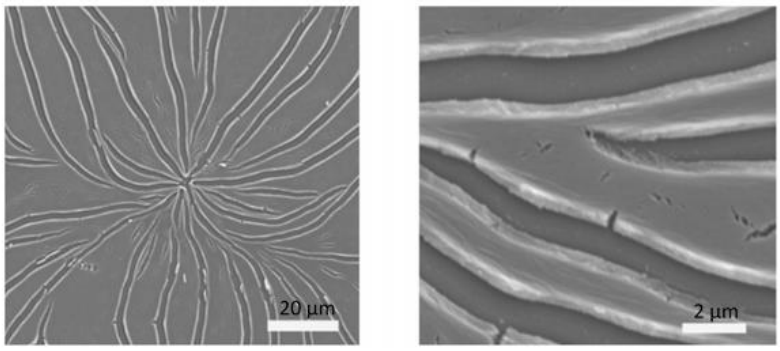

Figure 1-16: SEM micrographs of TiO_2 nanospider film on FTO glass templated with polyethylene glycol. Adapted from Ref.[101]

Fe_2O_3/PVA/PEG nanocomposite films have been synthesised and found to be more semiconducting in nature with a higher dielectric constant measured.[102] Another type of template used is that of activated carbon, which acts as a structure-directing hard template. This has been used for the preparation of tantalates (Ta_2O_5 and $NaTaO_3$) which was shown to improve photocatalytic performance.[103]

Poly(vinyl chloride)-g-poly(oxyethylene methacrylate) (PVC-*g*-POEM) has also been used as an efficient copolymer template for SnO_2. This graft copolymer has both a hydrophilic (POEM) and a hydrophobic component (PVC), in which metal oxide precursors can bind to the POEM side chains as shown in Figure 1-17. After high temperature calcination, the polymer is removed resulting in a highly porous structure with improved electron transport and suppression of recombination. High porosity can help increase the contact between the catalyst film with the surounding electrolyte in a PEC cell, and was able to enahnce the activity in a dye-sensitised solar cell.[104] This graft copolymer has also been used in templating for $MgTiO_3$ and TiN films.[105,106] This demonstrates a highly valuable polymer templating method that can be used to increase uniformity of films, as well as increasing microporosity that can be useful within PEC cells. More commercially available polymers have also been used such that of Triton X-100 (polyoxyethylene octyl phenyl ether) which is a non-ionic surfactant with a hydrophilic polyethylene oxide chain and hydrophobic aromatic group. This has been used to prepare porous photoelectrodes, for example in TiO_2, $LaFeO_3$ and $YFeO_3$ fabrication.[74,107,108]

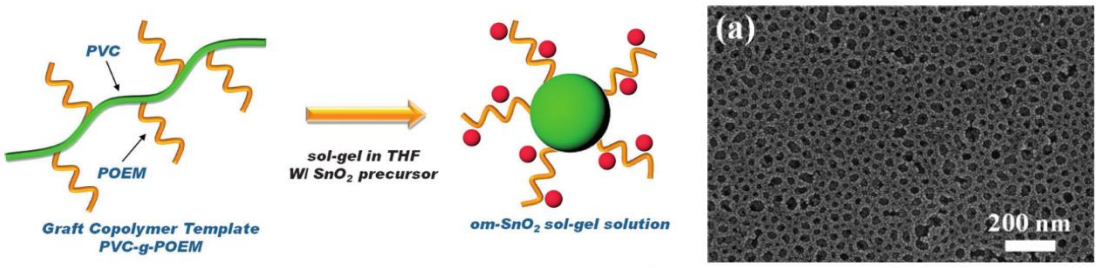

Figure 1-17: Schematic of the templating of SnO_2 with PVC-g-POEM through a sol-gel synthesis and FE-SEM micrograph of templated SnO_2 (right). Adapted from Ref.[104] *with permission from Wiley.*

Graphene oxide (GO) can also be used as a sacrificial template to alter resultant surface morphology. Polyoxotitanium clusters have been combined with GO and then heated to high temperatures to remove GO, in order to form pure titania which has replicated GO's unique 2D honeycomb network. This acts to increase surface area through directing nucleation and growth and ultimately increase photocatalytic activity for hydrogen evolution.[109] It appears the use of GO as a sacrificial template has resulted in directed structural growth of pure metal oxides, which could be especially useful in preparation of materials that often exhibit low surface areas.

After surveying the literature there appears to be many semiconductors that have been extensively investigated as p-type and n-type semiconductors for PEC processes. Many suffer from problems with recombination, stability and light absorption, with fewer instances of research into p-type photocathodes. As mentioned previously, perovskite oxides are a promising group of compounds, but have not yet achieved high photocurrent densities compared to other materials and so can benefit greatly from further investigation. As discussed, $LaFeO_3$ and $PrFeO_3$ are of high interest due to favourable band gaps, good stability and activity for photocatalytic processes, hence a more detailed examination of work reported for these materials is required.

1.6 Lanthanum iron oxide ($LaFeO_3$)

$LaFeO_3$ (LFO) is a highly suitable material for water splitting due to its narrow band gap (2-2.5 eV) and photocatalytic activity. LFO particles have been synthesised and

characterised through common techniques such as X-ray diffraction (XRD) and Ultra-violet visible light spectroscopy (UV-Vis), the latter can be used determine approximate band gap energies (Figure 1-18). It can be seen for LFO there is a distinct double peak feature within the UV-Vis spectra due to direct and indirect electronic transitions.[110] Literature has shown various synthesis methods to prepare LFO, and the applications it is suitable for. The most common synthesis method used is a sol-gel synthesis, using lanthanum and iron nitrates with citric acid as a complexing agent, combined with high temperature calcination to produce LFO nanoparticles. This highlights the ease at which LFO can be synthesised as well as the abundancy and non-toxicity of the starting materials. LFO can also be synthesised through a hydrothermal method which can lead to larger particle sizes of up to 200 nm in diameter[111], but benefits from low temperatures and a relative control over particle sizes through a simple and cost effective process.

There appears to be a high sensitivity of LFO nanoparticles to sinter on application of high temperature calcination during synthesis. Li et al found that on increasing calcination temperature during a sol-gel synthesis, decreases both measured surface area and activity. With the highest activity for RhB degradation provided by LFO calcined at 500 °C, with a measured surface area of 21.9 $m^2 g^{-1}$.[70] A similar relationship was found when studying the activity of LFO for hydrogen evolution. At a calcination temperature of 500 °C a more loose and porous material was observed under SEM, whilst at a higher temperature of 900 °C, a more irregular porous morphology

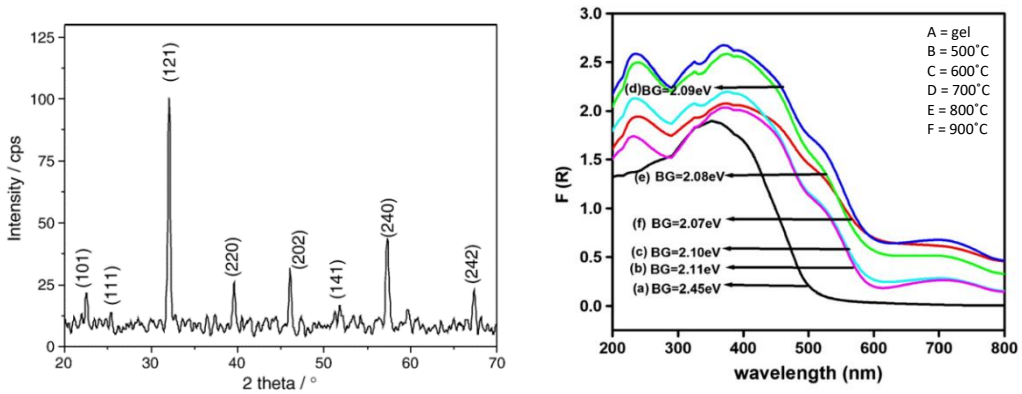

Figure 1-18: XRD spectra of $LaFeO_3$ (left)[112] and UV-Vis spectra of $LaFeO_3$ prepared by a sol-gel method at different temperature calcinations (right). Adapted from Ref.[113]

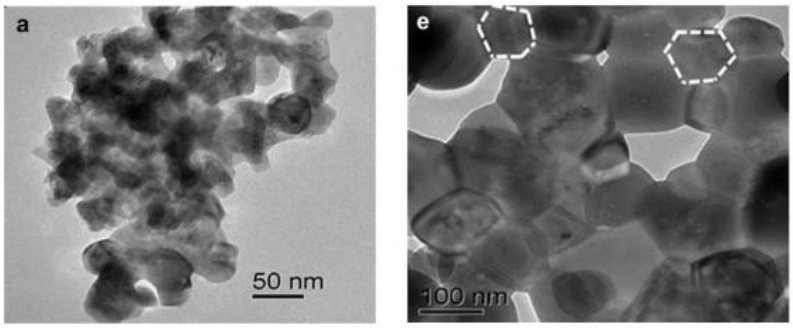

Figure 1-19: HR-TEM micrographs of LFO calcined at 500 °C (left) and 900 °C (right). Reproduced from Ref.[113]

appeared which was more nano hexagonal in shape (Figure 1-19). Particle sizes increased from 24 nm to 104 nm with an increase of activation temperature from 500 to 900 °C, with calculated surface areas of 25.8 and 5.8 $m^2 g^{-1}$ respectively.[113] This shows that heavy sintering can have drastic effects on overall activity due to losses in active surface area and morphology changes. Despite this, LFO synthesis shows benefits over other metal oxides due to the cost-effective nature, high abundancy of precursors and facile preparation.

1.6.1 Photocatalytic activity of $LaFeO_3$

There have been numerous studies into LFO being photocatalytically active for a wide range of processes. LFO synthesised using a sol-gel method with glucose as a complexing agent was prepared and shown to be active for the photocatalytic degradation of p-chlorophenol by 49 % under visible light. The double perovskite La_2FeTiO_6 was also measured and found to be superior with a degradation of p-chlorophenol at 62 %. Showing both the potential of both $LaFeO_3$ and La_2FeTiO_6.[114] As mentioned previously, floral like LFO nanoparticles have shown to be active for both the degradation of methylene blue (MB) and rhodamine B (RhB), showing vast improvements when compared to bulk LFO with a recorded surface area of 90.3 $m^2 g^{-1}$ and a degradation efficiency of MB at 92.9 %.[69] This additionally demonstrates the sensitivity of LFO activity on particle structure.

Photocatalytic activity of LFO has been enhanced through introducing further materials to form heterojunctions. LFO nanoparticles for instance have been

successfully grown on reduced graphene oxide (rGO). 15 nm particles of the perovskite were anchored onto rGO, which serves as a 2D template that can direct nucleation and growth of LFO particles, in so doing reducing sintering at high temperatures. A BET surface area of 121 m^2 g^{-1} was recorded, which is a vast improvement on non-templated samples. rGO is highly conductive and so can beneficially increase charge separation, reducing the likelihood of electron-hole recombination. This prepared $LaFeO_3$-rGO showed superior photocatalytic activity for MB and RhB compared to pristine LFO and commercial TiO_2.[93] Montmorillonite (MMT) has also been used as a support to prevent aggregation of particles and hence improve photocatalytic activity.[115] Additionally a g-C_3N_4/$LaFeO_3$ nanocomposite has been prepared and demonstrated to enhance photocatalytic activity for the HER. On 1 wt % loading of Pt, a hydrogen evolution of 1152 µmol h^{-1} g^{-1} was achieved compared to 247 µmol h^{-1} g^{-1} for LFO alone. This increase was attributed to the enhanced charge separation of electron-hole pairs by accelerating interfacial charge carrier recombination.[116]

Further research has demonstrated that LFO is active for hydrogen evolution from photocatalytic water reduction. When synthesised through a sol-gel method and calcined at 500 °C, a hydrogen evolution of 1290 µmol was seen from a solution of 20 % MeOH/H_2O over 3 hours.[113] Additionally, a hydrogen evolution of 3315 µmol h^{-1} g^{-1} was achieved for LFO under visible light with ethanol as a sacrificial

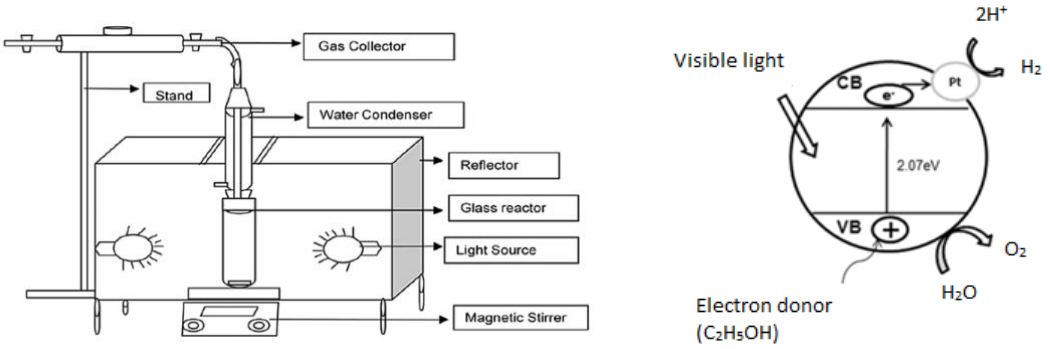

Figure 1-20: Schematic of photocatalytic hydrogen evolution reactor (left) and proposed mechanism for hydrogen generation by Pt-$LaFeO_3$ (right). Adapted from Ref.[85] *with permission from Elsevier.*

donor and Pt co-catalyst. This was measured using a photoreactor with a 200 W tungsten light source as shown in Figure 1-20. A relationship between activity, catalyst and Pt dosage was observed, with 0.1 g catalyst and 19 µL platinum being optimal conditions found.[85] This demonstrates the beneficial use of Pt as a co-catalyst, to assist the mechanism of water reduction to evolve hydrogen. As mentioned previously within this Chapter, to allow for overall photocatalytic water splitting to be a commercially viable route for hydrogen production, a solar-to-hydrogen efficiency of 5-10 % is needed. Due to this not always being reported for photocatalytic investigations, it can be more useful to compare achieved H_2 evolution rates to a top performing material. TiO_2 based photocatalysts provide the most promising results in terms of heterogeneous photocatalysis. A CdS/TiO_2 catalyst with Pt co-catalyst achieved a H_2 generation of 128.3 mmol h^{-1} g^{-1} (128300 µmol h^{-1} g^{-1}).[117] Hence, this achieved hydrogen evolution can be used as a benchmark when comparing H_2 evolution rates, but it is more indicative and useful to calculate STH efficiency. This shows that there is further work needed for $LaFeO_3$ photocatalysts to compete with these higher activity materials.

1.6.2 Photoelectrochemical activity of $LaFeO_3$

Interestingly, LFO photoelectrodes have shown both activity for water reduction, and in fewer cases water oxidation. With respect to water oxidation, metal doping has been achieved by a sol-gel method with a range of different metal dopants (10 % doping), with a subsequent calcination of 500 °C. These powders were then mixed with ethanol and PEG 400 to be pasted onto FTO-glass by a doctor blading method. These were then tested for PEC water oxidation, and it was determined that doping of Cu into the perovskite structure ($LaFe_{0.9}Cu_{0.1}O_3$) provided the highest recorded photocurrent density of +990 µA cm^{-2}. Approximately, an activity of +10 µA cm^{-2} was recorded for undoped LFO, which is relatively low compared to other n-type semiconductors. Electrochemical impedance spectroscopy (EIS) measurements were completed and demonstrated on doping with metals there was an accelerated charge transport, showing lower levels of impedance (Figure 1-21).[79]

There are much more frequent reports of LFO films demonstrating p-type character. LFO photocathodes with a band gap of 2.0 eV have been prepared through a sol-gel synthesis with nitrate precursors and citric acid, and fabrication through spin coating

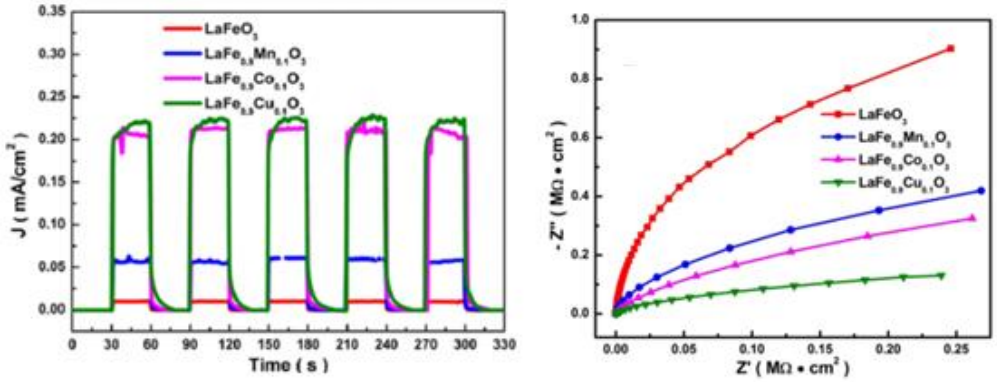

Figure 1-21: Chopped light current response at 1 V of metal doped-$LaFeO_3$ (left) and EIS measurements of doped-$LaFeO_3$ (right). Reproduced from Ref.[79]

onto an FTO-glass substrate. A photocurrent density of approximately -10 µA cm^{-2} at -0.25 V_{AgCl} in O_2-saturated electrolyte was recorded. This photocurrent was enhanced through metal doping, that allowed for metal ions to be incorporated into the perovskite structure, thus highlighting the benefit of using perovskites due to this structural flexibility. Here, they used Mg and Zn as dopants, with a 5 % doping of Mg providing the biggest increase in photocurrent to -50 µA cm^{-2}.[108]

Nickel nanoparticles have additionally been used in conjunction with LFO photocathodes to increase activity. For a bare LFO photocathode prepared through spray pyrolysis, a maximum photocurrent of -36 µA cm^{-2} at +0.6 V_{RHE} was reported with an increase to -66 µA cm^{-2} on the addition of 2.84 mmol Ni nanoparticles. This increase was attributed to the excitement of surface plasmon resonances on addition of Ni, which enables enhanced light harvesting. An increase in H_2 generation of 2.64 times to 0.048 µmol cm^{-2} h^{-1} was seen on the addition of Ni.[118] Additional research from this group demonstrated this effect with the addition of plasmonic Ag nanoparticles, which achieved a photocurrent of -74 µA cm^{-2} at +0.6 V_{RHE}, with a hydrogen generation of 0.053 µmol cm^{-2} h^{-1} with no applied bias.[119] Another technique that has shown to improve light harvesting for LFO films, is through incorporating an Au buffer layer between the FTO substrate and LFO. This FTO/Au/LFO electrode demonstrated a photocurrent of -19.6 µA cm^{-2} at +0.6 V_{RHE} (compared to -4.8 µA cm^{-2} for FTO/LFO), due to enhanced light harvesting and better charge separation.[120]

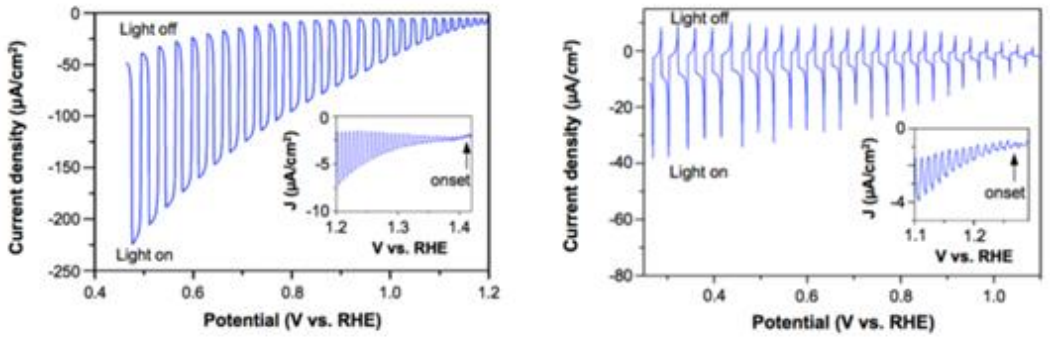

Figure 1-22: Chopped light LSV curves for electrodeposited LFO films for oxygen reduction (left) and for water reduction (right). Reproduced from ref.[121]

Higher photocurrents densities have been achieved for LFO photocathodes through electrodeposition of a plating solution containing $La(NO_3)_3 \cdot 6H_2O$, $FeCl_2 \cdot 4H_2O$, and KNO_3 to deposit a 1:1 ratio of $La(OH)_3$ and $Fe(OH)_3$, which was then converted to high surface area nanoporous LFO at 600 °C for 3 hours. This LFO photocathode was found to have a band gap of 2.1 eV and was measured for its ability for PEC oxygen reduction. To measure this, an O_2-saturated electrolyte (0.1 M NaOH) was used and generated a photocurrent density of -100 μA cm^{-2} at +0.73 $V_{RHE,}$ maintaining a stable photocurrent of -96 μA cm^{-2} over 1 hour with no visible photocorrosion without using a protection layer. It reports here that LFO is catalytic for O_2 reduction but was also measured for its activity towards water reduction independently through purging the electrolyte with N_2. In which the photocurrent density after 2 minutes was -1.5 μA cm^{-2} at +0.73 V_{RHE}, however still showed a photocurrent onset of +1.27 V_{RHE} (Figure 1-22).[121]

Further, more recent work from this group investigated the effects of atomic doping on photon absorption and carrier transport of LFO photocathodes. Here, they demonstrated the doping of LFO through the substitution of La^{3+} with K^+, showed K-doping increases majority carrier density and decreases the band gap of LFO, in which theoretical studies agreed. A photocurrent density of -238 μA cm^{-2} at +0.6 V_{RHE} was reported for these K-doped LFO films in O_2-saturated electrolyte (compared to a pristine activity of -124 μA cm^{-2}).[81] Tahir et al also investigated LFO photoelectrodes prepared by spray pyrolysis for PEC water reduction. These LFO films achieved a photocurrent density of -160 μA cm^{-2} at +0.26 V_{RHE} and demonstrated unbiased spontaneous H_2 production from PEC water reduction. This appears to be the highest

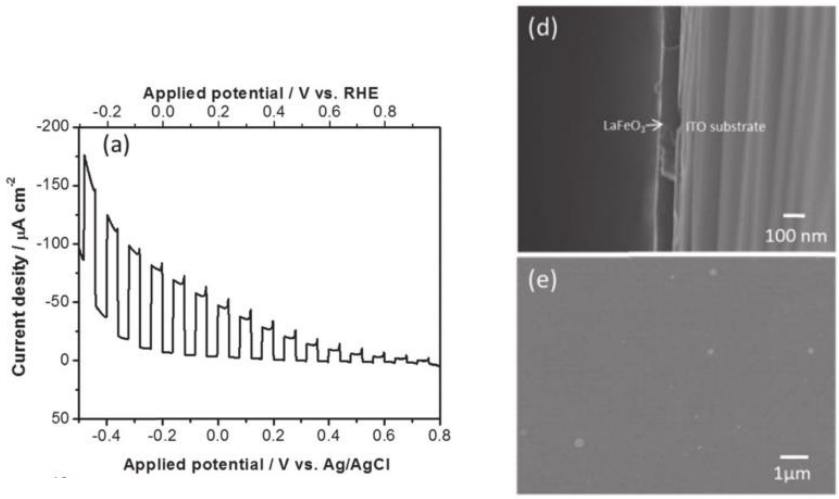

Figure 1-23: Current-potential curves for $LaFeO_3$ (left) and SEM micrographs for the cross-view and top view of $LaFeO_3$ films. Adapted from Ref.[122]

photocurrent achieved for bare LFO photocathodes.[123]

A $LaFeO_3/Ag_3PO_4$ heterojunction has been synthesised and investigated for the photocatalytic degradation of phenol. This novel heterojunction achieves greater visible light absorption and enhanced catalytic activity. The degradation of phenol was 5.8 times faster than that of LFO alone, attributed to efficient electron-hole separation as electrons travel from the CB in LFO to the CB of Ag_3PO_4, whilst holes diffuse from the VB from Ag_3PO_4 to LFO. The photocurrent density achieved for pristine LFO was recorded at approximately -10 µA cm^{-2} and increased to -130 µA cm^{-2} on application of this heterojunction.[124] A further heterojunction has been created with CuO that assisted in increasing photochemical and PEC activity of LFO.[125] Modifying film preparation method can additionally increase activity of LFO films through using pulsed laser deposition (PLD) onto ITO glass. This study details that pervious work lacks a successful outcome in producing high quality LFO films, due to lack of sophisticated preparative techniques. Under AM 1.5 G illumination, a photocurrent density of -64.5 µA cm^{-2} at 0 V_{RHE} was observed (Figure 1-23). This improved current achieved with long durability is thought to be due to the high quality of films produced with good contact between the $LaFeO_3$ and ITO. On creation of a p-$LaFeO_3$/n-Fe_2O_3 photocell in this work, 11.5 µmol h^{-1} of H_2 was produced from PEC water splitting. This demonstrates the importance of creating high quality thin films.[122]

More revealing studies into the PEC properties of LFO nanoparticles demonstrate that there is a restricted mobility of photogenerated charge carriers. A low overpotential for the oxygen evolution reaction was also exhibited, which suggests that this reaction is in competition with hole collection at the back contact, this in turn reduces the photocurrent conversion efficiency for hydrogen generation.[98] This detrimental transfer of holes to the electrolyte clearly needs to be addressed in order to improve the selectivity for HER. Recent work has been done in order to combat this through applying a TiO_2 hole blocking layer on LFO. This TiO_2 layer acts as an effective barrier for hole transfer to the electrolyte, thus supressing the competitive OER for hole collection at the back contact of the LFO electrode. An increased photocurrent density for HER of -15 μA cm^{-2} at +0.5 V_{RHE} was achieved with an impressive cathodic photocurrent onset potential of close to +1.5 V_{RHE} (under Ar-saturated electrolyte). A 10-fold increase in response compared to bare LFO.[126] This demonstrates the poor electronic properties and potential inefficiencies that LFO exhibits when considering it as an active material for PEC processes. Hence, there is a clear reliance within work reported in the literature to use dopants, co-catalysts and heterojunctions in order to enhance the activity of lanthanum iron oxide, to a level in which it can compete with other metal oxide semiconductors available.

It is useful to compare achieved photocurrents of a material within the literature to maximum theoretical values, to attain whether maximum efficiency is reached. Although a specific study into the theoretically achievable photocurrent for $LaFeO_3$ has not been found, there have been studies to calculate the theoretical photocurrent of materials based on band gap. This can be used as a target achievable photocurrent for $LaFeO_3$ when considering a band gap of approximately 2.0 eV, which corresponds to a photocurrent of about 15 mA cm^{-2} (Figure 1-24). However, many assumptions have been made during these calculations, such as there being maximum conversion efficiencies with all photons being converted to electrons, and so may not be a realistic guide to assess a material's performance.[29]

After a focused look into the work published thus far into the photocatalytic activity of LFO for various processes such as water splitting, is appears that there is great potential for LFO to become a more promising photocathode for water reduction under

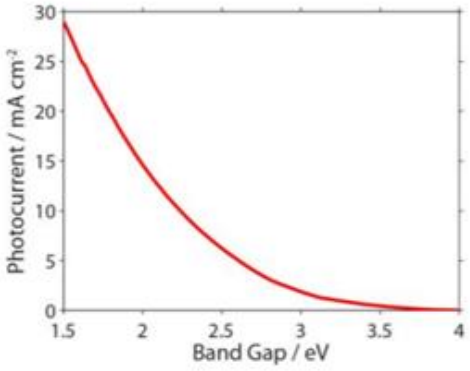

Figure 1-24: Theoretical maximum achievable photocurrent calculated from material band gap assuming 100 % conversion efficiency. Adapted from ref.[29]

simulated sunlight. It has displayed activity enhancements on metal doping such as with Cu and Co and has clearly benefited from templating during synthesis to influence growth and stabilisation of nanoparticles. These techniques have been implemented in order to increase charge separation properties as well as reducing high levels of sintering through the use of templates. In general, it appears that the main limitations of LFO is that of its relatively low surface area, due to the sensitivity of particle sintering, inefficient electron-hole separation, poor film quality and limited selectivity for HER. These discussed issues, as well as the promise shown, demonstrates that LFO clearly deserves further investigation into its role in PEC water reduction.

1.7 Praseodymium iron oxide ($PrFeO_3$)

A much more understudied and less well-known perovskite oxide is praseodymium iron oxide, $PrFeO_3$ (PFO). PFO has been previously investigated for its use in CO_2 sensing applications[127] where in which the PFO was synthesised using a sol-gel method with praseodymium nitrate, iron nitrate and citric acid which was then dried at 100 °C and calcined at a range of temperatures between 400 and 800 °C for 4 hours. An increase in crystallinity with increasing calcination temperature was found, with PFO calcined at 700 °C displaying the highest CO_2 sensing response. Moreover, PFO has shown activity in nitrite detection when combined with MoS_2. PFO was synthesised with a sol-gel method and deposited onto a glassy carbon electrode and showed a strong response to nitrite.[128]

Further to this demonstrated ability to be used in sensing applications, it has been reported to be active for photocatalytic processes. PFO has been synthesised and calcined at 800 °C with a determined band gap of 2.4 eV. This PFO powder displayed activity for photocatalytic degradation of methyl orange under visible light.[129] As well a dye degradation, there has been an investigation into the activity of PFO for water reduction. In this study, they synthesised PFO using a sol-gel, template and combustion methods. They reported crystal sizes from XRD measurements for PFO to be 20, 17 and 15 nm for sol-gel, template and combustion methods, respectively. BET surface area measurements were also completed with the highest surface area of 15.7 $m^2 g^{-1}$ being achieved for a template method. UV-Vis measurements revealed a calculated band gap of approximately 2.08 eV, encompassing the visible light region. The PFO powders were then tested for their photocatalytic activity for water reduction within a photochemical reactor under visible light irradiation. PFO particles were dispersed in a water/ethanol solution where ethanol was acting as a sacrificial donor, additionally a Pt co-catalyst was used to promote hydrogen generation. The measured rates of H_2 evolution for the sol-gel, template and combustion methods were 2847, 2132 and 1986 μmol h^{-1} g^{-1}, respectively. This appears to be the only demonstration in the literature of the water reduction capabilities of PFO.

Despite there being a great scarcity of reports on the synthesis and activity of PFO, let alone for PEC processes, it does display many promising advantages such as those generally reported for perovskite oxides. Moreover, PFO offers a band gap within the visible light region (2.08 eV), good stability, non-toxicity and abundant precursors with facile preparation methods. At the time of writing, there appears to be just a single demonstration of its photocatalytic ability for water reduction, and no investigation into its potential as a photoelectrode for PEC processes. Further investigation and insights are clearly required into PFO for its potential application in solar PEC processes.

1.8 Conclusions

After a focussed look at the use of metal oxide semiconductors for photocatalytic and photoelectrochemical applications, it is clear that there are a selection of common issues that are reported and addressed. The three major elements that are needed to be

considered when choosing an appropriate semiconductor, are that of electron transport properties, stability and light harvesting capabilities. In general, there are fewer examinations of p-type photocathodes for PEC processes compared to n-type photoanodes, hence it was decided that further work should be done in this area. After surveying research reported into active p-type materials, perovskite oxides seem very promising candidates which possess structural flexibility, facile synthesis, good stability and activity for water reduction. $LaFeO_3$ (LFO) in particular is active for solar PEC processes, however currently exhibits very low photocurrents in the majority of cases. This can be in part attributed to poor electron-hole separation and low surface area with lack of optimisation of LFO film fabrication, where the quality and appearance of the film are rarely, if ever, discussed. It can be suggested that many of the poor photocurrents recorded are due to the lack of appreciation for the effects that film preparation method has on film quality and ultimate activity. In general, there are limited in depth studies into LFO photocathodes, let alone a focus on microstructure changes and film quality in relation to fabrication method. In addition, the exploration of more understudied perovskite oxides such as $PrFeO_3$ (PFO) appears to be of interest due to currently unknown PEC properties. In the case of PFO, it has already showed photocatalytic activity both in terms of dye degradation and water reduction but is yet to be explored for its application as a photoelectrode for PEC processes. Hence, research aims of this Thesis will include the synthesis and investigation of $LaFeO_3$ and $PrFeO_3$ for photocatalytic and photoelectrochemical processes.

1.9 Research aims and objectives

The main aims of this Thesis were to first successfully synthesise $LaFeO_3$ particles through a sol-gel method and subsequently fabricate active photocathodes to be used within a photoelectrochemical cell. A focus was made into exploring various film fabrication techniques with their subsequent characterisation to establish the effects deposition has on film quality in terms of coverage and uniformity. Additionally, an investigation was done into the PEC properties of PFO photocathodes that had yet to be explored, and hence were both valuable and insightful in terms of establishing viable p-type perovskite semiconductors. Specific objectives included:

- Optimise the synthesis of $LaFeO_3$ particles using a sol-gel synthesis with citric acid, followed by characterisation by XRD, HR-TEM and UV-Vis with an examination of the activity for photochemical water reduction.
- Fabrication of $LaFeO_3$ photoelectrodes onto fluorine-doped tin oxide coated aluminoborosilicate glass (FTO-ABS) through various preparation methods, such as doctor blading, spray pyrolysis and spin coating to be examined within a photoelectrochemical cell.
- Establish the influence of fabrication method on electron transport properties, surface area, film quality and photocurrent density.
- Explore techniques that enable enhancements in photoelectrochemical activity such as that in using co-catalysts or passivation layers.
- Synthesise $PrFeO_3$ particles using a sol-gel method and subsequently prepare optimised photocathodes to be measured for PEC activity.
- Complete a 3-month research sabbatical at the Helmholtz Center Berlin for Materials and Energy (HZB) investigating the fabrication of metal-insulator-semiconductor junctions for photoanodes.

Chapter 2

2 Methods and materials

2.1 Sol-gel synthesis of $LaFeO_3$ particles

3 g $La(NO_3)_3.6H_2O$ (Fisher, 99.995 %) and 2.8 g $Fe(NO_3)_3.9H_2O$ (Fisher, 99+ %) were added to 5.3 g citric acid (Sigma Aldrich, 99.5 %) (1:1:4) in 100 ml distilled H_2O. This was then stirred for 48 hours. The sol was then placed in a 100 °C oven overnight to dry. The dried powder was then ground and pre-calcined at 500 °C for 2 hours, and then calcined further at varying temperatures of 500, 600 and 700 °C for 4 hours (10 °C min^{-1}). Adapted from Ref.[71]

Figure 2-1: Photographs of a sol-gel synthesis of $LaFeO_3$ particles.

2.2 Photocatalytic testing

0.1 g of a $LaFeO_3$ particles were dispersed in 100 ml of 20% MeOH (Sigma Aldrich, 99.8 %)/H_2O solution which was placed in a quartz reaction vessel. This was then sonicated for 5 minutes under dark conditions. This solution was then stirred on a magnetic stirring plate at 800 rpm. A halogen lamp was then placed inside the reactor and sealed. In order to prevent the reactor from overheating, a flow of cool water was flowed through a cooling jacket around the lamp. A gas chromatograph was connected to the inlets and outlets of the reactor. Air and nitrogen cylinders were opened to 4 bar pressure and the mass flow regulator was switched on. This was initially set to 30 ml min^{-1} in order to flush the reactor and then turned down to 1 ml min^{-1} for measurement. The gas chromatograph was switched on, followed by the lamp, with the quantity of the gases leaving the reactor (H_2) being measured over time. The concentration of H_2

exiting the photocatalytic reactor was calculated by comparing to a reference gas mixture with a known concentration of H_2 at 5000 ppm (4450 mg m^3). This provided a signal area on the GC spectra of 390019, which was used as a standard to determine the concentration of H_2 for an unknown effluent gas mixture. Values reported were that of the highest H_2 evolution achieved over a 2 day period, after at least a 5 hour measurement.

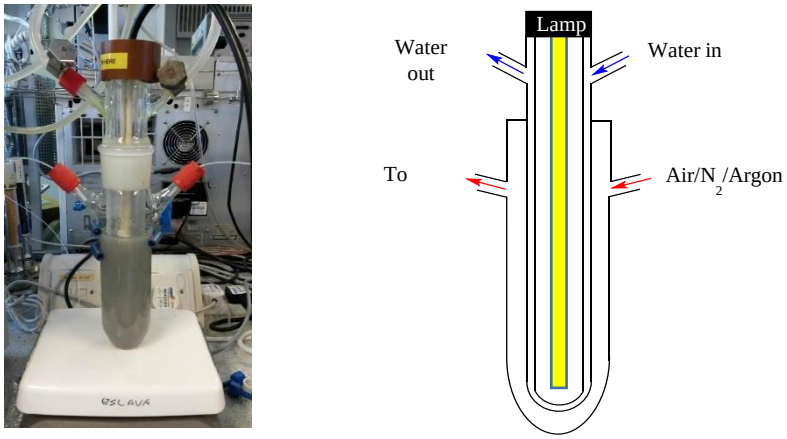

Figure 2-2: Photochemical reactor set-up to monitor hydrogen evolution.

2.3 LFO-A film fabrication using a doctor blading method

0.16 g of LFO powder sample was added to 0.45 g of 10% ethyl cellulose (Sigma Aldrich, 48.0-49.5% (w/w) ethoxyl basis) in ethanol (Sigma Aldrich, ≥99.5 %), 0.65 g terpineol (Sigma Aldrich, anhydrous) and 0.8 ml ethanol. This was stirred and sonicated for a total of 3 times. This suspension was then gently heated on a hotplate to half the original volume (16.8 wt % suspension). These pastes were then coated onto fluorine-doped tin oxide coated aluminoborosilicate (FTO-ABS) glass

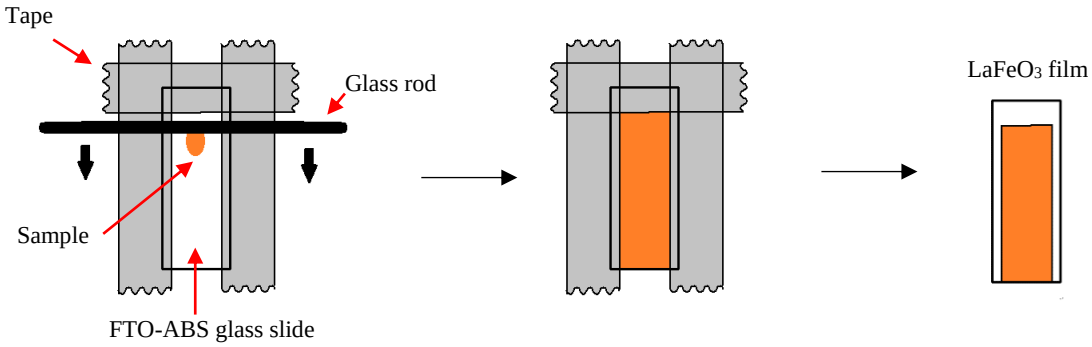

Figure 2-3: Schematic of a doctor blading method.

(Solaronix, CH) via a doctor blading method. These films were then annealed at an optimized temperature of 700 °C for 2 hours. The deposition was carried out twice for an optimised photocurrent. These films were named LFO-A.

2.4 LFO-B film fabrication using spray pyrolysis of milled powders

The prepared $LaFeO_3$ powders were first milled by adding to a sealed 100 ml glass sample bottle containing approximately 10 g of 2 mm alumina beads with an approximate ratio of material to media being 0.5:1. This was then placed on a rolling mill for 24 hours. The ground $LaFeO_3$ powder was then sonicated in dimethylformamide (DMF) (Sigma Aldrich, 99.8 %) at a concentration of 1.46 g L^{-1} for 72 hours and subsequently left to settle for 48 hours. The supernatant was then transferred into a small glass container attached to a Clarke airbrush gun. This solution was then sprayed onto an FTO-ABS glass slide at an approximate distance of 10 cm, situated on a hotplate set to 200 °C to evaporate the DMF. This was completed using several up and down motions moving from left to right along the glass for up to 10 times. The resulting film was then annealed at 600 °C for 2 hours. The deposition was carried out twice for an optimised photocurrent. These films were named LFO-B.

2.5 LFO-C film fabrication using spray pyrolysis of precursors

3 g $La(NO_3)_3.6H_2O$ (Fisher, 99.995 %) and 2.8 g $Fe(NO_3)_3.9H_2O$ (Fisher, 99+ %) were added to 5.3 g citric acid (Sigma Aldrich, 99.5 %) (1:1:4) in 100 ml distilled H_2O. This was then stirred for 48 hours. The solution was then transferred into a container attached to a Clarke air brush gun and sprayed onto the FTO-ABS glass at an approximate distance of 10 cm. This was done using up and down motions moving from left to right along the glass of up to 10 times. This was performed on a hotplate

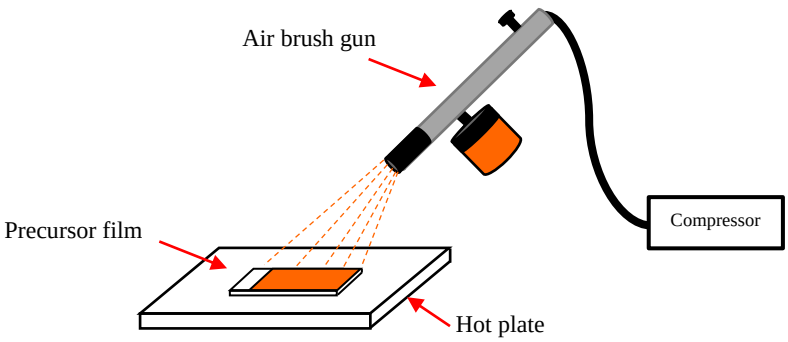

Figure 2-4: Schematic of a spray pyrolysis method.

set to 150 °C in order to evaporate the water present. The resulting films were then annealed at temperatures ranging from 500-700 °C for 2 hours. These films were named LFO-C.

2.6 LFO-D film fabrication using spin coating with PVC-*g*-POEM

One solution was prepared of 0.24 g PVC-*g*-POEM and 4 g tetrahydrofuran (THF) (Sigma Aldrich, ≥99.9 %). Another solution was prepared of 0.2 g $La(NO_3)_3.6H_2O$ (Fisher, 99.995 %), 0.19 g $Fe(NO_3)_3.9H_2O$ (Fisher, 99+ %) and 0.35 g citric acid (Sigma Aldrich, 99.5 %) in 0.5 ml deionised water. These solutions were then stirred overnight, combined and stirred for a further 24 hours. FTO-ABS glass was attached using double sided tape onto a spinning disk controlled using a small motor. 0.1 ml of polymer/nitrate solution was then dropped onto the glass substrate, evenly covering the slide. The motor was then set to 4000 rpm for 15 seconds to produce a thin film. This was then left to air dry. The film was then annealed at 500 °C for 20 minutes to remove the polymer and then heated to an optimised 600 °C for 2 hours to form the perovskite film (3.8 °C min^{-1}). The deposition and calcination were carried out four times for an optimised photocurrent. These films were named LFO-D.

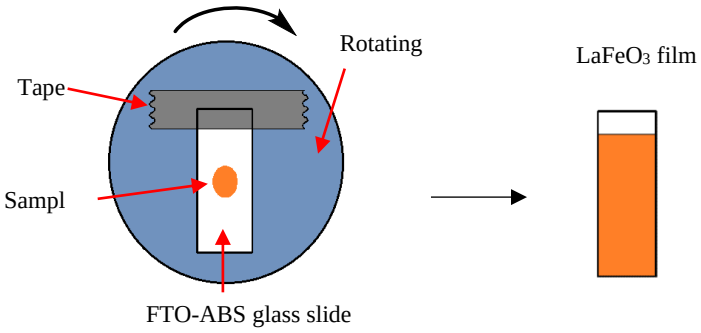

Figure 2-5: Schematic of a spin coating method.

2.7 Synthesis of PVC-*g*-POEM at Yonsei University

PVC-*g*-POEM was synthesised by dissolving 6 g PVC (M_w = 80000 g mol^{-1}, average M_n = 47000 g mol^{-1}) in 50 ml n-methyl-2-pyrrolidone (NMP) under stirring at 50 °C for 4 h. After cooling to room temperature, 12 g POEM, 0.1 g CuCl and 0.25 ml 1,1,4,7,10,10-hexamethyltriethylenetetramine (HMTETA) were added to the solution.

This was stirred and purged with nitrogen for 30 min. The polymerization was performed at 90 °C for 36 hours. The synthesized graft copolymer was precipitated in 500 ml methanol and washed 3 times with methanol for 4 hours. The resultant polymer was dried at 50 °C in an oven overnight. This was conducted by Min Su Park at Yonsei University, South Korea.

2.8 LFO-E film fabrication using spin coating with Triton X-100

One solution was prepared of 1 ml Triton X-100 polymer and 1 ml tetrahydrofuran (THF) (Sigma Aldrich, ≥99.9 %). Another solution was prepared of 0.2 g $La(NO_3)_3{\cdot}6H_2O$ (Fisher, 99.995 %) 0.19 g $Fe(NO_3)_3{\cdot}9H_2O$ (Fisher, 99+ %) and 0.35 g citric acid (Sigma Aldrich, 99.5 %) in 0.5 ml deionised water. These solutions were then stirred overnight, combined and stirred for a further 24 hours. FTO-ABS glass was attached using double sided tape onto a spinning disk controlled using a small motor. 0.1 ml of polymer/nitrate solution was then dropped onto the glass substrate, evenly covering the slide. The motor was then set to 4000 rpm for 30 seconds to produce a thin film. This was then left to air dry. The film was then annealed at 500 °C for 20 minutes to remove the polymer and then heated to an optimised 600 °C for 2 hours to form the perovskite film (3.8 °C min^{-1}). The deposition and calcination were carried out three times for an optimised photocurrent. These films were named LFO-E.

2.9 C-LFO film fabrication using spin coating without a template

A solution was prepared of 2 ml tetrahydrofuran (THF) (Sigma Aldrich, ≥99.9 %) and another solution was prepared of 0.2 g $La(NO_3)_3{\cdot}6H_2O$ (Fisher, 99.995 %), 0.19 g $Fe(NO_3)_3{\cdot}9H_2O$ (Fisher, 99.995 %) and 0.35 g citric acid (Sigma Aldrich, 99.5 %) in 0.5 ml deionised water. These solutions were then stirred overnight, combined and stirred for a further 24 hours. 0.1 ml of solution was then dropped onto the FTO-ABS glass substrate, evenly covering the slide and attached to a spinning disk. The motor was then set to 4000 rpm for 30 seconds to produce a thin film and calcined at 600 °C for 2 hours. These films were named C-LFO and were used as a control film to compare to polymer templating methods.

2.10 LFO-F film fabrication using an in situ hydrothermal synthesis

A solution of 1.5 g $La(NO_3)_3 \cdot 6H_2O$ (Fisher, 99.995 %) + 1.14 g $K_4[Fe(CN)_6] \cdot 3H_2O$ (Sigma, 98.5-102 %) + 0.67 g citric acid (Sigma Aldrich, 99.5 %) in 30 ml distilled water was prepared. 10 ml of this solution was then placed in an autoclave vessel, along with clean FTO-ABS glass slides that were immersed in the solution. This was sealed and placed into an oven at optimised conditions of 180 °C for 18 hours. These films were then taken out, washed with water and ethanol and dried at 100 °C. These films were then calcined at 600, 700 and 800 °C for 2 hours to form LFO and were named LFO-F.

2.11 Photoelectrodeposition of platinum onto LFO-D electrodes

An optimal solution of 0.005 mM chloroplatinic acid (H_2PtCl_6) (Sigma Aldrich, 8 wt% in H_2O) was prepared with 0.1 M Na_2SO_4 (Sigma Aldrich, ≥99.0 %) in distilled H_2O. This solution was then used in a PEC quartz cell with an LFO-D working electrode, Pt counter and Ag/AgCl reference electrode. A constant optimised potential between +0.2 and -0.6 V_{AgCl} was applied with constant solar illumination for between 10 and 20 s. These Pt deposited LFO-D films were then annealed at 500 °C for 30 minutes to achieve an increased photocurrent. Various concentrations of H_2PtCl_6 were used as well as changing deposition potential and deposition time for optimisation.

2.12 Deposition of CuO in the production of LFO/CuO heterojunction

0.01 g CuO nanopowder (Sigma Aldrich) was dispersed in 1 mL THF and 1 mL Triton X-100 and left to stir overnight. 0.05 mL of this solution was then deposited on FTO-ABS glass placed on a 200 °C hotplate through drop casting. The resulting film was then calcined at 500 °C for 1 hour.

2.13 Deposition of NiO to prepare a hole transport layer

A 0.4 M solution of nickel acetate tetrahydrate ($Ni(OCOCH_3)_2 \cdot 4H_2O$) (Sigma Aldrich, 98 %) in methanol was prepared. A solution of 0.4 M diethanolamine (Sigma Aldrich, ≥98 %) was added dropwise until the solution turned a dark green colour from light green, signifying the formation of $Ni(OH)_2$. This solution was then spin coated onto

FTO-ABS at 2000 rpm for 15 seconds and calcined at 500 °C for 1 hour to form a NiO hole transport layer.[97]

2.14 Sol-gel synthesis of $PrFeO_3$ particles

1.5 g $Pr(NO_3)_3.6H_2O$ (Fisher, 99.9 %), 1.4 g $Fe(NO_3)_3.9H_2O$ (Fisher, 99.995 %) and 2.65 g citric acid (Sigma Aldrich, 99.5 %) (1:1:4) were added to 50 mL distilled water and left to stir for 72 hours. The solution was then dried overnight at 100 °C, and then pre-calcined at 500 °C for 4 hours and then at 700 °C for 2 hours with a ramp rate of 10 °C min^{-1}. This was done at different calcination conditions for optimisation. This was performed by MEng student Hayley Pickering.

2.15 PFO-A film fabrication using doctor blading

0.08 g of PFO powder was added to a 10 % ethyl cellulose (Sigma Aldrich, 48.0-49.5% (w/w) ethoxyl basis) in ethanol (0.22 mL), terpineol (0.32 mL) and ethanol (0.4 mL) solution. The solution was then sonicated and stirred 3 times, then two drops of the solution were added onto the glass and deposited using doctor blading. The film was then annealed at 600 °C for 2 hours (10 °C min^{-1}. This was performed by MRes student Sophie Thomas.

2.16 PFO-B film fabrication using spray pyrolysis of precursors

3 g $Pr(NO_3)_3 \cdot 6H_2O$ (Fisher, 99.9 %) and 2.8 g $Fe(NO_3)_3 \cdot 9H_2O$ (Fisher, 99.995 %) were added to 5.3 g citric acid (Sigma Aldrich, 99.5 %) (1:1:4) in 100 ml distilled H_2O. This was then vigorously stirred for 48 hours. This solution was then deposited on an FTO-ABS glass slide by spray pyrolysis. The solution was sprayed using several up and down motions moving from left to right along the glass for up to 10 times. The resulting films were then calcined at 500, 600 and 700 °C for 2 hours. The deposition (spray and calcination) was carried out three times for an optimised photocurrent. These films were named PFO_500 °C, PFO_600 °C and PFO_700 °C.

2.17 Atomic layer deposition of SnO_2 completed at HZB

A home-built ALD reactor was used to deposit SnO_2 onto silicon wafers and $BiVO_4$ films on FTO coated glass slides. This was performed using alternating exposures of

tetrakis(dimethylamino) tin (TDMASn) and H_2O (or O_2 plasma). TDMASn was held in a stainless-steel bubbler maintained at 40 °C and is connected to the ALD reactor that was set to various reactor temperatures of 120, 140, 155, 170, 185 and 200 °C for optimisation. The TDMASn exposure times used were between 0.25 and 10 seconds and the H_2O exposure times used were between 0.1 and 1 seconds, argon was used to purge between exposures of precursors.[130]

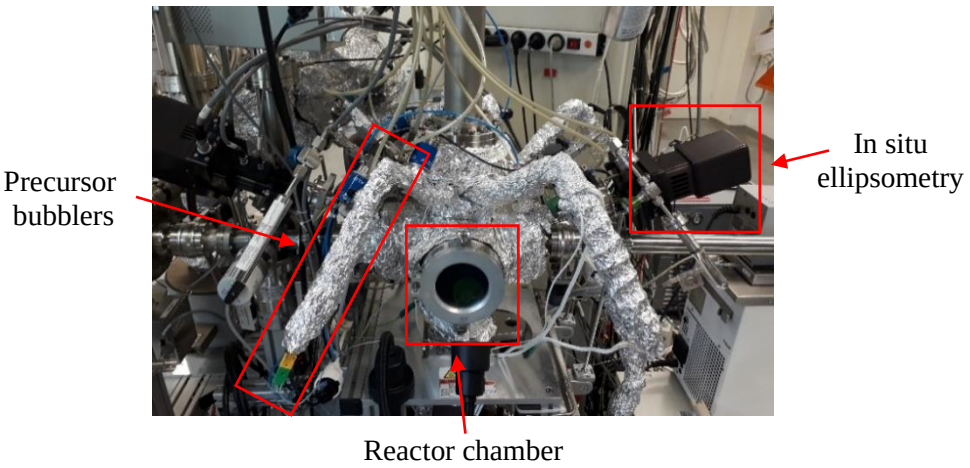

Figure 2-6: Home-built ALD reactor.

2.18 Photoelectrochemical measurements completed at HZB

A custom Teflon cell with 6 mm opening for electrode exposure to the electrolyte was used for PEC measurements in a three-electrode configuration with Pt counter electrode and Ag/AgCl reference electrode. A 1 M KPi electrolyte with a 0.5 M Na_2SO_3 hole scavenger (HS) (pH 7) was used for electrodes without co-catalysts and used without a hole scavenger when co-catalysts were deposited. The applied potential was controlled by a potentiostat (EG&G 283, Princeton Applied Research) and a WACOM Class AAA solar simulator (WXS-50S-5H) was used as the illumination source (AM 1.5 G, 100 mW cm^{-2}).

Characterisation and Theory

2.19 Photoelectrochemical measurements

PEC measurements were carried out in a three-electrode PEC quartz cell with working electrode, Pt counter electrode, an Ag/AgCl reference electrode, and a 0.1 M Na_2SO_4 electrolyte of pH 12 (adjusted with NaOH). A 300 W Xe lamp equipped with an

AM1.5G solar simulator filter (LOT Quantum Design) was used with an 8mm-diameter masked area. The intensity was measured to be 100 mW cm^{-2}, determined by the distance to the working electrode (these irradiation conditions are herein referred as "1 sun"). An external potential (provided by Ivium CompactStat) was linearly swept from +0.2 to -1.12 V_{AgCl} at a rate of 20 mV s^{-1} under chopped simulated sunlight. Standard deviations of photocurrents (represented with ±) were calculated from more than 3 samples with mean values stated. Frontside and backside illumination was completed for each film with the maximum achieved photocurrent density being reported.

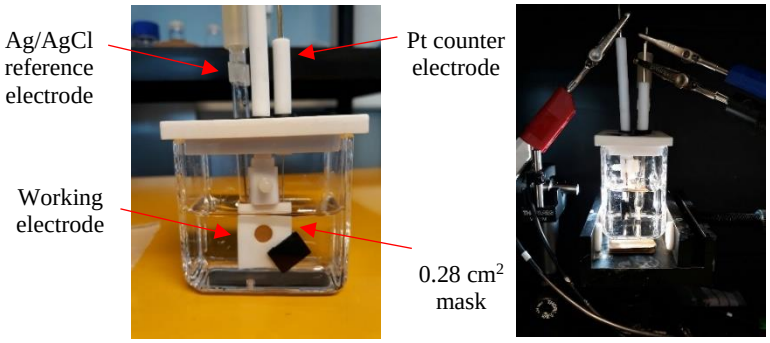

Figure 2-7: 3-electrode PEC system with Pt reference electrode and Ag/AgCl reference electrode in a quartz cell.

2.20 Electrochemically active surface area measurements

Electrochemically active surface area (ECSA) measurements were carried out by conducting cyclic voltammetry (CV) between +0.2 to -0.3 V_{AgCl} at varying scan rates between 10 and 250 mV s^{-1}. The difference in anodic and cathodic current densities recorded at -0.03 V_{AgCl} was plotted against scan rate. These CV measurements provide information on capacitance and is indicative of how much material is in contact with the electrolyte. The double layer capacitance (C_{dl}) can be calculated by dividing the gradient by two, where C_{dl} is directly proportional to the ECSA:

$$ECSA \propto C = \frac{dQ/dt}{dE/dt} = \frac{i(E)}{v}$$

where C is the electrochemical capacitance, $i(E)$ is the current measured at potential E and v is the scan rate.[131] These ECSA values can then be compared relative to other

values to determine difference in surface area when looking at the gradient of scan rate versus current.

2.21 Electrochemical impedance spectroscopy measurements

Electrochemical impedance spectroscopy measurements (EIS) were carried out under dark conditions, with a 0.1 M Na_2SO_4 electrolyte, a DC voltage of -0.3 V_{AgCl} and an AC potential frequency range 10^5-0.1 Hz with an amplitude of 5 mV. This was then used to create Nyquist plots (Z' vs. Z", real and imaginary impedance values respectively) to reveal information on film impedance (resistance). Where Z' is the measured impedance and Z'' is calculated from capacitance using the following equation.

$$C = \frac{-1}{FZ''}$$

These EIS measurements were then completed at different potentials between 0 and +0.5 V_{AgCl} to obtain Mott-Schottky plots. These were carried out at fixed frequencies of 10, 100 and 1000 Hz using the following equation:

$$\frac{1}{c^2} = \frac{2}{A^2 N_D e \varepsilon_0 \varepsilon}\left(V - V_{fb} - \frac{K_b T}{e}\right)$$

where C is the capacitance, A the electrode area, N_D the hole carrier density, e the elemental charge, ε_0 the permittivity of the vacuum, ε the relative permittivity of LFO ($6x10^3$), V the applied potential, V_{fb} the flat band potential, K_b the Boltzmann constant and T the temperature. The flat band potential (V_{fb}) was calculated through the extrapolation to the X-axis from the linear part of the Mott-Schottky plot.[123] The hole carrier density was then determined from these plots using the following equation:

$$N_D = \left(\frac{2}{A^2 e \varepsilon \varepsilon_0}\right)\left(\frac{d(1/C^2)}{d(V)}\right)^{-1}$$

2.22 RC limited photocurrent measurements

Electrochemical impedance spectroscopy (EIS) measurements for RC limited current calculations were carried out in 0.1 M Na_2SO_4 with a DC of -0.3 V_{AgCl} and AC

potential frequency range 10^5-0.1 Hz with an amplitude of 5 mV under dark conditions. Experimental transient photocurrents were obtained under chopped illumination (1 sun) at -0.3 V_{AgCl} with a data collection interval of 0.01 seconds. These were then compared with the RC limited photocurrent calculated from the general expression.

$$j_{ph} = j_{max}\left[1 - e^{-t/RC}\right]$$

where j_{ph} is the calculated RC limited photocurrent, j_{max} is the maximum photocurrent measured from the experimental transient photocurrent, t is time and RC is resistance multiplied by capacitance.[132] The time in which it takes for the maximum of the experimental transient to reach the maximum of the RC limited transient is determined (rise time). Longer rise times elude to increased density of trap states causing higher rates of electron-hole recombination and poorer charge separation.

2.23 Incident photon-to-current conversion efficiency

Incident photon-to-current efficiency (IPCE) measurements were calculated using the same a 300 W Xe lamp and a triple grating Czerny-Turner monochromator. A SEL033/U photodetector (International Light Technologies) was used to measure the intensity of monochromatic light at the equivalent position to the working electrode. IPCE can then be calculated at different wavelengths of light using the following equation:

$$IPCE = \frac{j\ x\ 1239.8}{\lambda\ x\ P}$$

where j is the photocurrent density measured, λ is the wavelength of light illumination and P is the incident photon flux.

2.24 H_2 production measurements from PEC water reduction

H_2 generation measurements were carried out in a gas-tight PEC single cell with a Pt counter electrode and Ag/AgCl reference electrode. The cell was purged with N_2 for 1 h to expel atmospheric oxygen. The working electrode was subjected to a constant potential of +0.43 V_{RHE} under constant simulated solar illumination (1 sun) for 6 hours. A build-up of evolving gases was maintained during this time through accumulation in the headspace and were measured using gas chromatography

(Shimadzu Nexis GC-2030) in a closed circuit, where gases were re-circulated with a peristaltic pump. The concentration of H_2 was calculated by comparing to a reference gas mixture of known H_2 concentration (0.127 µmol, peak area 461618).

2.25 UV-Vis spectroscopy

Ultraviolet-visible light spectroscopy (UV-Vis) measures either the absorbance or reflectance of a sample on illumination of radiation in the UV and visible regions, due to excitation of electrons. Absorbance of light is governed by Beer-Lambert's law:

$$A = \log\left({}^{I_0}/_{I}\right)$$

where A is absorbance, I_0 is the intensity of incident light and I is the transmitted light. Reflectance can also be measured with the ratio I/I_0 where I_0 is the reflectance of a reference sample. UV-Vis analysis was conducted using a Cary Series UV-Vis diffuse reflectance Spectrometer evaluating the F(R) functional for wavelengths between 200 and 800 nm. Diffuse reflectance was measured using an integrating sphere and a KBr standard. The band gap energy (Eg) of all the LFO films was determined using Tauc plots of $[F(R)h\nu]^{1/r}$ versus energy ($h\nu$) with determination of the x-axis intercept. Where r is the optical transition and F(R) is the Kubelka-Munk function which is calculated from $F(R)=(1-R)^2/2R$, where R is the reflectance of the sample.

2.26 High-resolution transmission electron microscopy

High-resolution transmission electron microscopy (HR-TEM) involves a beam of electrons being transmitted through a sample which are then focused on an imaging device. An image is created of varying contrasts due to the differences in thickness and crystal structure within the sample. HR-TEM micrographs were acquired using a JEM-2100Plus microscope with a 200 kV maximum operating voltage. An area of the sample under TEM was selected to obtain a selected area electron diffraction (SAED) pattern. This pattern observed consists of sharp diffraction spots which are representative of lattice reflections, which can be used to determine lattice spacing.

2.27 Field-emission scanning electron microscopy

Field-emission scanning electron microscopy (FE-SEM) involves the scanning of a surface with high energy electrons that interact with the sample. Commonly, secondary electrons can be emitted after excitation by the sample atoms, where the number and intensity can be measured which can reveal topography information. There can also be back scattered electrons from deeper within the sample that are of higher energy, that can be used for EDX measurements. FE-SEM micrographs were obtained using JEOL 6301F, with an acceleration voltage of 5 keV. Energy dispersive X-ray spectroscopy (EDX) was used for mapping analysis of the elemental distribution through an Oxford INCA X-ray analyzer.

2.28 BET surface area measurements

BET specific surface area measurements are determined through the measuring of the adsorption of N_2 gas on the surface of porous materials at 77 K. This Brunauer-Emmett-Teller method allows for the relation of the measured gas adsorbed by a material, to the amount of accessible internal pores, revealing information on a material's porosity. Hence, adsorption isotherms are produced that can be used to calculate specific surface area. BET surface area measurements were completed on a Micrometrics 3Flex surface and porosity analyser.

2.29 Powder X-ray diffraction

X-ray diffraction is a technique used to analyse crystalline materials through the diffraction of X-ray radiation. X-rays are fired at a sample which are then scattered by electrons in the sample, the X-ray beam is then rotated to alter the incident angle producing a diffraction pattern. XRD diffraction patterns can then be compared to known diffraction peaks for the material of interest using the ICDD database. To determine d-spacing from XRD diffraction data Bragg's law is used:

$$n\lambda = 2dsin(\theta)$$

where n is the order of reflection (n = 1), λ is the wavelength of X-ray radiation, d is the lattice spacing and θ is the angle of incident radiation. The crystal domain size can also be determined using the Scherrer equation:

$$\tau = \frac{K\lambda}{\beta\cos(\theta)}$$

where K is the shape factor (0.89) and β is the full width half maximum (FWHM) of a chosen diffraction peak. XRD patterns were obtained from a STOE STADI P double setup, equipped with Mythen detectors, using pure Cu-Kα_1 radiation (λ= 1.540562 Å) with a range of 2θ from 20 to 80 °.

2.30 X-ray photoelectron spectroscopy

X-ray photoelectron spectroscopy (XPS) involves irradiating a surface with an X-ray beam which causes the ejection of an electron from the sample surface (1-10 nm). The kinetic energy of these electrons are then measured and can be related to their binding energy with the following equation:

$$KE = h\nu - BE$$

This can then allow for the determination of elemental state as binding energy depends on the specific element and its chemical environment. A spectra of binding energy versus intensity is created where a particular BE region can be measured to confirm the presence of particular surface elements. XPS measurements were completed on a Kratos Axis Ultra DLD system using monochromatic Al Kα X-ray source operating at 150 W (10 mA x 15 KV). Binding energies were referenced relative to adventitious carbon at 284.6 eV. Spectral processing was performed using CasaXPS version 2.3.22. For XPS completed at HZB in the work in Chapter 7 an XPS with a monochromatic Al Kα X-ray-source (1486.74 eV) with a Specs Focus 500 monochromator was used. The analyser was supplied by SPECS (Phoibos 100) and a source-to-analyser angle of 54° was used.

2.31 Ultraviolet photoelectron spectroscopy

Ultraviolet photoelectron spectroscopy (UPS) works on the same principles as XPS. A beam of UV light irradiates a surface which causes the ejection of a surface electron at the depth of approximately 2-3 nm. The kinetic energy of the electrons emitted is determined and converted to binding energy. Due to the lower energy photons used in this technique compared to XPS, the photoemissions are limited to the valence band which is useful for VB energy level determinations such as fermi level (E_f). UPS was performed with a He I source (21.21 eV) and two measurements were conducted

where the ground of the sample holder was used to subject the sample to a 0 or 2 V bias. All spectra were measured using a pass energy and step size of 10 and 0.05 eV, respectively.

2.32 Fourier transform-infrared spectroscopy

FT-IR measures the absorption spectrum of a material by illuminating a sample with infrared radiation. This technique can be used to determine surface functional groups. A Perkin Elmer Frontier FTIR instrument equipped with a DRIFT attachment for powders and an improved resolution MCT detector was used.

2.33 Surface profilometry

Surface thickness measurements can be obtained by using contact profilometry where a diamond stylus is moved across a sample where it measures small surface variations due to stylus displacement. This measure of displacement can be used to determine the surface profile and thickness which can be measured with an accuracy of 10 nm. These measurements were obtained from a Dektak 6M mechanical contact profilometer.

2.34 Ellipsometry

Ellipsometry is based upon measuring the change of the polarisation of light after being reflected by a sample. This change is related to the thickness of the material which can then be calculated. *R*eal-time spectroscopic ellipsometry (RTSE) on a J.A. Woollam Co. Inc., M-2000X, 210–1000 nm were carried out and was directly attached to the atomic layer deposition reactor. This allowed for in situ surface thickness measurements where the windows (fused silica) in the optical path were partially protected by a nitrogen flow (99.9999%). The thickness of the native oxide on the Si wafers were fitted to a model prior to each deposition, following the approach described by Herzinger et al.[133]

2.35 Electron beam evaporation

Electron beam evaporation is a form of physical vapour deposition process in which a target anode is bombarded with an electron beam from a tungsten filament source. This electron beam causes the atoms of a target material to vaporise and then precipitate into solid form onto a sample. Films were first covered with an aluminium shadow mask with a single spot opening (area = ~ 0.24 cm^2) at the centre of the film. A Pt and Ni target was used to deposit 4 nm of Pt and 4 nm of Ni onto the substrate films, where film thickness was determined using a quartz microbalance calibrated to the density of Pt.

2.36 Gas chromatography

Gas chromatography (GC) measurements were conducted on a Shimadzu Nexis GC-2030 with He carrier gas and a barrier ionisation detector (BID) with CP-Sil 8CB 30 m x 0.32 mm x 0.25 µm column. A gas mixture of H_2 at a concentration of 0.127 µmol was used as a reference mixture with a determined standard peak area of 461618. This was then used to determine H_2 concentration from measured samples.

Chapter 3

3 Synthesis of $LaFeO_3$ particles for photocatalytic water reduction

The work detailed within this Chapter outlines the synthesis of $LaFeO_3$ particles. This work does not possess specific and defined synthesis aims, for example producing $LaFeO_3$ nanoparticles, which is common in the area of photocatalysis. Rather, this work provides an initial introduction to the synthesis and characterisation techniques needed for metal oxide preparation to form a basis of work for future Chapters.

3.1 Synthesis of $LaFeO_3$ particles

Lanthanum iron oxide was prepared through a sol-gel synthesis with the combination of lanthanum and iron nitrates with citric acid in deionised water in a 1:1:4 ratio. This was then stirred and dried in a 100 °C oven overnight, this was then pre-calcined at 500 °C for 4 hours to remove any organic material. A second calcination step was then completed at 500, 600 and 700 °C for 2 hours, to determine an optimised activation temperature (Method 2.1). These synthesised powders were then characterised by X-ray diffraction (XRD) to establish whether pure LFO was formed for each calcination temperature. It was confirmed for all cases that orthorhombic LFO peaks were found in the XRD spectra when compared to the reference $LaFeO_3$ diffraction

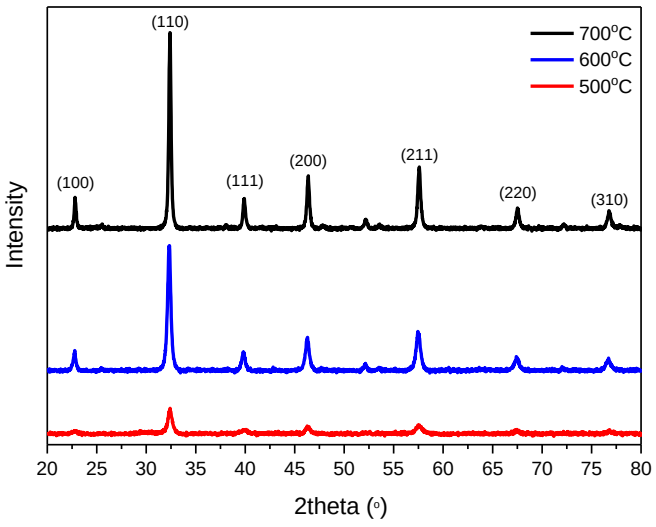

Figure 3-1: XRD patterns for LFO powders calcined at 500, 600 and 700 °C.

pattern obtained from the International Centre for Centre for Diffraction data (ICDD database) (Figure 3-1). However, it cannot be claimed for certain there are no impurities present, as these could be in the amorphous phase, to further confirm the purity of these $LaFeO_3$ particles XPS can be done in the future.

It appears on increasing calcination temperature there are stronger and more intense diffraction peaks, suggesting an increase in crystallinity. For a calcination temperature of 500 °C, there is a prevalence of broader and less distinct peaks suggesting a much less crystalline product was formed at this temperature. Hence, it appears that a higher temperature of either 600 or 700 °C is more beneficial. The Scherrer equation was then used to calculate the crystal domain size of each of these prepared LFO particles as shown in Equation 10:

$$\tau = \frac{K\lambda}{\beta \cos(\theta)}$$

Equation 10: Scherrer equation to calculate crystal domain size.

where K is the shape factor (0.89) and β is the full width half maximum (FWHM) of a chosen diffraction peak (Method 2.29). These were determined to be 15, 20 and 30 nm for 500, 600 and 700 °C respectively. This demonstrates an increase in crystal size with an increase in calcination temperature, which could be explained due to increased particle sintering opportunities at higher temperatures.

These LFO particles were then further characterised using high-resolution transmission electron microscopy (HR-TEM) to establish any changes in particle size and structure on the application of different calcination temperatures (Figure 3-2). Initial measurements can be undertaken with smaller particles of around 14-20 nm in width being observed on calcination at 500 °C with limited definition, on increase in temperature to 600 °C, elongation of particles occurs resulting in more defined and rounded edges with lengths of around 30 nm (widths of 13-17 nm). At an increased temperature of 700 °C, these particles appear larger in size as well as being more rounded, with approximate particle widths of 60-80 nm. Lattice distances were determined to be 0.28, 0.33 and 0.48 nm for particles calcined at 500, 600 and 700 °C, showing an effect on the crystal structure with higher temperatures providing larger

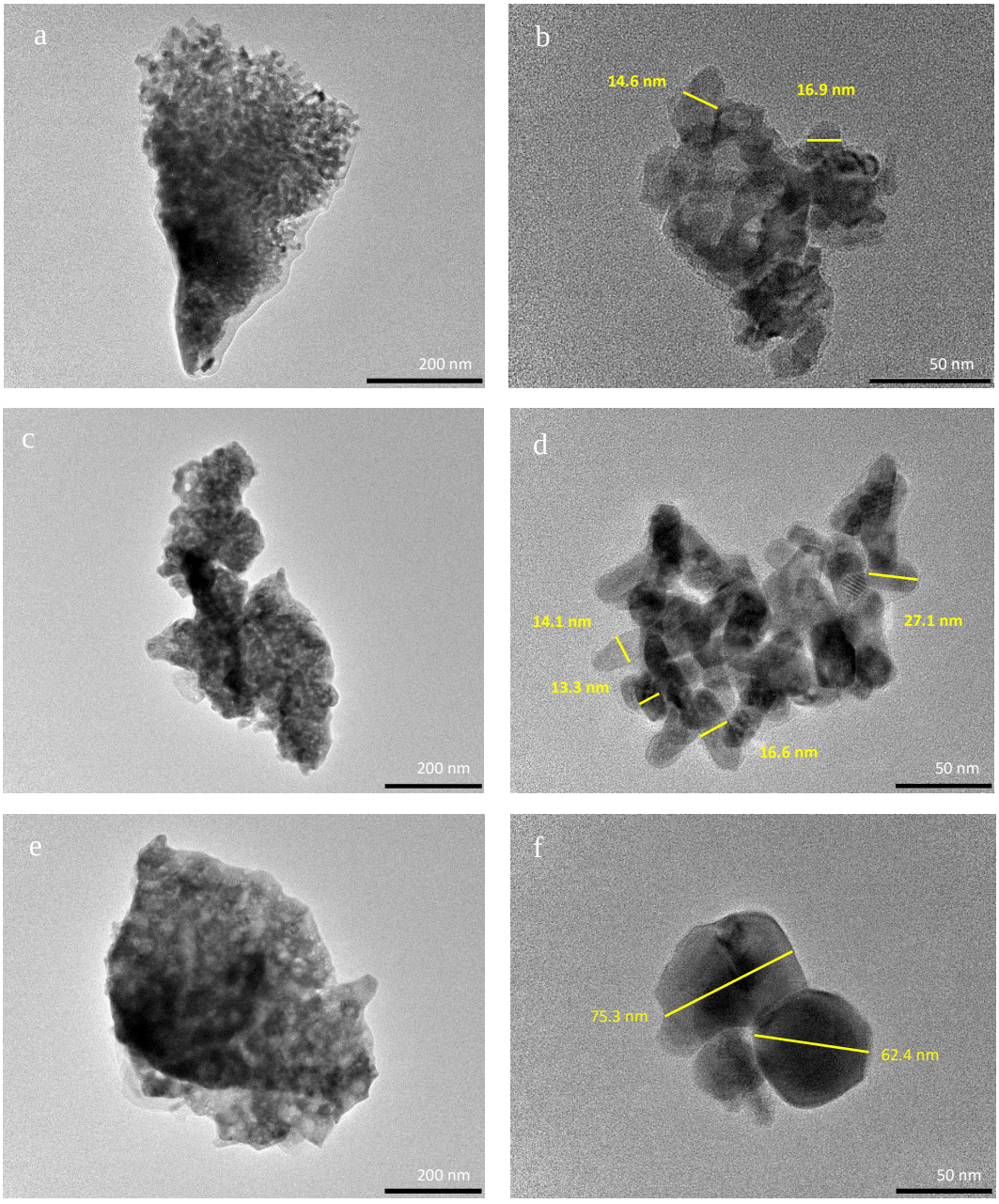

Figure 3-2: HR-TEM micrographs of LFO particles calcined at (a, b) 500 °C, (c, d), 600 °C and (e, f) 700 °C.

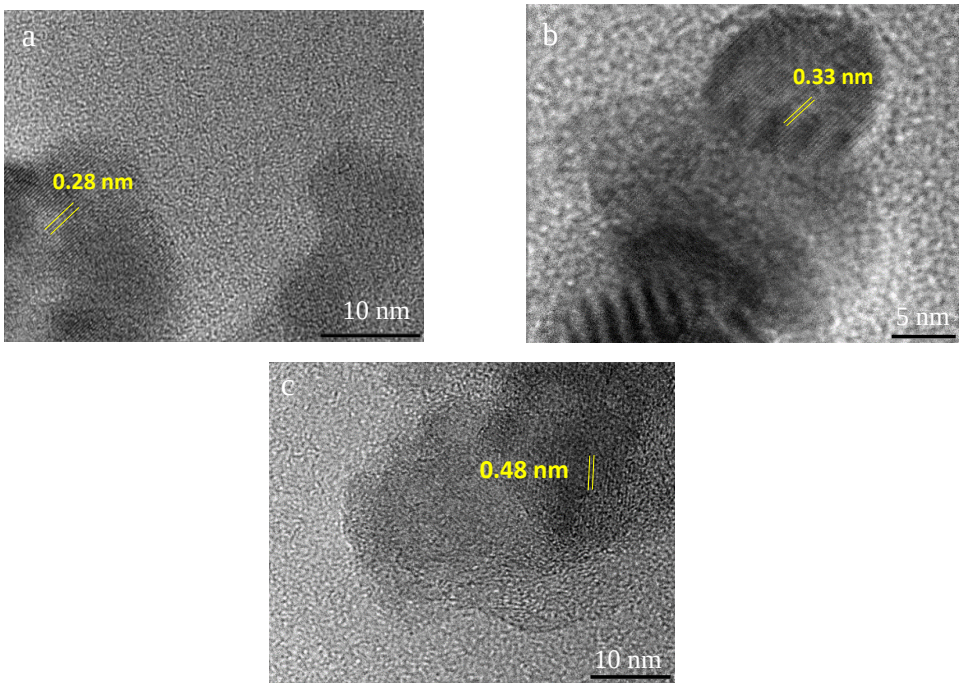

Figure 3-3: HR-TEM micrographs of LFO calcined at (a) 500 °C, (b) 600 °C and (c) 700 °C with determined lattice distances.

lattice distances (Figure 3-3). However, in all cases definitive particle sizes cannot be determined due to particle agglomeration, making it difficult to establish singular particle size, especially in the case of LFO particles calcined at 700 °C. Despite this attempt to determine particle size, it much more likely that these are not in fact nanometre scale particles as initially suggested. It can be seen that the synthesis of nanoparticles cannot be suggested in this case, due to the formation of large sintered particles with difficult to impossible accurate determination of particle size. It is common in the area of photocatalysts that the accurate and reliable formation of nanoparticles is needed to maximise performance in terms of active surface area. Hence, future work would be needed to modify and optimise this sol-gel synthesis so that nanoparticles can be produced, which was not within the aims of this particular work. In general, it appears at higher temperatures there could be increases in particle sintering as seen in Figure 3-2, which agrees with crystal domain size calculations from XRD measurements. This effect of temperature on particle size and structure has been previously reported within the literature for LFO particles.[113]

Additionally, it is important to determine the specific surface area of these LFO particles, as this can be very influential in catalysis as a high surface area could suggest

a greater area for photocatalysis, and hence could enhance activity. Therefore, Branauer-Emmett-Teller (BET) specific surface area measurements were obtained and calculated for these LFO powders to be 8.5 ± 0.4 $m^2 g^{-1}$, 6.8 ± 0.4 $m^2 g^{-1}$, and 4.2 ± 0.2 $m^2 g^{-1}$ for calcination temperatures of 500, 600, and 700 °C respectively. These values are lower than that achieved within the literature for a comparable synthesis method that achieved BET surface areas in the range of 26, 23 and 20 $m^2 g^{-1}$ for calcinations of 500, 600 and 700 °C.[113] This appears to show a decrease in specific surface area on application of higher calcination temperatures, which is in agreement with the increases in particle size seen in the HR-TEM micrographs and crystal domain size calculations. However, these values lie below the accurate detection limit of BET measurements (~20 $m^2 g^{-1}$), hence cannot be used to make any conclusive remarks on the changes in specific surface area between these calcination conditions. Nevertheless, these measurements reveal the relatively low surface areas achieved for LFO, and thus shows the potential requirement to increase this active surface area which may in turn increase ultimate photocatalytic activity.

Ultraviolet-visible light spectroscopy (UV-Vis) measurements were obtained in order to better understand the light absorbing properties of this material. Figure 3-4 shows the UV-Vis absorbance spectrum for each LFO powder, where for each calcination temperature there is an absorption edge at about 580 nm, which encompasses the visible light region. Thus, demonstrating one of the main advantages of using ferrite perovskites in solar light photocatalysis, as visible light illumination forms a large proportion of the solar light spectrum. Diffuse reflectance was also measured, which was then converted using the Kubelka-Munk function to F(R) (Equation 11).

$$F(R) = \frac{(1-R)^2}{2R}$$

Equation 11: Kubelka-Munk function for conversion from resistance to F(R).

This F(R) value can then be used within the Tauc equation (Equation 12). Where hv is the energy of the light reflected, n is the optical transition, A is absorbance and E_g is the band gap energy.

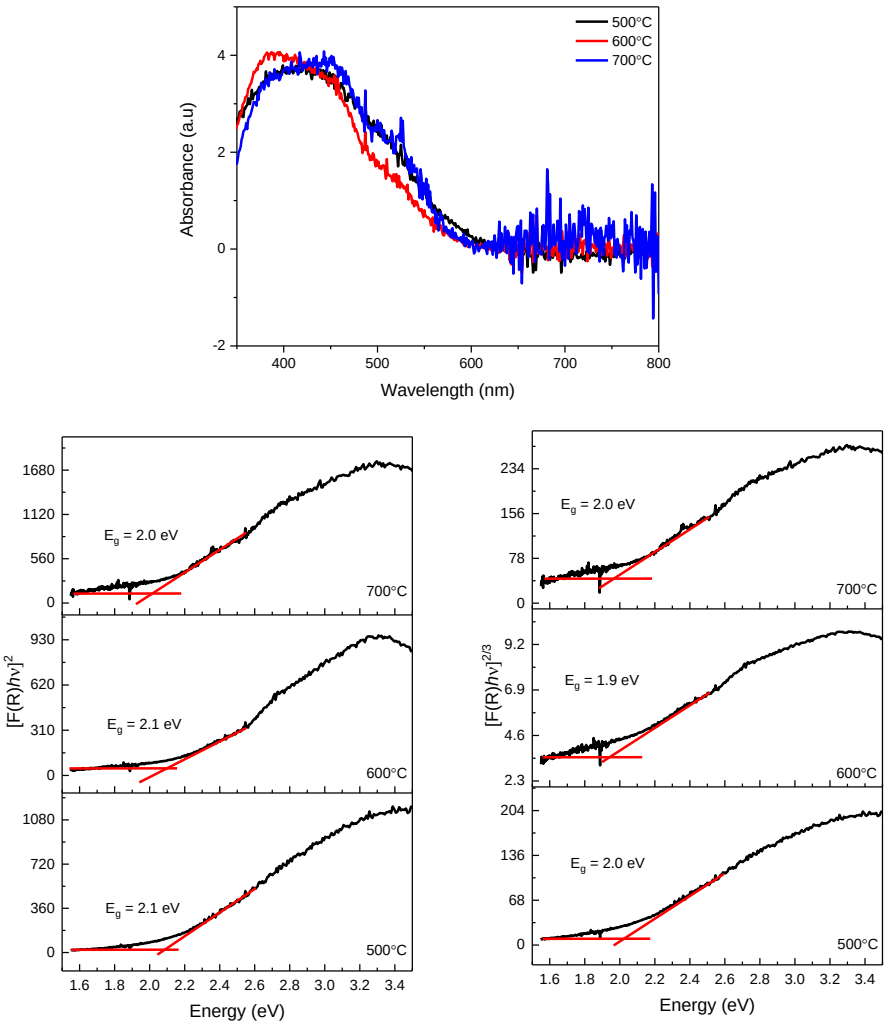

Figure 3-4: UV-Vis spectra of LFO powders calcined at 500, 600 and 700 °C (top) and Tauc plot determination using the Kubelka-Munk function considering a direct allowed and direct forbidden transition (bottom).

$$[F(R)h\nu]^{1/n} = A(h\nu - E_g)$$

Equation 12: Tauc equation for the determination of energy band gap.

A Tauc plot can then be created with $[F(R)h\nu]^{1/n}$ versus energy ($h\nu$) and by determining the x-axis intercept you can obtain the optical band gap (E_g) (Figure 3-4).

Due to the optical transitions in these complex and polycrystalline LFO particles, featuring potential elemental disorder and band tailing, a deviation from standard direct transitions can be observed. Hence, both a direct allowed (n = 1/2) and direct forbidden (n = 3/2) optical transitions were considered. For LFO powders calcined at

500, 600 and 700 °C a calculated band gap range of 1.9 to 2.1 eV was found (Figure 3-4), which are all within the visible light region (580-610 nm) and are comparable to stated literature values, such as 2.15[115] and 2.11 eV.[113]

3.2 Photocatalytic measurements

These synthesised LFO nanoparticles were then measured for their activity in photocatalytic water reduction. This activity was measured through the use of a gas tight photochemical slurry reactor with an effluent line connected to a gas chromotograph (GC) to measure evolving gases (Figure 3-5). LFO was dispersed in a H_2O/MeOH solution (80:20), where methanol acts as a photogenerated hole scavenger, and placed in a quartz reaction vessel. This reactor was then illuminated by an Xe lamp and the gases being evolved over time were measured by GC (Method 2.2). It was found that measurable amounts of H_2 was seen for all calcined LFO powders. The amount of H_2 produced was calculated from comparing to a GC peak area achieved from a known concentration of H_2 within a gas mixture. The rates of H_2 evolution were found to be 55, 133, 137 μmol h^{-1} g^{-1} for calcination temperatures of 500, 600 and 700 °C respectively. This demonstrates that these synthesised LFO particles are active for photochemical water reduction, which is expected due to previous reports within the literature.

It appears that a lower calcination temperature of 500 °C provides the lowest rate of hydrogen evolution, with an increase of 82 μmol h^{-1} g^{-1} being reported when the calcination temperature was increased to 700 °C. At higher temperatures there are

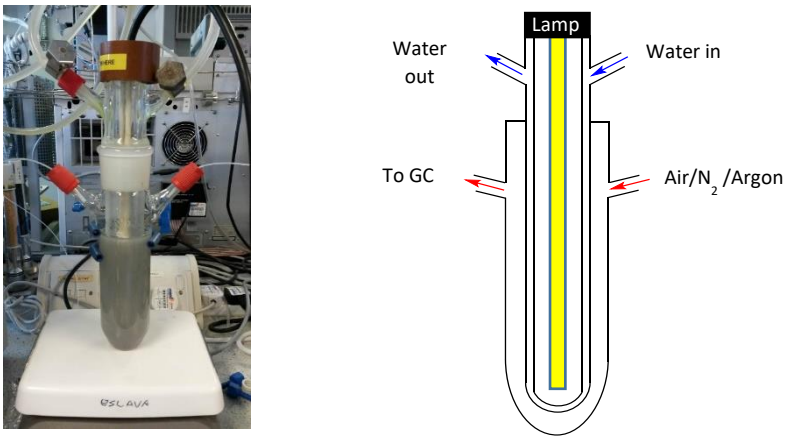

Figure 3-5: Photochemical slurry reactor used to measure activity for photocatalytic water reduction with a schematic of the reactor.

more sintering opportunities, which is expected to reduce active surface area and increase particle sizes, despite this higher activity being seen. However, XRD measurements revealed that at higher temperatures there are more distinct peaks, suggesting a greater level of crystallinity (Figure 3-1). Therefore, there is a trade-off between crystallinity and surface area when trying to optimise calcination conditions, as a temperature of 500 °C results in the smallest particle sizes (largest surface area) but perhaps lacks crystallinity. Moreover, it could be suggested that at lower calcination temperatures there might be increased defect states, that could cause limitations in activity and decreased charge separation, but future further analysis would be needed to confirm this. The results seen here are considerably lower than that in the literature, for example a H_2 evolution of 8600 μmol h^{-1} g^{-1} for LFO prepared through a sol-gel method and a 500 °C calcination was achieved, suggesting further optimisation would be required.[113] This also highlights the lack of activity for LFO particles for hydrogen evolution when compared to the benchmark high performing titania (128300 μmol h^{-1} g^{-1} with a Pt co-catalyst).[117]

This work has demonstrated the importance of calcination temperature on ultimate catalytic activity. However, there were multiple issues that arouse when measuring photocatalytic activity in this way, especially in terms of reactor design. It was notably very difficult to sufficiently disperse particles within the solution of the reactor. The area in which the solution presides was very narrow due to the constraints the compartment containing the lamp and cooling jacket produces, which can be seen in Figure 3-5. Hence, the stirrer bar at the bottom of the reactor undoubtedly failed to evenly distribute the particle suspension within the reactor, meaning that not all of the powder was illuminated with light, or could have limited contact with the water/ethanol solution thus limiting photocatalytic water reduction. As a result, there is a distinct lack of confidence when comparing between samples due to these high levels of inconsistency between measurements, due to these described dispersive effects, which causes lack of clarity with respect to illuminated surface area. Caution must therefore be taken when considering these measurements into the activity for water reduction, with increases in the reliability of the measurements needed through potential reactor re-design.

3.3 Conclusions

$LaFeO_3$ microparticles have been successfully synthesised using a simple sol-gel method with calcination temperatures of 500, 600 and 700 °C which was confirmed by XRD measurements. The measured energy band gaps of these LFO particles was approximately 2.1 eV and is within stated literature values, such as 2.15[115] and 2.11 eV.[113] A demonstration into the ability of these LFO microparticles for photocatalytic water splitting was shown, achieving a maximum hydrogen generation of 137 μmol h^{-1} g^{-1} for LFO powder calcined at 700 °C, which is much lower than that reported in the literature.[113] However, there are vast improvements that can be made with reference to synthesis process being optimised towards nanoparticle synthesis. In addition, improvements are required with respect to photocatalytic measurements due to lack of confidence in reactor design.

Chapter 4

4 Fabricating $LaFeO_3$ electrodes for photoelectrochemical processes

It has been previously demonstrated in Chapter 2 that LFO particles are active for the generation of hydrogen from photocatalytic water reduction. It was discussed that there were some problems associated with the photocatalytic activity measurements obtained for LFO nanoparticles with respect to dispersion effects caused by poor reaction design. Another aim as outlined in Section 1.9, was to prepare thin film LFO electrodes through the application of various fabrication methods to evaluate activity for photoelectrochemical processes, which is explored within this Chapter.

4.1 Doctor blading of $LaFeO_3$ particles (LFO-A)

Synthesised LFO particles as prepared in Chapter 2 were deposited on a glass substrate to fabricate photoelectrodes, which can lead to a more controlled and reproducible determination of photocatalytic activity. A PEC cell is commonly used to determine activity of photoelectrodes with a 3-electrode set-up, including a working electrode (LFO), Ag/AgCl reference electrode and a platinum counter electrode. The experimental apparatus used is displayed in Figure 4-1. Firstly, the working electrode was fabricated through dispersing previously synthesised LFO particles (calcined at 500, 600 and 700 °C) in a solution of ethanol and terpineol and then deposited onto fluorine-doped tin oxide coated aluminoborosilicate glass (FTO-ABS glass) using a

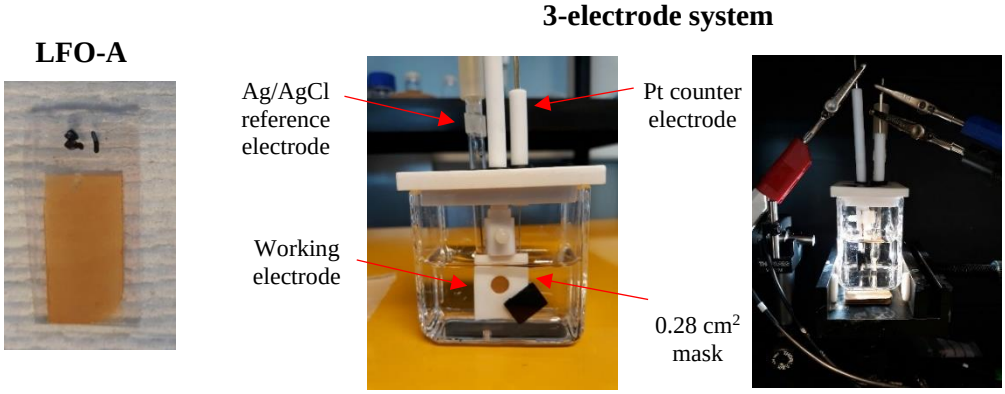

Figure 4-1: Photographs of a prepared film via a doctor blading method onto FTO-ABS glass and the 3-electrode system set-up used for PEC measurements.

doctor blading method (Method 2.3). These films were then annealed to the glass substrate through the application of 500 °C for 2 hours, and were subsequently labelled as LFO-A. These LFO-A films were then measured for their photoresponse as a working electrode within a PEC cell. Figure 4-1 shows a photograph of a prepared LFO-A film after fabrication through doctor blading.

X-ray photoelectron spectroscopy (XPS) was used to characterise these LFO-A films and to confirm the presence of LFO on the FTO-ABS substrate. XPS involves irradiating a surface with an X-ray beam which causes the ejection of an electron from the sample surface. The kinetic energy of these electrons are then measured and can be related to their binding energy with the following equation:

$$KE = hv - BE$$

Equation 13: Relationship between binding energy and kinetic energy used for XPS measurements.

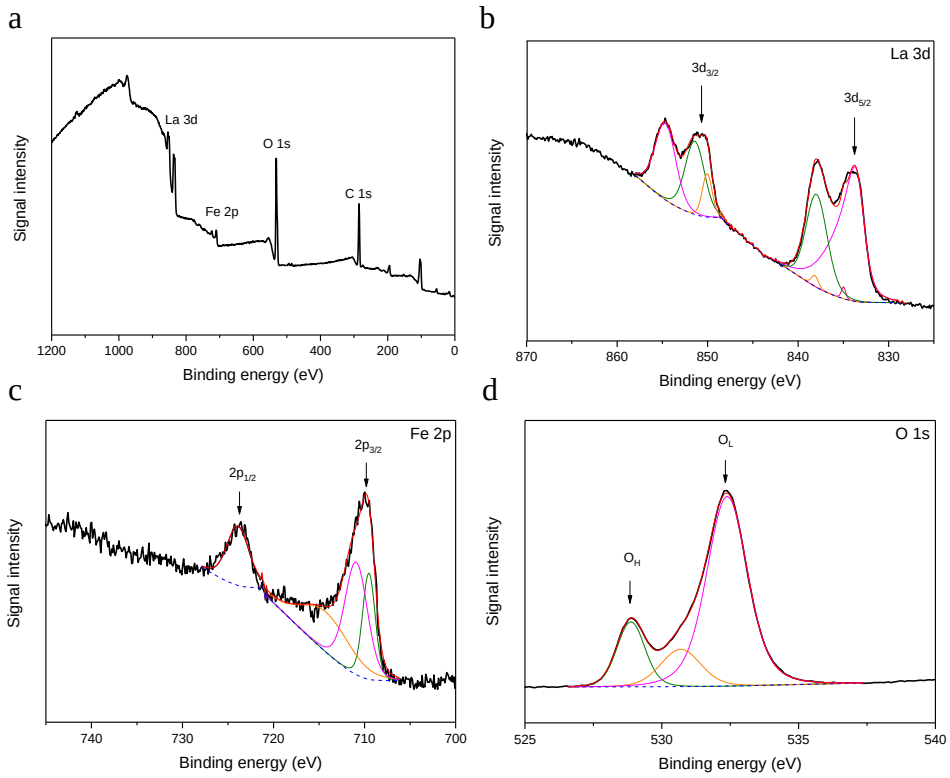

Figure 4-2: (a) XPS survey spectrum and spectra of (b) La 3d, (c) Fe 2p and (d) O 1s for film LFO-A calcined at 600 °C with an annealing temperature of 500 °C.

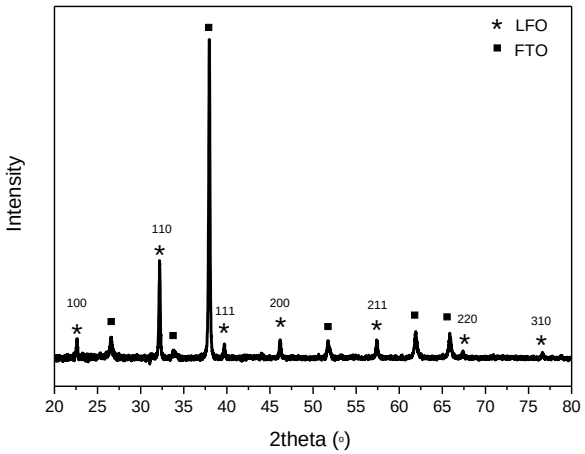

Figure 4-3: XRD spectrum of LFO-A film calcined at 600 °C with an annealing temperature of 500 °C.

This can then allow for the determination of elemental state. Figure 4-2 shows the XPS spectra of these films include that of La 3d, Fe 2p and O 1s orbitals. Figure 4-2b and c show binding energies corresponding to La $3d_{5/2}$ (834 eV), La $3d_{3/2}$ (851 eV), Fe $2p_{3/2}$ (710 eV) and Fe $2p_{1/2}$ (724 eV). Figure 4-2d corresponds to crystal lattice oxygen (O_L) and hydroxyl oxygen (O_H). The O_L signal at 529 eV can be attributed to La-O and Fe-O contributions from the LFO crystal lattice. The second signal at 532 eV can be associated with hydroxyl groups arising from chemisorbed water. CasaXPS software determined the La:Fe ratio to be 1:0.8, close to the desired 1:1. XRD was performed to further confirm the presence of LFO on the substrate, with all diffraction peaks corresponding to phase pure LFO with a calculated crystal domain size of 44 nm (Figure 4-3).

4.1.1 Photoelectrochemical measurements

Firstly, the optimal LFO calcination temperature was investigated by determining which temperature provided the highest photocurrent density. Two LFO layers were applied to the FTO-ABS glass substrate to maximise activity recorded. Linear sweep voltammetry (LSV) measurements were conducted under chopped simulated sunlight (AM 1.5 G filter at 100 mW cm^{-2}), with a 0.1 M Na_2SO_4 (pH 12) electrolyte (Method 2.19). During all PEC measurements within this Chapter the electrolyte used is unpurged and has been exposed to air. This is an important consideration when comparing recorded photocurrents with literature values, as the presence of oxygen

can enhance activity through acting as a sacrificial electron acceptor. This is described in more detail in Section 4.7, but this must be clearly reported in the literature as the selectivity for particular PEC processes can be diminished if oxygen is present.

Figure 4-4 shows chopped light LSV curves obtained during these measurements, which can be used to determine photocurrent density. On the chopping of light, distinctive 'bumps' appear in the LSV measurement, due to the generation of photogenerated electron-hole pairs producing a cathodic photocurrent response which can be measured. The photocurrent density was measured at the water reduction potential -0.91 $V_{AgCl,}$ which was calculated from the modified Nernst equation (Equation 8), considering the water reduction potential for a reversible hydrogen electrode (0 V_{RHE}) and the pH 12 electrolyte used. Figure 4-4 shows that a calcination temperature of 600 °C achieved the highest photocurrent density of -2.6 μA cm^{-2} compared to -0.9 and -1.1 μA cm^{-2} for 500 and 700 °C. This is consistent with the appearance of poor crystallinity of powders calcined at 500 °C and the low surface area of those calcined at 700 °C, offering a prediction that a calcination of 600 °C is beneficial. Along with the hydrogen evolution data reported in Section 3.2, this suggests the optimal calcination most likely lies between 600 and 700 °C. However, these are very low photocurrents achieved with no error bars established, producing difficulties in applying definitive conclusions into optimal calcination temperature in terms of PEC activity.

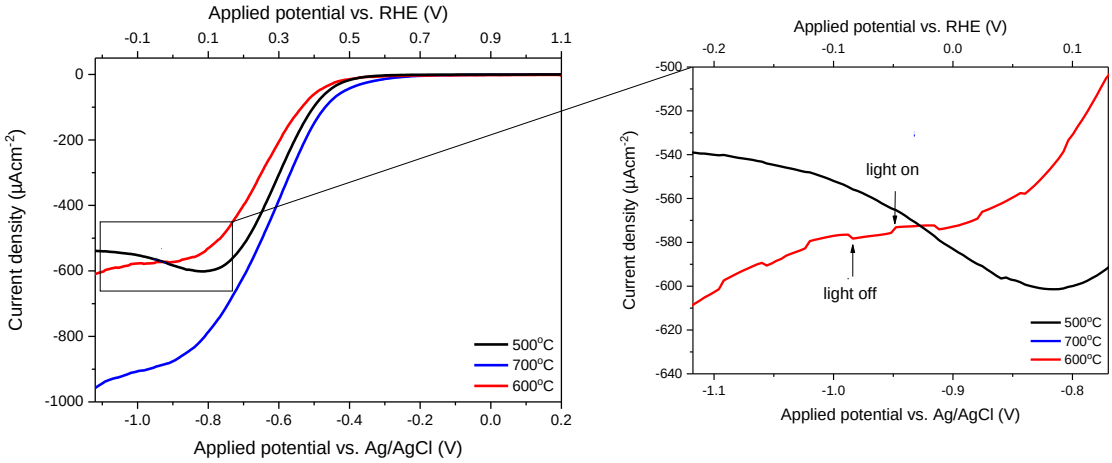

Figure 4-4: Chopped light LSV curves for LFO-A films on backside illumination calcined at temperatures of 500, 600 and 700 °C, with focussed area of interest.

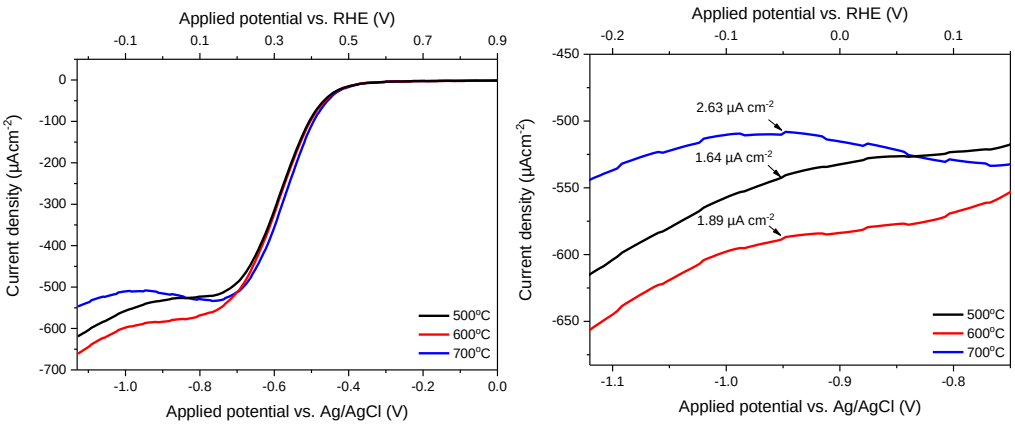

Figure 4-5: Chopped light LSV curves for LFO-A films on backside illumination with annealed at 500, 600 and 700 °C (left), with focused area of interest (right).

In addition to investigating the optimal calcination temperature for LFO particles, the annealing temperature during film fabrication was considered, which can affect the sintering of particles upon the FTO-ABS glass. This can therefore determine the quality of contact formed between the LFO particles and the conductive FTO, which can influence charge transfer. For an LFO calcination temperature of 600 °C, an annealing study was conducted, in which the films were prepared through doctor blading, and then were annealed to the glass substrate at 500, 600 and 700 °C for 2 hours. Figure 4-5 shows the photocurrent densities achieved for these films at different annealing temperatures. A higher photocurrent was achieved on the increasing of annealing temperature, with 700 °C achieving a photocurrent density of -2.6 μA cm^{-2} when compared to -1.6 μA cm^{-2} for a 500 °C annealing. This is most likely due to the prevalence at higher temperatures for greater annealing of particles onto the FTO surface, which can improve surface contact. Simply, this increase in activity could also be due to particles being calcined further during annealing, giving rise to improved crystallinity and decreased defect states. In any case, higher temperatures of above 500 °C appears to be beneficial during synthesis and film fabrication. Despite this attempt to enhance the photocurrent observed, through optimisation of deposition, it is still abundantly clear that these photocurrents are extremely low.

To establish a possible cause for such low activities reported, FE-SEM micrographs were captured of these LFO-A films annealed at 700 °C, to observe film quality produced. Figure 4-6 shows these FE-SEM micrographs, where a distinct lack of

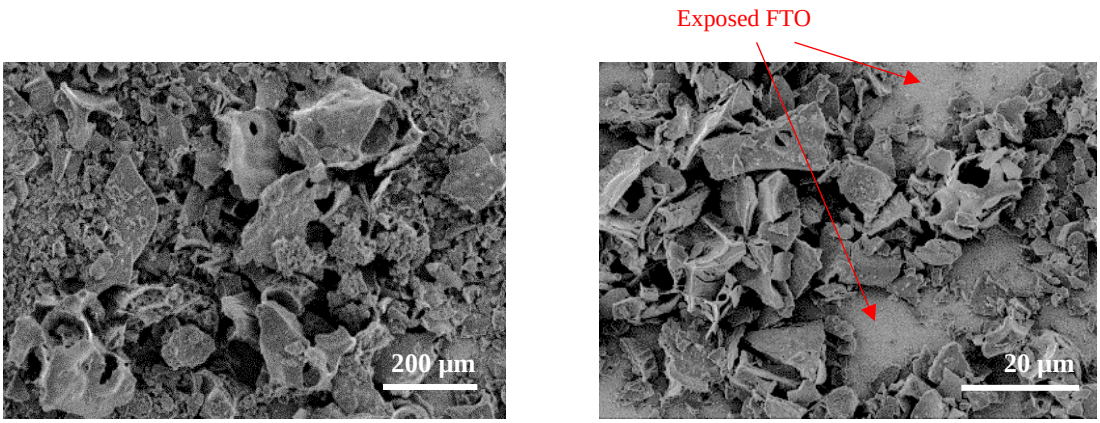

Figure 4-6: FE-SEM micrographs of an LFO-A film annealed at 700 °C for 2 hours.

coverage of the LFO particles on the glass substrate can be seen and so failing to take advantage of the entire substrate area. This is demonstrated through the presence of micrometer-sized particles and large areas of exposed FTO resulting in lack of active surface area. This doctor blading fabrication method has failed in producing a uniform reproducible film of high coverage despite two LFO layers, which is desired for thin film photoelectrodes. This poor film quality could explain to an extent the poor photocurrent density recorded, due to the absence of high-quality films. Overall, a doctor blading method with LFO powders clearly failed to produce the desired outcome, due to poor photocurrents and poor film quality due to large LFO particles having limited contact with the conductive FTO. This will inevitably limit both the light absorption and charge transport to the back contact. Therefore, to improve the appearance and quality of these LFO photocathodes, different fabrication methods are needed to be explored in order to optimise deposition process and ultimately enhance PEC activity.

4.2 Spray pyrolysis of milled $LaFeO_3$ particles (LFO-B)

One of the major problems seen with the doctor blading method used in Section 4.1, was the appearance of large particles on the FTO substrate. One way to decrease these LFO particle sizes is through prior sonication in solvents. This has already been shown to be beneficial in reducing particle sizes. Therefore, sonication of LFO particles was applied here to reduce particles sizes and hence increase active surface area. To further assist in reducing particle sizes, the LFO powder was first ball milled for 24 hours with 2 mm alumina beads. A Malvern Mastersizer instrument was used to determine

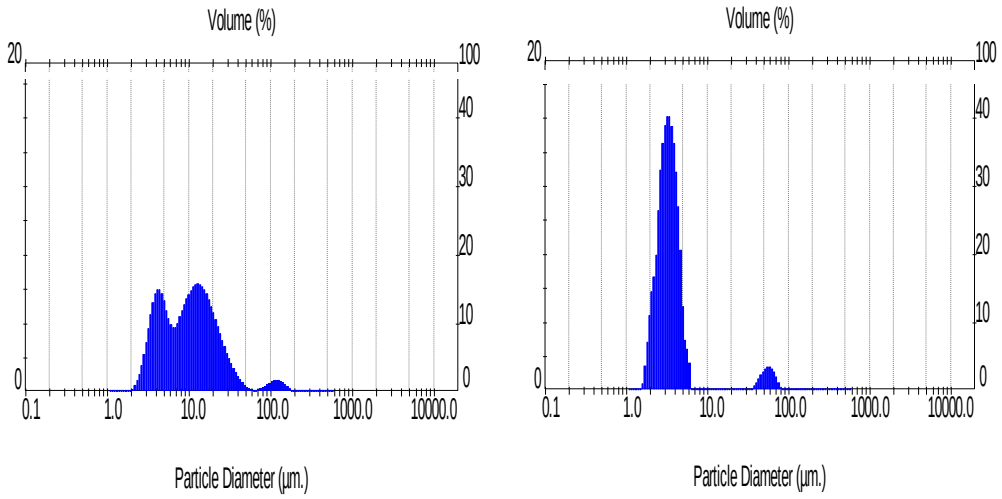

Figure 4-7: Malvern Mastersizer particle size analysis of LFO particles before milling (left) and after two days of roll milling with alumina beads (right).

particle size distributions before and after milling. After milling it was seen that the average particle size distribution narrowed and decreased to the region of 1-10 µm, with a size distribution before milling being between 10-50 µm (Figure 4-7). This also confirms that this sol-gel synthesis produces particles that are micrometre in size and not nanometre. These milled powders were first dispersed in dimethylformamide (DMF) and then sonicated for 72 hours and then allowed to settle for 48 hours. As opposed to doctor blading, a spray pyrolysis method was utilised here by transferring the supernatant (containing the refined LFO powder) into a Clarke air brush gun with attached compressor. This was sprayed in an up and down motion 5 times from left to right onto FTO-ABS glass situated on a hotplate set to 150 °C to evaporate the solvent. This was then annealed at various temperatures (600, 700 and 800 °C) for 2 hours, with a second annealed LFO layer being applied. These films were labelled as LFO-B (Method 2.4).

XRD measurements confirmed the presence of phase pure LFO for these LFO-B films with a calculated crystal domain size of 35 nm. Tauc plots were created and determined a band gap of 2.2 eV, after considering direct allowed and direct forbidden optical transitions (Figure 4-8). Additionally, XPS in Figure 4-9b to d show spectra of La 3d, Fe 2p and O 1s orbitals. Binding energies corresponding to La $3d_{5/2}$ (834 eV), La $3d_{3/2}$ (850 eV), Fe $2p_{3/2}$ (710 eV) and Fe $2p_{1/2}$ (724 eV). Figure 4-9d corresponds to

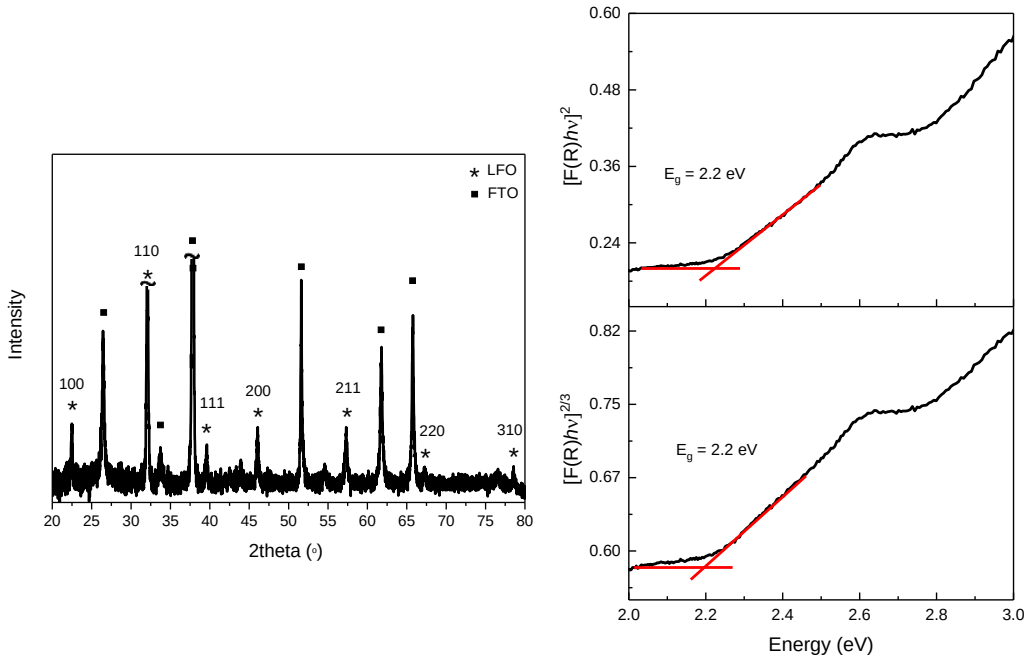

Figure 4-8: XRD spectrum (left) and Tauc plots of LFO-B films annealed at 600 °C (right).

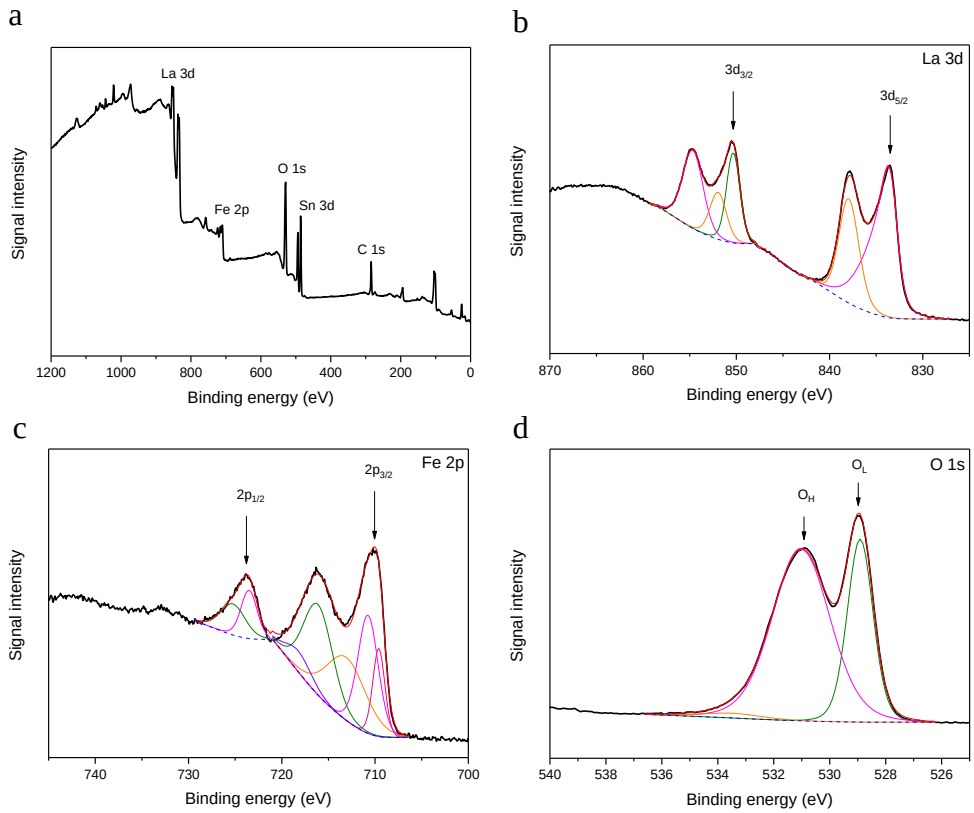

Figure 4-9: (a) XPS survey spectrum and spectra of (b) La 3d, (c) Fe 2p and (d) O 1s for film LFO-B annealed at 600 °C.

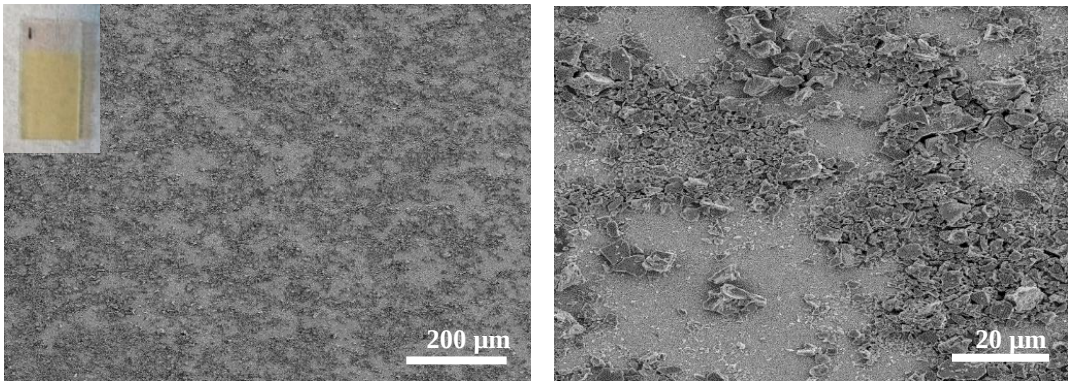

Figure 4-10: FE-SEM micrographs of LFO-B films prepared through spray pyrolysis, with insert of a photograph of a fabricated LFO-B film annealed at 600 °C.

crystal lattice oxygen (O_L) and hydroxyl oxygen (O_H). The O_L signal at 529 eV can be attributed to La-O and Fe-O contributions from the LFO crystal lattice. The second signal at 531 eV can be associated with hydroxyl groups arising from chemisorbed water. The atomic ratio of La:Fe was determined to be 1:1.1 using CasaXPS software. FE-SEM micrographs were obtained of these LFO-B films to determine whether film coverage and uniformity were improved with this method. Figure 4-10 shows that there is a distinct reduction in particle sizes due to the prior sonication of the LFO powders compared to LFO-A films, with spray pyrolysis enabling a more uniform size distribution than a doctor blading method. However, there is still an absence of complete coverage on the FTO surface, eluding to poor film quality.

4.2.1 Electrochemical measurements

With any type of working electrode it is vital to determine electrochemical properties such as electrical capacitance and resistance which dictates performance. In simple electrical circuits the resistance of a circuit element can be determined by Ohm's law.

$$R = \frac{V}{I}$$

Equation 14: Ohm's law relating voltage and current to resistance of a circuit element.

For an ideal capacitor the determination of resistance follows Ohm's law at all voltages and is consistent over a range of frequencies. However, for real life circuit

elements their properties are more complex so cannot be simplified in this way. Hence, the determination of resistance is done in the form of impedance which describes the ability of a material to resist electrical current. This can be calculated using electrochemical impedance spectroscopy (EIS) that measures the impedance (real component: Z') over different AC frequencies. It also measures an imaginary impedance value from capacitance as shown in Equation 15 (imaginary component: Z''). Where C is capacitance, F is angular frequency (2πf) and Z'' is the imaginary component of impedance. A Nyquist plot can then be created using Z' vs Z'' where the gradient of each plot for different materials can be used to determine changes in resistivity between samples. In addition, capacitance can be calculated from Z'' using Equation 15, to determine whether there is a frequency dependence, which can be indicate deviation from ideal capacitor behaviour. Capacitance was calculated at 10, 100 and 1000 Hz to examine whether there are consistencies across different frequencies (Method 2.21).

$$C = \frac{-1}{FZ''}$$

Equation 15: Determination of capacitance from EIS measurements.

Figure 4-11 shows that the capacitance possesses a frequency dependence, which strongly suggests that these prepared LFO-B films deviate from ideal capacitive behaviour, hence equivalent electrical circuits were not fitted.

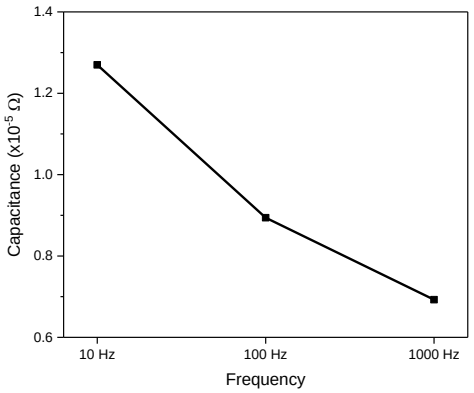

Figure 4-11: Capacitance values determined from EIS measurements as a function of frequency measured at -0.3 V_{AgCl}.

Despite this, Mott-Schottky plots were created using the following equation:

$$\frac{1}{c^2} = \frac{2}{A^2 N_D e \varepsilon_0 \varepsilon}\left(V - V_{fb} - \frac{K_b T}{e}\right)$$

Equation 16: Mott-Schottky equation for determination of electronic properties.

where C is the capacitance, N_D the hole carrier density, e the elemental charge, ε_0 the permittivity of the vacuum, ε the relative permittivity of LFO ($6x10^3$), V the applied potential, V_{fb} the flat band potential, K_b the Boltzmann constant and T the temperature. Mott-Schottky plots can help confirm whether an electrode displays p or n-type behaviour, the charge carrier density (N_D) and the flat band potential (V_{fb}), which has been extracted previously for p-type semiconductors, including LFO.[123] This was completed by conducting EIS measurements at different potentials and at different fixed frequencies of 10, 1000 and 1000 Hz. It can be seen in Figure 4-12 that the slopes within these Mott-Schottky plots are negative, which confirms these LFO-B films are p-type in character (photocathodes). From the determined gradient of the linear portion of these slopes, the carrier (hole) density can be determined using Equation 16. Hence, the carrier (hole) density was determined to be $1.5x10^{16}$, $8.2x10^{15}$ and $6.5x10^{15}$ cm^{-3} for frequencies 10, 100 and 1000 Hz respectively, whereas previously reported values include $6x10^{17}$ and $15x10^{18}$ cm^{-3}.[99,123] Additionally, the flat band potential (V_{fb}) was determined through finding the X-axis intercept of these plots which was +1.70±0.36 V_{RHE} (+0.55 V_{RHE}). Using this determined V_{fb} in conjunction with the band gap of 2.2 eV, a relative band alignment can be created that confirms this LFO band structure encompasses the water reduction potential (Figure 4-13). Overall, this confirms that these LFO-B films are both p-type in character and have the appropriate band alignment to take part in water reduction. However, serious caution is needed when considering these determined N_D and V_{fb} due to problems with extracting information from EIS measurements taken for porous films of unknown unknown exact electrode area. Additionally, the dielectric constant (ε) for ferrites are very large and uncertain making accurate determination of carrier density difficult, as well the issue of frequency dependence of the slopes, has resulted in these determinations for LFO films to be avoided within the literature.[121] In addition, it has

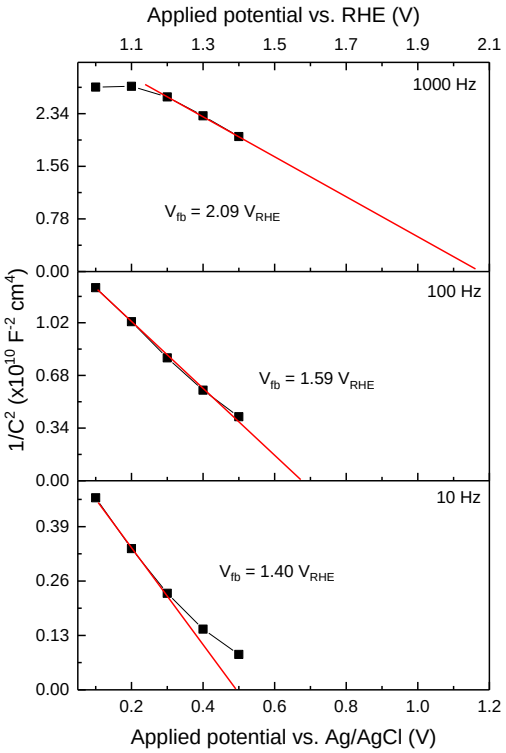

Figure 4-12: Mott-Schottky plots completed at -0.3 V_{AgCl} for LFO-B at different frequencies.

$$N_D = \left(\frac{2}{A^2 e \varepsilon \varepsilon_0}\right)\left(\frac{d(1/C^2)}{d(V)}\right)^{-1}$$

Equation 17: Calculation of carrier density from Mott-Schottky plots.

been previously examined how there are multiple pitfalls in determining flat band potential especially in relation to nanostructured films. Depending on which experimental technique is used this dictates a wide range of V_{fb} determinations, hence highlighting the caution needed when extracting information from impedance analysis.[134] Hence, with further prepared LFO films less weight is given to this analysis.

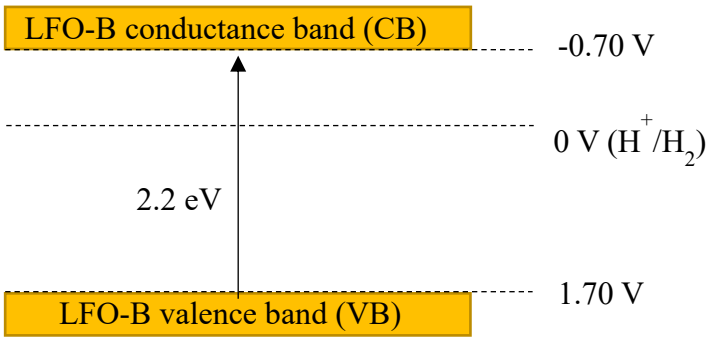

Figure 4-13: Relative band alignment for LFO-B with reference to calculated band gap and flat band potential.

4.2.2 Photoelectrochemical measurements

PEC measurements were then obtained for these LFO-B films annealed at 600, 700 and 800 °C. Figure 4-14 shows at an annealing temperature of 600 °C the highest photocurrent density of -11 µA cm^{-2} was achieved, compared to 4 and < 1 µA cm^{-2} at -0.91 V_{AgCl} for annealing temperatures of 700 and 800 °C. This shows an increase in photocurrent compared to a pristine LFO-A film prepared through doctor blading (-2.6 µA cm^{-2}), which could be due to the visible decrease in particle sizes achieved. It was also shown on increasing the annealing temperature the activity decreases, which could be due to sintering effects as seen and discussed previously. To increase this photocurrent further, during the spray pyrolysis of the supernatant solution, 10 deposition strokes were applied, as opposed to the original 5 strokes to increase the deposition onto the glass substrate. This was then annealed at the optimal temperature of 600 °C, which was completed twice to maximise coverage. In this instance it was decided that it was more beneficial to measure the photocurrent density at a more positive potential of -0.48 V_{AgCl}, due to increased photocurrents seen and due to the rapid decrease in current below approximately -0.6 V_{AgCl}. The appearance of this LSV feature is discussed later in Section 4.7. Hence, the photocurrent seen in Figure 4-15 was determined to be -37±5 µA cm^{-2} at -0.48 V_{AgCl}, which is an impressive increase in activity compared to doctor blading. To attain how stable these LFO-B films are, they were subjected to chopped simulated sunlight over 1 hour at a constant applied potential of -0.48 V_{AgCl}. It was found that after a 15-minute stabilisation period, there was a decrease in photocurrent of 24 %, demonstrating some room for improvement in terms of stability (Figure 4-15).

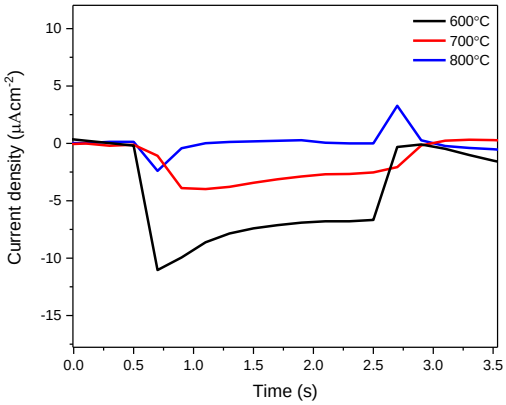

Figure 4-14: Chopped light current vs. time measurements at a constant potential of -0.91 V_{AgCl} for LFO-B films at point of interest for different annealing temperatures.

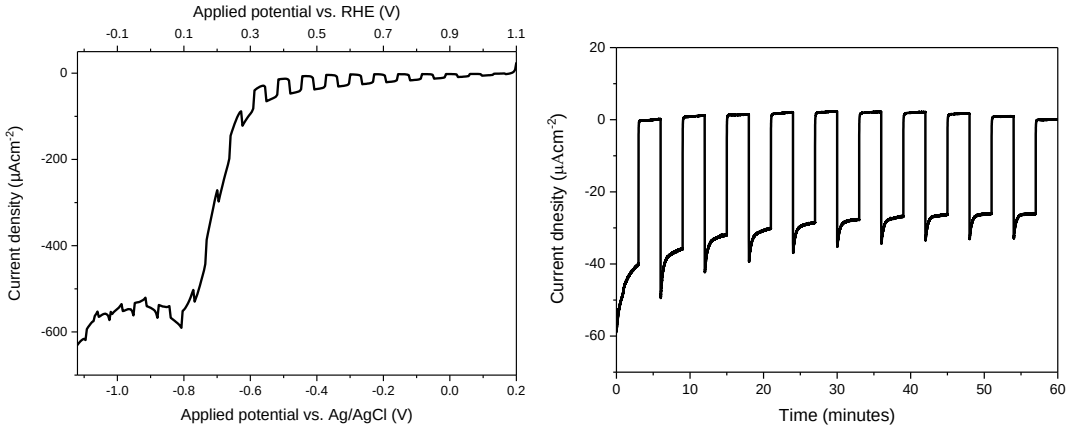

Figure 4-15: Chopped light LSV measurements for LFO-B films annealed at 600 °C prepared with 10 strokes during spray pyrolysis (left) and stability measurement at -0.48 V_{AgCl} over 1 hour (right).

Overall, this has demonstrated that milling and sonication of LFO particles followed by a spray pyrolysis method, is a valuable technique to achieve visibly smaller particle sizes with a more consistent size distribution than a doctor blading method used previously (LFO-A, Section 4.1). With this increased surface area in contact with the FTO, increases in photocurrent were achieved due to this higher level of contact established between the LFO particles and the FTO, allowing for more charge transfer opportunities. However, despite this improvement there is still apparent poor coverage upon the substrate with large portions of FTO still being exposed. Additionally, a single uniform layer was not formed which is problematic when considering

reproducibility and film quality. A different approach is therefore needed to address this, for example through the deposition of LFO precursors directly onto the glass substrate with subsequent heating to form LFO. This can help improve contact between particles and FTO, as there is in situ formation.

4.3 Spray pyrolysis of $LaFeO_3$ precursors (LFO-C)

It is very common to deposit metal oxide precursors directly upon an appropriate substrate during the preparation of films.[135] Hence, for LFO film fabrication lanthanum and iron nitrates in a citric acid solution were deposited directly onto FTO-ABS glass using spray pyrolysis, and then annealed at high temperatures to form LFO in situ. This resulted in just one heating step instead of two as seen in previous techniques (calcination and annealing), which would hopefully limit sintering opportunities as well as on a broader perspective reduce overall energy requirements. An added benefit to this is that the active LFO particles are formed directly upon the FTO which could allow for better charge extraction due to a greater likelihood for better quality contact with the conductive substrate. These LFO films prepared through spray pyrolysis of precursors were labelled LFO-C. The solution of nitrate precursors, citric acid in water was stirred for 48 hours and then deposited using spray pyrolysis with 5 strokes in up and down motions across the FTO substrate and then

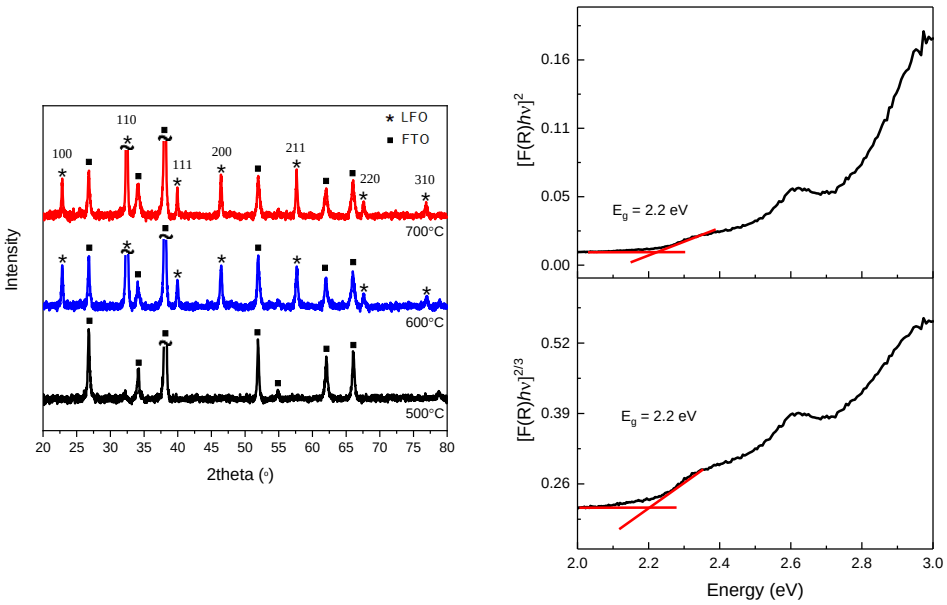

Figure 4-16: XRD spectra for LFO-C films calcined at 500, 600 and 700 °C for 2 hours (left) and Tauc plots for a LFO-C film calcined at 600 °C.

annealed at 500, 600 and 700 °C for 2 hours, this was then repeated for up to 3 layers (Method 2.5).

Firstly, characterisation of these films was done to establish the successful formation of LFO directly on the glass substrate. XRD measurements were completed, and phase pure LFO diffraction peaks were identified for annealing temperatures of 600 and 700 °C, with a crystal domain size of 30 nm for a calcination of 600 °C, suggesting that LFO was successfully formed. No diffraction peaks were seen for an annealing temperature of 500 °C, which could be due to a failure of the formation of LFO or simply a lack of crystallinity (Figure 4-16). Tauc plots were created which determined a band gap of 2.2 eV, after considering direct allowed and direct forbidden optical transitions (Figure 4-16). XPS was conducted for LFO-C calcined at 600 °C, to further confirm the presence of LFO. Figure 4-17b to d show spectra of La 3d, Fe 2p and O 1s orbitals. Binding energies corresponding to La $3d_{5/2}$ (834 eV), La $3d_{3/2}$ (850 eV), Fe $2p_{3/2}$ (710 eV) and Fe $2p_{1/2}$ (724 eV). Figure 4-17d corresponds to crystal lattice oxygen (O_L) and hydroxyl oxygen (O_H). The O_L signal at 529 eV can be attributed

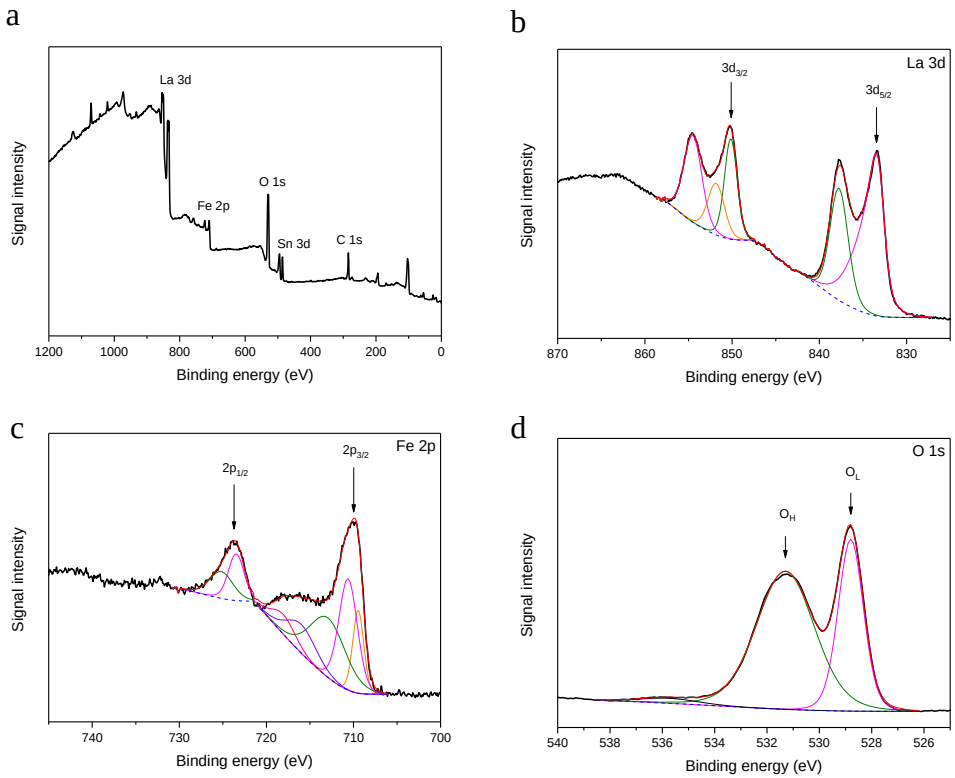

Figure 4-17: (a) XPS survey spectrum and spectra of (b) La 3d, (c) Fe 2p and (d) O 1s for film LFO-C calcined at 600 °C.

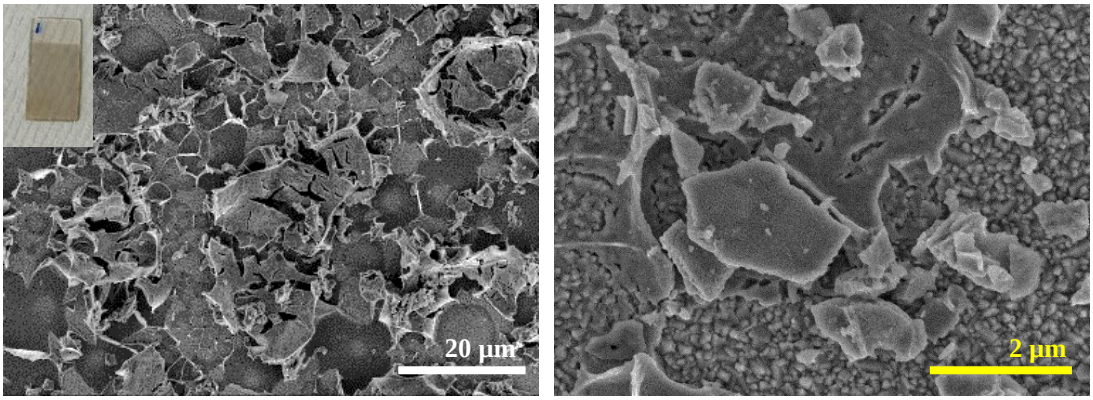

Figure 4-18: FE-SEM micrographs of a LFO-C film calcined at 600 °C with photograph of this prepared film (insert).

to La-O and Fe-O contributions from the LFO crystal lattice. The second signal at 531 eV is associated with hydroxyl groups arising from chemisorbed water. The La:Fe atomic ratio was found to be 1:1, which was the desired ratio during synthesis. FE-SEM micrographs of LFO-C annealed at 600 °C show that LFO has a cracked and non-uniform appearance with rough, uneven and irregular morphology (Figure 4-18). This cracked appearance could be due to the burning off the organic elements within the precursor, preventing a single uniform layer from being formed. Despite this, these are slight improvements in coverage compared to LFO-A and LFO-B films. Although at higher magnifications there is still the persistent presence of large portions of FTO exposed.

4.3.1 Electrochemical measurements

As with LFO-B, a dependence of capacitance on frequency was found with these LFO-C films (Figure 4-19), which was determined from EIS measurements as outlined in Section 4.2.1, which stresses the problems with extracting electronic properties from these porous films. Mott-Schottky plots were created from EIS measurements using Equation 16 for 10, 100 and 1000 Hz, which confirmed these LFO-C films are p-type with a V_{fb} of 1.67±0.18 V_{RHE} (Figure 4-19). Considering a determined band gap of 2.2 eV and the calculated V_{fb} shows that these LFO-C films encompass the water reduction potential (Figure 4-20). Carrier (hole) density was calculated using Equation 17, which was determined to be 5.2×10^{17}, 1.5×10^{17} and 1.8×10^{16} cm^{-3} for 10, 100 and 1000 Hz respectively, however caution is needed.

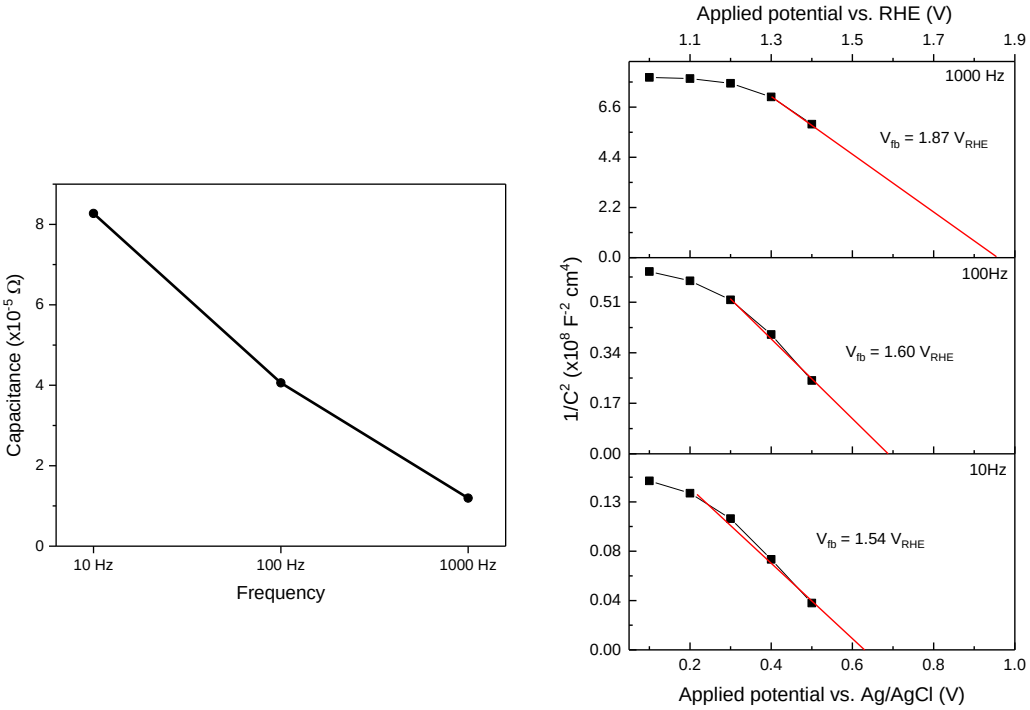

Figure 4-19: Capacitance values determined from EIS measurements as a function of frequency measured at -0.3 V_{AgCl} (left) and Mott-Schottky plots completed at -0.3 V_{AgCl} for LFO-C at different frequencies.

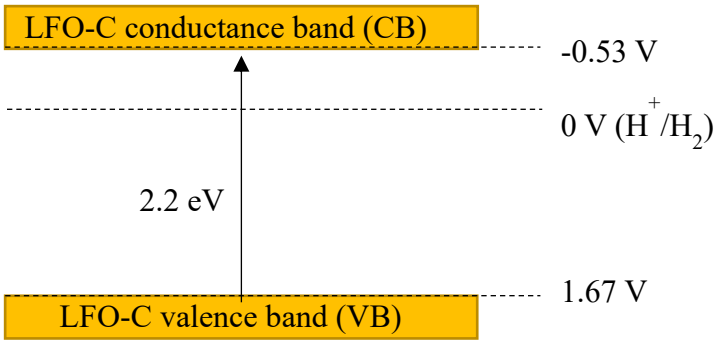

Figure 4-20: Relative band alignment for LFO-C with reference to calculated band gap and flat band potential.

4.3.2 Photoelectrochemical measurements

PEC measurements were then obtained for these LFO-C films, where it was found that no activity was seen for LFO-C annealed at 500 °C, whilst photocurrents of -69.1 and -14.9 µA cm^{-2} at -0.48 V_{AgCl} for temperatures of 600 and 700 °C respectively were

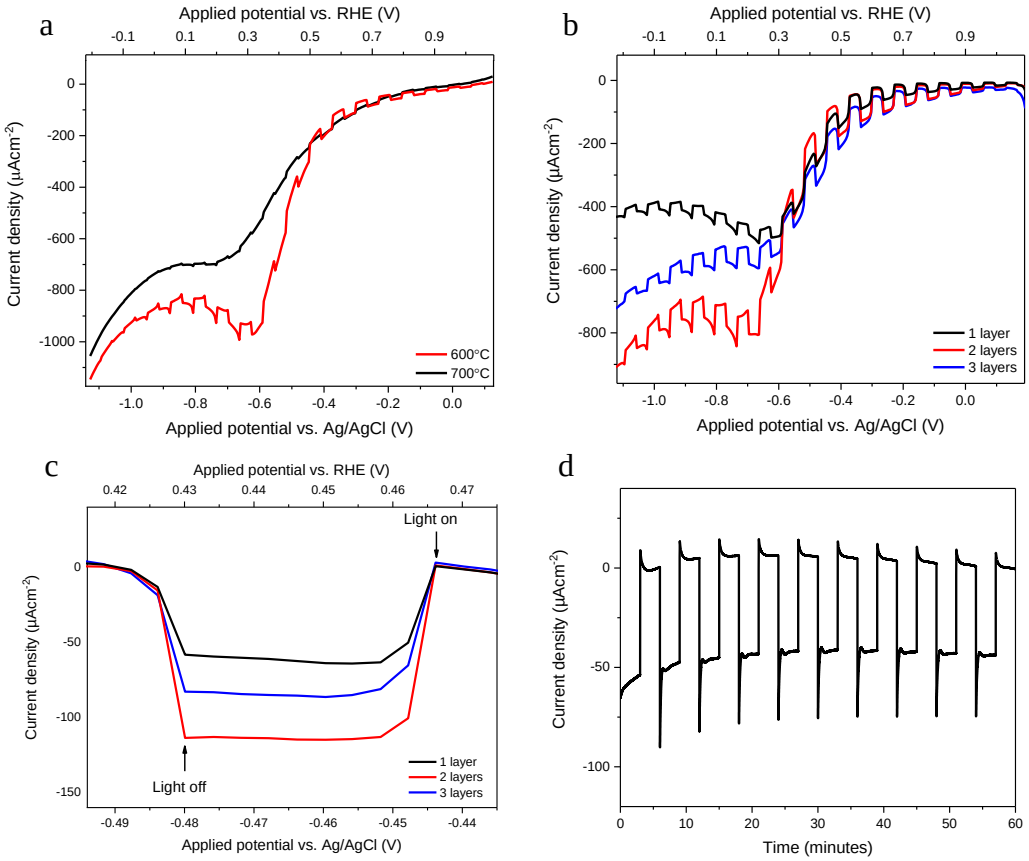

Figure 4-21: Chopped light LSV measurements for (a) LFO-C calcined at 600 and 700 °C using 5 strokes during deposition, (b) LFO-C calcined at 600 °C using 10 strokes during deposition with multiple layers, (c) magnification of point of interest for multiple layers and (d) stability study of LFO-C (600 °C) over 1 hr at -0.48 V_{AgCl}.

found (Figure 4-21a). Further films were then made with 10 stokes during spray pyrolysis rather than 5 with a subsequent 600 °C annealing, repeated up to 3 times to optimise film thickness and to increase photocurrent through the application of additional stokes during deposition. PEC measurements showed that on application of 10 strokes during spray pyrolysis for each applied layer had enhanced photocurrent. A maximum photocurrent density of -112±10 µA cm^{-2} at -0.48 V_{AgCl} was achieved after 2 layers were applied (Figure 4-21b and c) which is an increase on films prepared with just 5 strokes per layer, concluding that 10 strokes is optimal during spray pyrolysis. When a further layer was added to this, the activity decreased to -92 µA cm^{-2}, suggesting that two applied layers provides the optimal amount of material for maximised photocurrent. A stability test was then conducted, where after

1 hour of chopped solar illumination, and a 15-minute stabilisation period, there was a decrease in photocurrent of 11 % (Figure 4-21d), an improvement on LFO-B films (24 %). This suggests that forming LFO directly onto the substrate assists in creating stronger interactions between the particles and the substrate, resulting in this increased stability and vast increase in activity.

The optimised photocurrent density achieved here for LFO-C, is a markable increase on the activity recorded for LFO-A and LFO-B films (-3 and -37 μA cm^{-2}), it can be proposed that spray pyrolysis of nitrate precursors is able to enhance photocurrent due to improved contact with the FTO. A further investigation is later made to probe further this increased photocurrent in Section 4.8 in terms of charge transport and active surface area. Moreover, it was found that these LFO-C films were more stable than LFO-B, further highlighting the benefits of utilising this preparation method. In addition, these LFO-C films possessed much less visible risk of abrasion when applying the mask and clip during PEC measurements compared to LFO-A and LFO-B, with no washing away of LFO in contact with the electrolyte which was especially seen with LFO-A films.

Despite these increases in photocurrent, there were clear and recurring issues due to the persistent failure in achieving maximum substrate coverage and particle uniformity, which would prove problematic in terms of reproducibility. An additional issue with this film fabrication method was the lack of formal spray deposition apparatus which could accurately control the deposition process, which will inevitably result in the lack of high levels of reproducibility. The equipment used for this work involved the use of a simple handheld airbrush gun, which during deposition was moved with up and down motions across the substrate. Although measures were taken to try to make depositions consistent, there was still an obvious lack of ultimate control over the deposition process. Primarily, inconsistencies could arise with controlling the distance above the substrate that the precursors are deposited, and the even distribution of stokes across the substrate. Hence, further work is needed to investigate additional techniques for the in situ formation of LFO onto the FTO substrate, including more reproducible methods of deposition that allow for increases in uniformity. One such way to do this is through the use of spin coating that can be more accurately controlled,

in conjunction with a structure directing agent that can help with both reproducibility and uniformity.

4.4 Graft co-polymer templating with PVC-*g*-POEM (LFO-D)

To address the above discussed problems with LFO films produced thus far, such as poor coverage, uniformity and reproducibility, polymer templating was investigated. Polymer templating has been previously shown to be highly beneficial in improving substrate coverage and reducing particle aggregation. In particular, templating can be done with a graft co-polymer such as poly(vinyl chloride)-*g*-poly(oxyethylene methacrylate) (PVC-*g*-POEM), which has already been shown to be a beneficial templating agent for SnO_2 and $MgTiO_3$ that enabled increased porosity and uniformity.[104,105] Here, lanthanum and iron nitrates with citric acid in water were mixed with PVC-*g*-POEM in THF (6 %) then deposited onto FTO-ABS glass through spin coating, then annealed at high temperatures (500-700 °C) to remove the polymer and form LFO (Method 2.6). The PVC-*g*-POEM graft co-polymer was obtained from collaborators at Yonsei University where it was synthesised by Min Su Park (Method 2.7). This method was implemented to enable the polymer to behave as a sacrificial template to direct particle growth and minimise agglomeration, to produce higher quality more uniform films. The use of spin coating was chosen here in order to introduce increased reproducibility than the previously used spray pyrolysis, which can be done through the accurate controlling of spin speed and time. These fabricated films were labelled as LFO-D.

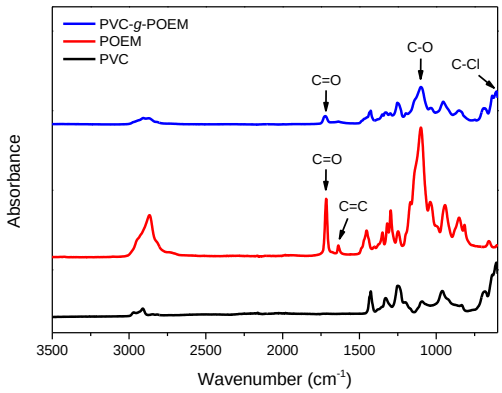

Figure 4-22: FT-IR spectra of PVC-g-POEM, POEM and PVC to highlight successful polymer formation.

Firstly, characterisation by Fourier transport-infrared spectroscopy (FT-IR) was performed to demonstrate the formation of this co-polymer. Characteristic absorbance peaks were found for the PVC chains (C-Cl, 607 cm^{-1}) and the POEM side chains (C=O, 1722 cm^{-1}, C-O, 1098 cm^{-1}). The decrease in absorbance corresponding to the C=C (1632 cm^{-1}) in PVC-*g*-POEM was consistent with most of the PVC bound to the POEM chains (Figure 4-22). XRD analysis confirmed the formation of LFO onto the substrate with an absence of any impurities with a calculated crystal domain size of 22 nm. UV-Vis measurements determined a band gap range of 2.0 to 2.2 eV from Tauc plots considering direct allowed and direct forbidden optical transitions (Figure 4-23). XPS was done to further confirm the presence of LFO and determine the La:Fe ratio to be 1:0.8, which shows a 20% A-site enrichment. A-site segregation is commonly observed in perovskite oxide materials, displaying a very complex dependence of the nature of the A and B sites.[74,98,136,137] Figure 4-24 displays the XPS spectra of LFO-D films including that of La 3d, Fe 2p and O 1s. Figure 4-24b and c show binding energies corresponding to La $3d_{5/2}$ (834 eV), La $3d_{1/2}$ (851 eV), Fe $2p_{3/2}$ (710 eV) and Fe $2p_{1/2}$ (724 eV). Figure 4-24d corresponds to crystal lattice oxygen (O_L) and hydroxyl oxygen (O_H). The O_L signal at 529 eV can be attributed La-O and

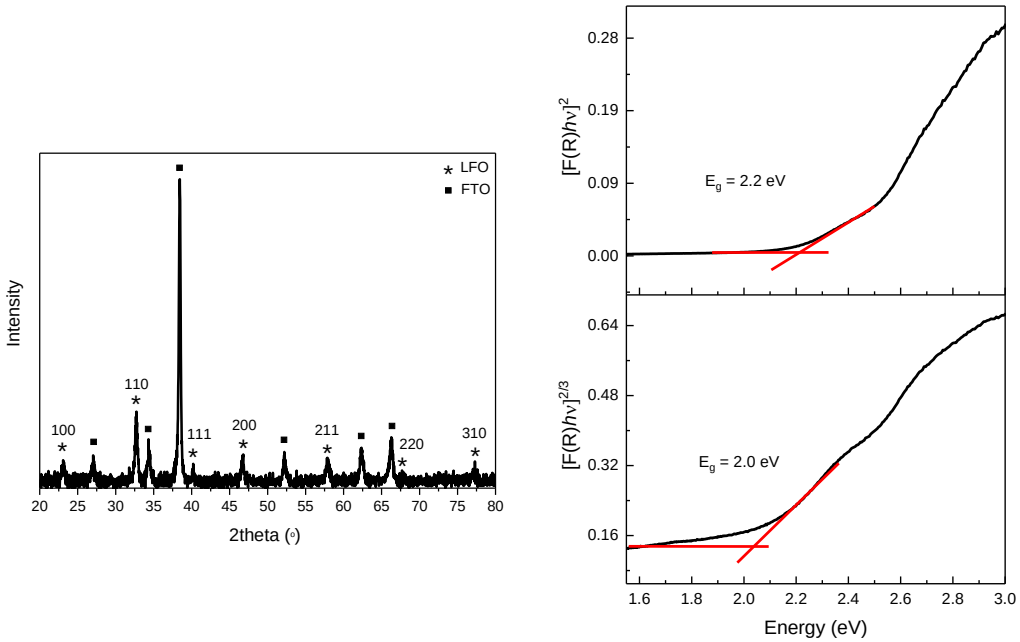

Figure 4-23: XRD spectrum of LFO-D calcined at 600 °C (left) and Tauc plots (right).

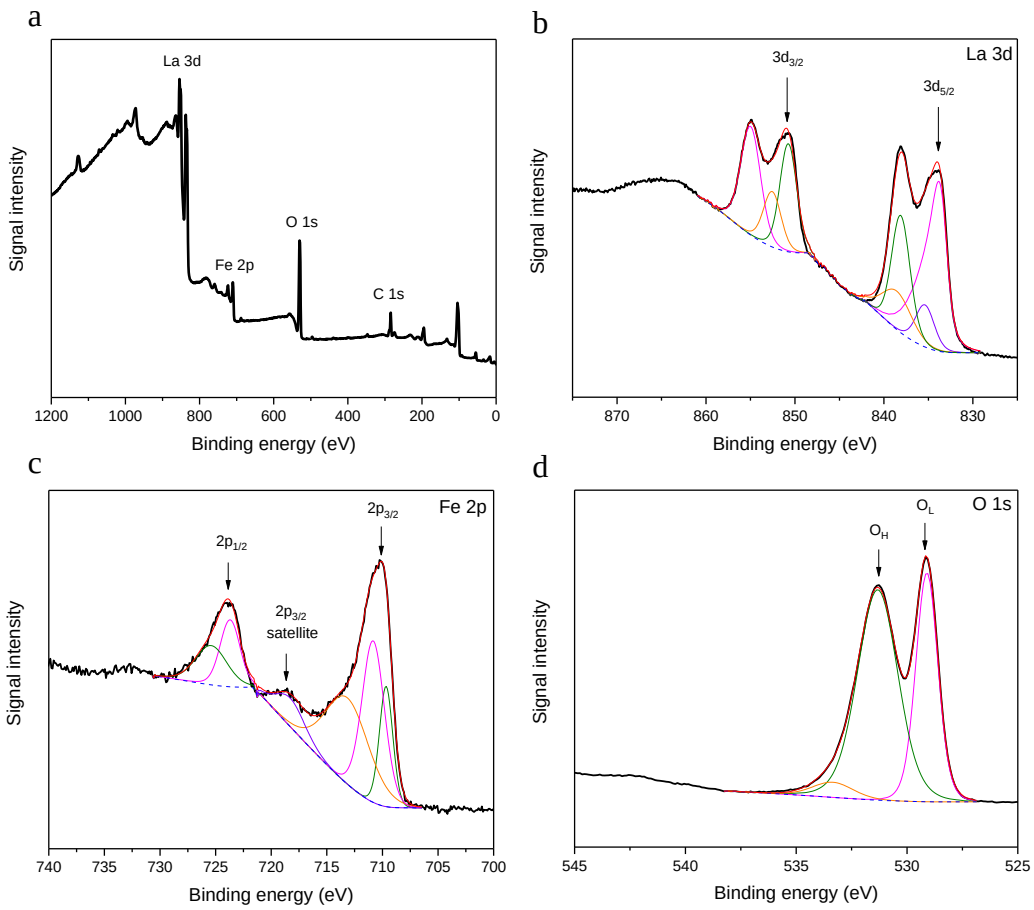

Figure 4-24: (a) XPS survey spectrum and spectra of (b) La 3d, (c) Fe 2p and (d) O 1s for film LFO-D calcined at 600 °C.

Fe-O contributions from the LFO crystal lattice. The second signal at 531 eV can be associated with hydroxyl groups arising from chemisorbed water.

FE-SEM micrographs were taken of these LFO-D films after the application of up to 4 annealed LFO layers, to assess the effect of multiple layers on film quality. It can be seen in Figure 4-25 after just a single LFO layer being applied there is a clear enhancement in uniformity with a marked avoidance of large sintered particles on the surface compared to LFO-A, -B, and -C. However, there are small areas of visibly exposed FTO at this magnification that are covered on the application of a second LFO layer. Again, after the application of a third and fourth layer, coverage is improved still with porous and uniform films being demonstrated. It can be seen from all FE-SEM micrographs that using a PVC-*g*-POEM graft co-polymer template accompanied by spin coating, enables the production of a high-quality film with respect to surface coverage and uniformity. This has been achieved through directing

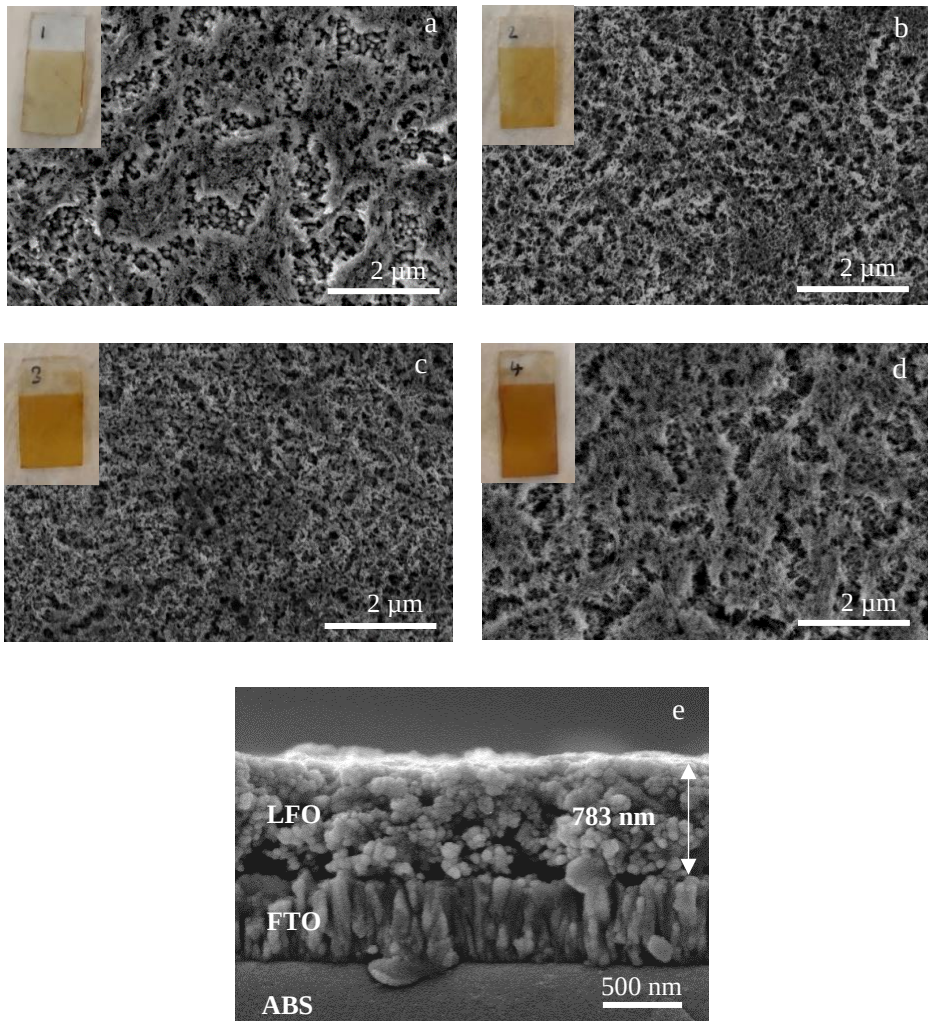

Figure 4-25: FE- SEM micrographs of LFO-D films with (a) 1, (b) 2, (c) 3 and (d) 4 applied LFO layers and (e) cross-section micrograph, with inserts of photographs of each LFO-D film.

growth and preventing agglomeration of LFO particles during formation, due to the presence of the polymer template forming micelle structures with the precursors (Figure 1-17). A cross-section FE-SEM micrograph was captured to determine a film thickness of approximately 783 nm when 4 layers are applied. In addition, a surface profilometer was used to determine the thickness of LFO on addition of each LFO layer which were recorded to be 122, 239, 480 and 765 nm for 1, 2, 3 and 4 layers. From this cross-section, it further confirms that the application of the initial LFO layer contained small portions of FTO that are not fully covered, which was rectified by the application of further layers. It is abundantly clear that these LFO-D templated films

exhibit much improved film quality in terms of uniformity, coverage and porosity compared to LFO-A, -B and -C films. Due to this, it could be predicted that these LFO-D films will display enhanced photocurrent densities as there is an increased exploitation of the total substrate area for active particles to reside.

4.4.1 Electrochemical measurements

EIS measurements were obtained, and as before a frequency dependence on capacitance was observed, highlighting its deviation from an ideal capacitor as well as the difficulties in extracting reliable information from these measurements (Figure 4-26). Nevertheless, Mott-Schottky plots were created which confirmed p-type behaviour indicative of a negative slope, with a determined V_{fb} of 1.71±0.14 V_{RHE}, and with a band gap of 2.0-2.2 eV confirming the incorporation of the water reduction potential (Figure 4-27). Carrier (hole) density was calculated to be $8.7x10^{16}$, $3.9x10^{16}$ and $9.7x10^{15}$ cm^{-3} for 10, 100 and 1000 Hz respectively, but as described previously a great deal of caution is needed when considering the accuracy of these values.

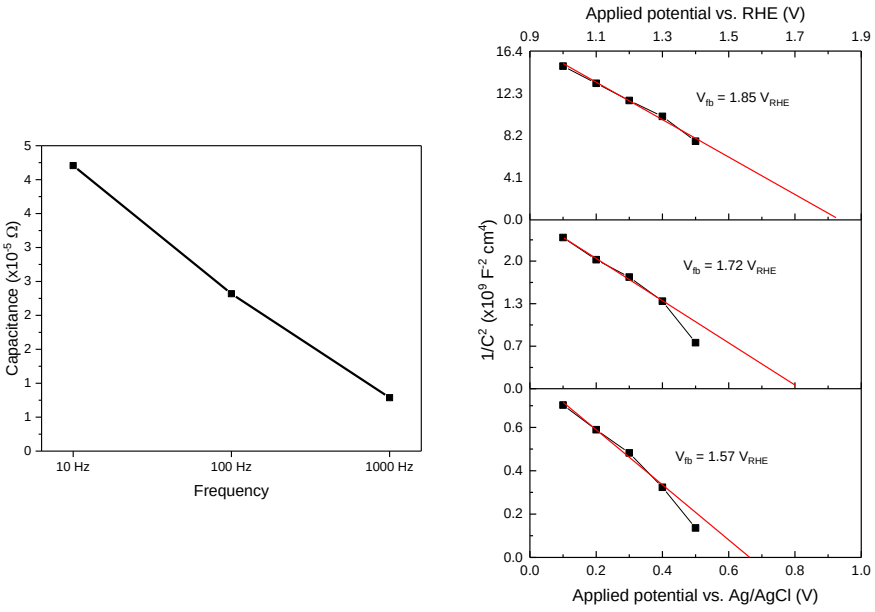

Figure 4-26: Capacitance values determined from EIS measurements as a function of frequency measured at -0.3 V_{AgCl} (left) and Mott-Schottky plots completed at -0.3 V_{AgCl} for LFO-D at different frequencies.

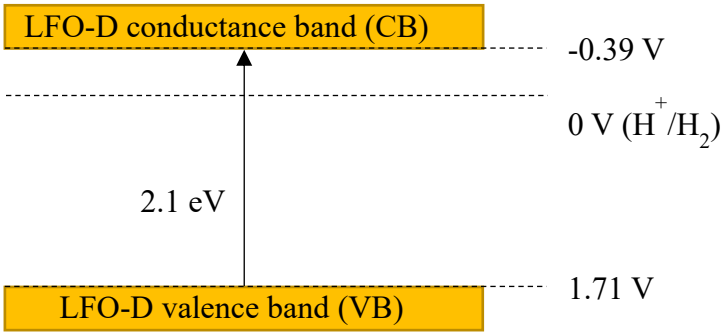

Figure 4-27: Relative band alignment for LFO-D with reference to calculated band gap and flat band potential.

4.4.2 Photoelectrochemical measurements

PEC measurements of these LFO-D films revealed photocurrent densities of -80±7, -110±4, -131±9, -148±6 and -117±9 µA cm^{-2} at -0.48 V_{AgCl} for 1, 2, 3, 4 and 5 LFO layers applied respectively (Figure 4-28a). Demonstrating that the application of 4 spin coated annealed LFO layers is optimal for a maximised photocurrent. This photocurrent of -148±6 µA cm^{-2} (Figure 4-28b) exceeds all previously achieved photocurrents for LFO-A, -B and -C that achieved just -3, -37 and -112 µA cm^{-2} respectively. After conducting a stability measurement, after a 15-minute stabilisation period, there was a decrease in photocurrent of just 9 % after 1 hour (Figure 4-28c) It appears that incorporating this sacrificial polymer template was highly beneficial for film quality and for enhanced photocurrents, which could be due to the improved coverage resulting in higher active surface areas. This was the first reported instance of LFO being templated with this graft co-polymer to fabricate photocathodes. Further investigations in relation to any increases in surface area and changes in charge transport efficiencies is discussed later in Section 4.8 for all fabricated films. Although, these initial results for using PVC-*g*-POEM as a graft co-polymer template for film fabrication were very promising, problems were later encountered.

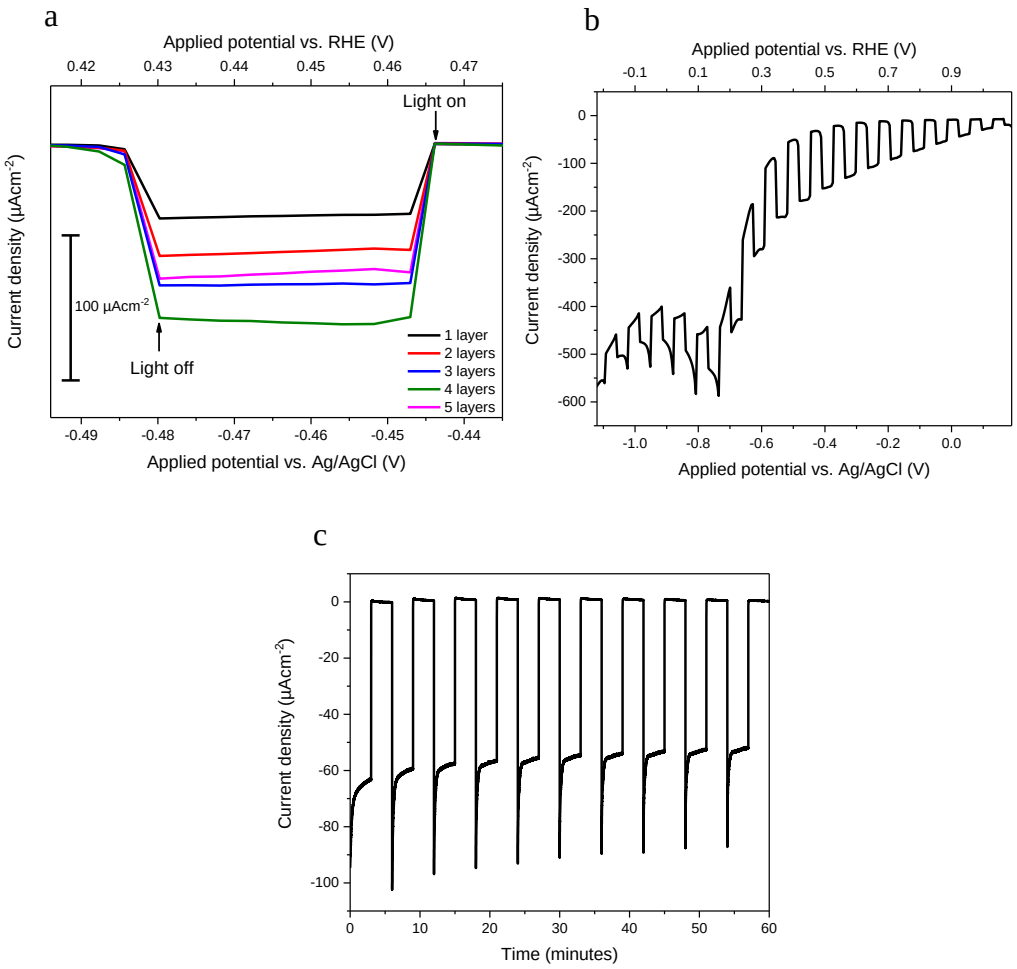

Figure 4-28: (a) Chopped light LSV measurements for LFO-D films annealed at 600 °C with 4 LFO layers applied, (b)comparison between films with 1-5 LFO layers applied and (c) chopped light stability measurement held at -0.48 V_{AgCl}.

4.4.3 Reproducibility problems encountered with PVC-*g*-POEM

During the first instances of using PVC-*g*-POEM as a polymer template for LFO films produced impressive and reproducible results and were subsequently denoted as Batch 1. However, after the synthesis of this first batch problems arouse with the use of new batches of polymer sent by our collaborators. This resulted in failures in reproducing previously attained photocurrents with subsequently synthesised batches of this polymer. It was noted that there were issues arising in relation to temperature control during synthesis, which could result in changes in the binding between PVC and POEM. Namely, it was thought that POEM could have bound in an elevated proportion resulting in the co-polymer being more hydrophilic in nature, which can

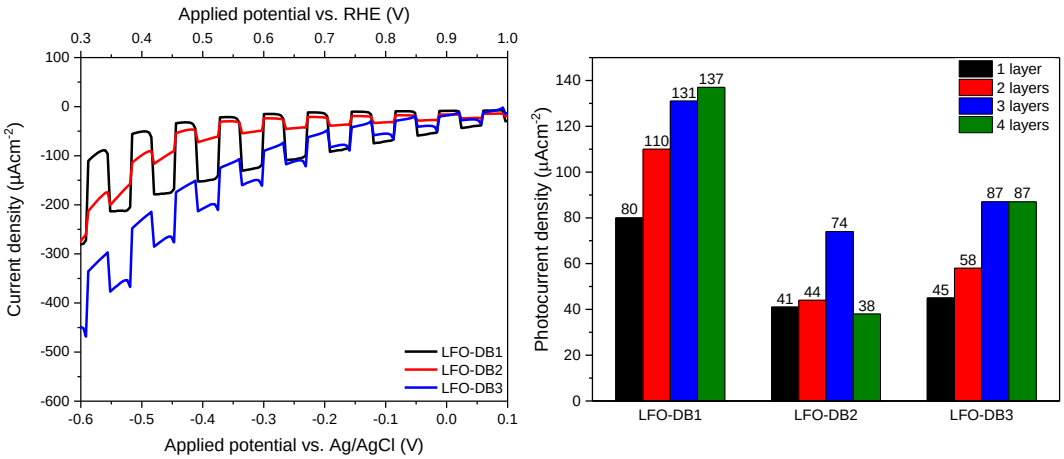

Figure 4-29: Chopped light LSV measurements comparing different synthesised batches of PVC-g-POEM (left) and summary of photocurrents achieved (right).

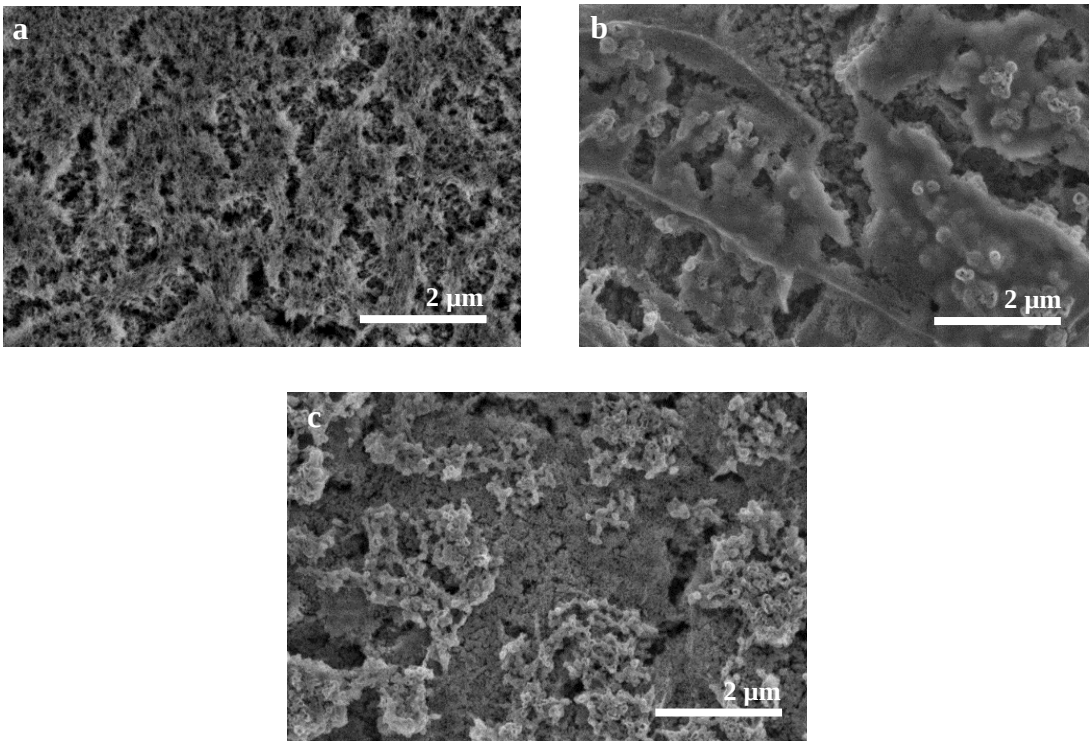

Figure 4-30: FE-SEM micrographs of (a) LFO-DB1, (b) LFO-B2 and (c) LFO-DB3 films using different synthesised batches of PVC-g-POEM.

detrimentally alter its ability to produce the desired templated LFO films. For ease of comparison, the successful Batch 1 PVC-*g*-POEM used initially was named LFO-DB1 and the two subsequent polymer batches were named LFO-DB2 and LFO-DB3. Firstly, PEC measurements were obtained to attain whether reproducible

photocurrents of up to -148 µA cm^{-2} at -0.48 V_{AgCl} can still be achieved with LFO-DB2 and LFO-DB3. It can be seen from these PEC measurements in Figure 4-29 that there are significant decreases in the photocurrent achieved when comparing with the original LFO-DB1 films. LFO-DB2 achieved just -38 µA cm^{-2} and LFO-DB3 achieved -87 µA cm^{-2} at -0.48 V_{AgCl} on the application of 4 annealed LFO layers, with lower activities being observed for each applied layer (Figure 4-29).

FE-SEM micrographs were obtained of LFO-DB1 and LFO-DB2 to see whether there was to some extent a failure of the LFO templating process that could help explain the depreciation of activity seen. Figure 4-30a and b show that LFO-DB2 forms an initial porous LFO layer similar to LFO-DB1, which is then covered by larger more compact layers of LFO of limited porosity. Similarly, LFO-DB3 exhibited a different morphology still, with a denser appearance with a very uneven depth profile (Figure 4-30c). Overall, in both cases it appears that LFO-DB2 and LFO-DB3 possess clear differences in LFO morphology compared to that observed in the high performing LFO-DB1 films. It is apparent that the observed film quality for LFO-D films was not maintained using further batches of PVC-*g*-POEM, and hence reproducible high photocurrents ultimately was not achieved. This demonstrates that the issues arising within the polymer synthesis method resulted in major changes in the templating process, that had detrimental effects on activity of these LFO films. Additionally, this highlights the sensitivity that can arise when using structure directing agents within film fabrication methods. It is therefore unfortunately clear that the use of PVC-*g*-POEM as a sacrificial polymer template cannot be relied upon to be a reproducible templating method to produce high quality LFO films at this stage. Therefore, the use of a commercially bought polymer that could reignite the reliability for a polymer templating method due to better control of polymer synthesis and quality should be explored.

4.5 Polymer templating with Triton X-100 (LFO-E)

Triton X-100 (Polyethylene glycol *tert*-octylphenyl ether) is an inexpensive non-ionic surfactant that has been previously used for templating applications.[74,138] Similarly to PVC-*g*-POEM, Triton X-100 contains a hydrophobic group (aromatic hydrocarbon)

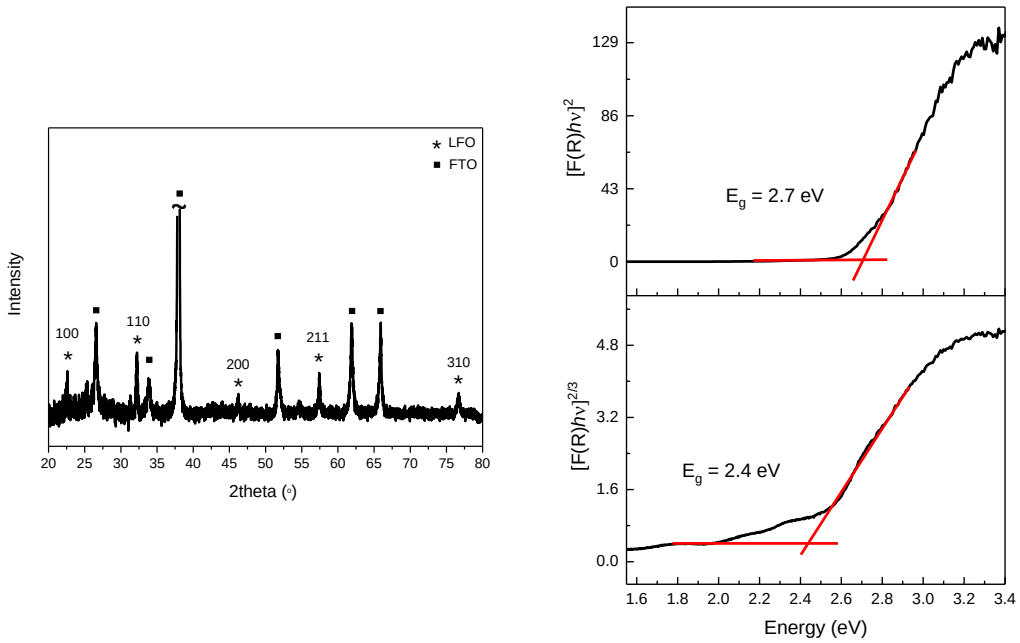

Figure 4-31: XRD spectrum of LFO-E annealed at 600 °C (left) and Tauc plots (right).

and a hydrophilic group (polyethylene oxide chain) which enables a micelle structure to be formed which assists in directing growth and reducing aggregation during LFO formation. Triton X-100 was mixed in a 1:1 ratio with THF and then stirred with lanthanum and iron nitrates overnight. This was then spin coated onto FTO-ABS and calcined at 600 °C to burn away the polymer and form LFO, this was repeated to deposit 4 calcined LFO layers and labelled as LFO-E (Method 2.8). XRD measurements confirmed the presence of phase pure LFO with a calculated crystal domain size of 34 nm, and Tauc plots revealed a band gap of between 2.4-2.7 eV as shown in Figure 4-31 when considering direct allowed and direct forbidden optical transitions. XPS spectra in Figure 4-32b and c of LFO-E films show binding energies corresponding to La $3d_{5/2}$ (839 eV), La $3d_{1/2}$ (855 eV), Fe $2p_{3/2}$ (715 eV) and Fe $2p_{1/2}$ (729 eV). The O 1s spectrum corresponded to crystal lattice oxygen (O_L) and hydroxyl oxygen (O_H). The O_L signal at 534 eV was attributed La-O and Fe-O contributions from the LFO crystal lattice. The second signal at 536 eV can be associated with hydroxyl groups arising from chemisorbed water (Figure 4-32d).

FE-SEM micrographs in Figure 4-33 show that, similar to LFO-D films, Triton X-100 has assisted in the templating of LFO during synthesis providing good coverage and uniformity on the substrate. These micrographs were taken for LFO-E with 3 LFO

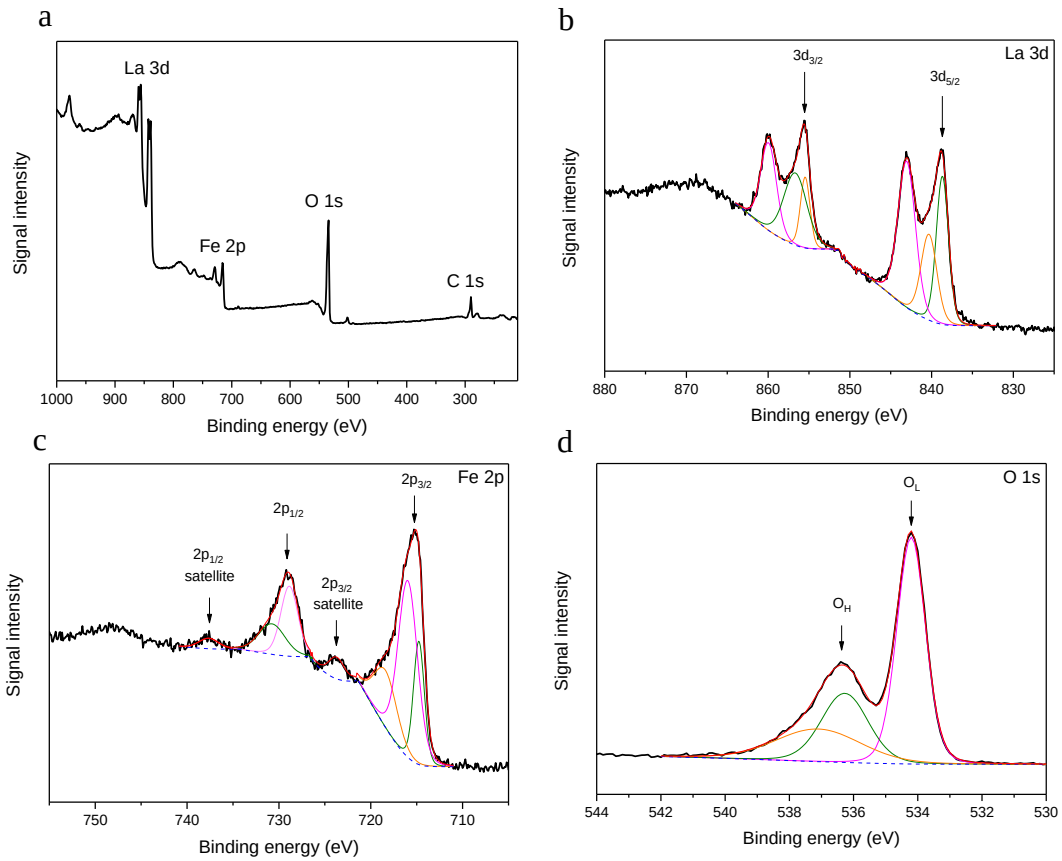

Figure 4-32: : (a) XPS survey spectrum and spectra of (b) La 3d, (c) Fe 2p and (d) O 1s of LFO-E films annealed at 600 °C .

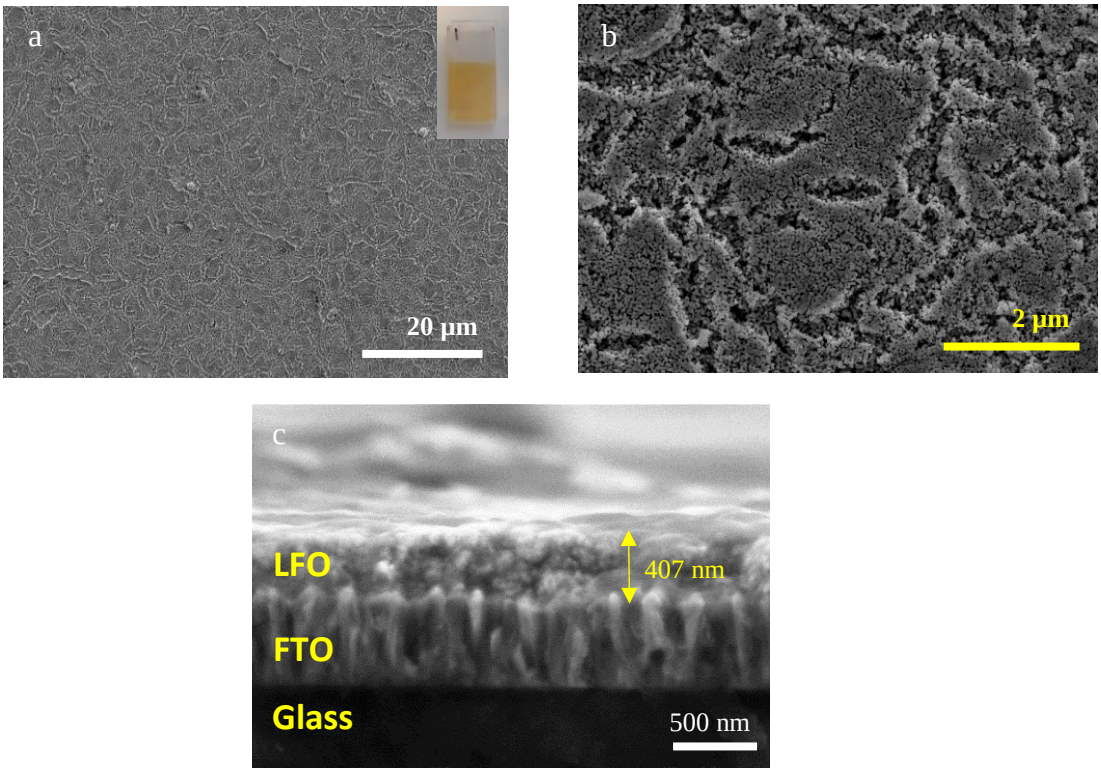

Figure 4-33: (a, b) FE-SEM micrographs of LFO-E films and (c) LFO-E cross-section, and insert of a photograph of an LFO-E film annealed at 600 °C.

layers applied where there is no visible FTO exposed with promising levels of porosity, that may contribute positively to charge transfer with the electrolyte due to an increased surface area. A cross-section micrograph of this LFO-E film revealed an approximate film thickness of 407 nm. The overall uniform and porous structure that is seen on the application of 3 layers, suggests Triton X-100 could be a suitable replacement to the previously used PVC-*g*-POEM for LFO film fabrication.

4.5.1 Electrochemical measurements

EIS measurements showed frequency dependence on capacitance showing LFO-E films display a deviation from an ideal capacitor as seen with LFO-B, -C and D. Mott-Schottky plots at 10, 100 and 1000 Hz confirmed p-type character and demonstrated a V_{fb} of 1.57±0.34 V_{RHE} (Figure 4-34). With a band gap between 2.4-2.7 eV, this demonstrates the incorporation of the water reduction potential (Figure 4-35). Additionally, carrier (hole) densities were calculated using Equation 17, at 10, 100 and 1000 Hz to be $2.4x10^{17}$, $5.9x10^{16}$ and $1.1x10^{16}$ cm^{-3} which are considered with caution as previously explained.

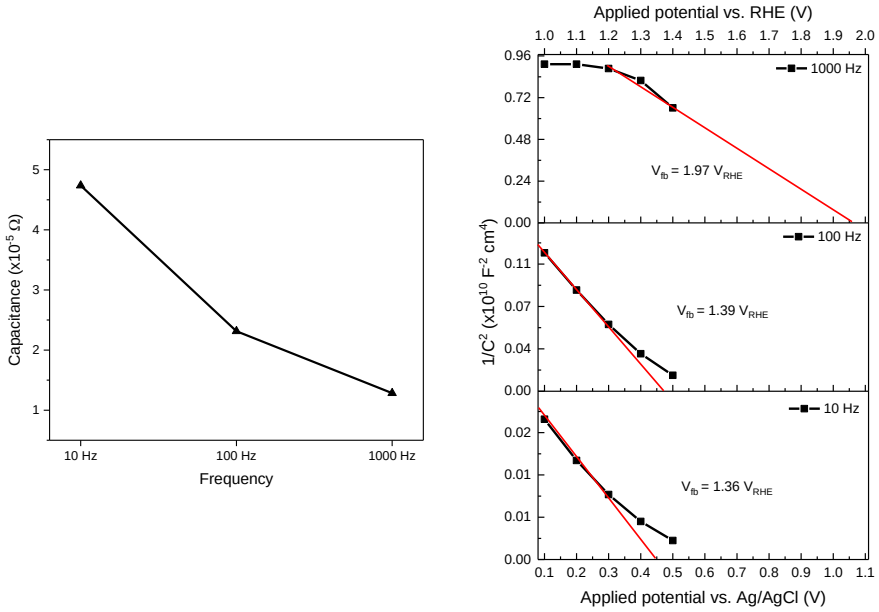

Figure 4-34: Capacitance values determined from EIS measurements as a function of frequency measured at -0.3 V_{AgCl} (left) and Mott-Schottky plots completed at -0.3 V_{AgCl} for LFO-E at different frequencies.

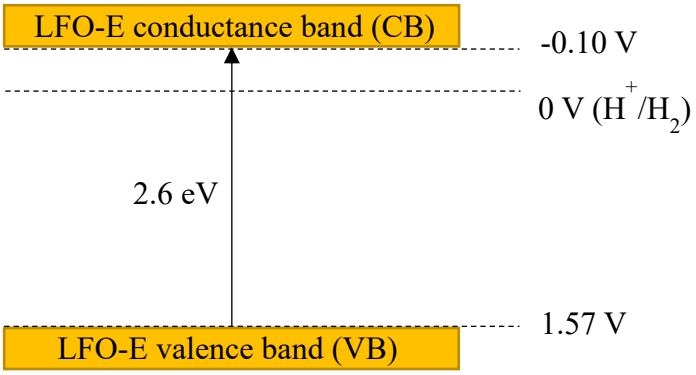

Figure 4-35: Relative band alignment for LFO-E with reference to calculated band gap and flat band potential.

4.5.2 Photoelectrochemical measurements

Firstly, the optimal annealing temperature for these LFO-E films was investigated. Multiple LFO layers were applied with annealing temperatures of 500, 600 and 700 °C. It was found the highest photocurrent density achieved was for an LFO-E film with 3 applied LFO layers annealed at 600 °C, which was recorded to be -161±6 µA cm^{-2} at -0.48 V_{AgCl}. Annealing temperatures of 500 °C and 700 °C achieved lower maximum photocurrents of -80 µA cm^{-2} and -94 µA cm^{-2} respectively (Figure 4-36a). Figure 4-36b shows the optimisation of the number of applied layers for an LFO-E film calcined at 600 °C, where 1, 2, and 4 LFO layers applied gave lower photocurrents of -73±11, -144±16, and -111±9 µA cm^{-2}. A stability measurement was additionally conducted, which showed a reduction of photocurrent of just 9 % after 1 hour and a 15-minute stabilisation (Figure 4-36c).

However, there are notably large standard deviations with the application of the first and second layer (11 and 16 respectively) with frontside illumination suggesting that incomplete coverage is present with variations in uniformity resulting in a larger degree of error. Additionally, on the application of 3 or more layers a higher photocurrent on backside illumination compared to frontside is seen, suggesting that the film is at a thickness where on frontside illumination the majority of the LFO being illuminated is not in contact with the FTO, supressing charge transport, and the light fails to reach those LFO particles on the FTO surface. On backside illumination, the particles that are in direct contact with the substrate are illuminated, assisting in charge

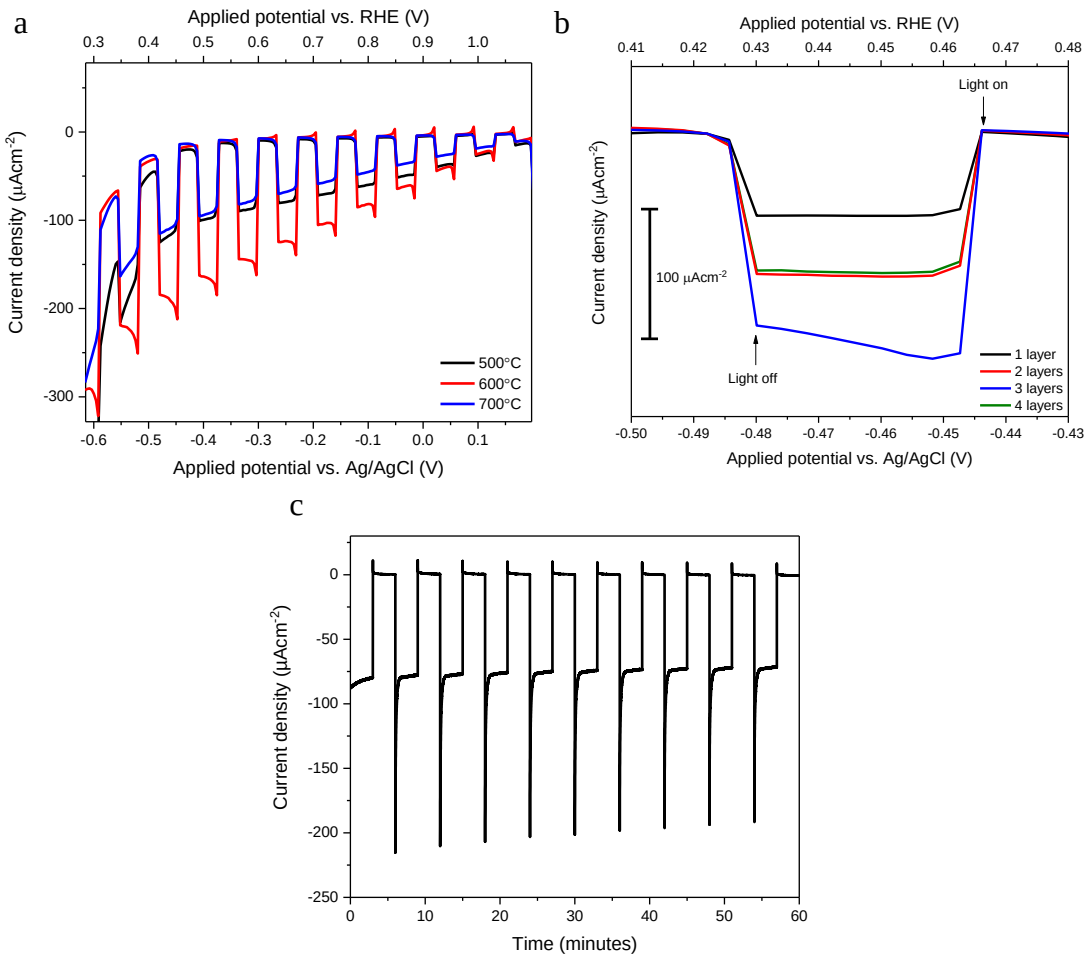

Figure 4-36: (a) Chopped light LSV measurements of LFO-E film calcined at 500, 600 and 700 °C (3 LFO layers), (b) comparison between the application of 1-4 LFO layers for LFO-E annealed at 600 °C and (c) stability measurement held at -0.48 V_{AgCl}.

extraction and higher photocurrents. Finally, to confirm the beneficial effects of incorporation of both a graft co-polymer (PVC-*g*-POEM) and a non-ionic surfactant (Triton X-100) into a LFO nitrate precursor solution for spin coating, a comparable solution is need to be prepared in the absence of any templating agent.

4.5.3 Polymer templating control film (C-LFO)

To prepare a control film to highlight the benefits of templating, an identical precursor solution was prepared with lanthanum and iron nitrates with citric acid in water, mixed with THF in the absence of a templating agent. This solution was spin coated onto the FTO-ABS substrate and annealed at 600 °C for 2 hours and labelled C-LFO (Method 2.9). FE-SEM micrographs in Figure 4-37 show two different magnifications for 1 and

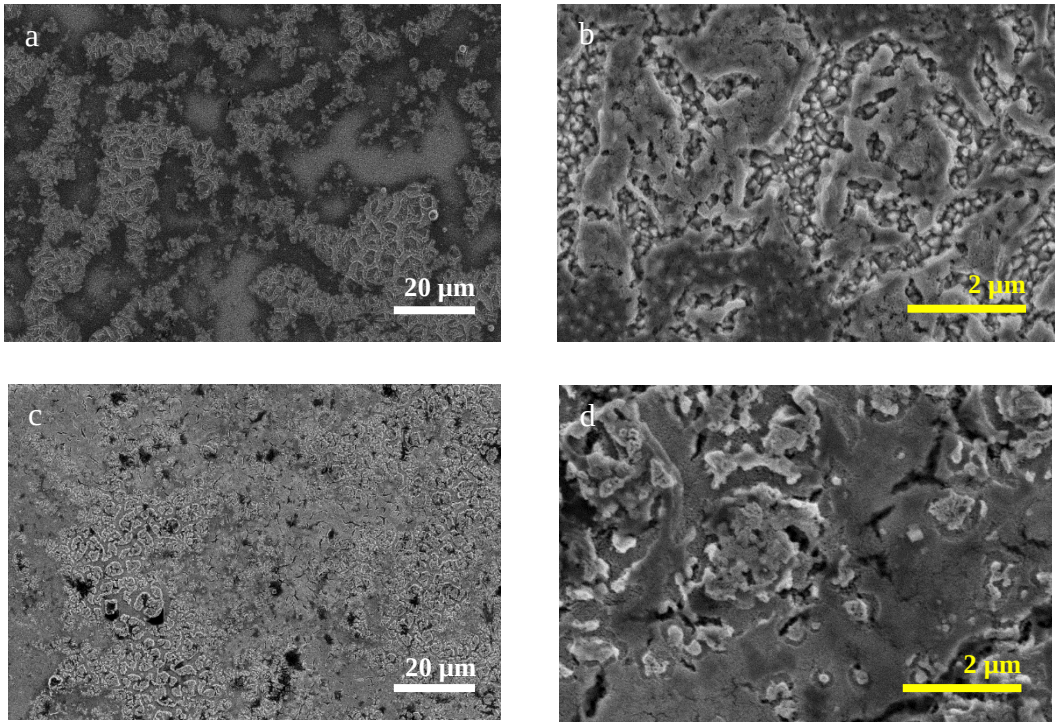

Figure 4-37: FE-SEM micrographs of C-LFO film after (a, b) 1 LFO layer applied and (c, d) 3 LFO layers applied.

3 LFO layers applied. On the application of 1 LFO layer there is a distinct lack of coverage and uniformity with a notable lack of porosity, potentially reducing charge transfer with the electrolyte. This coverage is improved when 3 LFO layers were applied, however the film still suffers from lack of porosity and uniformity. When considering the appearance of these comparable C-LFO films with LFO-D and LFO-E films, there is an obvious improvement when a templating agent is incorporated.

This improvement on incorporating a template with this fabrication method is highlighted further with the poor photocurrent densities achieved for these C-LFO films. The photocurrents recorded were -11, -25 and -33 µA cm^{-2} at -0.48 V_{AgCl} for 1, 2 and 3 LFO layers applied, when comparing these directly to LFO-D and LFO-E there is a clear reduction in activity (Figure 4-38). By fabricating control films, the benefits of using either PVC-*g*-POEM or Triton X-100 as sacrificial templates was emphasised well. Despite the advantages of polymer templating, further in situ based fabrication techniques can still be explored. When considering these templated films (LFO-D and LFO-E), there appears to be good levels of porosity but due to the

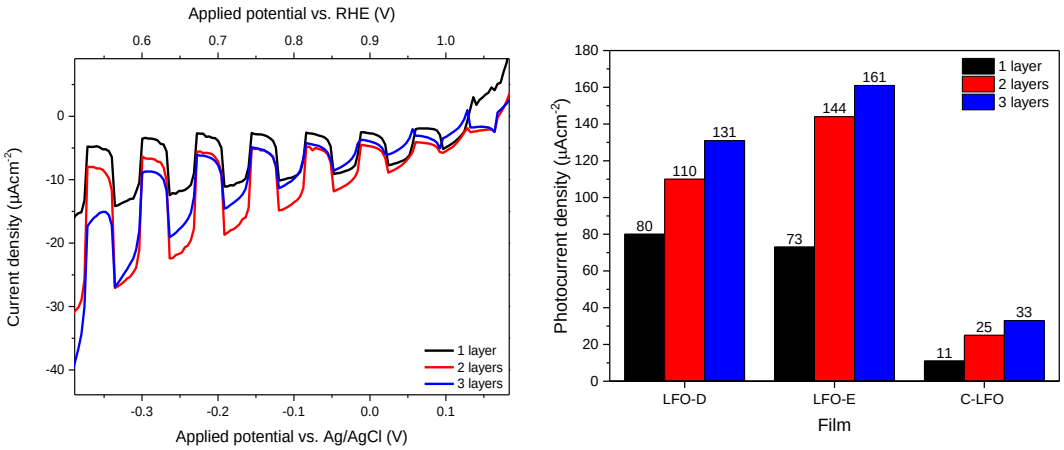

Figure 4-38: Chopped light LSV measurements for C-LFO on the application of 3 LFO layers (left) and comparison of photocurrent densities between LFO-D, LFO-E and C-LFO (right).

application of multiple layers to achieve optimal photocurrent, there is increased film thicknesses. It can be speculated that there is limited light scattering in these cases due to the high film densities observed, which could make it difficult for maximum light absorption of the active LFO deposited. One such method that can be utilised is a hydrothermal synthesis which can be adapted for an in situ growth of LFO directly on the substrate, which could result in advantageous morphology and reduction of energy and time consuming multiple high temperature heating steps.

4.6 In situ hydrothermal growth of $LaFeO_3$ (LFO-F)

Hydrothermal synthesis has been previously used for metal oxide preparation and has been utilised for LFO fabrication.[111,139] Growing LFO particles through a hydrothermal method may allow for the creation of interesting and beneficial morphologies especially if adapted for LFO growth directly on to a substrate. Hence, a hydrothermal method involving lanthanum nitrate and potassium ferric cyanide $K_3[Fe(CN)_6]$ precursors with citric acid was adapted to take place on a FTO-ABS glass substrate.[140] This was achieved through placing the precursors within an autoclave, along with FTO-ABS glass slides and heated at 180 or 230 °C for between 6 and 18 hours for optimisation. These films, named LFO-F, were then calcined at 600, 700 and 800 °C (Method 2.10). Higher temperatures were screened when compared with previous calcination temperatures used for LFO films fabrication due to the recorded higher temperatures being required for this synthesis method (800 °C).[140]

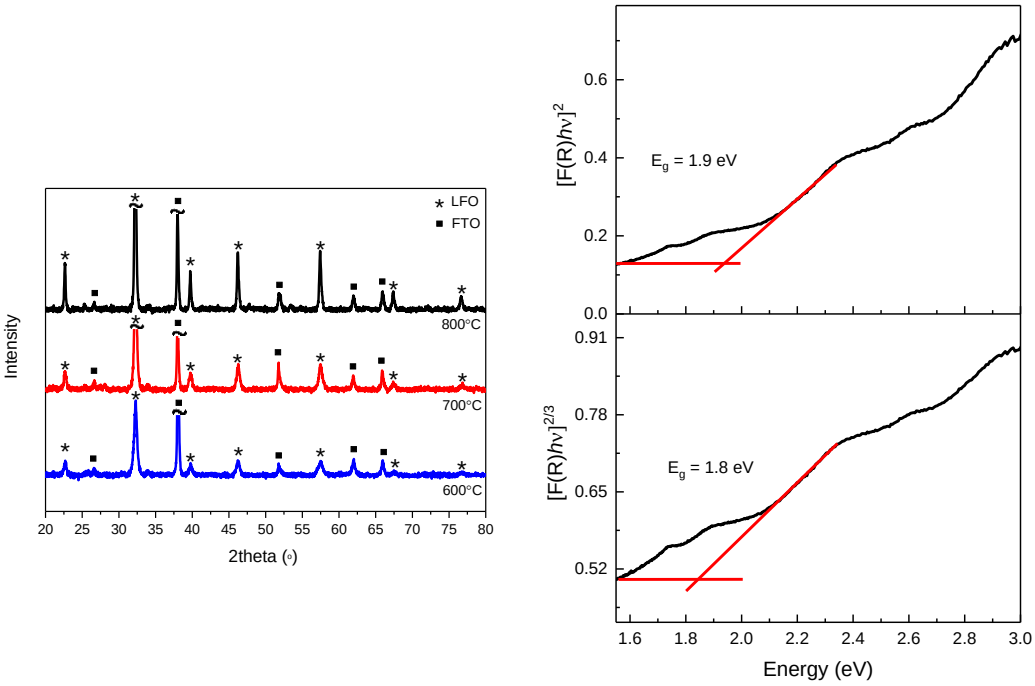

Figure 4-39: XRD spectra for LFO-F films calcined at 600, 700 and 800 °C (left) and Tauc plot (right).

XRD measurements of these LFO-F films confirmed the successful growth of LFO at all calcination temperatures between 600-800 °C. The Scherrer equation was then used to determine crystal domain sizes which were calculated to be 17, 20 and 34 nm for 600, 700 and 800 °C, displaying an increase in size on application of higher temperatures which could be explained due to sintering. Tauc plots determined a band gap between 1.8 and 1.9 eV considering direct allowed and direct forbidden optical transitions, which is well within the visible light region (Figure 4-39). XPS spectra shown in Figure 4-40b and c additionally confirms the presence of LFO, which display the binding energies corresponding to La $3d_{5/2}$ (834 eV), La $3d_{1/2}$ (850 eV), Fe $2p_{3/2}$ (710 eV) and Fe $2p_{1/2}$ (724 eV). The O 1s spectrum corresponds to crystal lattice oxygen (O_L) and hydroxyl oxygen (O_H). The O_L signal at 529 eV was attributed to La-O and Fe-O contributions from the LFO crystal lattice. The second signal at 531 eV is associated with hydroxyl groups arising from chemisorbed water (Figure 4-40d).

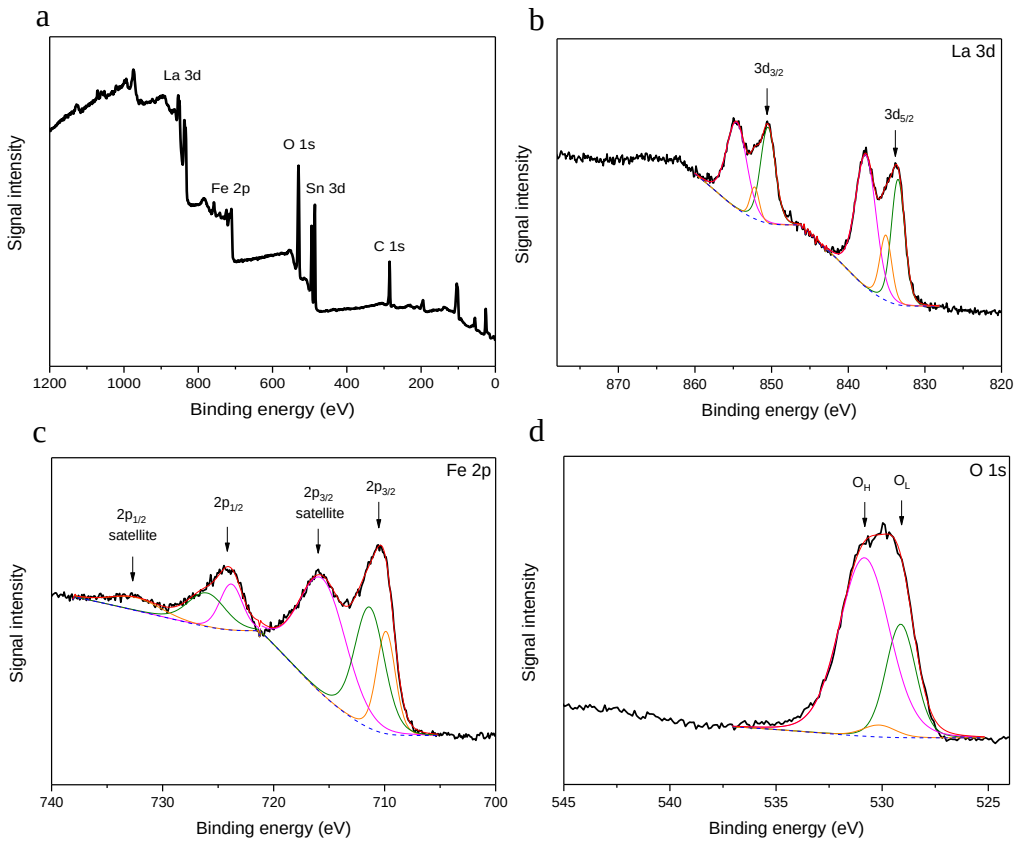

Figure 4-40: (a) XPS survey spectrum and spectra of (b) La 3d, (c) Fe 2p and (d) O 1s for LFO-F films calcined at 800 °C.

4.6.1 Photoelectrochemical measurements

Firstly, optimisation of this adapted hydrothermal method is needed in terms of changes in reaction time, temperature and precursor concentration during film fabrication. Table 2 displays the different reaction conditions investigated including reaction temperatures of 180 and 230 °C, with reaction times ranging from 6 to 18 hours. For each condition 3 films were prepared and calcined at 600, 700 and 800 °C. For these PEC measurements the photocurrent density was recorded at a slightly more positive potential at -0.41 V_{AgCl}, due to the more pronounced cathodic current features for these films (addressed in Section 4.7), making it more unreliable to record activity at -0.48 V_{AgCl}, as done with previous films. LFO-F (i) films were prepared at 180 °C for 6 hours, and achieved a photocurrent density of -71, -22 and -18 µA cm^{-2} at -0.41 V_{AgCl} for the calcination temperatures of 600, 700 and 800 °C respectively. As seen in Figure 4-41a, there is a selection of undesirable features within the LSV, notably at

Table 2: A range of prepared LFO-F films with different reaction conditions.

Sample I.D	Temperature (°C)	Reaction time (hr)	Precursor conc. (g ml^{-1})
LFO-F (i)	180	6	0.11
LFO-F (ii)	180	12	0.11
LFO-F (iii)	180	18	0.11
LFO-F (iv)	180	12	0.17
LFO-F (v)	230	12	0.11

-0.2 V_{AgCl}, which are not seen in previous PEC measurements for LFO films. It can be postulated that a reaction time of 6 hours is insufficient in allowing for the complete reaction of precursors, resulting in reducible species still being present during measurement. Such reductive features are not seen at a calcination of 800 °C for LFO-F (i), suggesting that perhaps this higher temperature is able to remove any excess precursor, with the highest activity being achieved for a 600 °C calcination. An increase in reaction time was then investigated for LFO-F (ii) films which were heated for 12 hours as opposed to 6 hours. PEC measurements in Figure 4-41b revealed that the feature seen at -0.2 V_{AgCl} for LFO-F (i) is not present, possibly suggesting that a longer reaction time is required to eliminate these proposed reducible precursor species. These LFO-F (ii) films demonstrate an increased activity, with calcination temperatures of 600, 700 and 800 °C, achieving -52, -85 and -81 µA cm^{-2} at -0.41 V_{AgCl}. This shows for these reaction conditions that higher calcination temperatures are preferable. Next, LFO-F (iii) films were prepared with an increased reaction time of 18 hours at 180 °C. This increase in reaction time allowed for enhanced photocurrents of -71, -87 and -133 µA cm^{-2} at -0.41 V_{AgCl} that are displayed in Figure 4-41c and Figure 4-41d. To allow for comparison with previous LFO-A, -B, -C, -D and -E films a photocurrent of -152 µA cm^{-2} was recorded at -0.48 V_{AgCl} for an 800 °C calcination. This increase in activity could be due to the increased reaction time allowing for a higher level of reaction completion, minimising the likelihood of the presence of precursors whilst maximising LFO formation.

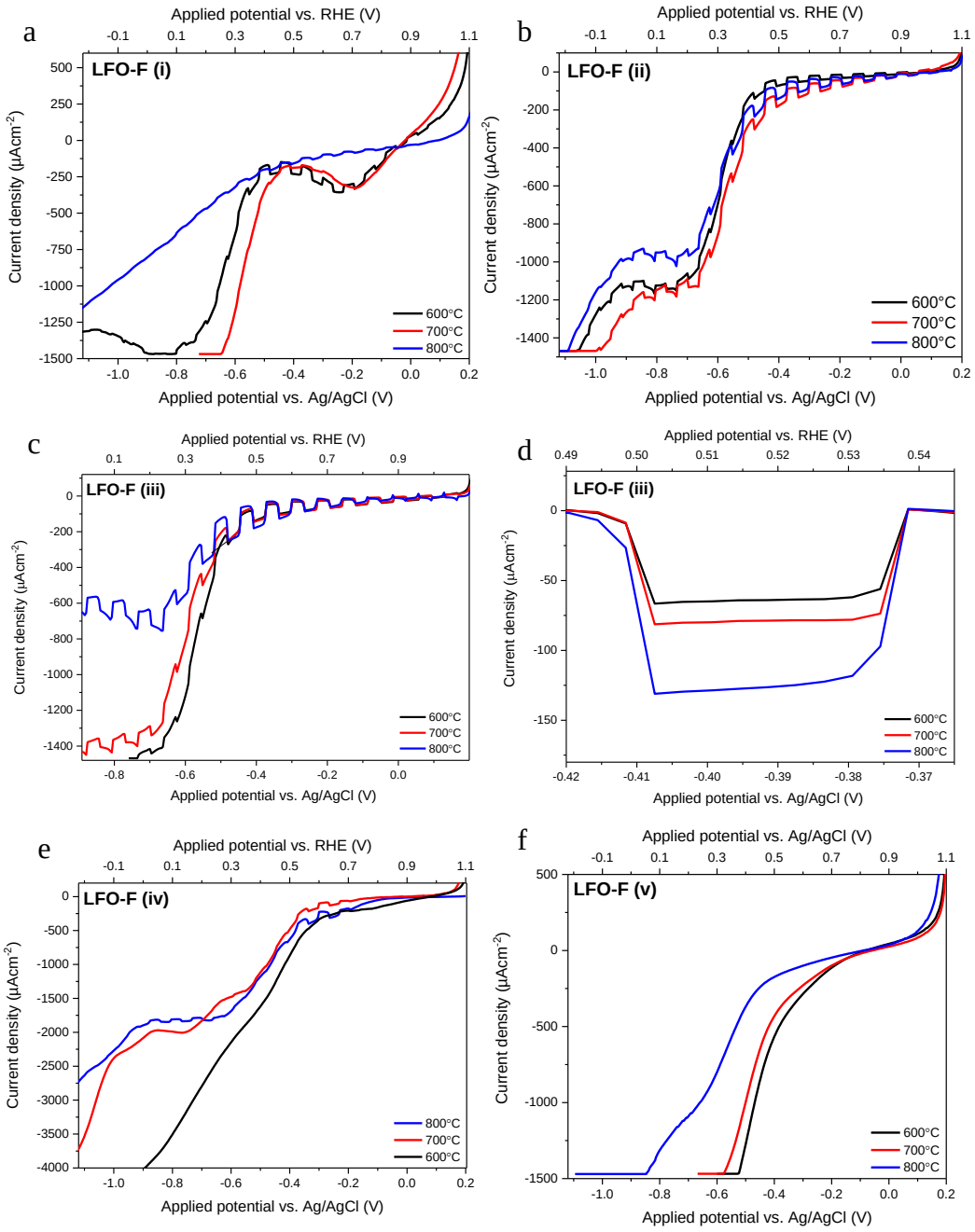

Figure 4-41: Chopped light LSV measurements for LFO-F films with different reaction conditions (i to v) at different calcination temperatures of 600, 700 and 800 °C.

Further to changes in reaction times, concentration of the precursors was also manipulated. LFO-F (iv) films were prepared with an increased precursor concentration of 0.17 g ml^{-1} (compared to 0.11 g ml^{-1}), with the intention to increase the amount of LFO formed on the substrate. This was completed with a reaction time and temperature at 180 °C and 12 hours respectively. A decrease in activity was seen when comparing to LFO-F (ii), achieving 0, -73 and -24 µA cm^{-2} at -0.41 V_{AgCl} for

600, 700 and 800 °C (Figure 4-41e). At higher concentrations of precursors there is a lower water content to the reaction mixture, following perhaps that a lower extent of hydrolysis may occur during the reaction, which may hinder the synthesis of LFO on the substrate. A higher reaction temperature of 230 °C was investigated with a precursor concentration of 0.11 g ml^{-1}, and reaction time of 12 hours named LFO-F (v). No photocurrent was recorded for these reaction conditions at any of the calcination temperatures (Figure 4-41f), suggesting that a lower temperature is optimal, with higher reaction temperatures providing too harsh conditions for the active LFO to successfully form on the substrate. Overall, the best achieving reaction conditions was that of 180 °C for 18 hours at a precursor concentration of 0.11 g ml^{-1} (LFO-F (iii) films), stability of this LFO-F film is discussed later in Section 4.8.

After optimising the reaction conditions, further characterisation of the best performing films was done to determine the appearance and morphology of the LFO upon the substrate. Hence, FE-SEM micrographs were obtained of LFO-F (iii) films calcined at different temperatures in order to determine how LFO has grown onto the substrate, and how this is influenced by temperature. Figure 4-42 shows at all temperatures there appears to be very interesting in situ hydrothermal growth of spherical LFO particles. This type of growth can be very advantageous for PEC applications due to the exhibited higher surface area and potential for increased light scattering between the LFO spindles, enhancing light absorption. When these LFO-F (iii) films were calcined at 600 °C, an initial LFO layer is visible of cracked and compact appearance on the FTO surface, from which the LFO spindles grow. Interestingly, the bulk LFO spindle like material emanates from these observed islands rather than directly from the FTO surface, suggesting this initially formed incomplete compact LFO layer is important for propagation and growth (Figure 4-42a). At a higher magnification it appears that these particles most closely resemble nano cubes of limited porosity (Figure 4-42b). Films calcined at 700 °C similarly show the growth of LFO spindles protruding from the FTO surface with small portions of the initial cracked LFO layer visible, as seen before at 600 °C (Figure 4-42c). The density of spindles appear to be higher at this temperature, and at closer magnification there is a prevalence of a much more porous and spherical LFO morphology from beneath the LFO cuboidal structure, as seen in Figure 4-42d. This morphology would be more

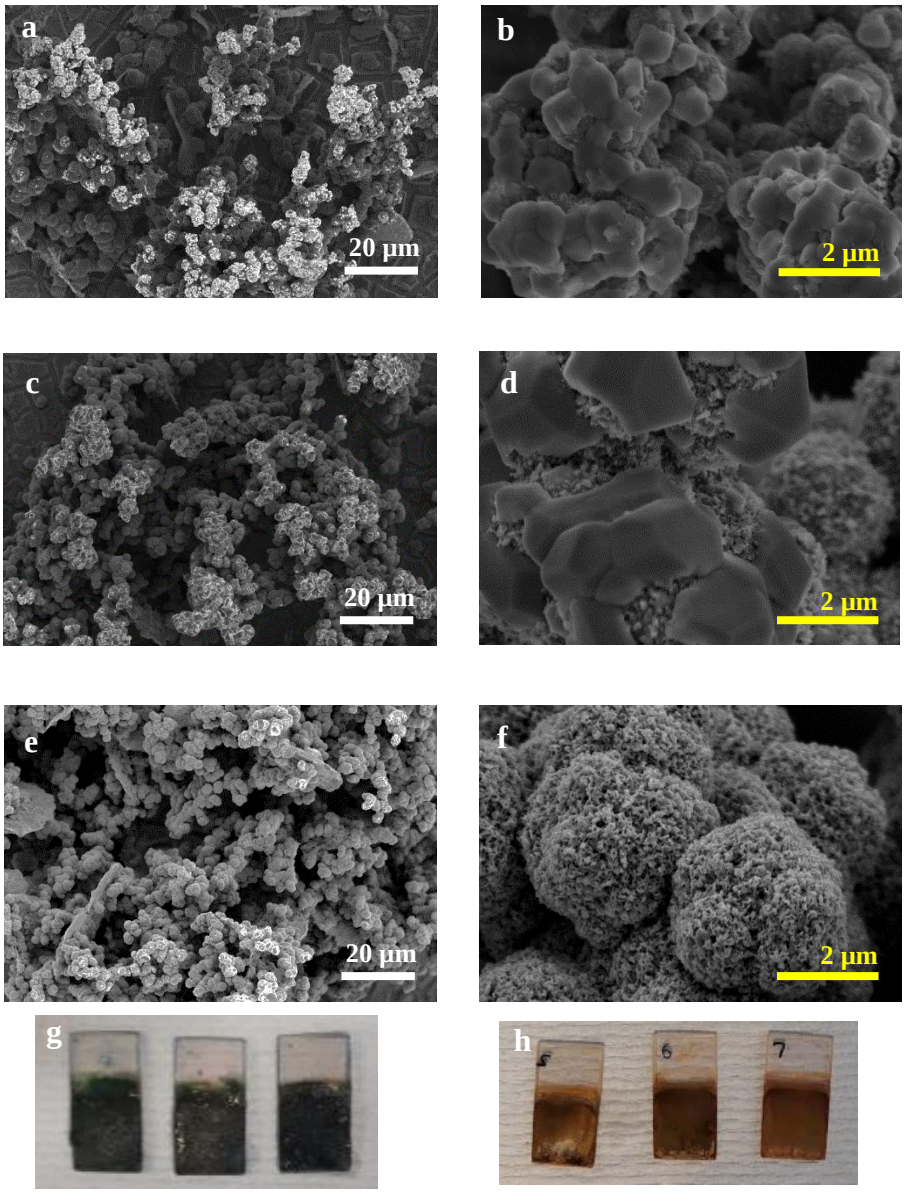

Figure 4-42: FE-SEM micrographs of LFO-F (iii) films calcined at (a, b) 600 (c. d) 700 and (e, f) 800 °C with photographs of films (g) before and (h) after calcination.

favourable for maximising particle/electrolyte interactions. On increasing temperature further to 800 °C, there is a marked disappearance of the cuboidal structure as seen in films calcined at 600 and 700 °C, with the particles seen at higher magnification being more spherical and porous in appearance (Figure 4-42e and f). Higher temperatures appear to favour the formation of these more porous spherical particles and limit the presence of the cuboidal morphology and display higher densities of LFO spindles. The PEC measurements discussed previously for these LFO-F (iii) films were -71, -87 and -133 µA cm^{-2} at -0.41 V_{AgCl} for 600, 700 and 800 °C respectively (Figure

4-42d), which could be explained due to these observed beneficial changes in morphology and increased density of LFO on the substrate at higher temperatures.

4.6.2 Electrochemical measurements

To probe further the effects of calcination on morphology, electrochemically active surface area (ECSA) measurements were done to quantify the changes in active surface area on increasing temperature. This was completed by conducting cyclic voltammetry (CV) measurements of these LFO-F films between +0.2 to -0.3 V_{AgCl} at varying scan rates between 10 and 250 mV s^{-1} (Figure 4-43). CV measurements for these films display the ability of the semiconductor in contact with the electrolyte to retain charge. As a voltage is applied to the film, current is generated which can be measured from the difference between the cathodic and anodic current at a particular potential. This can be seen as a measure of the capacitance which is proportional to the amount of material in contact with the electrolyte, hence the electrochemically active surface area. This is a relative technique so can be used to determine surface area between comparable samples that should have the same area exposed to the electrolyte on measurement. The difference between the cathodic and anodic current at -0.03 V_{AgCl} was then recorded and then plotted against scan rate, where in which the double layer capacitance can be determined by dividing the gradient by 2, which is proportional to ECSA, as seen in Equation 18 (Method 2.20).[131]

$$ECSA \propto C = \frac{dQ/_{dt}}{dE/_{dt}} = \frac{i(E)}{v}$$

Equation 18: Determination of ECSA.

The double layer capacitance (C_{dl}) was calculated to be 0.027, 0.051, and 0.074 mF for 600, 700 and 800 °C, which was then related to the amount of LFO exposed to the electrolyte (~$1.5x10^{-4}$ g) to give 177, 338 and 494 mF g^{-1} (Figure 4-44). It can be seen at increased scan rate, capacitance appears higher due to the limited time available for charge to dissipate after the application of potential, whereas slower scan rates allow for a longer time for recombination processes to dominate and hence produce lower charge capacitance. This shows that increasing calcination temperature increases the ECSA of these LFO-F films. This is in agreement with what is observed in FE-SEM

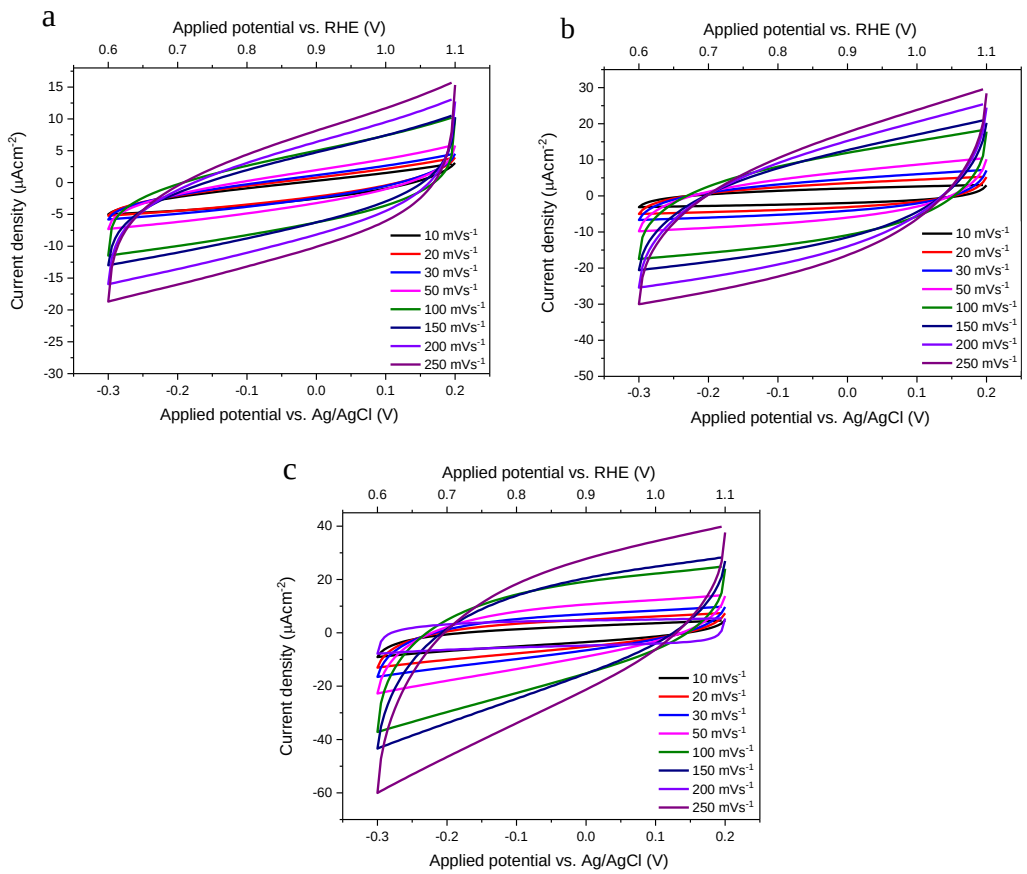

Figure 4-43: CV curves at scan rates between 10 and 250 mV s^{-1} for LFO-F (iii) calcined at (a) 600, (b) 700 and (c) 800 °C.

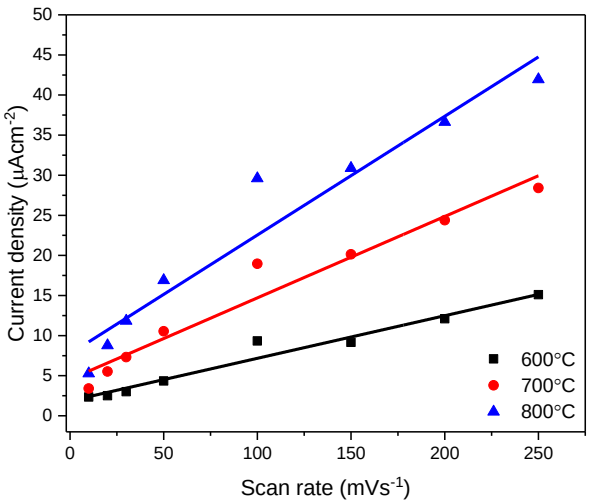

Figure 4-44: Current density vs. scan rate plots for LFO-F (iii) calcined at 600, 700 and 800 °C.

micrographs (Figure 4-42), as these show that increasing calcination temperature resulted in more porous and spherical LFO particles of greater density, which would follow that greater surface area should be observed.

Additionally, in order to establish whether calcination temperature could affect the charge transport properties of the LFO on the substrate, EIS measurements were carried out in the dark in order to create a Nyquist plot. From these impedance measurements at different frequencies, the RC time constant can be calculated by taking the resistance at high frequency and multiplying by the capacitance at low frequency. This RC constant was then be used in Equation 19 where j_{ph} is the RC limited photocurrent, j_{max} is the maximum photocurrent achieved experimentally and t is time. This determined RC limited transient can then be compared to the experimental transient photocurrent recorded to determine rise time. Rise time is the time it takes for the maximum experimental photocurrent to reach the maximum RC limited photocurrent. These determined rise times can then provide an insight into charge transport characteristics.[132]

$$j_{ph} = j_{max}\left[1 - e^{-t/RC}\right]$$

Equation 19: RC limited photocurrent determination.

Rise times for each calcined film can be seen in Figure 4-45, and were determined to be 0.04, 0.05 and 0.04 s for calcinations of 600, 700 and 800 °C respectively. This shows that there is no significant difference seen between temperatures, strongly suggesting that on increasing calcination temperature there is no change or improvement in charge transport properties. Ordinarily, if slower rise times are observed then poorer rates of charge extraction are suggested, due to increased density of trap states, whereas faster rise times can suggest better and more efficient charge extraction. However, in this case no large differences in rise time are seen, which suggests that the increase in photocurrent on increasing calcination temperature cannot be explained due to better charge transport, but to perhaps the increased surface area, better morphology and increased light scattering (Figure 4-42).

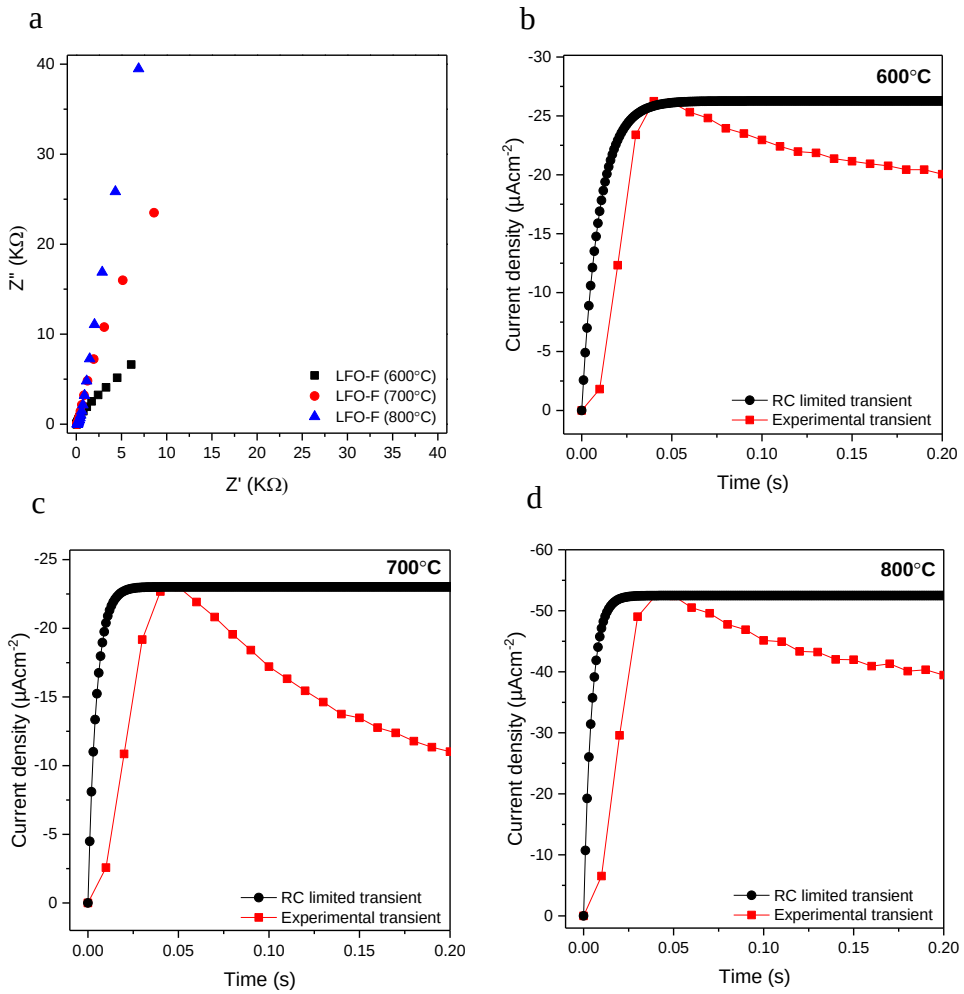

Figure 4-45: (a) EIS measurements for LFO-F (iii) films at -0.3 V_{AgCl} and experimental photocurrent transients compared with RC limited transients for LFO-F (iii) films calcined at (b) 600, (c) 700 and (d) 800 °C.

In summary, the highest photocurrent achieved for these LFO-F films was -152 μA cm^{-2} at -0.48 V_{AgCl} and is comparable to that of LFO-D (-148 μA cm^{-2}) and LFO-E (-161 μA cm^{-2}), and exceeds activity recorded for LFO-A, B and C. Hence, this appears to be a very promising novel method for LFO photocathode fabrication. However, it should be noted that despite the interesting and beneficial morphology of these LFO-F films, the LFO deposited on the substrate was found to be very susceptible to coming away through gentle abrasion of the surface which can be seen from the photographs of these films (Figure 4-42g and h). In addition, as briefly mentioned previously, all LSV measurements conducted for LFO films displayed a sharp increase in cathodic current below -0.5 V_{AgCl}. Hence, this is needed to be

addressed, especially in terms of dark current as there are clearly additional reductive processes occurring.

4.7 Addressing LSV features

In all cases during LSV measurements a considerable increase in negative current at potentials more negative than -0.5 V_{AgCl} is exhibited. This suggests that there are further reductive processes occurring at these lower potentials, resulting in vast increases in negative current in both light and dark conditions. This persistent feature could be potentially attributed to oxygen reduction occurring at the working electrode, which has been discussed previously to take place on exposed areas of FTO.[74] This can be demonstrated by conducting LSV in the dark of bare FTO-ABS glass, with electrolyte conditions involving O_2 being present and in the absence of O_2 through purging with N_2. Figure 4-46a shows the current density of bare FTO-ABS glass before and after N_2 purging. It can be clearly seen that when oxygen is present within the electrolyte a rapid increase in negative current was seen from below -0.5 V_{AgCl}, that can be attributed to the oxygen reduction reaction (ORR). When this O_2 is expelled after purging this dark current drastically diminishes and is closer to 0 which would be expected, thus supporting that ORR is taking place. As seen from previous FE-SEM micrographs there are large exposed areas of FTO after LFO deposition especially with fabrication methods using doctor blading (LFO-A) and spray pyrolysis

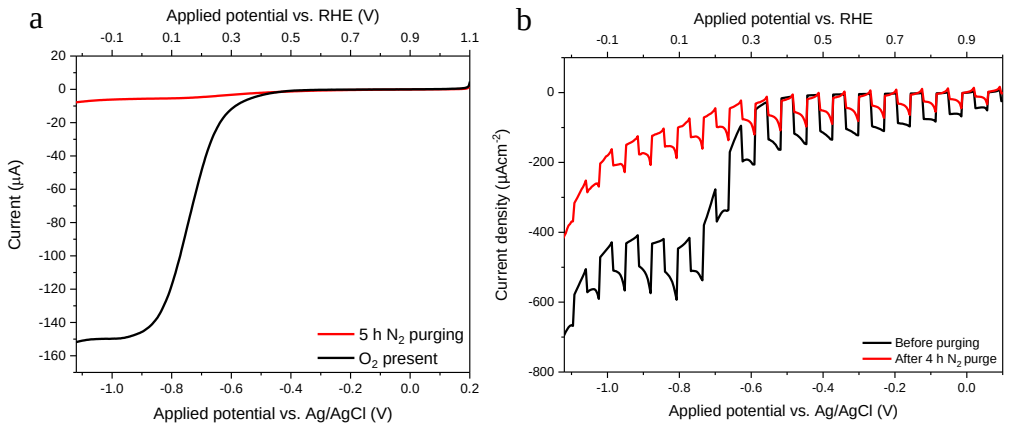

Figure 4-46: (a) LSV measurements in the dark for a bare FTO glass with and without N_2 purging and (b) a comparison before and after N_2 purging for an LFO-D film (right).

(LFO-B and LFO-C), which will undoubtedly exacerbate the presence of the dark current due to ORR taking place on the FTO.

Additionally, as well as the FTO providing a surface for ORR in the dark, LFO has been reported to be an active in photocatalytic oxygen reduction. Wheeler et al found that LFO achieves low photocurrents for water reduction, however in the presence of oxygen these photocurrents increase due to oxygen reduction.[121] It was noted here that oxygen is acting as a sacrificial electron acceptor, that allows for increased photocurrent that cannot be then prescribed completely to water reduction. This has also shown to be the case for other photocathodes such as $CuFeO_2$.[141] To demonstrate this, LFO-E films were measured under chopped light LSV in O_2 containing Na_2SO_4 and then again after N_2 purging (Figure 4-46b). Similarly, to bare FTO, there is a reduction in dark current with an increase in the appearance of cathodic spikes, which is indicative of higher levels of electron-hole recombination. This further confirms the behaviour of O_2 being an electron acceptor which would reduce opportunities for electron-hole recombination, hence there are less pronounced cathodic spikes. This reduction in dark current was also accompanied by a decrease in photocurrent of 63 % at -0.48 V_{AgCl}. Due to this, extra care is required when reporting photocurrent achieved in terms of PEC water reduction due to the competitive ORR, hence future work should incorporate provisions such as co-catalysts to try and direct electrons towards HER. However, this highlights the application of LFO in oxygen reduction reactions that has been previously shown in solid oxide fuel cells[142] and exhibits the potential to be used within fuel-free PEC cells, which take part in water oxidation and oxygen reduction to generate electricity.[143]

Overall, various film fabrication methods for LFO photocathodes have been explored separately, and so a more direct comparison of all fabricated LFO films would be of benefit, with a focus on further characterisation in terms of electrochemical measurements (ECSA and EIS). Observing these films together will enable a clearer understanding of the effects of fabrication on morphology as well as electrical properties.

4.8 Comparison of $LaFeO_3$ film fabrication methods

To better understand the effects of film preparation on ultimate quality and performance, further characterisation and analysis was completed for all LFO films. Hence, for ease of comparison all LFO films were compared directly to highlight the advantages made on changing fabrication method. In addition, further electrochemical measurements were completed to establish a difference for instance in the ECSA and in the electron transport properties between these films. Table 3 shows a summary of the LFO films fabricated within this Thesis where the sample I.D has been reiterated.

Firstly, the FE-SEM micrographs obtained for each film were collated to establish the changes in morphology, quality and appearance of these films (Figure 4-47). As found in the previous sections, there is a distinct lack of coverage and uniformity for films LFO-A and LFO-B, with large portions of FTO visibly exposed, failing to utilise the available space on the substrate. There are improvements when utilising spray pyrolysis and nitrate precursors providing a better coverage but with a persistent lack of uniformity (LFO-C). On application of polymers PVC-*g*-POEM (LFO-D) and Triton X-100 (LFO-E), both are able to drastically improve film quality in terms of coverage and uniformity, whilst also providing a greater level of porosity than films LFO-A, -B and -C. Quite strikingly, employing an in situ hydrothermal synthesis method changes the morphology of the deposited LFO significantly, with the creation of spindle like structures protruding from the FTO surface. Compared to all the previously fabricated films, this morphology is largely advantageous due to the high levels of light scattering that could be achieved as well as the visibly enhanced surface area. Photographs taken of these prepared films as shown in Figure 4-47 can also provide an insight into film quality. It was observed for films LFO-A, -B, -C and -F

Table 3: Summary of each film fabrication method used with the corresponding sample identification.

Sample identification	Preparation method
LFO-A	Doctor blading of LFO powder
LFO-B	Spray pyrolysis of ball milling and sonicated LFO powder
LFO-C	Spray pyrolysis of nitrate precursors
LFO-D	Spin coating with polymer templating (PVC-*g*-POEM)
LFO-E	Spin coating with polymer templating (Triton X-100)
LFO-F	In situ hydrothermal synthesis onto substrate

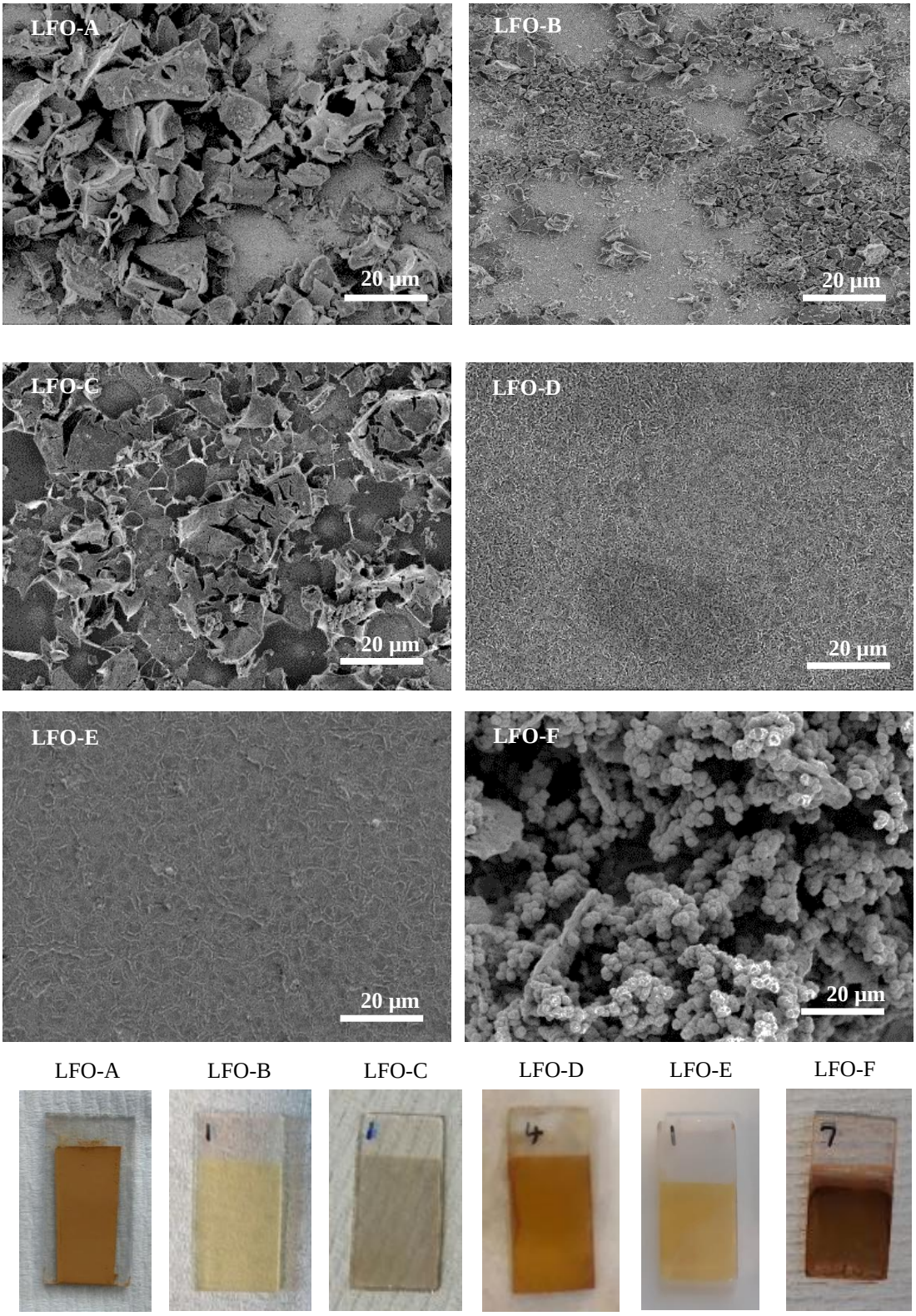

Figure 4-47: FE-SEM micrographs of all LFO films (top) and photographs of prepared films (bottom).

that during measurements it was common for abrasion of the surface to occur resulting in LFO coming away from the substrate, suggesting poor attachment of the LFO. However, for templated films LFO-D and LFO-E this was not the case, as small abrasions to the surface did not result in LFO to come away from the substrate, highlighting an increase in stability for these films. These visible improvements in film quality are seen in both FE-SEM micrographs and photographs and is reflected through the increased photocurrent densities and stability achieved for polymer templating methods.

4.8.1 Photoelectrochemical measurements

Figure 4-48a shows the normalised PEC measurements for all LFO films at a point of interest of -0.43 to -0.50 V_{AgCl}, taken from the highest achieved photocurrent for each film. There is a clear enhancement in photocurrent on optimising fabrication method, with the higher quality LFO-D, -E and -F films achieving the highest photocurrent densities of -148, -161 and -152 µA cm^{-2} at -0.48 V_{AgCl}. To establish whether these enhanced photocurrents are married with increases in stability, long term stability measurements were completed under chopped solar illumination at -0.48 V_{AgCl} over 1 hour. As LFO-A did not produce photocurrent at this potential this stability measurement was not completed. After a 15-minute stabilisation period the photocurrent was measured, and again at the end of the measurement to calculate the photocurrent loss during this time. For films LFO-B, C, D, E and F a reduction in photocurrent density of 24, 11, 9, 9 and 18 % were found respectively. The least stable film is that created with the spray pyrolysis of an exfoliated LFO powder (LFO-B), which is expected due to gentle grazing on the surface resulting in removal of LFO, suggesting a poor adhesion to the surface and hence decreased physical stability.

Similarly, there were notable signs of abrasion for LFO-C films after measurement and accidental grazing, but only appeared to have a 11 % reduction in photocurrent, hence providing greater stability than LFO-B. This could be due to better contact between the LFO and the FTO, which can be speculated due to the formation of the LFO directly upon the substrate. A marginal increase in stability was attained for polymer templated films (LFO-D and LFO-E), both with photocurrent reductions of 9 %. For these films there were no visible signs of grazing during testing or when the

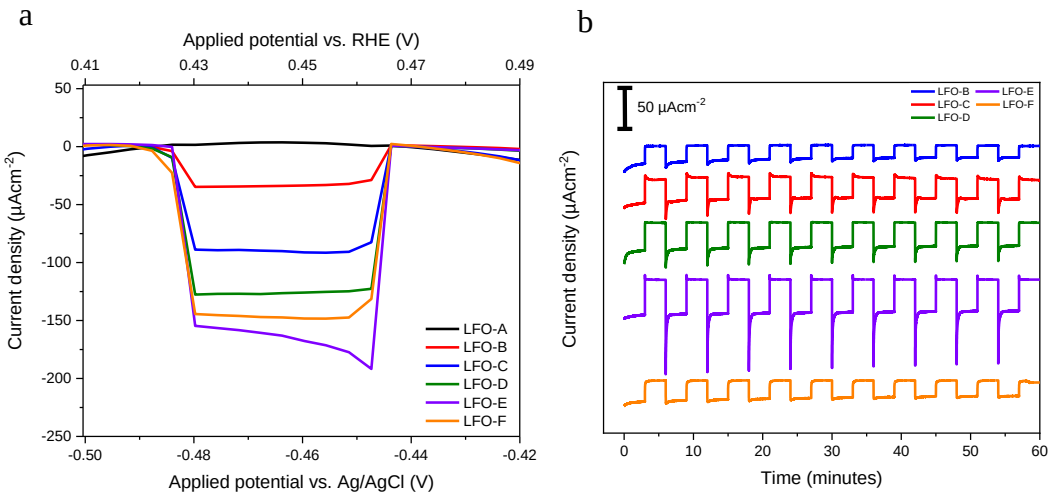

Figure 4-48: Normalised chopped light LSV measurements for all prepared LFO films at point of interest (left) and compiled stability measurements for all LFO films (right).

mask is clipped to the substrate, displaying relatively good stability. Finally, hydrothermally grown LFO films (LFO-F) showed a photocurrent reduction of 18 % over 1 hour, here there were also signs of abrasion during measurement which could have contributed to this reduction in photocurrent over an extended time period. In summary, due to physical stability effects and perhaps smaller contributions of chemical stability there is an increased level of stability for polymer templated films. This coupled with higher photocurrents achieved demonstrates the benefits of this fabrication method. However, to probe stability further additional measurements would be required with extended stability measurements over 1 hour in duration.

Moreover, it was investigated whether these LFO films achieve good cathodic onset potentials, hence extended LSV measurements were obtained under chopped solar illumination (Figure 4-49). Onset potential can be very important due the preference of a photoactive semiconductor to generate photocurrent at a range of applied potentials that would provide greater versatility for PEC applications. Films LFO-B, -C, -D and -E all displayed a photocathodic onset potential of approximately +0.5 V_{AgCl} (+1.4 V_{RHE}), which has also been reported in literature and said to be the largest onset potential for a single absorber photocathode.[99] For example this onset is much higher than the +0.5 V_{RHE} typically obtained for Cu_2O photocathodes.[41] This demonstration is useful in highlighting one of the main advantages of using LFO photocathodes for PEC applications.

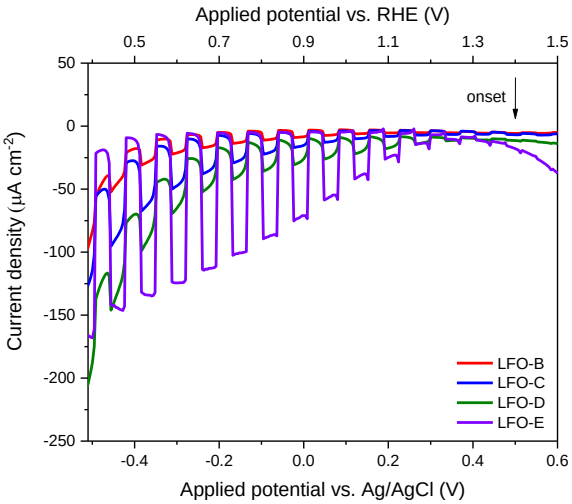

Figure 4-49: Chopped light LSV measurements from -0.5 to 0.7 V_{AgCl} for LFO-B, -C, -D and -E to determine onset potential.

Next, incident photon-to-current efficiency (IPCE) measurements were obtained for LFO-C, -D and -E films to establish conversion efficiencies. This can help establish the ability of these LFO films to convert the solar energy absorbed to electrical current, through measuring the photocurrent achieved on illumination at different wavelengths of light. Equation 20 was then used to calculate this efficiency, where J is the photocurrent recorded, P is the light intensity and λ is the wavelength of light.

$$IPCE\ (\%) = \left(\frac{1240\ \times J}{P\ \times\ \lambda}\right) \times 100$$

Equation 20: Incident photon-to-current efficiency (IPCE) calculation.

It can be observed from Figure 4-50 that for films LFO-C, -D and -E, IPCE values of 6, 12 and 12 % were recorded respectively at 320 nm. This demonstrates that the polymer templated films LFO-D and LFO-E possess higher conversion efficiencies, which could suggest better charge mobility than LFO-C films prepared through spray pyrolysis. This can be suggested due to the preferable morphology that a templating method provides on film fabrication, with an increased surface area that can assist in charge transport and reduce charge recombination. The polymer templating methods therefore not only provide increased photocurrent but have better conversion efficiencies that further highlights the benefits of this fabrication technique.

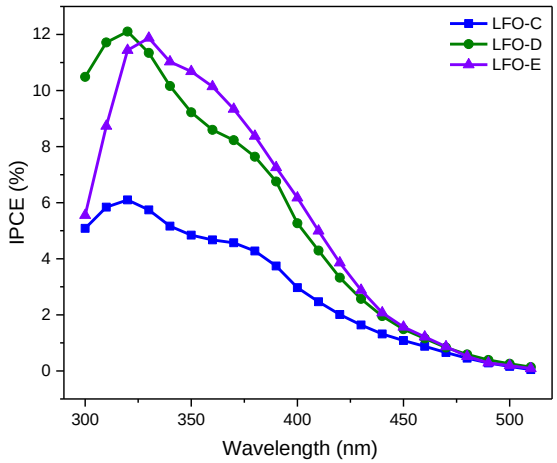

Figure 4-50: IPCE measurements conducted at -0.3 V_{AgCl} for LFO-C, -D and -E.

Additionally, there is no difference between LFO-D and LFO-E (12 %) which suggests that using the more reproducible and commercially available Triton X-100 does not compromise quality in terms of IPCE. Unfortunately, films LFO-A, -B did not produce sufficient photocurrent to record IPCE and due to time constraints IPCE was not recorded for LFO-F. In addition, band gap energies were extracted from these IPCE measurements. Tauc plots were created, as used with UV-Vis measurements, based upon an expression derived from the Gaertner equation.[144] This expression can then be plotted against energy to determine the band gap energy through x-axis extrapolation, considering both direct allowed forbidden and direct allowed optical transitions (Figure 4-51). This produced band gaps of 2.6-2.8 eV, 2.8-2.9 eV and 2.4-2.9 eV for LFO-C, -D and -E. These appear slightly higher than what would be anticipated, hence highlighting the issue in extracting band gap energies from complex ferrites that could feature elemental disorder and band tailing.

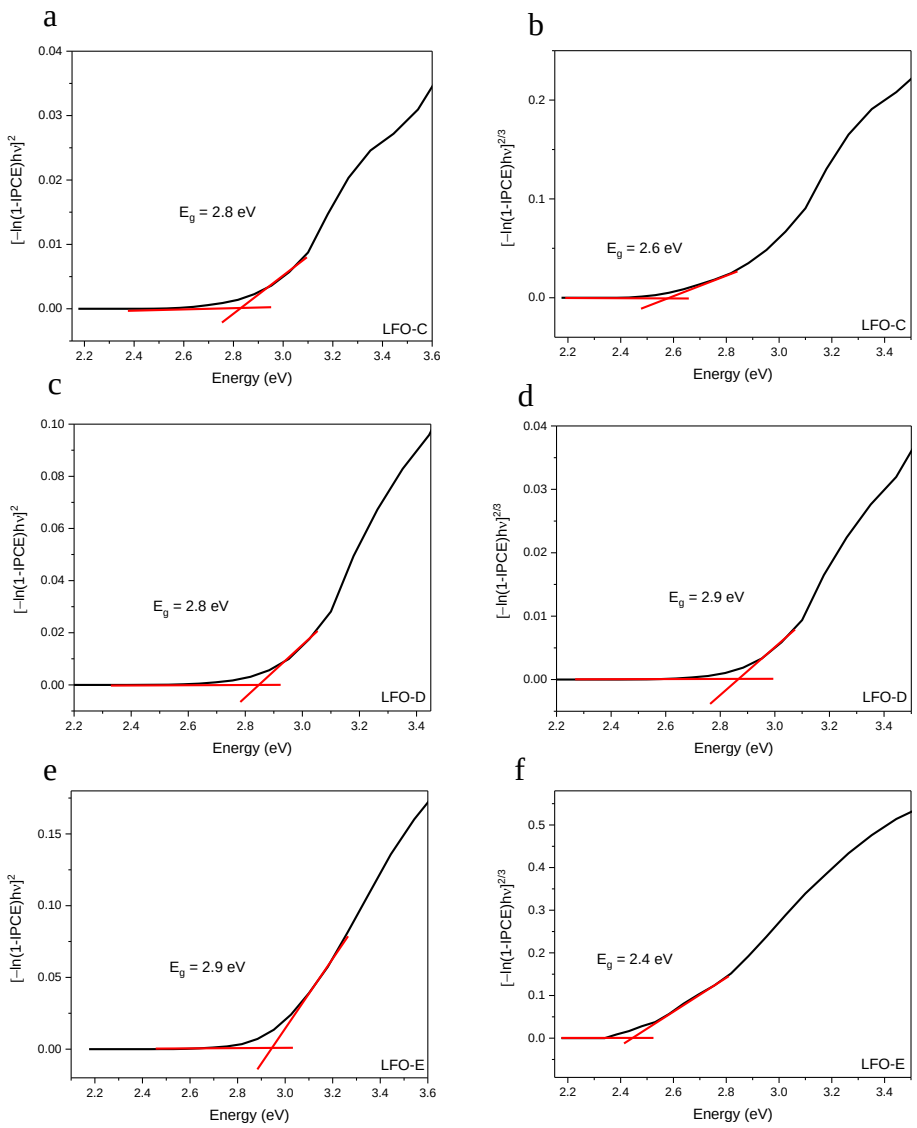

Figure 4-51: Tauc plots employing IPCE for (a, b) LFO-C and (c, d) LFO-D and (e, f) LFO-E to determine band gap using a direct forbidden optical transition (n=3/2) or and a direct allowed transition (n=1/2).

4.8.2 Electrochemical measurements

As mentioned previously, FE-SEM micrographs show drastic changes in morphology and suggests increases in surface area. In order to achieve some level of quantification for this, ECSA measurements were completed. This was done to confirm the increases in surface area for films prepared through the polymer templating and hydrothermal synthesis methods. As described previously, CV measurements were completed between +0.2 to -0.3 V at varying scan rates between 10 and 250 mV s^{-1} (Figure 4-52).

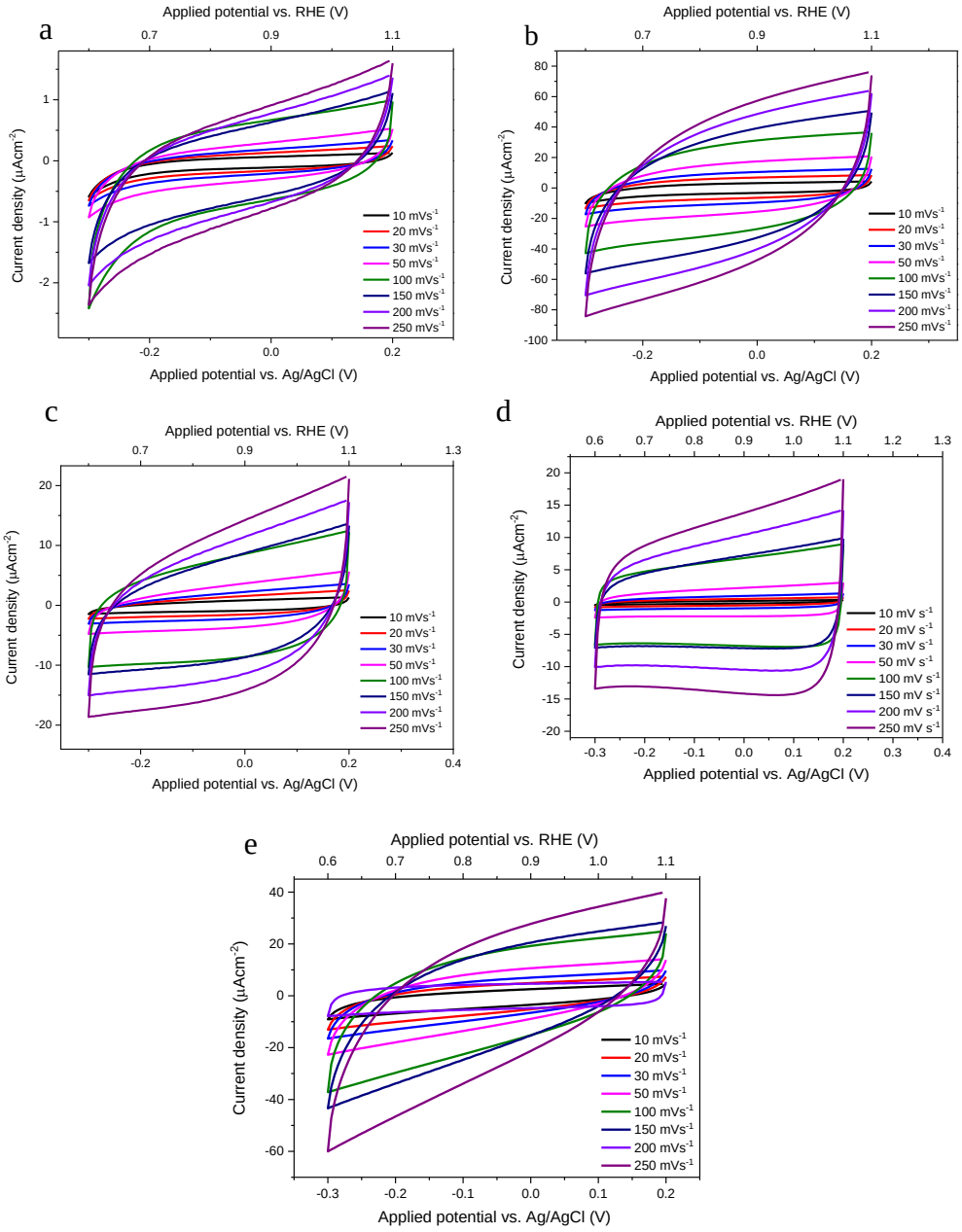

Figure 4-52: Cyclic voltammetry curves at scan rates between 10 and 250 mV s^{-1} for (a) LFO-B,(b) -C, (c) -D, (d) -E and (e) -F.

The difference in cathodic and anodic current at -0.03 V_{AgCl} was then plotted against scan rate to determine ECSA (Equation 18, Method 2.20). Due to the optimisation of each film preparation method involving the deposition of different weights of LFO onto the substrate, this value was then be divided by the deposited weight in order to make direct comparisons between films. For each film the double layer capacitance was calculated to be 0.001, 0.003, 0.161, 0.054, 0.066, and 0.074 mF for LFO-A, -B,-*C*, -*D*, -E and -F (Figure 4-53). Which with respect to the amount of LFO material

exposed to the electrolyte during the measurement, translated to 0.2, 20, 153, 363, 437 and 494 mF g-1 respectively. These ECSA values are in good agreement with what is observed from FE-SEM micrographs of these films (Figure 4-47), as LFO-D and LFO-E provide much higher coverage with greater porosity, which was corroborated with increased ECSA values of 363 and 437 mF g-1. The highest ECSA value is seen for LFO-F films that were prepared by an in situ hydrothermal method, which again is entirely expected due to the presence of LFO spindles that possess visibly increased porosity and surface area in contact with the electrolyte. This could go some way in explaining the enhanced photocurrents recorded for these films, however it is also important to consider electronic properties of these LFO films with respect to efficiency of charge transport.

Additionally, with any photoelectrode it is important to consider and quantify charge transport properties especially in terms of the ease of charge transfer and likelihoods of electron-hole recombination. Hence, to further compare these LFO films, EIS measurements were completed to determine RC limited photocurrent as outlined in Section 4.6. In brief, from these EIS measurements RC limited photocurrent transients can be determined (Equation 19) and compared to experimentally determined photocurrents to establish rise time. Rise time is the time in which the experimental photocurrent reaches the calculated RC limited transient, depending on the

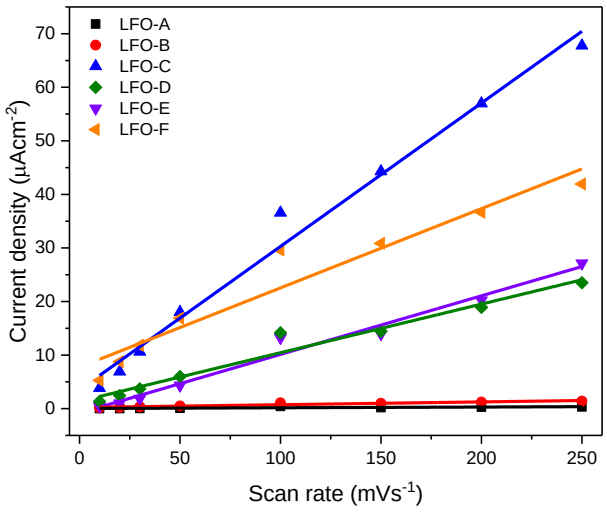

Figure 4-53: Current density vs. scan rate plots for LFO films (A-F).

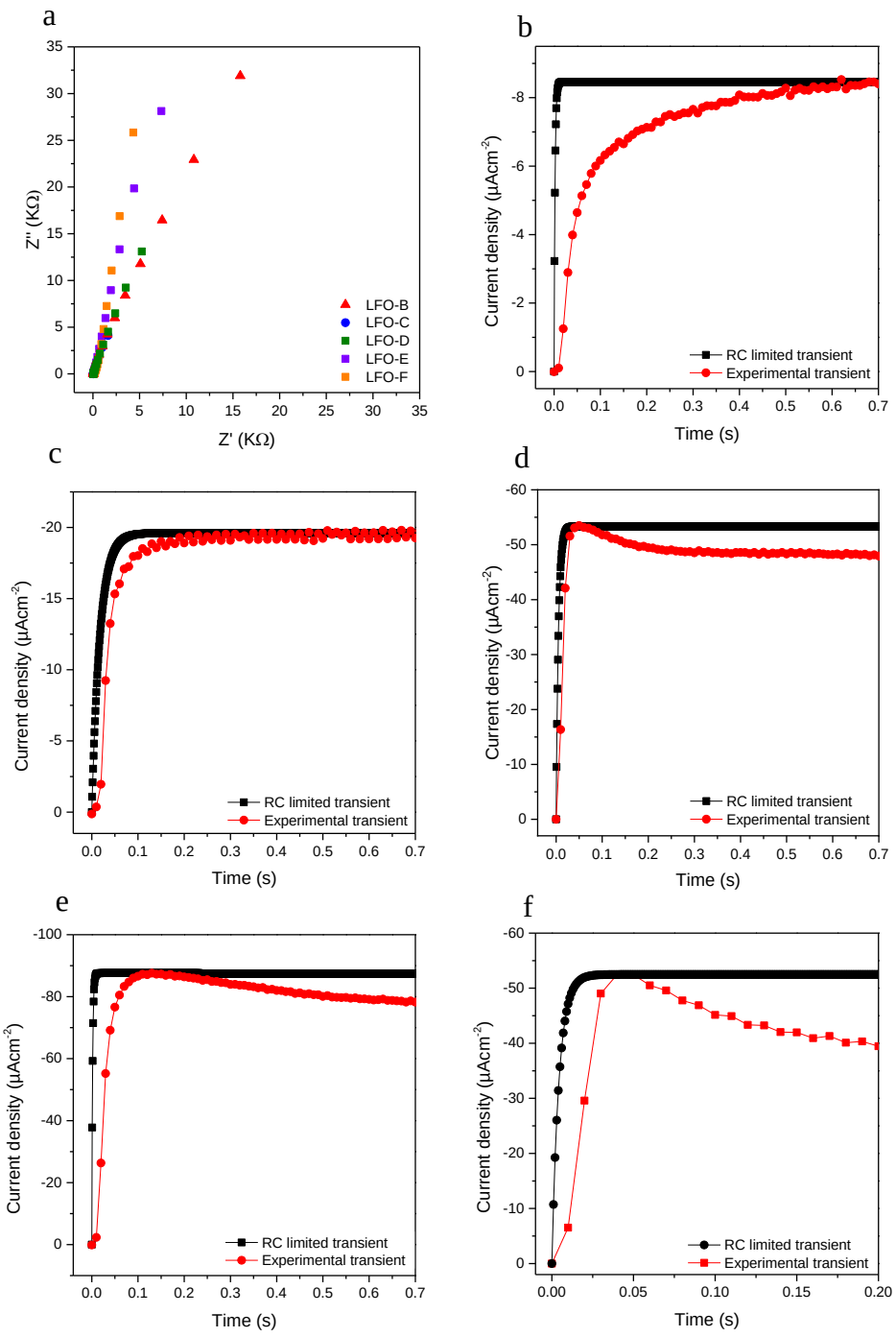

Figure 4-54: (a) EIS measurements for LFO films with RC limited photocurrent and experimental photocurrent transient comparisons for (b) LFO-B, (c) LFO-C, (d) LFO-D, (e) LFO-E and (f) LFO-F.

comparative time in which this occurs it can reveal how efficient charge separation occurs within these photocathodes. All LFO films were measured for impedance and photocurrent responses at -0.3 V_{AgCl}, apart from LFO-A due to the absence of any photoelectrochemical activity at this potential. RC values were determined to be

0.00212, 0.0179, 0.00508 and 0.00177 s for LFO-B, LFO-C, LFO-D and LFO-E respectively, from impedance measurements at -0.3 V_{AgCl} in the dark. Figure 4-54b shows that LFO-B has the slowest calculated rise time of 0.68 s compared to LFO-C, LFO-D, LFO-E and LFO-F which display faster rise times of 0.35, 0.05, 0.13 and 0.04 s respectively (Figure 4-54c, d, e and f). The slowest rise time for LFO-B indicates increased electron-hole recombination with slower carrier collection which could be due to increased density of trap states. LFO-C, LFO-D, LFO-E and LFO-F show faster rise times, suggesting improved rates of charge extraction, and hence lower likelihood for recombination. Additionally, it is seen that on the application of a polymer template or with hydrothermal growth (LFO-D, -E and -F) faster rise times are observed (0.05, 0.13 and 0.04 s), suggesting better charge mobility in agreement with the higher photocurrents and enhanced conversion efficiencies achieved. Overall, it can be suggested that LFO-D, LFO-E and LFO-F films achieve enhanced photocurrent densities compared to other fabrication techniques because of increased surface area that can improve light harvesting, as well as better charge separation efficiencies due to lower density of trap states.

Overall, when comparing these different preparation methods for LFO photocathodes, it is apparent that incorporating a polymer templating method possesses multiple advantages. Increases in stability, surface area and film quality were all achieved alongside enhanced photocurrents and conversion efficiencies. Additionally, on using a hydrothermal synthesis method, a substantially different surface morphology of high porosity and surface area is achieved with good photocurrent. On further electrochemical analysis it was discovered that films LFO-D, -E and -F demonstrate increased charge mobility compared to the poor performing LFO-B and LFO-C films, which could be explained due to better surface morphology and contact with the conductive FTO. It was abundantly clear when fabricating photoelectrodes for PEC applications, that the preparation method was vital to allow for optimised activity and it is important to explore how different methods affect film quality and electrochemical properties. After this optimisation and detailed exploration of LFO films, it was measured, for the best performing film (LFO-E), whether PEC processes were possible. In particular PEC water reduction to produce H_2 was explored, due to this being the suggested ultimate application for these LFO photocathodes.

4.9 Photoelectrochemical hydrogen evolution

It has been demonstrated that these LFO films display p-type behaviour with recordable cathodic photocurrent, with templated LFO-E films achieving the highest photocurrent of -161 µA cm^{-2} at -0.48 V_{AgCl}. As addressed in Section 4.7, there are competing PEC processes present when using this LFO-E photocathode within a PEC cell, such as that of oxygen reduction that can occur on the LFO particles and the FTO. This results in depressed photocurrents when in a purged system, which will reduce water reduction capabilities. This is evidently problematic as the ultimate application of these photoelectrodes is primarily for H_2 evolution from PEC water reduction. Hence, despite this reduced photocurrent in the absence of oxygen, these LFO films were investigated for their ability to evolve hydrogen from water.

In order to measure activity for PEC water reduction, a gas-tight PEC cell was used with a Pt counter electrode and Ag/AgCl reference electrode, and LFO-E as the working electrode. The cell was first purged with N_2 for 30 minutes to expel any atmospheric oxygen, in order to avoid ORR. The LFO-E working electrode was then illuminated continuously with simulated solar light (100 mW cm^{-2}) at -0.48 V_{AgCl} for 6 hours. The light was chopped at intervals to establish the location of the dark current for accurate determination of photocurrent throughout the measurement (Figure 4-55). Evolving gases were collected within the headspace of the cell and measured using

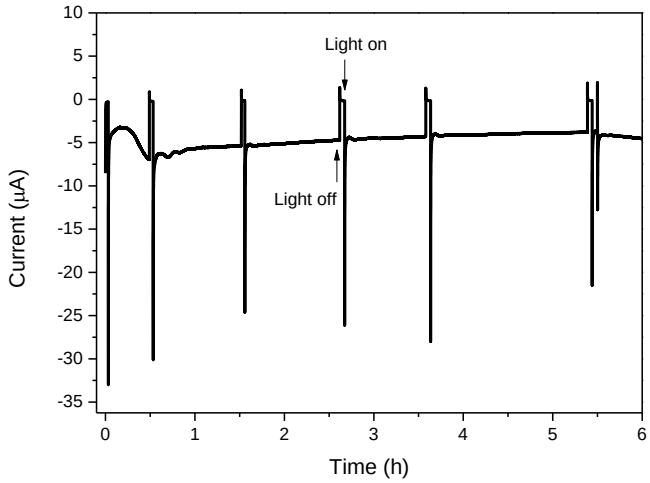

Figure 4-55: Current density data from H_2 evolution measurement at a potential of -0.48 V_{AgCl} under constant solar illumination (100 mW cm^{-2}).

GC within a closed circuit, in which the gases were re-circulated using a peristaltic pump. A build-up of H_2 was achieved within the headspace and was measured every 2 hours in order to calculate the rate of H_2 evolution.

The amount of H_2 measured was found to be ~0, 0.08 and 0.09 µmol for 2, 4 and 6 hours respectively, with a rate of 0.05 µmol cm^{-2} h^{-1} over 6 hours. This successfully demonstrates the ability of these LFO films to generate H_2 from solar PEC water reduction, despite relatively low photocurrents achieved on N_2 purging. The faradaic efficiency (FE) for hydrogen evolution was calculated using Equation 21.

$$FE = \frac{H_2 \; n \; F}{Q}$$

Equation 21: Faradaic efficiency calculation.

Where H_2 is the amount of hydrogen moles formed and measured, n is the number of electron moles needed to form one molecule of hydrogen (*i.e.* 2), F is the Faraday constant, and Q is the generated charge during the experiment (*i.e.* the integral of photocurrent over time). FE was calculated to be 23 % at 4 h and 16 % at 6 hours. However, this can be seen as inaccurate due to the absence of a reference for 100 % FE that can be completed using a Pt working electrode and applying the same current measured when LFO-E is used as the working electrode. Due to time constraints this was not done, but nonetheless provides an insight into the low efficiencies for PEC water reduction. These relatively low efficiencies can be explained due to the presence of oxygen within the cell. This is the case despite prior purging of the cell with N_2, due to oxygen being evolving from the Pt counter electrode during the reaction. Hence, the oxygen ultimately accumulating in the cell will compete with protons reduction to H_2, which could explain the low efficiencies obtained. As part of future work, in order to attempt to minimise this effect of competitive ORR, the incorporation of HER co-catalysts can be implemented to help direct electrons to proton reduction. Additionally, a more favourable PEC cell set-up could be made with using a H-shape design that separates H_2 and O_2 evolution reactions.

4.10 Conclusions

This Chapter has primarily addressed the importance of considering the affects that film fabrication method has on film quality and overall activity for photoelectrochemical processes. It was found that using a doctor blading method with LFO particles was insufficient in producing films of high LFO coverage on the glass substrate with demonstrated poor activity (LFO-A). Hence, the bulk of this Chapter was dedicated to exploring further film fabrication methods in order to increase film quality in terms of particle coverage, uniformity and reproducibility. Initially, LFO powders were milled and sonicated in order to reduce particle size and increase surface area in conjunction with a spray pyrolysis deposition method (LFO-B). This allowed for a visible reduction in particle size and increased electrochemically active surface area, in addition to increases in photocurrent from -3±1 to -37±5 μA cm^{-2} at -0.48 V_{AgCl} when compared to LFO-A. Despite this, LFO-B films failed to utilise all available space on the substrate, leaving large areas of exposed FTO when observed under FE-SEM. Further increases in activity were achieved through using a spray pyrolysis method with nitrate precursors and subsequent calcination to form LFO directly on to the FTO-ABS glass substrate (LFO-C). FE-SEM micrographs confirmed a better coverage than that of LFO-A and LFO-B, however there was distinct irregularity in these films with a cracked appearance and exposed FTO still being visible. An enhanced photocurrent of -112±10 μA cm^{-2} at -0.48 V_{AgCl} was recorded, which can be attributed to better contact between the LFO and the FTO resulting from the synthesis of LFO directly onto the substrate.

A polymer templating method was also employed to improve film quality, using both PVC-*g*-POEM (LFO-D) and Triton X-100 (LFO-E) with nitrate precursors, and a spin coating deposition. In both cases, a vast improvement in substrate coverage, uniformity and porosity was achieved which was accompanied with enhanced photocurrents and better stability. LFO-D achieved -148±6 μA cm^{-2}, whilst LFO-E achieved -161±6 μA cm^{-2} at -0.48 V_{AgCl}, with increased incident photon-to-current efficiency of 12 % for both LFO-D and -E compared to 6 % for LFO-C. These enhancements can be explained due to increases in film quality and surface area due to the appearance of highly uniform and porous LFO. Additionally, it was found from electronic impedance spectroscopic measurements that these polymer templated films

displayed faster rates of charge extraction as demonstrated by faster determined rise times of 0.05 and 0.13 s compared to 0.68 and 0.35 s for LFO-B and -C, which can help explain the increased IPCE and photocurrent found. ECSA measurements also showed that with this templating method increases in surface area were achieved with double layer capacitance values of 0.2, 20, 153, 363, 437 mF g^{-1} for LFO-A, -B, -C, -D and -E, respectively.

Finally, a hydrothermal synthesis method was employed to allow for the growth of LFO particles in situ onto the FTO-ABS glass substrate (LFO-F). This method resulted in the appearance of LFO spindles growing from the FTO surface showing interesting morphology under FE-SEM. This morphology could be beneficial for light scattering and increased contact with the electrolyte. A good photocurrent of -152 µA cm^{-2} at -0.48 V_{AgCl} was recorded. An increased ECSA was also found with a double layer capacitance of 494 mF g^{-1}, which would be expected due to the visibly high surface area resulting from multiple porous LFO spindles on the glass substrate. These LFO-F films displayed the best rates of charge extraction from EIS measurements (rise time of 0.04 s) compared to all other LFO films, suggesting this interesting morphology was advantageous for charge separation.

Overall, this examination of different film fabrication methods revealed vast changes in film quality upon an FTO-ABS glass substrate as well as on ultimate photoelectrochemical activity. The best results were achieved by combining a non-ionic surfactant (Triton X-100) with nitrate precursors and then depositing onto FTO-ABS glass through spin coating. This resulted in high quality films with improved coverage, uniformity and increased contact with the FTO, displaying a maximum photocurrent of -161±6 µA cm^{-2} at -0.48 V_{AgCl} (+0.43 V_{RHE}) and an IPCE of 12 % at 320 nm and -0.3 V_{AgCl}, with a high cathodic photocurrent onset of +0.5 V_{AgCl}. This photocurrent achieved is similar to the highest reported within the literature for LFO photocathodes (-160 µA cm^{-2} at +0.26 V_{RHE}).[123] These LFO-E films also showed greater levels of charge extraction and improved stability, with just a 9 % reduction in photocurrent after 1 hour of chopped light illumination. Despite showing large decreases in photocurrent when atmospheric O_2 is expelled from the electrolyte, these films were still able to produce H_2 from water reduction when measured in a N_2

purged gas-tight cell attached to a gas chromatograph. This demonstrated the ability of these LFO films to be active in PEC water reduction with a rate of H_2 evolution 0.05 µmol cm^{-2} h^{-1} over 6 hours. After this optimisation of LFO film fabrication method it was then explored whether photocurrent can be enhanced further through investigating the application of co-catalysts, heterojunctions and charge transport layers.

Chapter 5

5 Exploration of the enhancement of photoelectrochemical activity of $LaFeO_3$ photocathodes

Previously in Chapter 3, the optimisation of film fabrication was extensively explored and was found that incorporating a sacrificial polymer template offered enhanced film quality, photocurrent, charge transport and stability of LFO photocathodes. After this optimisation, it can now be explored whether photocurrent can be increased further through exploiting the benefits of commonly used techniques, such as applying co-catalysts, creating heterojunctions and applying passivation layers. The integration of such methods is widespread in the area of photoelectrodes and can provide dramatic improvements in activity. This Chapter provides an initial exploration of potential techniques to enhance photocurrent, which can hopefully provide a basis for future more complete pieces of work.

5.1 Platinum co-catalyst deposition

In order to enhance activity of photoelectrodes, it is extremely common to deposit co-catalysts on the surface of the metal oxide to assist in charge transfer to the electrolyte. A good example of this is platinum, which can act as a site for water reduction by extracting charge from the surface of the semiconductor. To investigate this, platinum was deposited on LFO-D films (prepared with a PVC-*g*-POEM polymer template) through an adapted photoelectrochemical deposition method using chloroplatinic acid solution (H_2PtCl_6).[145] There are multiple parameters that are needed to be explored in order to optimise this deposition process, such as precursor concentration, potential of deposition and deposition time. Firstly, platinum was

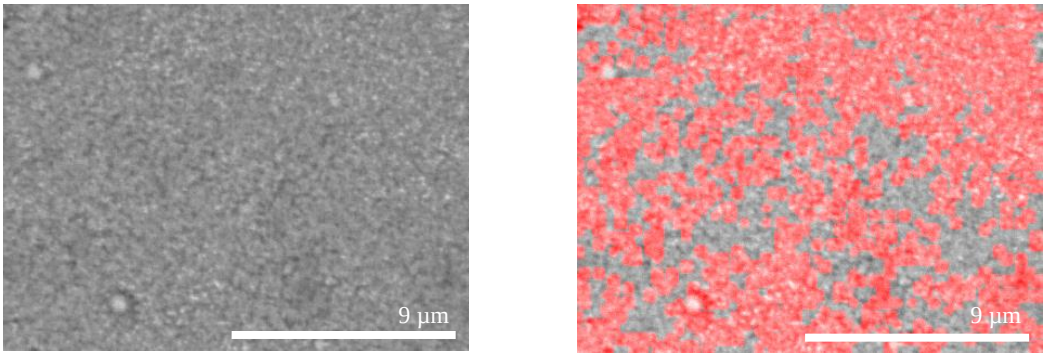

Figure 5-1: SEM micrograph of LFO-D after Pt deposition completed at -0.2 V_{AgCl} for 10 s with a 2.5 mM H_2PtCl_6 solution (left) and EDX elemental mapping of Pt (right).

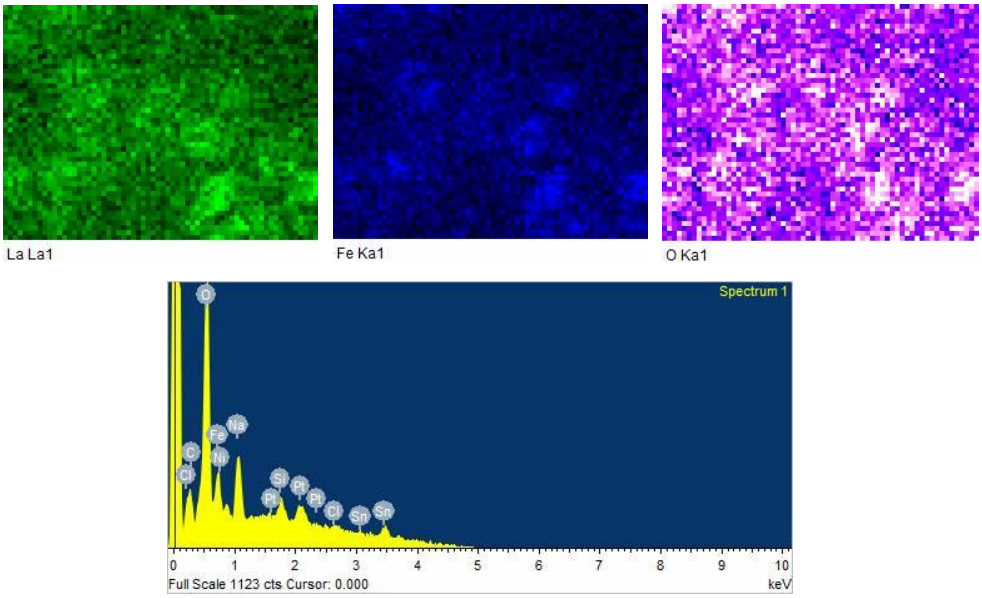

Figure 5-2: SEM micrographs with EDX anlaysis for LFO-D films after the deposition of platinum, showing the presence of La, Fe and O with displayed elemental spectrum.

deposited onto LFO-D films that had only a single calcined LFO layer, with various concentrations of H_2PtCl_6 in 0.1 M Na_2SO_4, in a 3-electrode system at an applied constant potential of between -0.6 and +0.2 V_{AgCl} (Method 2.11). To confirm the successful deposition of Pt on the LFO surface, SEM micrographs were obtained with energy-dispersive X-ray spectroscopy (EDX) analysis. It can be seen in Figure 5-1, that EDX analysis reveals the presence of Pt particles on the LFO surface, as well as the expected La, Fe and O (Figure 5-2). This confirms this chosen PEC deposition of Pt using a H_2PtCl_6 solution allowed for successful Pt deposition.

To examine the effect of precursor concentration on Pt deposition, various solutions of H_2PtCl_6 in 0.1 M Na_2SO_4 were prepared as follows, 2.5 mM H_2PtCl_6 (solution A), 1.25 mM H_2PtCl_6 (solution B), 0.5 mM H_2PtCl_6 (solution C), 0.05 mM H_2PtCl_6 (solution D) and 0.005 mM H_2PtCl_6 (solution E). Pt was then deposited using a constant potential of -0.2 V_{AgCl} which was held for 10 s. It was found that when the deposition was conducted with solution A (2.5 mM H_2PtCl_6) onto an LFO-D (1 layer) film, there was an initial decrease in photocurrent from -62 to -38 µA cm^{-2} (at -0.48 V_{AgCl}) (Figure 5-3a) when PEC measurements were completed directly after the deposition step. This film was then subsequently heated to 500 °C for 30 minutes in attempt to remove any defect states and improve the contact between the Pt particles

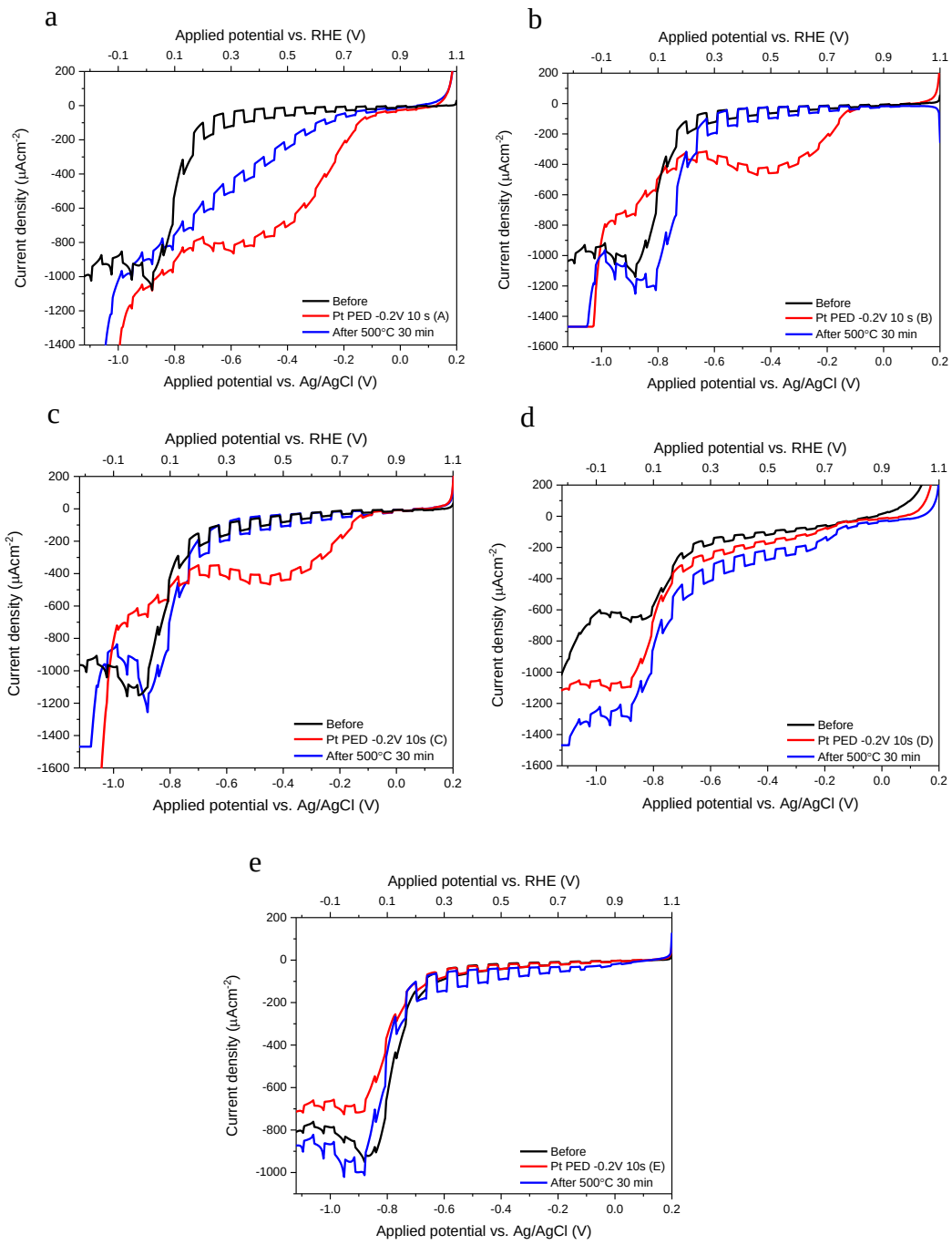

Figure 5-3: Chopped light LSV measurements before Pt deposition, after Pt deposition and after a calcination step of 500 °C for 30 min for (a) H_2PtCl_6 solution A, (b) B, (c) C, (d) D and (e) E.

and LFO particles. After this heating step there was a negligible increase in photocurrent to -65 µA cm^{-2}, demonstrating that these conditions are not preferable and further optimisation is required. It can be postulated that this H_2PtCl_6 concentration is too high, which can result in increased levels of Pt deposition that could contribute in increased light scattering, limiting the light absorption of LFO.

Hence, lower concentrations were examined, with each subsequent deposition incorporating a post deposition heating step at 500 °C (for 30 min). Solution B (1.25 mM H_2PtCl_6) was next used, and after deposition the photocurrent decreased from -55 to -42 µA cm^{-2} which increased to -95 µA cm^{-2} (+72 %) after heating to 500 °C (Figure 5-3b), demonstrating the benefit of a lower concentration H_2PtCl_6 solution. Pt deposition using solution C (0.5 mM H_2PtCl_6) increased photocurrent from -55 to -92 µA cm^{-2} (+67 %) after heating (Figure 5-3c). A similar increase in photocurrent was observed when using solution B, demonstrating no clear advantage of using 0.5 mM over 1.25 mM H_2PtCl_6, apart from reducing the expense of H_2PtCl_6 by using a lower concentration solution. Figure 5-3d shows decreasing the concentration to 0.05 mM H_2PtCl_6 (solution D), increased the photocurrent by +175 % (-29 to -80 µA cm^{-2}). A further decrease in concentration to 0.005 mM H_2PtCl_6 (solution E) also exhibited a good increase in recorded photocurrent, from -33 to -67 µA cm^{-2}, an increase of +103 %.

It appears that changing the concentration of H_2PtCl_6 used in the PEC deposition of platinum has a strong effect on any enhancements in photocurrent seen. This is expected, as the concentration of the deposition solution will ultimately impact the amount and size of the Pt that is deposited, which can have impacts on the resultant activity. Lower concentrations of H_2PtCl_6 appear to be beneficial (0.05 and 0.005 mM), which can be postulated due to the deposition of fewer or smaller Pt nanoparticles that can help reduce potentially detrimental light scattering, which would diminish absorption. There is a reduction in photocurrent when decreasing H_2PtCl_6 concentration from 0.05 to 0.005 mM, which could be due to this lower concentration not providing enough Pt to be deposited.

As seen within the literature, deposition potential can also have vast effects on ultimate catalytic activity through changes in nanoparticle morphology[146,147]. For H_2PtCl_6 solutions D (0.05 mM) and E (0.005 mM), a potential of +0.2 V_{AgCl} and -0.6 V_{AgCl} were used during a 10 s deposition to optimise deposition potential. Concerning solution D, there was an increase in photocurrent density of +26 % when a potential of +0.2 V_{AgCl} was applied, and an increase of +37 % when -0.6 V_{AgCl} was used (Figure 5-4a and b). This can be compared with the +175 % increase shown in Figure 5-3 for

an applied deposition potential of -0.2 V_{AgCl}. This seems to suggest that a more negative potential of -0.6 V_{AgCl} is not beneficial, which could be due to excessive deposition of Pt nanoparticles that could hinder light absorption. In addition, a higher potential of +0.2 V_{AgCl} is also seen to be detrimental, suggesting that this potential is insufficient for optimal Pt deposition. For H_2PtCl_6 solution E, a deposition potential of -0.6 V_{AgCl} gave rise to a photocurrent increase of +142 % and a potential of +0.2 V_{AgCl} providing no increase in photocurrent (Figure 5-4c and d). Comparing this to Figure 5-3 where an increase of +103 % was observed for a potential of -0.2 V_{AgCl}, it appears here that a more negative deposition potential is beneficial. This can be explained due to fewer available reductive species in solution E, hence requiring more negative reduction conditions to achieve similar activity enhancements to a more concentrated solution.

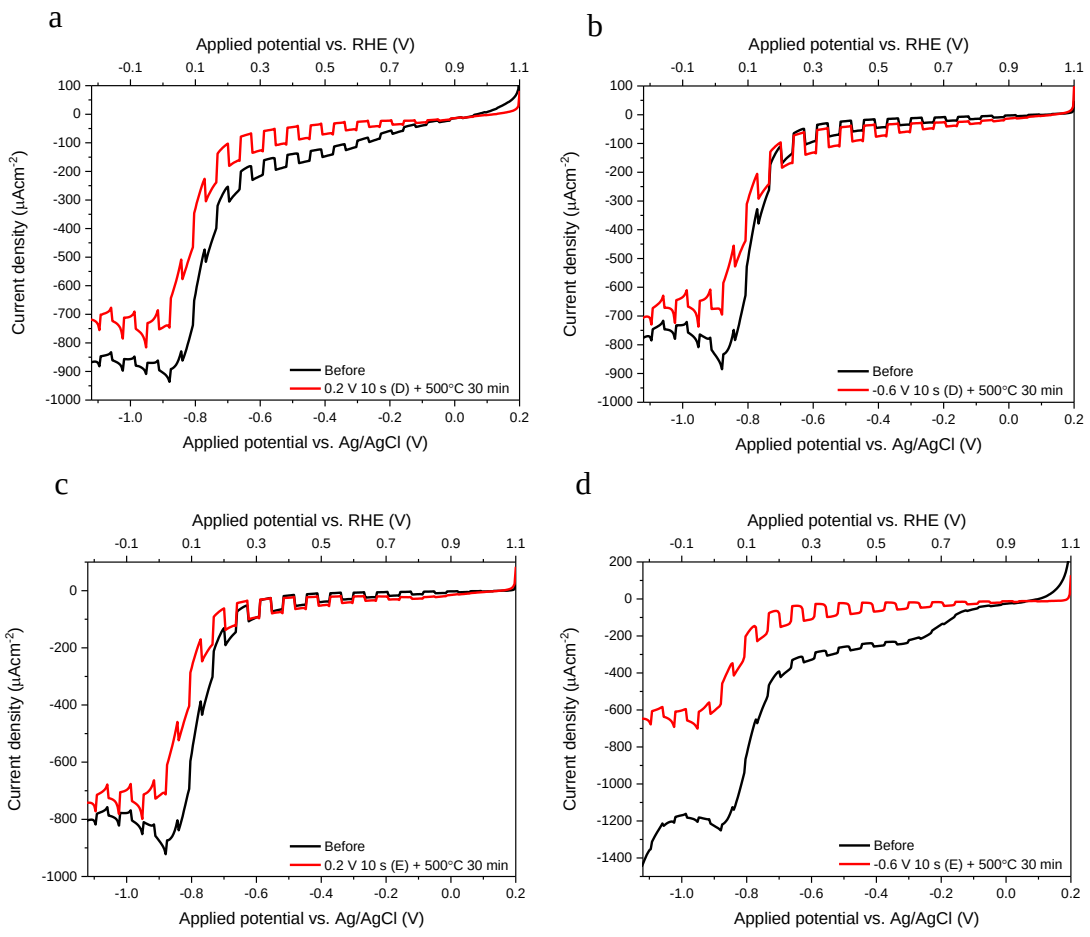

Figure 5-4: Chopped light LSV measurements for Pt depositions for solution D at (a) +0.2 V_{AgCl} and (b) -0.6 V_{AgCl} and for solution E at (c) +0.2 V_{AgCl} and (d) -0.6 V_{AgCl}.

All Pt PEC depositions completed thus far have been completed upon just 1 calcined LFO-D layer, to simplify optimisation. However, the maximum photocurrent for bare LFO-D films was reported at 3/4 LFO calcined layers, hence Pt depositions need to be completed on these thicker films. Here, an applied potential of -0.6 V_{AgCl} was used for 20 s with solution E onto LFO-D films with 3 and 4 applied LFO layers. PEC measurements were then completed on both frontside and backside illumination, due to the increased thickness of these films. For an LFO-D film with 3 applied LFO layers, a photocurrent of -64 µA cm^{-2} was achieved which increased to -133 µA cm^{-2} (an increase of 108 %) demonstrating the beneficial effect of Pt on the surface for frontside illumination. However, for these thicker films the highest photocurrent is achieved on backside illumination (-113.8 µA cm^{-2}) which increased by just +12 % to -128 µA cm^{-2} on Pt deposition (Figure 5-5). This can be explained due to the increased thickness of LFO films when comparing to those used previously, the deposition of Pt will occur at the LFO surface and so will be in contact with the outer most particles of the film. This being the case, on frontside illumination these LFO particles in contact with Pt will be able to absorb light and generate electrons that can transfer to the Pt, hence the effect of Pt being present can be demonstrated. However, on backside illumination the light will struggle to reach these outermost LFO particles at the surface where the Pt lies, and will only illuminate the LFO particles closer to the glass substrate, which would require electrons to travel further distances to reach the Pt on

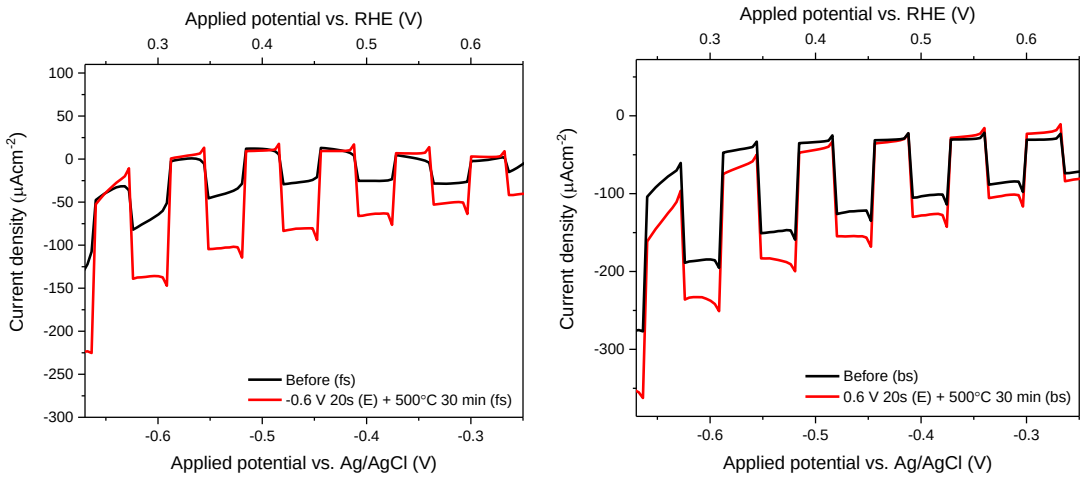

Figure 5-5: Chopped light LSV measurements with frontside illumination for LFO-D (3 layers) before and after Pt deposition (left) and on backside illumination (right).

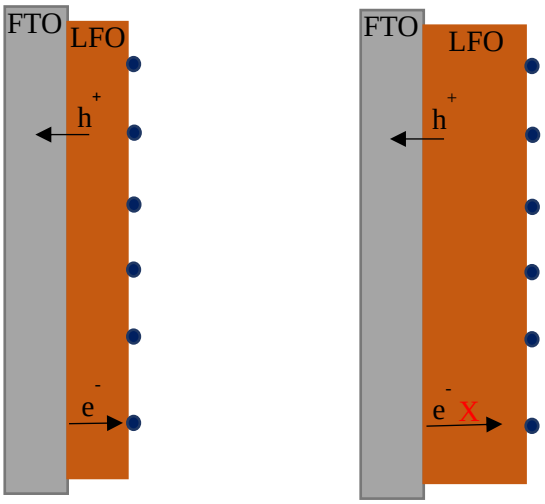

Figure 5-6: Schematic of the proposed effect Pt deposition on a single LFO layer film (left) and on a multiple LFO layer film on illumination (right).

the surface. Therefore, the increase in photocurrent is much less pronounced on backside illumination, which can be demonstrated with the schematic created in Figure 5-6. In addition, the same deposition was completed on LFO-D films with 4 applied LFO layers. On frontside illumination, the photocurrent density decreased from -114 to -99 µA cm^{-2}, and on backside illumination there is no change in photocurrent remaining at -128 µA cm^{-2} (Figure 5-7). It appears that when Pt is deposited on a 4 layer LFO-D film there is no improvement in photocurrent due to the increased thickness (~780 nm, Figure 4-25). As discussed previously, the generated

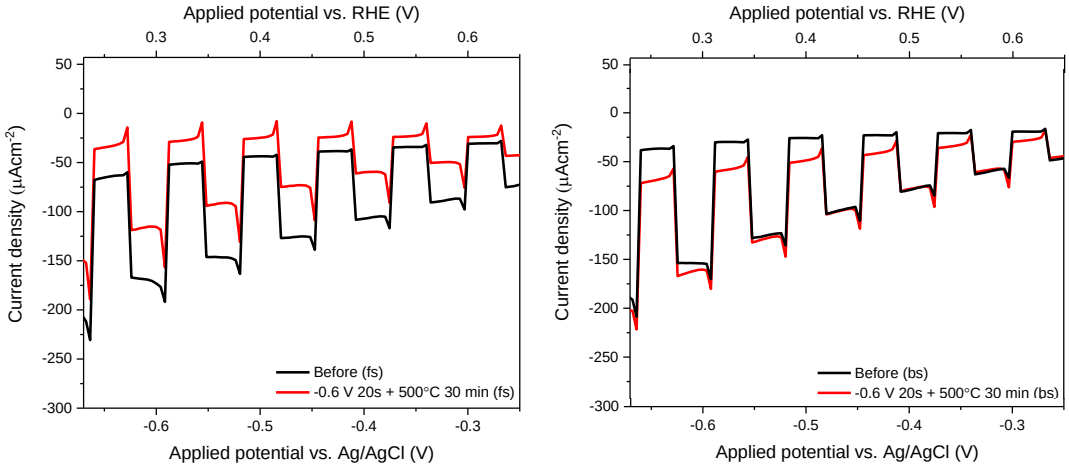

Figure 5-7: Chopped light LSV measurements with frontside illumination for LFO-D (4 layers) before and after Pt deposition (left) and on backside illumination (right).

photoexcited electrons may well be hindered in reaching the Pt on the LFO surface due to the distance, and so the beneficial effects of incorporating a Pt co-catalyst is not exhibited. It appears from this work that these thick LFO-D films are incompatible from benefiting from Pt deposition, hence many attempts in reducing the thickness of these films whilst maintaining high photocurrent were employed without success (not shown).

5.2 Semiconductor heterojunction with CuO

Another technique to enhance photocurrent is that of forming semiconductor heterojunctions. Combining two semiconductor materials within a photoelectrode can assist in increasing charge separation through charge transfer between materials with suitable band alignments. It has been shown previously that a CuO/LFO nanocomposite has been fabricated, that showed enhanced photocatalytic activity for dye degradation, and thus demonstrates its suitability for heterojunction formation with LFO photoelectrodes.[125]

Firstly, CuO films were fabricated using CuO nanopowder (Sigma Aldrich) mixed with Triton X-100 and THF, which was then drop casted onto an FTO-ABS glass substrate upon a 200 °C hotplate, and then calcined at 500 °C for 1 hour (Method 2.12). This CuO was then tested for PEC activity on frontside and backside illumination, and additionally tested for long term stability over chopped solar

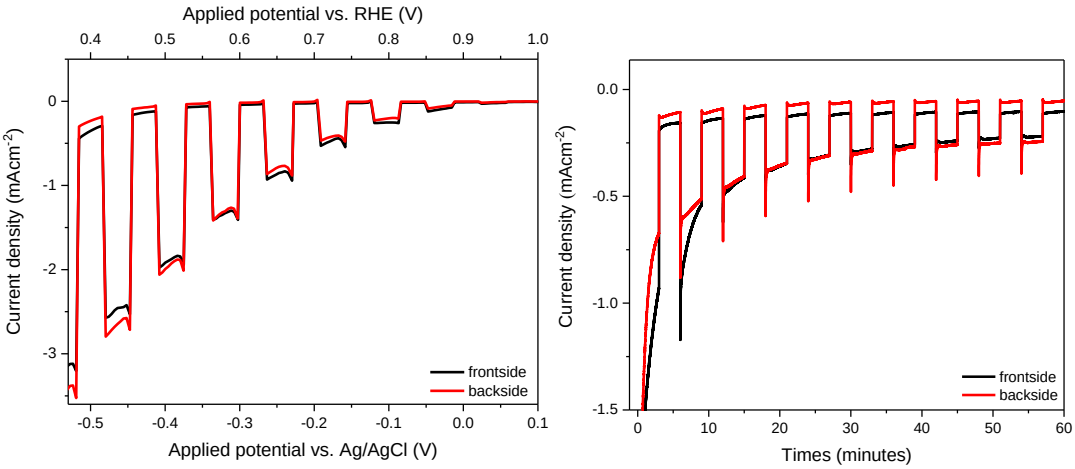

Figure 5-8: Chopped light LSV measurements for CuO films with front and back illumination (left)and PEC stability measurements conducted at -0.48 V_{AgCl} (right).

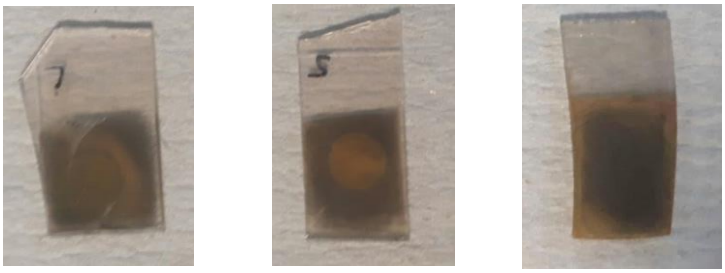

Figure 5-9: Photographs of CuO films prepared through drop casting after PEC measurements were obtained on frontside illumination (left) and backside illumination (middle) and photograph of a CuO/LFO film (right).

illumination over 1 hour. An impressive photocurrent density of -2.4 mA cm^{-2} at -0.48 V_{AgCl} was achieved which is expected due to the well-established high photocathodic activity of CuO, with a photocurrent of -2.8 mA cm^{-2} on backside illumination (Figure 5-8). The stability of these photocathodes are poor, demonstrating a retention of photocurrent of just 18 % and 38 % on frontside and backside illumination after 1 hour. The higher stability found when illuminating from the back could be due to restricted light absorption for all CuO particles present, diminishing photodegradation. It can be seen from the photographs in Figure 5-9 that regardless of whether frontside or backside illumination was used, there is visible degradation of the CuO. This is demonstrated by the change in colour from black/dark grey to a yellow/orange. This can be attributed to the self photocorrosion of CuO to metallic Cu[148], which would be expected from this unprotected photocathode.

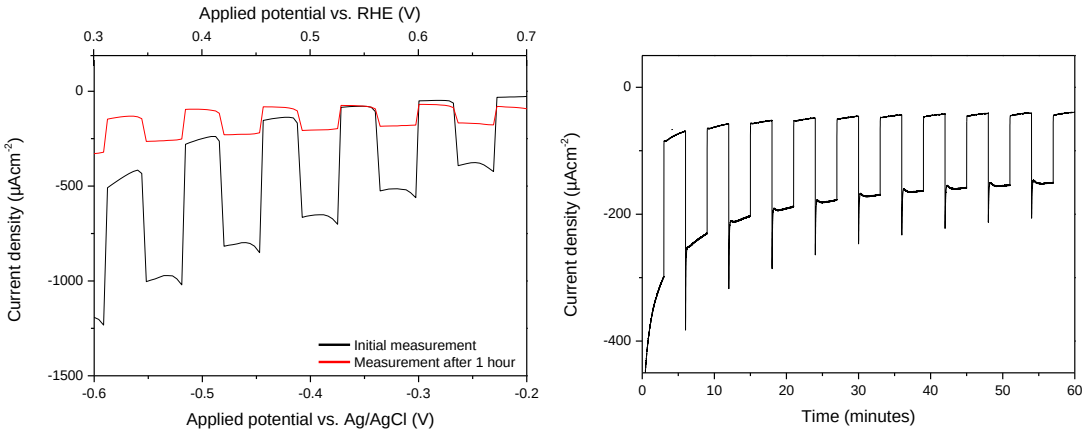

Figure 5-10: Chopped light LSV measurements of a CuO/LFO film (left) and stability measurement with chopped illumination at a constant potential of -0.48 V_{AgCl} (right).

In order to fabricate a CuO/LFO heterojunction, a CuO photoelectrode was first prepared as described above, and then subsequent LFO layers were deposited using spin coating and polymer templating (LFO-D). These CuO/LFO films were then tested for their PEC activity and examined for their stability over 1 hour chopped light illumination. It was found that a lower photocurrent of -0.61 mA cm^{-2} (decreased to -0.14 mA cm^{-2} after 1 hour) was achieved compared to -2.4 mA cm^{-2} at -0.48 V_{AgCl} for CuO alone. This was accompanied by an increase in stability, with 60 % of the initial photocurrent being maintained after 1 hour chopped illumination (Figure 5-10). This decrease in photocurrent can be attributed to the LFO layers blocking light from getting to the more active CuO, thus limiting the generation of photocurrent. This protection provided by the LFO layers will also reduce photodegradation through protecting the CuO from the electrolyte, that can help limit corrosion, hence an increase in stability is achieved. It can also be seen from the photographs in Figure 5-9 that no visible degradation is observed, as seen for bare CuO.

However, it was intended to produce a heterojunction between these two semiconductors that should provide increased photocurrent through the reduction of electron-hole recombination. An increased photocurrent is not achieved suggesting that a beneficial heterojunction is not formed in this case, or that the blocking of the light reaching the CuO reduces the photogeneration of electrons too vastly to demonstrate any beneficial contact between LFO, compared to bare CuO. Due to time constraints a more in-depth analysis with further fabrication of these CuO/LFO photocathodes was not completed. It is abundantly clear that optimisation of the preparation of this proposed heterojunction is needed to accomplish any improvement in the efficiency of LFO photocathodes. It would also be wise to conduct further analysis to confirm that an appropriate heterojunction is viable in relation to energy band alignments between these two semiconductors, as well as optimising the thicknesses of both CuO and LFO whilst considering the photoinstability of CuO. Additionally, as part of future work other semiconductors can be investigated in order to create heterojunctions to improve charge separation and transfer, ideally with a more stable material than that of CuO.

5.3 Passivation and blocking layers

Another technique to assist in improving charge transport properties, is to reduce interfacial recombination upon the FTO substrate. When there are large portions of exposed FTO after LFO film fabrication, there is an increased introduction for the potential of interfacial charge recombination. This can be alleviated through the introduction of a thin blocking layer that can reduce potential recombination sites upon the FTO, through providing conformal coverage on the conductive substrate. This interfacial blocking layer can be achieved through the use of a continuous mesoporous structure between the conductive FTO and the LFO. This has been demonstrated previously through the deposition of a mesoporous WO_3 layer (using a PVC-*g*-POEM polymer templating method), with subsequent deposition of WO_3 nanoflakes upon this interfacial layer.[100] In particular, this technique can be especially useful for LFO-F films that were prepared through an in situ hydrothermal synthesis method, as this method produces good photocurrent but results in a lack of conformal coverage upon the FTO substrate. These areas of exposed FTO were a result of the random growth of LFO spindles, which could limit achievable photocurrent due to this introduction of charge recombination sites upon the FTO as demonstrated. Hence, it was decided to employ this interfacial blocking layer method with LFO-F films, in order to increase charge separation capabilities, through first depositing a single polymer templated LFO-D layer and then subsequent LFO deposition through a hydrothermal method as shown in Figure 5-11. An additional potential benefit of having an initial LFO layer

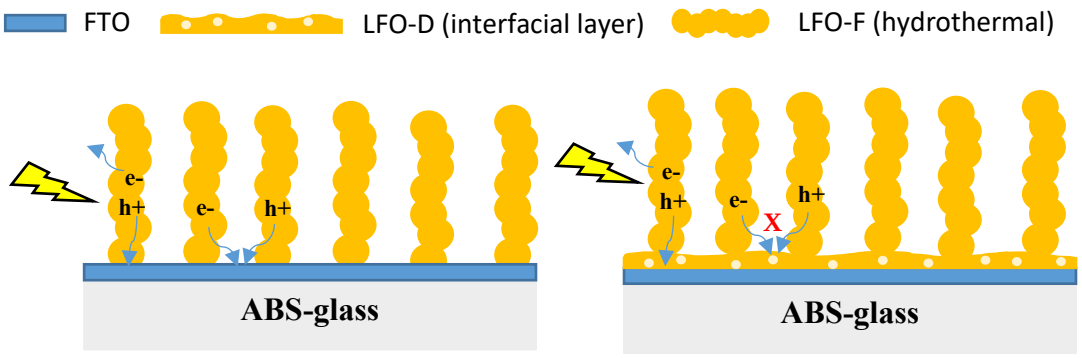

Figure 5-11: Schematic showing the proposed electron-hole recombination at the FTO surface for LFO-F films (left) and the effect of the incorporation of an interfacial mesoporous blocking layer (right).

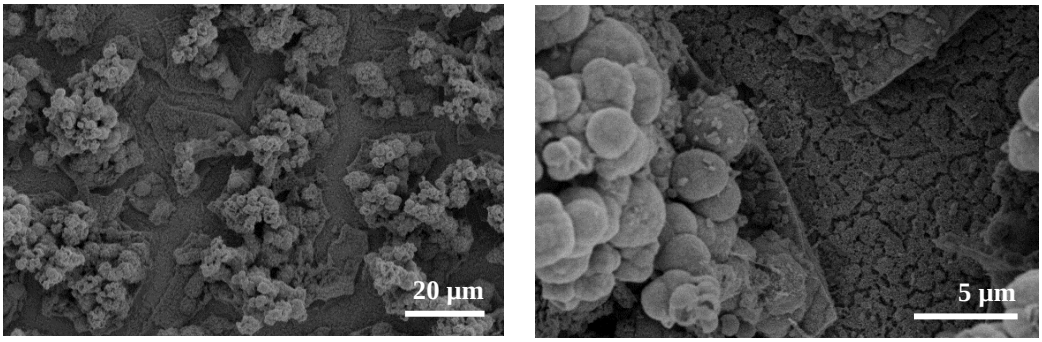

Figure 5-12: FE-SEM micrographs of hydrothermally grown LFO-F film calcined at 800 °C with a LFO-D interfacial blocking layer.

prior to the hydrothermal growth, is that it could provide further propagation sites for growth, as LFO spindles appear to only grow from compact LFO islands formed during synthesis, and not directly from the FTO surface.

The LFO-D films were first prepared then transferred to an autoclave and immersed in a solution of lanthanum nitrate and potassium ferric cyanide $K_3[Fe(CN)_6]$ precursors with citric acid and heated at 180 °C for 18 hours and calcined at 800 °C. Firstly, FE-SEM micrographs were obtained to establish whether the LFO-F spindles were able to grow upon the interfacial LFO-D blocking layer. It can be seen in Figure 5-12, that a characteristic LFO-D layer is seen on the FTO substrate with the expected LFO spindles also being observed. As seen previously, the LFO spindles still propagate from small compacted LFO islands that form during the hydrothermal synthesis and have not formed from the LFO-D interfacial layer, which would have been beneficial. Nevertheless, there should be a reduction in electron-hole recombination on the FTO surface due to this initial LFO-D layer providing better FTO coverage than pristine LFO-F films. PEC measurements were then obtained to attain whether any enhancement in photocurrent was achieved. Figure 5-13 shows an increase in photocurrent at -0.42 V_{AgCl} from -68 to -93 µA cm^{-2} (+37 %). This suggests that the incorporation of the initial LFO blocking layer has been successful in enhancing photocurrent, which could be attributed to this attempted reduction of interfacial recombination. However, this increase in photocurrent density could also be attributed to the increased amount of LFO material present on this film, resulting in increased light absorption and charge generation. Further electrochemical characterisation is needed to confirm whether the introduction of this proposed

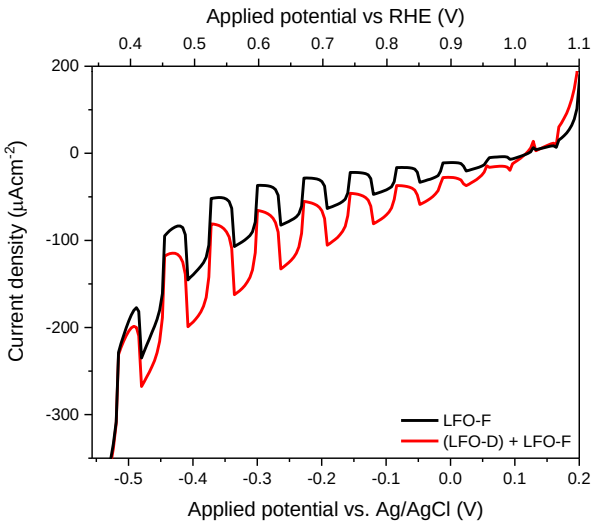

Figure 5-13: Chopped light LSV measurements for an LFO-F film calcined at 800 °C with and without the addition of an LFO-D interfacial blocking layer.

blocking layer reduces recombination, namely in the form of determining RC limited photocurrent transients. Conducting these further measurements will help establish if these LFO-F films, with an interfacial blocking layer, achieves faster rates of charge extraction compared to LFO-F films alone. Due to time constraints these measurements were unable to be completed, however this method displays some promise and would be especially useful for LFO films with large areas of exposed FTO.

As well as investigating interfacial blocking layers, further blocking layers can be employed that have strong hole transport properties. Due to previous literature reporting the competition between water oxidation at the LFO/electrolyte interface with hole collection at the back contact (FTO), it seems that a hole transport layer could prove beneficial here.[98] Hence, it was briefly investigated whether depositing a NiO layer, which is known to be an efficient hole transport layer due to its high work function, would prove beneficial. In this case, NiO can help promote the formation of an ohmic contact formation with the LFO which can assist in charge transport.[97] It was hence attempted to create this NiO hole transport layer incorporated with LFO-F film fabrication. NiO was first synthesised through spin coating a solution of $Ni(OH)_2$ with subsequent calcination at 500 °C for 1 hour (Method 2.13, taken from Wei et al).[97] An

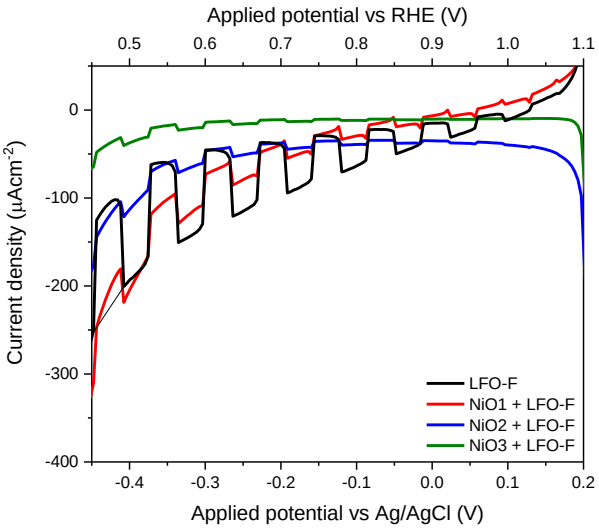

Figure 5-14: PEC measurements for LFO-F films prepared with a NiO hole transport layer with 1, 2 and 3 layers applied.

in situ hydrothermal synthesis was then completed to form LFO-F upon the NiO hole transport layer, with 1, 2 and 3 spin coated NiO layers being investigated. As shown in Figure 5-14, there is a reduction in photocurrent when 1, 2 and 3 spin coated NiO layers were applied before LFO-F growth, with recorded photocurrents of -54, -27 and -14 µA cm^{-2} respectively. It was also observed that there were visible signs that LFO growth was hindered when incorporating NiO layers, with visible film quality being much poorer than LFO-F alone. This could be due to the NiO layer providing a poor site for propagation and growth of the LFO spindles, which is suggested due to the dramatic decrease in activity on application of multiple NiO layers, however further work would be needed to confirm the failure of the complete growth of these films.

5.4 Conclusions

It is extremely common to incorporate co-catalysts, heterojunctions or passivation/ blocking layers to semiconductor materials to increase photoelectrochemical activity. Some of these methods were explored here as potential future techniques to achieve increased photocurrent. Firstly, platinum was deposited upon LFO-D photocathodes in order to enhance photocurrent through providing Pt nanoparticles as further reductive sites. After successfully depositing Pt using photoelectrodeposition, it was found that when just 1 LFO-D layer is used, an enhancement in activity was seen.

When multiple LFO layers are applied (optimal for photocurrent) with subsequent Pt deposition, increases in photocurrent were not achieved, due to increased film thickness resulting in difficulties in charge transport to the Pt. Further work is required into incorporating co-catalysts that are able to enhance activity even with thicker LFO films that are required for optimal photocurrent. In addition, due to issues of selectivity for PEC processes, a more selective co-catalyst for hydrogen evolution could be explored such as RuO_x. In addition, it was very briefly examined whether a heterojunction could be created with CuO, however due to time constraints further analysis was not completed. Due to this, it was not attained whether a favourable interaction was created at the CuO/LFO interface, although an increase in stability for CuO was seen most likely due to the protection LFO provides. In addition, a CuO/LFO heterojunction has already been demonstrated for photocatalytic degradation of aqueous contaminants, hence more novel nanocomposites should be considered in the future.[125]

Also, it has been reported that LFO photocathodes possess a competition of holes between the oxygen evolution reaction and hole collection at the back contact, thus techniques were explored to reduce this. Another possible issue is that of electron-hole recombination at the FTO surface, both problems can be addressed through introducing interfacial blocking layers or hole transport layers. These were both attempted briefly here with the use of a mesoporous templated LFO as an interfacial blocking layer with subsequent addition of hydrothermally grown LFO-F spindles, which helped enhance photocurrent. Further electrochemical measurements are needed however to establish whether improvements in charge separation were achieved. Additionally, NiO was incorporated within LFO-F films to act as a hole transport layer, however this failed to increase photocurrent due to issues arising in the successful growth of LFO upon the NiO layer. Future work can include further more in depth exploration of these techniques, incorporating further hole transport layers, or applying a hole blocking layer upon the LFO to stop holes migrating to the electrolyte, which has been done with TiO_2.[99]

Chapter 6

6 Synthesis of $PrFeO_3$ particles for photocatalytic water reduction

As described within Chapter 1, there are numerous advantages in investigating ferrite-based perovskite oxides, such as good stability, abundancy and visible light activity. The work within this Thesis thus far has reported the fabrication of LFO photocathodes for PEC processes, which was investigated due to the promise and room for improvement shown for this perovskite within the literature. However, there are clearly alternative active and appropriate perovskites that can be additionally investigated. $PrFeO_3$ (PFO) for instance has been used in applications such as that in chemical sensing[127,128] and currently has demonstrated one instance of showing activity for photocatalytic water reduction.[73] Hence, it is believed at the time of writing, there are no cases in which PFO has been demonstrated as a photocathode for photoelectrochemical water reduction. Therefore, due to the activity of PFO for photocatalytic water reduction, its visible light activity and the scarcity of research into PFO, it was decided that it should be explored further as a photocathode.

6.1 Synthesis of $PrFeO_3$ particles

All work reported within Section 6.1 was conducted by MEng Chemical Engineering undergraduate student Hayley Pickering, as part of a 3rd year research project from February to March 2017 under my supervision.

Praseodymium iron oxide was prepared through a sol-gel method with the mixing of lanthanum and iron nitrates with citric acid in deionised water in a 1:1:4 ratio. This was then stirred and dried at 100 °C overnight to obtain a dried powder. This was then subjected to various calcination conditions that are described in Table 4 involving the presence and absence of a pre-calcination step in order to remove the majority of organic material, and then a further calcination step at higher temperature (Method 2.14). These synthesised PFO particles were labelled as HP1, 2, 3 and 4 as seen in Table 4.

Table 4: Sample descriptions for PFO particles calcined with different conditions.

Sample I.D	Calcination conditions
HP1	Pre-calcination: 500 °C for 5 h Calcination: 700 °C for 5 h
HP2	Pre-calcination: 500 °C for 5 h Calcination: 700 °C for 2 h
HP3	Calcination: 700 °C for 2 h
HP4	Calcination: 700 °C for 5 h

Each of these PFO powders were first examined using XRD, which demonstrates the successful formation of PFO with peaks consistent with phase pure PFO. Using the Scherrer equation, the coherent crystal domain size was determined for samples HP1, 2, 3 and 4 to be 19.8, 18.7, 19.6 and 20.1 nm, respectively (Figure 6-1a). This shows very little change in particle size, with HP2 providing the smallest crystal domain size. BET specific surface area measurements were also done to establish approximate surface area for these powders, which were found to be 8.7, 10.3, 8.3 and 9.0 $m^2 g^{-1}$ for powders HP1, 2, 3 and 4 respectively. These determined surface areas are relatively low and lie below the accurate detection limit of BET measurement, hence conclusive remarks cannot be made with respect to the effect of calcination conditions on specific surface area. Nevertheless, this provides an insight into one of the known issues of perovskite oxides compounds, such as that of low surface area, due to the need of high temperature activation. UV-Vis measurements were obtained in order to create Tauc plots to determine energy band gap. As done previously with LFO, both direct allowed (n = 1/2) and direct forbidden (n = 3/2) optical transitions[149] were considered due to the lack of knowledge of optical properties and large polycrystallinity of PFO (Figure 6-1b and c). Band gaps of these PFO powders were determined to be 2.1, 2.1, 2.1-2.4 and 2.1 eV for HP 1, 2, 3 and 4 respectively. All of which exhibit little variation on optical transition used and lie within the visible light region, which is in agreement with literature values (2.08 eV).[73]

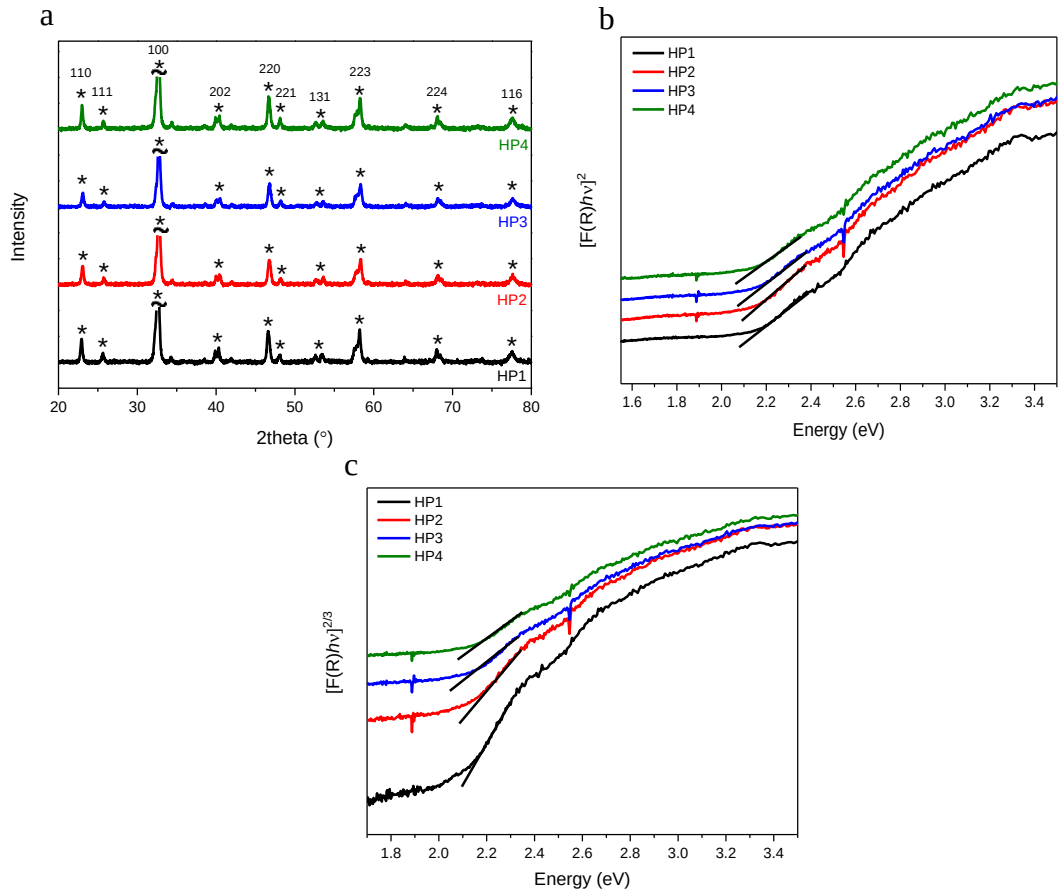

Figure 6-1: (a) XRD spectra for PFO particles and (b, c) Tauc plots for PFO films calcined under various conditions (HP1-4).

To characterise these PFO particles further, HR-TEM micrographs were obtained to determine particle sizes (Figure 6-2). HP1 gave a particle size range of 40-50 nm, HP2 20-40 nm, HP3 40-60 nm and HP4 30-40 nm, with corresponding lattice distances of 0.282, 0.159, 0.277 and 0.400 nm. This demonstrates minute variations in particle size with the smallest being for HP2, which corresponds to the highest BET determined surface area between samples, as well as the smallest particle size calculated using XRD (18.7 nm). The highest range of particle sizes is for HP3, that is in agreement with the lowest determined surface area. However, as described before in Chapter 3 these particles are most likely to be large agglomerates of a micrometre size demonstrating a failure in producing more desired nanoparticles. Nanoparticles are preferable due to larger active surface areas, but the work detailed here was to increase awareness of synthesis and characterisation methods, rather than specifically for the

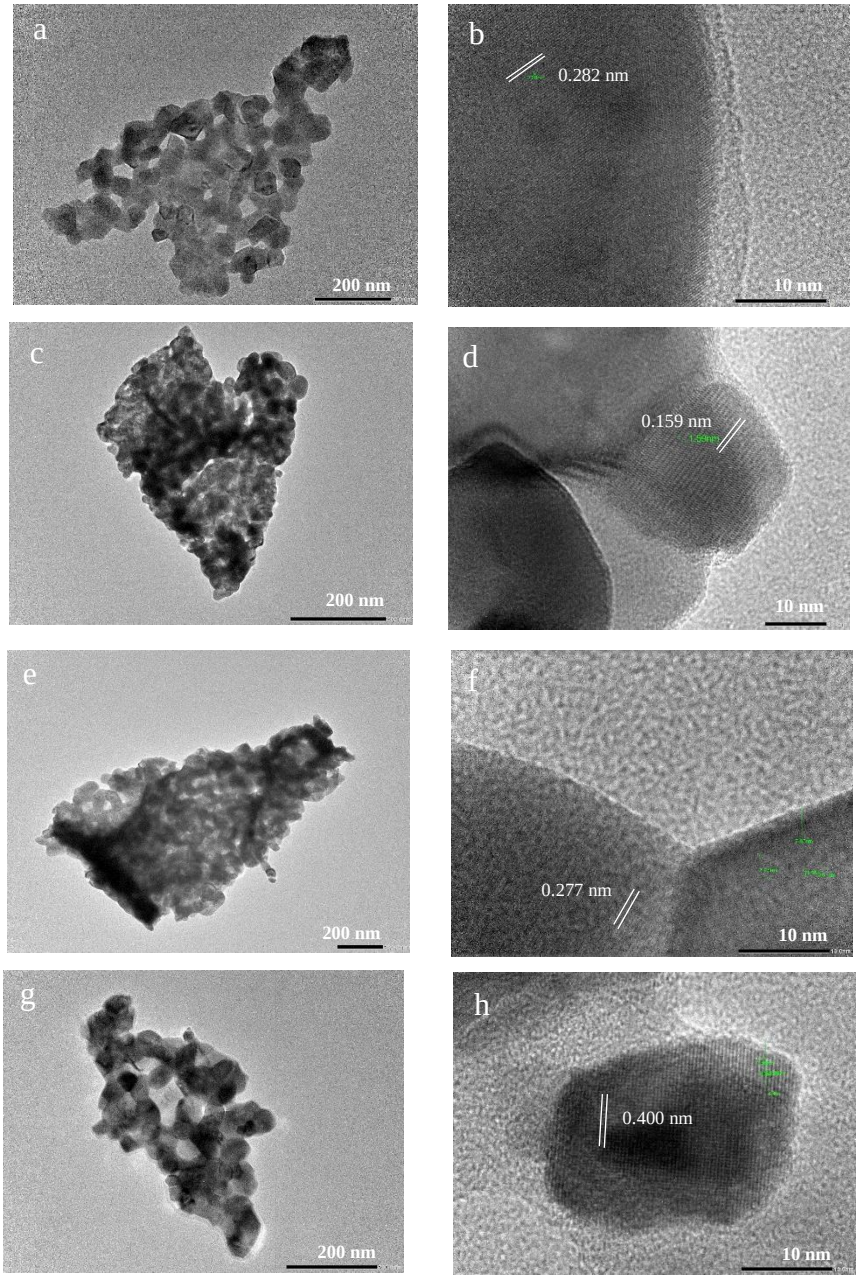

Figure 6-2: HR-TEM micrographs of (a, b) HP1, (c, d) HP2, (e, f) HP3 and (g, h) HP4.

creation of nanoparticles. This relationship between calcination time and particle size distributions have been somewhat examined, however, due to the inaccuracies described above involving the lower detection limit of BET, this relationship was not further examined. It would be expected that with longer duration of higher temperature calcinations, there would be increases in particle sizes due to increased time of sintering opportunities. This can be seen when comparing HP1 and HP4. HP1 involved a pre-calcination step of 500 °C for 5 hours and then further calcination at

700 °C for 5 hours, whereas HP4 has no pre-calcination. There is a higher particle size distribution for HP1 (40-50 nm) compared to HP4 (30-40 nm), thus supporting increased sintering with increased calcination steps. However, the same effect is not seen for HP2 and HP3, as the addition of a pre-calcination step decreased particle sizes, as HP2 shows a range of 20-40 nm and HP3 shows 40-60 nm. This could be due to inaccuracies of measuring particle size distribution from a single particulate cluster in the HR-TEM micrographs, and hence is not entirely representative of these particles as a whole.

6.1.1 Photocatalytic measurements

Each of these prepared groups of PFO particles were then tested for their activity in photocatalytic hydrogen evolution. This was done by dispersing the PFO particles in a 20 % methanol/water solution in a quartz reaction vessel. The solution was then illuminated for 5 hours and the evolving gases were measured by GC every 15 minutes, to determine whether any hydrogen is evolved (Method 2.2). For each synthesised PFO powder the rates of hydrogen evolution were determined to be 29.2, 35.7, 24.3 and 25.0 μmol h^{-1} g^{-1} for samples, HP1, 2, 3 and 4 respectively. This demonstrates the activity of these PFO powders for photochemical water splitting. The highest rate of hydrogen evolution is achieved for HP2, which can be in part attributed to the possession of the smallest particle sizes and highest surface area. A higher surface area is advantageous for water splitting as there is a greater area of the PFO in contact with the water to assist in water reduction. These achieved rates of H_2 evolution can then be compared to literature values, which have been reported to be 2847 μmol g^{-1} h^{-1} after using PFO powder synthesised using a sol-gel method.[73] This value vastly exceeds that achieved in this work, however 1 mg of a platinum co-catalyst was used in this reported case, hence would increase activity for water reduction drastically. Unfortunately, the activity for pristine PFO was not reported here so a direct comparison cannot be made.

As mentioned previously in Chapter 3, there were limitations involved within this experimental method to measure activity for photocatalytic water reduction. In particular, the apparatus used allowed for restrictions in dispersion of the PFO particles, potentially resulting in the lack of all dispersed PFO being illuminated by

the light. This can occur due to the limited space between the outer reactor vessel and the inner compartment that incorporates the cooling jacket and lamp. This relatively small area visibly hinders particle dispersion, due to the stirrer bar being unable to create sufficient turbulence. Additional issues arouse in the heat produced from the halogen lamp used that can cause temperature fluctuations within the solution that could have caused irregularities in reproducibility between samples.

Overall, four different calcination conditions were examined for a sol-gel synthesis of PFO. These different calcination conditions involved the presence and absence of a pre-calcination step, as well as changing calcination duration. Characterisation of these powders showed small changes in particle size and surface area. HP2 (pre-calcination 500 °C for 5 hours, calcination 700 °C for 2 hours) demonstrated the highest BET surface area, as well as the smallest particle size range as seen under HR-TEM and XRD. Small particle sizes are advantageous as it provides a larger surface area for catalysis which was demonstrated by the increased rate of H_2 evolution for HP2 (36 μmol g^{-1} h^{-1}). However, overall it was difficult to make any definitive conclusions due to the inaccuracies of BET at these low surface areas, and the problems arising from the experimental set-up to measure photocatalytic water splitting. Future work is needed to improve this body of work, for example a range of different calcination temperatures are needed to be investigated as well as number of calcination steps and duration, which were not investigated here. It is well known that calcination temperature can have large effect on particle formation and ultimate catalytic activity, hence it could be possible to attain higher activity PFO.[113] In particular, the design issues involved with the apparatus needs to be addressed with a focus on better particle dispersion.

6.2 Doctor blading of $PrFeO_3$ particles (PFO-A)

As completed for LFO particles synthesised in Chapter 3, these PFO particles can also be fabricated into photoelectrodes to measure their activity for PEC processes. All work contained within Section 6.2 has been conducted by MRes Catalysis student, Sophie Thomas from February to April 2018 under my supervision.

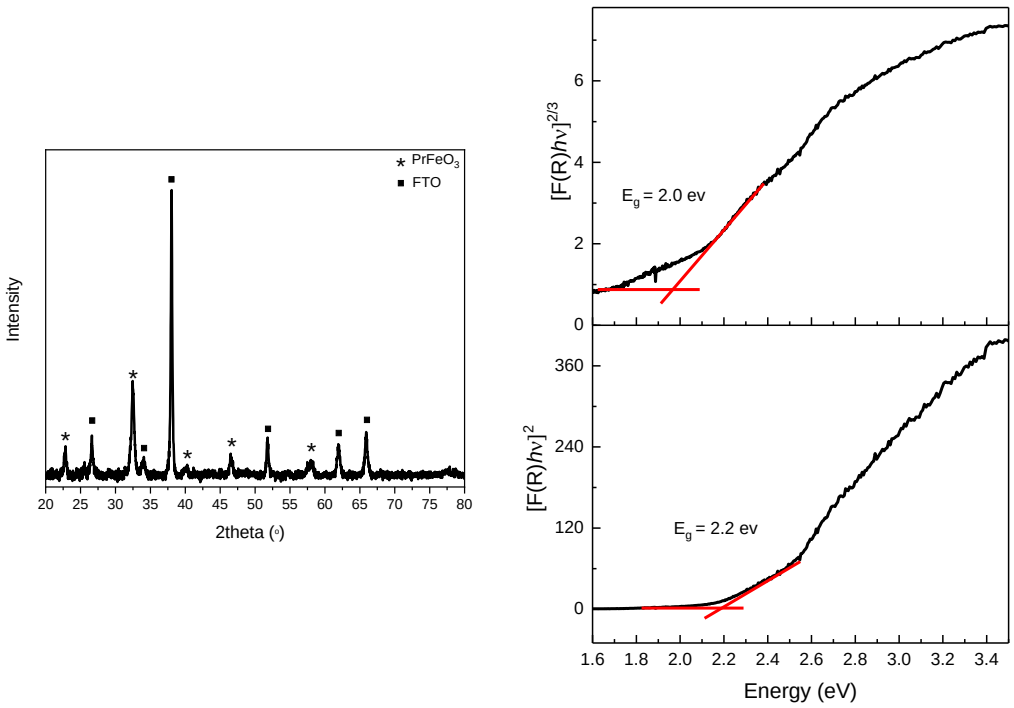

Figure 6-3: XRD spectrum of a PFO-A film prepared by doctor blading (left) and Tauc plots of PFO-A annealed at 600 °C (right).

To fabricate PFO electrodes, PFO particles were deposited onto an FTO-ABS glass substrate using a doctor blading method. Firstly, a solution of $Pr(NO_3)_3.6H_2O$, $Fe(NO_3)_3.9H_2O$, citric acid and deionised water was prepared and left to stir for 72 hours, which was then dried and calcined at 600 °C for 4 hours. This dispersion was then sonicated in ethyl cellulose/EtOH and terpineol solution, and then deposited using doctor blading onto a glass substrate then annealed at 600 °C for 2 hours, these films we named PFO-A (Method 2.15). XRD measurements were obtained, which confirm the presence of phase pure PFO present on the substrate, and UV-Vis measurements revealed a band gap between 2.0-2.2 eV when considering both direct allowed and direct forbidden optical transitions (Figure 6-3). FE-SEM micrographs were obtained to determine the quality of these PFO-A films in terms of coverage on the substrate (Figure 6-4). There seems to be very large areas of exposed FTO on the surface, with very sparsely deposited PFO particles of varying sizes (15 to <5 µm). Hence, it can be seen that a doctor blading method is not able to produce a good quality PFO film, as seen before with LFO films prepared using the same method. It can also be proposed that the contact between the PFO and the FTO due to large particles not in complete contact with the substrate, that could result in poor photocurrent.

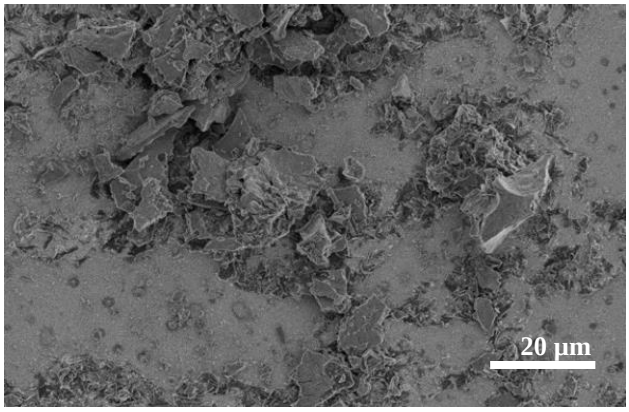

Figure 6-4: FE-SEM micrograph of a PFO-A film annealed at 600 °C prepared through doctor blading.

6.2.1 Photoelectrochemical measurements

PEC measurements were then performed in a 3-electrode system with chopped solar illumination with an applied potential range from +0.2 to -1.12 V_{AgCl}. Very little photocurrent was detected at very negative potential, with a photocurrent density of -1.99 µA cm^{-2} at -0.98 V_{AgCl} on front side illumination was recorded as seen in Figure 6-5. This exceedingly low photocurrent recorded can be explained in part due to the general poor quality of these PFO films. Overall, it appears that doctor blading of PFO particles does not produce high quality films that fail to achieve reasonable levels of cathodic photocurrent. Alternate fabrication methods can be employed to attempt to achieve better quality films, such as that depositing PFO precursors directly onto the FTO-ABS glass substrate as done for LFO photocathodes.

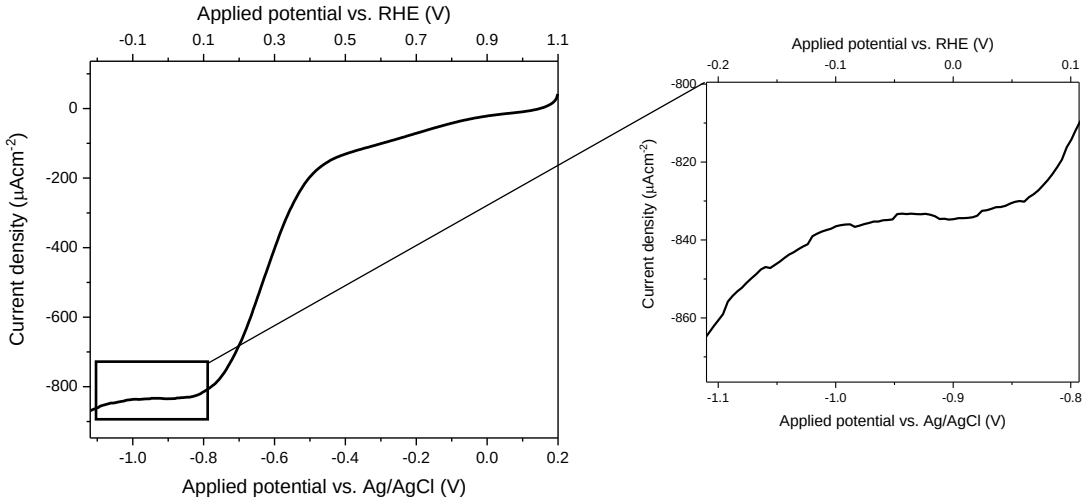

Figure 6-5: Chopped light LSV measurements of PFO-A films prepared through doctor blading and annealed at 600 °C, with a focus on the point of interest.

6.3 Spray pyrolysis of $PrFeO_3$ precursors (PFO-B)

The work outlined in this Section 6.3 was completed by myself.

It has been shown in literature that it can be beneficial to deposit precursors onto a substrate and then using a heating step to form metal oxides directly onto the substrate, which can provide a higher quality contact between the particles and the conductive FTO.[135] Hence, praseodymium nitrate, iron nitrate and citric acid (1:1:4) were dispersed in water then stirred overnight. This solution was then deposited on the substrate using spray pyrolysis, which were then calcined at 500, 600 and 700 °C to form the PFO directly on the substrate (PFO-B). Future work would undoubtedly involve the investigation of using a polymer templating method for PFO film fabrication, that showed to be highly beneficial in the case of LFO photocathodes (Sections 4.4 and 4.5).

Firstly, XRD was performed to confirm whether the formation of PFO directly on the substrate was successful for all calcination temperatures (Figure 6-6). It was found that peaks for phase pure PFO are seen for the XRD spectra of PFO-B_600 °C and PFO-B_700 °C. No PFO peaks are seen for a calcination temperature of 500 °C, which could demonstrate an absence of the formation of PFO on the FTO-ABS, or simply a lack of crystallinity at this temperature. Using the Scherrer equation, the coherent crystal domain sizes were determined for calcination temperatures of 600 and 700 °C to be 25 and 30 nm respectively. Suggesting that a higher calcination temperature can result in increased particle sizes.

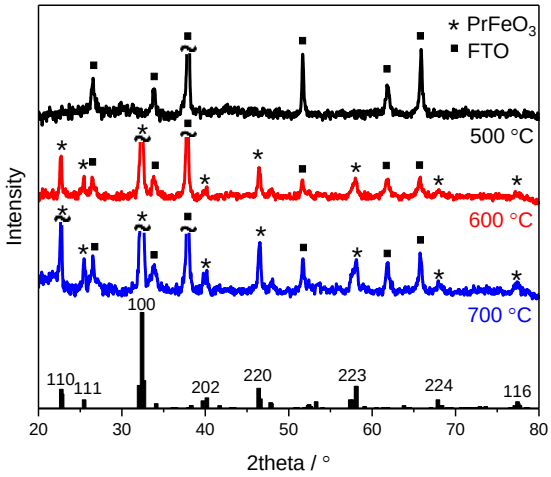

Figure 6-6: XRD spectra for PFO-B films calcined at 500, 600 and 700 °C.

XPS measurements were also completed for PFO_500 °C _600 °C and _700 °C to further confirm the presence of PFO for PFO_600 °C and _700 °C and to establish the presence of PFO for PFO_500 °C, due to the failure of XRD to do so at this temperature (Figure 6-7). Pr 3d, Fe 2p and O 1s. Figure 6-7a and b show binding energies corresponding to Pr $3d_{5/2}$ (932.8 eV), Pr $3d_{3/2}$ (953.4 eV), Fe $2p_{3/2}$ (710.2 eV) with satellite (717.9 eV) and Fe $2p_{1/2}$ (723.9 eV) with satellite (731.7 eV). *is*d corresponds to both crystal lattice oxygen (O_L) and hydroxyl oxygen (O_H). The O_L signal at 529.1 eV can be associated with Pr-O and Fe-O contributions from the PFO crystal lattice. The signal at 531.2 eV can be attributed to hydroxyl groups from chemisorbed water. CasaXPS software was used to determine Pr:Fe atomic ratios of these PFO-B films to be 1:0.7, 1:0.8 and 1:0.7 for PFO films calcined at 500, 600 and 700 °C. This demonstrated a deviation of up to 30 % A-site surface enrichment. It is common to observe A-site surface segregation in perovskite oxide materials, showing a complex

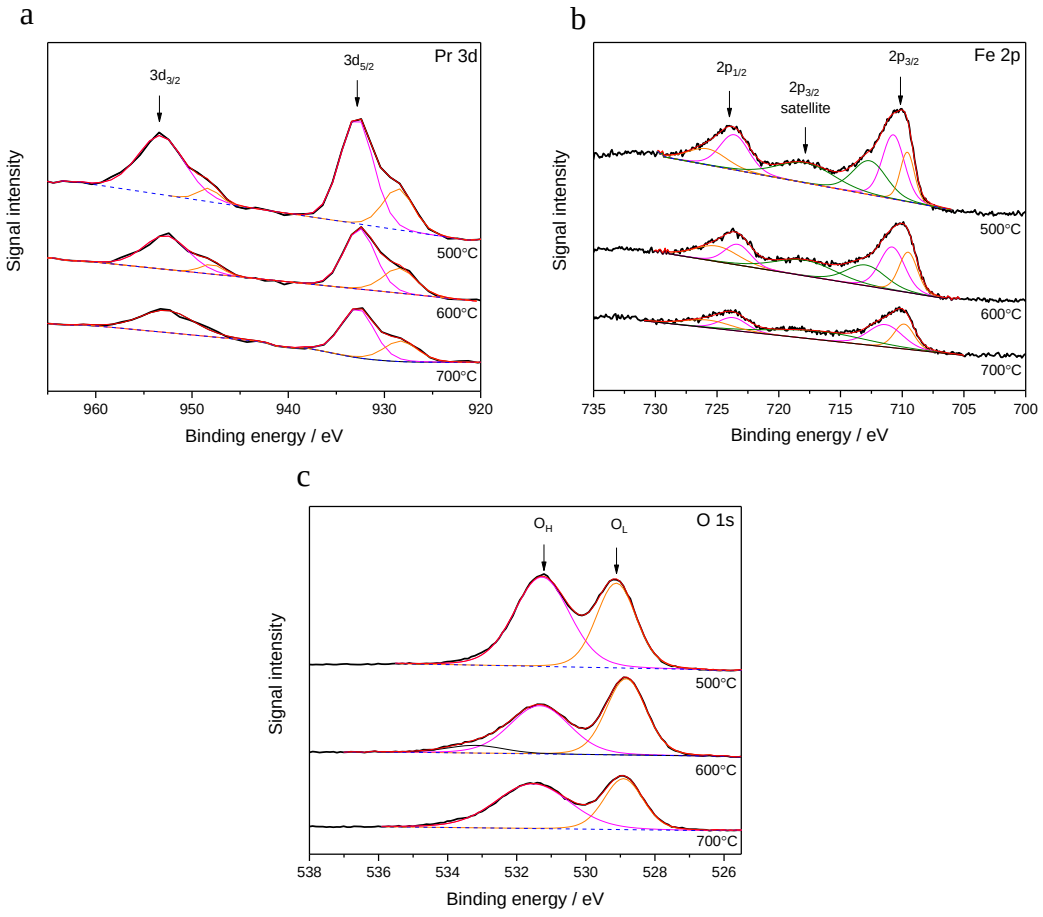

Figure 6-7: XPS spectra for PFO_500, 600 and _700 °C of (a) Pr 3d, (b) Fe 2p, (c) O 1s.

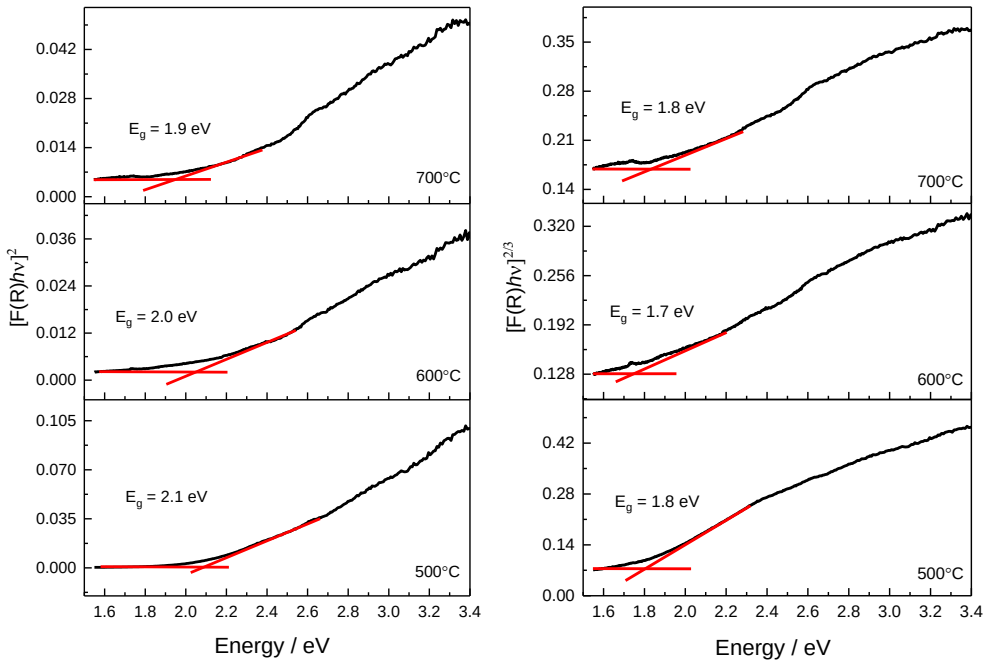

Figure 6-8: Tauc plots for films PFO_500 °C, _600 °C and _700 °C using a direct allowed optical transition (n =1/2) (left) and using a direct forbidden transition (n =3/2) (right).

dependence on the nature of the A and B sites.[74,137,150–152] This demonstrated Pr surface excess can affect charge extraction properties, which was not investigated within this work, and hence could be valuable to consider in future research. To establish energy band gap, Tauc plots were created from UV-Vis measurements of all these films (Figure 6-8). To most accurately determine band gap from Tauc plots, the relevant optical transition is required, but can be ill-defined due to these polycrystalline nanostructured films. Hence, both direct allowed (n = 1/2) and direct forbidden (n = 3/2) transitions were considered due to what is known from DFT calculations.[149] Band gaps were determined to be in the range of 1.7 and 2.1 eV which lie within the visible light region and is consistent to previously reported values.[73]

HR-TEM micrographs were obtained of these PFO powders after calcination at 500, 600 and 700 °C to determine the crystal phases of the calcined $PrFeO_3$ as well as the d-spacing. These powders were obtained from scraping away the PFO powder with a sharp implement from the FTO-ABS substrate from these PFO-B photoelectrodes.

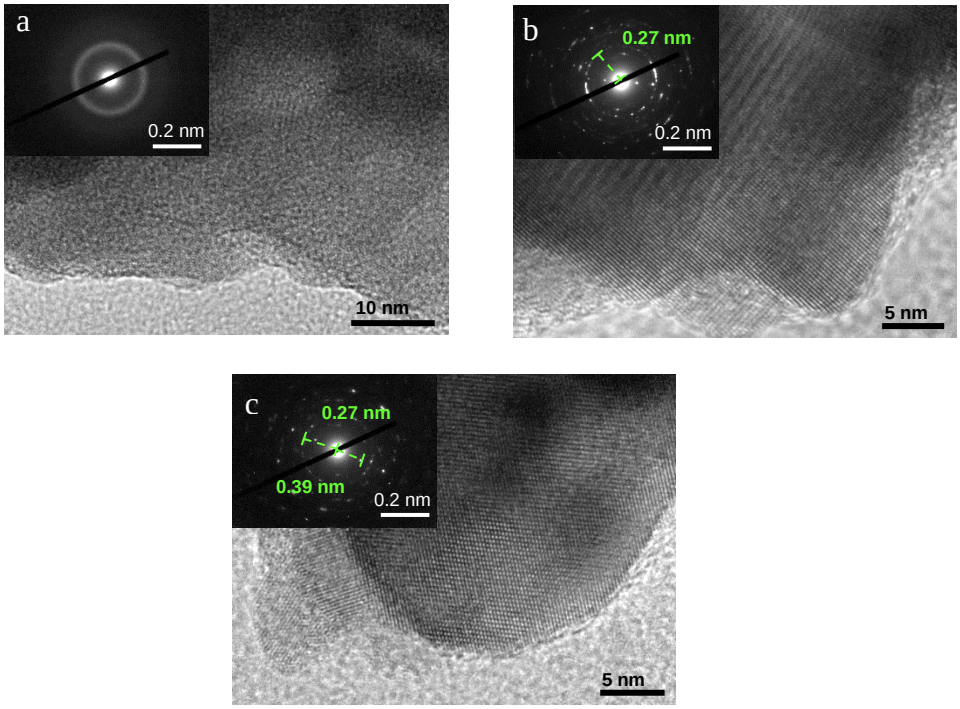

Figure 6-9: HR-TEM micrographs of (a) PFO_500 °C, (b) PFO_600 °C and (c) PFO_700 °C with SAED inserts including d-spacing determination.

Figure 6-9a shows that PFO_500 °C appears more amorphous in nature showing no crystallinity at high magnification, which is in agreement with the surface area diffraction (SAED) pattern (Method 2.26) which did not show any characteristic diffraction circles. This lack of crystallinity is expected due to the absence of any diffraction peaks at this temperature as seen with XRD (Figure 6-6). PFO_600 °C on the other hand, shows a defined lattice structure under HR-TEM as shown in Figure 6-9b, with the accompanying SAED demonstrating a d-spacing of 0.27 nm which corresponds to the (202) plane as determined from XRD using Bragg's law (Equation 22).

$$n\lambda = 2dsin(\theta)$$

Equation 22: Bragg's law for the determination of d-spacing from XRD data.

Where n is the order of reflection (n = 1), λ is the wavelength of x-ray radiation, d is the lattice spacing and θ is the angle of incident radiation.

In addition, PFO_700 °C also displays polycrystallinity with determined d-spacings of 0.27 and 0.39 nm corresponding to the PFO planes (202) and (223) as seen in

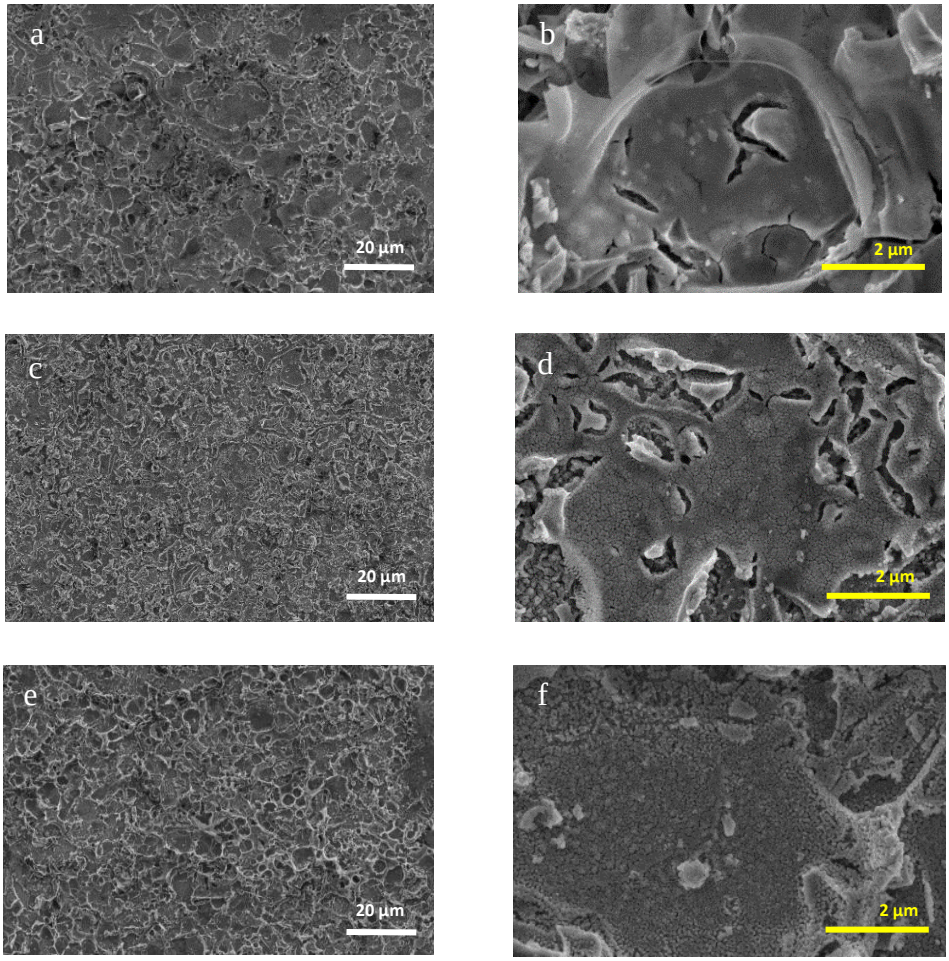

Figure 6-10: FE-SEM micrographs of PFO-B films on FTO-ABS glass prepared through spray pyrolysis (a, b) calcined at 500 °C, (c, d) 600 °C and (e, f) 700 °C.

Figure 6-9c. This in agreement with interplanar distances determined in the literature, which were found to be 0.39, 0.28 and 0.23 nm.[46]

FE-SEM micrographs were obtained of all fabricated PFO films calcined at 500, 600 and 700 °C to determine the extent of film coverage and uniformity as well as establishing if there are any morphology changes between calcination temperatures (Figure 6-10). It appears from all prepared LFO-B films there is good coverage upon the FTO surface with no FTO being visible, even on increasing magnification. In particular for PFO-B_500 °C, there is no exposed FTO visible in Figure 6-10b, suggesting a maximised coverage on the substrate. When considering morphology features, PFO-B_500 °C lacks visible porosity which could be detrimental for PEC processes, through increasing contact between particle and electrolyte. It can also be noted that for PFO-B_500 °C has a distinct cracked appearance with high surface

roughness and limited uniformity (Figure 6-10a and b). When calcination temperature is increased to 600 °C, this cracked appearance of the PFO remains which could be due to organic elements being burnt away during calcination (Figure 6-10c and d). In addition, there is more exposed FTO compared to PFO-B_500 °C. Despite this, there is a notable increase in porosity and decrease in surface roughness, with porosity potentially being advantageous in promoting semiconductor/electrolyte interactions. On increasing calcination temperature to 700 °C, this observed porosity is still present with little exposed FTO (Figure 6-10e and f). In summary, all fabricated PFO films exhibit good levels of surface coverage on the glass substrate, which helps to take advantage of the available substrate surface area. It is also seen that on increasing calcination temperature there is an increased level of porosity, however there is an unfortunate lack of uniformity demonstrated in all cases. This suggests in terms of films quality and PFO morphology, higher calcination temperatures of 600 and 700 °C are preferable.

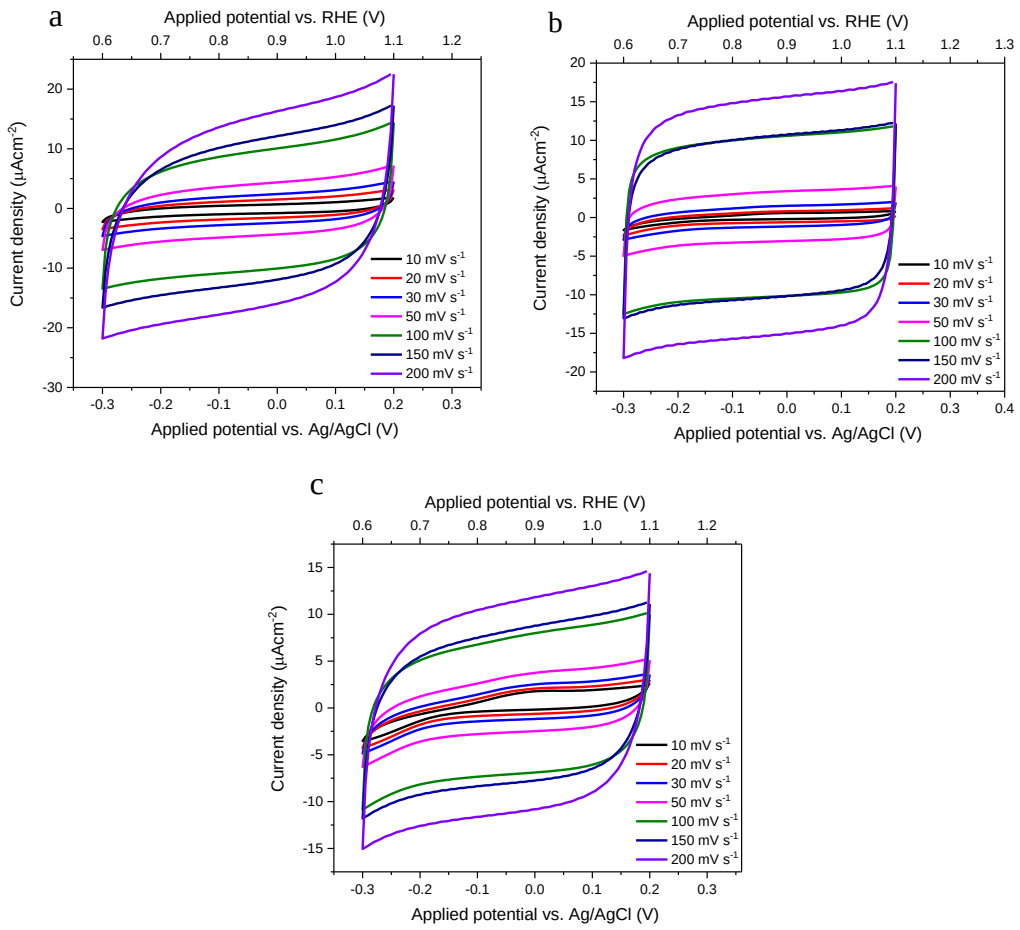

Figure 6-11: CV curves at scan rates between 10 and 200 mV s^{-1} for (a) PFO_500 °C, (b) PFO_600 °C and (c) PFO_700 °C.

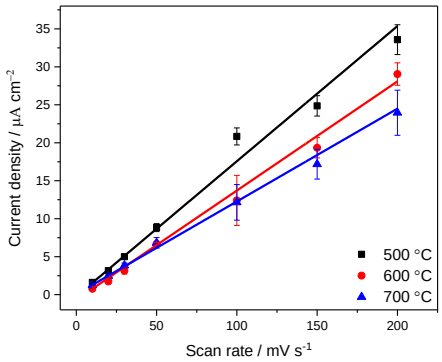

Figure 6-12: Capacitive current density vs. scan rate plots for PFO films to determine ECSA.

To attempt to quantify this change in morphology in terms of surface area when increasing calcination temperature, ECSA measurements were completed for each prepared LFO-B film through conducting CV measurements (Figure 6-11). It can be seen in Figure 6-12 that there are decreases in ECSA on increasing calcination temperature with values of 0.085, 0.072 and 0.058 mF cm^{-2} recorded for 500, 600 and 700 °C respectively. This can be explained due to higher levels of particle sintering on the application of higher temperatures. In general, it would be desirable to have a higher surface area film, in order to create greater contact between the PFO particles and the FTO, as well as with the electrolyte. This also depends on the fact that a higher surface area does not result in increased recombination sites in the PFO material.

6.3.1 Photoelectrochemical measurements

PEC measurements were then obtained to determine achievable photocurrent density for each PFO-B film. Firstly, multiple PFO layers were applied by spray pyrolysis and calcination up to 4 layers for PFO-B_600 °C. It was found that for the application of 1, 2, 3 and 4 calcined PFO layers, photocurrents of -64±9, -113±7, -130±0.6 and -122±5 µA cm^{-2} at -0.48 V_{AgCl} were recorded respectively (Figure 6-13a). This demonstrates that applying 3 calcined PFO layers achieved the highest photocurrent, and hence, 3 layers were applied for films PFO-B_500 °C and PFO-B_700 °C. PFO-B_500 °C achieved a photocurrent of -17±4 µA cm^{-2} and PFO-B_700 °C achieved -101±2 µA cm^{-2} at -0.48 V_{AgCl} for 3 calcined PFO layers (Figure 6-13b and c). PFO-B_600 °C produced the largest photocurrent, with a lower calcination

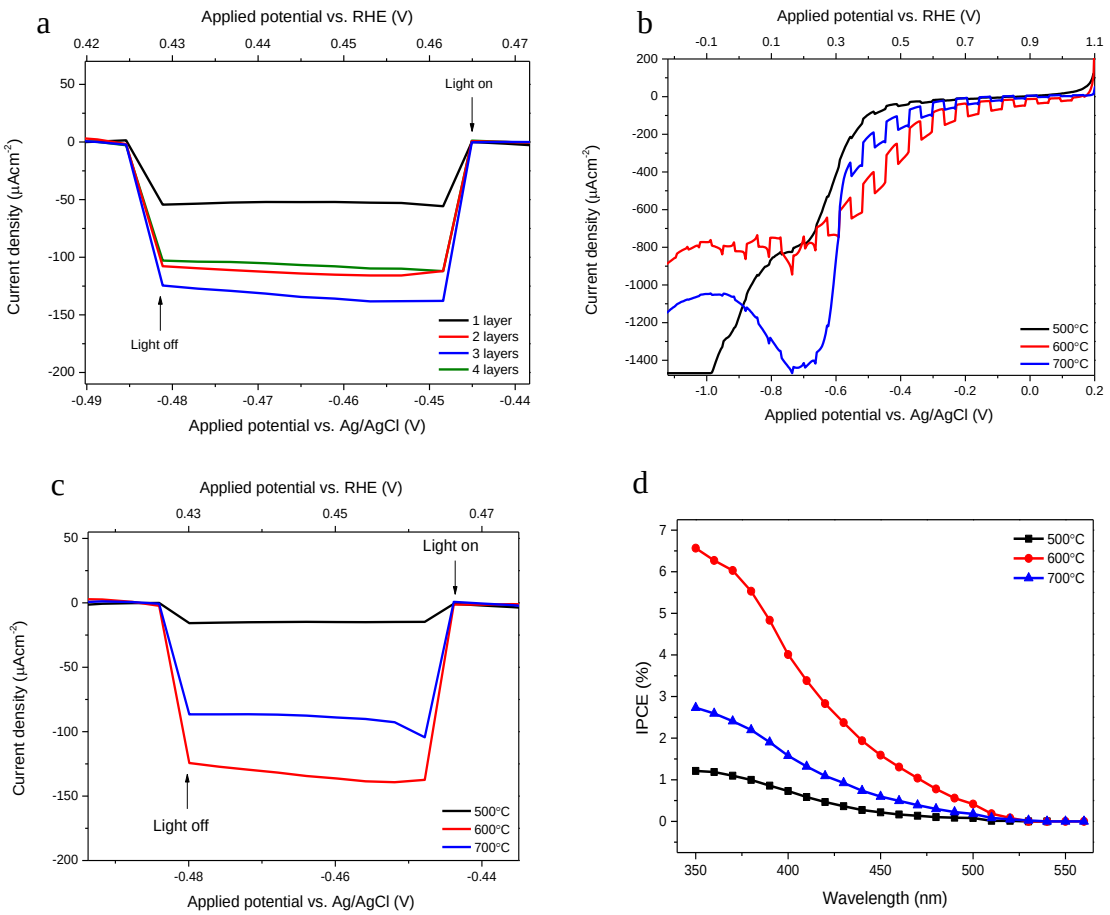

Figure 6-13: (a) Normalised current-potential measurements for multiple applied PFO layers, (b) LSV measurements of PFO-B films calcined at 500, 600 and 700 °C, (c) shown at point of interest and (d) IPCE measurements conducted at -0.3 V_{AgCl}.

temperature of 500 °C providing the poorest activity, further confirming that higher temperatures are beneficial for both film quality and photocurrent. IPCE measurements were also undertaken and demonstrated efficiencies of 1.2, 6.6 and 2.7 % at 350 nm (-0.3 V_{AgCl}) for calcination temperatures of 500, 600 and 700 °C respectively (Figure 6-13d). All of which exhibit relatively low efficiencies which could suggest a poor level of charge separation and transport within these PFO films.

As seen with LFO photocathodes, there could be a competition between the oxygen evolution reaction and hole collection at the back contact, that could also be limiting efficiency and activity.[98,99] Both in terms of achievable photocurrent and IPCE, it can be clearly seen that PFO-B_600 °C is superior to that of PFO-B_500 °C and PFO-B_700 °C, indicating that this is the optimal calcination temperature for these PFO films. Hence, PFO-B_600 °C was tested further to attain its stability when

illuminated under chopped light for a period of 1 hour. It was found that after 1 hour, there was just a 4 % reduction in photocurrent, displaying high levels of stability and thus clarifying the advantages of using perovskite oxides for PEC applications (Figure 6-14). An extended chopped light LSV measurement was obtained for PFO_600 °C, to determine the cathodic photocurrent onset potential, which was determined to be +1.4 V_{RHE} (+0.5 V_{AgCl}) (Figure 6-15). Similarly, to LFO films discussed previously this is a relatively high onset potential which exceeds that of other photocathodes such as Cu_2O, that typically report +0.5 V_{RHE}[41], demonstrating one of the benefits of these ferrite based perovskite oxides.

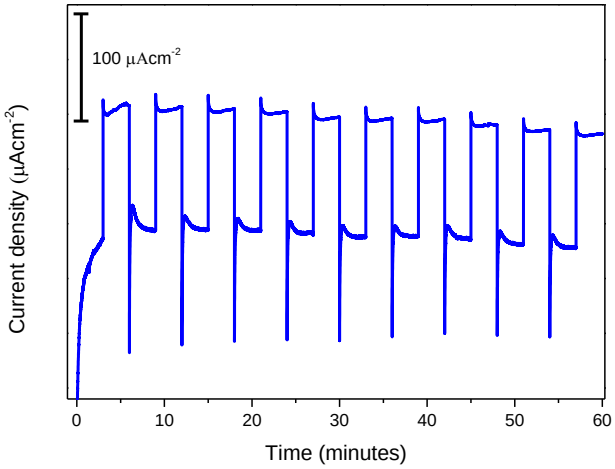

Figure 6-14: PEC stability measurement with chopped solar illumination over 1 hour at a constant potential of -0.48 V_{AgCl} for PFO-B_600 °C.

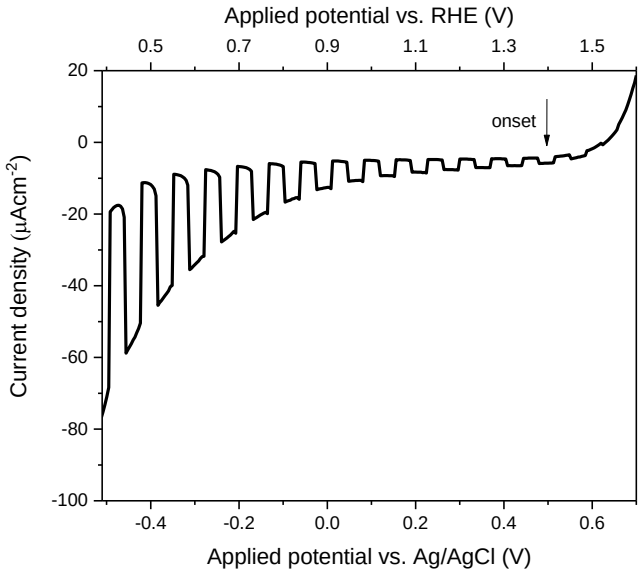

Figure 6-15: Chopped light LSV measurement from -0.5 to 0.7 V_{AgCl} for PFO-B_600 °C to determine cathodic onset potential.

6.3.2 Electrochemical measurements

EIS measurements were completed at -0.3V_{AgCl} in the dark to determine RC limited photocurrent using Equation 19. These were calculated for PFO-B calcined at 500, 600 and 700 °C and compared to experimental photocurrent transients to determine rise time which is indicative of charge separation properties (Method 2.22). Rise times were determined to be 1.25, 0.17 and 0.13 s for PFO-B_500 °C, _600 and _700 °C respectively (Figure 6-16). PFO-B_500 °C displays the slowest rise time of 1.25 s, which suggests a higher probability of electron-hole recombination due to an increased density of trap states. On increasing calcination temperature, faster rise times are achieved, which can indicate faster rates of charge extraction, which is in support of the enhanced photocurrent and IPCE achieved for these films. It can therefore be postulated that at a lower calcination temperature of 500 °C there are more defect

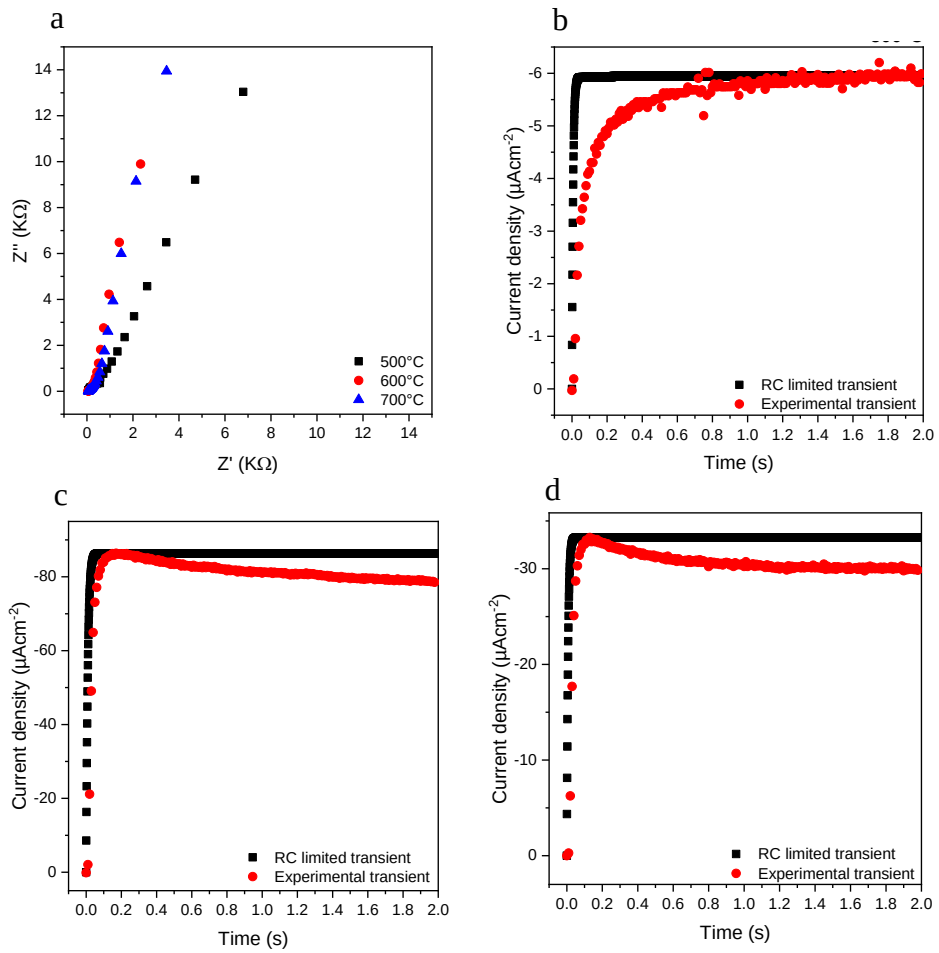

Figure 6-16: (a) EIS measurements used for RC calculations and experimental transient photocurrent compared with calculated RC limited transients for (b) PFO_500 °C (c) PFO_600 °C and (d) PFO_700 °C.

states that allow for an increased density of trap states, which would lead to poor charge separation and increased recombination. However, at higher temperatures (600 °C and 700 °C), the presence of defect states is diminished, resulting in better charge separation and the faster rise times observed.

EIS measurements were also used to construct Mott-Schottky plots of this optimised PFO_600 °C film. Firstly, capacitance was determined for different frequencies of 10, 100 and 1000 Hz using Equation 15 to observe whether this is consistent over a range of applied frequencies. Figure 6-17 shows a dependence of capacitance on frequency suggesting these porous PFO films significantly deviate from ideal capacitor behaviour, hence showing difficulties in extracting well-defined analysis from impedance data. Nevertheless, Mott-Schottky plots were created and confirmed these PFO films were p-type due to the negative slope observed, with a calculated V_{fb} of +1.83±0.19 V_{RHE} using Equation 16. When considering a band gap of 1.7-2.0 eV, as well as this determined V_{fb}, these PFO-B films showed a suitable conduction band edge for PEC water reduction (Figure 6-18). The carrier (hole) density was also calculated to be 1.3×10^{19} 5.4×10^{18} and 5.1×10^{17} cm^{-3} at 10, 100 and 1000 Hz

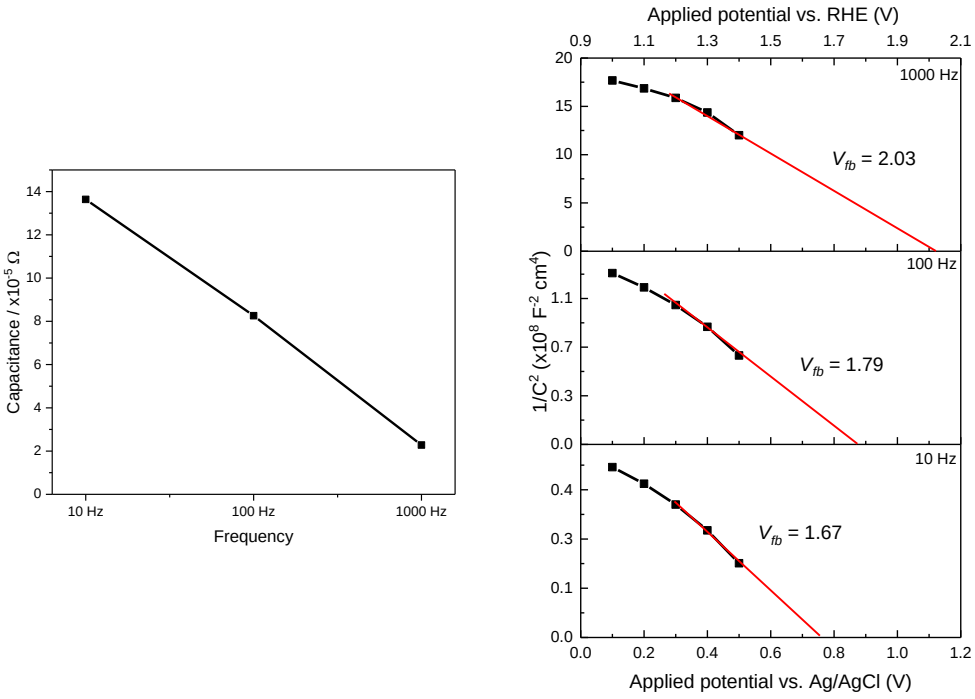

Figure 6-17: Capacitance as a function of frequency obtained from EIS measurements (left) and Mott-Schottky plot conducted at 100 Hz for PFO_600 °C (right).

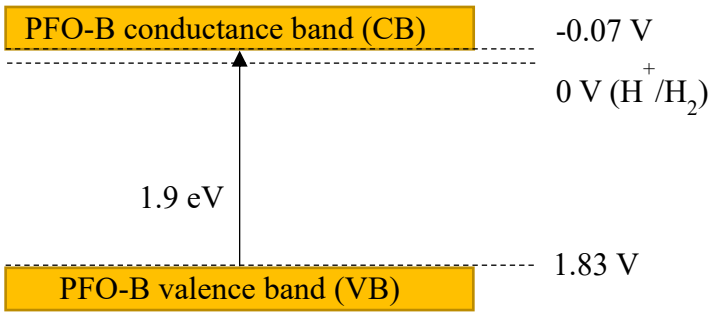

Figure 6-18: Relative band alignment for PFO-B with reference to calculated band gap and flat band potential.

respectively. However, higher levels of caution are needed when extracting information from impedance analysis due to the large and uncertain relative permittivity of ferrites (in this case 10^4)[153] and also with the issues associated with the complex capacitive behaviour of porous films.[134]

6.3.3 Addressing LSV features

As seen before in Chapter 4, there was an appearance of significant negative current below -0.5 V_{AgCl} as seen in Figure 6-13b. This can be attributed to oxygen reduction that can take place on any exposed FTO and potentially on the PFO surface. Oxygen can act as a sacrificial electron acceptor that will act to reduce electron recombination at the PFO surface and hence increase photocurrent. This is clearly problematic as the ORR would be competing with the HER, and so the entirety of the photocurrent cannot be attributed to HER as intended. This effect can be demonstrated by conducting PEC measurements in electrolyte that is exposed to air and when purged with N_2.

Figure 6-19 shows that after purging the electrolyte with N_2, there is a significant reduction in dark current especially below -0.5 V_{AgCl}, suggesting a decrease in the competitive ORR. There is a reduction in photocurrent of -79 % (at -0.48 V_{AgCl}) after purging thus demonstrating the effect of oxygen present. Hence, there are fewer photogenerated electrons available to take part in water reduction than previously suggested with PEC measurements used in electrolyte exposed to air. Further work is needed to increase photocurrent in purged systems to maximise electrons available for water reduction, such as the use of HER co-catalysts. But first it was examined whether despite this reduction in photocurrent in the absence of O_2, whether PEC

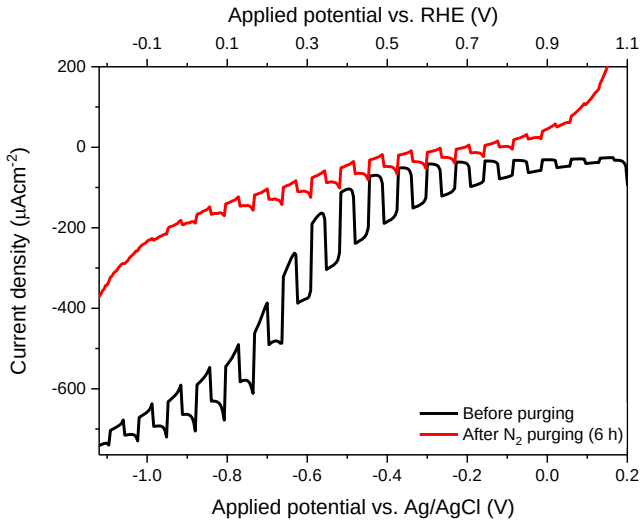

Figure 6-19: PEC measurements for PFO_600 °C in an unpurged (O_2 present) and a N_2 purged system (purged for 6 hours).

water reduction can still occur as demonstrated with LFO photocathodes.

6.3.4 Photoelectrochemical hydrogen evolution

With PEC water reduction as a potential application for these PFO photocathodes, it is important to demonstrate the ability of these films to evolve H_2 from water. This was done using a gas-tight PEC cell with Pt counter electrode and Ag/AgCl reference electrode. The working PFO_600 °C electrode was illuminated with solar light continuously for 6 hours with an applied potential of -0.48 V_{AgCl}. The light was chopped at intervals to establish the location of the dark current, which showed good stability over this time (Figure 6-20). Any H_2 evolved was collected within the headspace of the cell and analysed using GC and re-circulated using a peristaltic pump. The amount of H_2 measured was 0.0139, 0.0209 and 0.0270 µmol at 2, 4 and 6 hours respectively, with an overall rate of H_2 production after 6 hours being calculated to be 0.016 µmol cm^{-2} h^{-1}. Faradaic efficiency was also calculated to be 24 %, 20 % and 17 % for 2, 4 and 6 hours respectively, but a reference for 100 % FE efficiency was not used hence these values are not entirely accurate. This clearly demonstrates the ability of these PFO films to generate hydrogen from solar PEC water reduction, despite low photocurrent generation in the absence of O_2 (Figure 6-19). As discussed previously, HER co-catalysts can be used to direct reduction towards protons rather than oxygen reduction in addition to using a H-shape PEC cell.

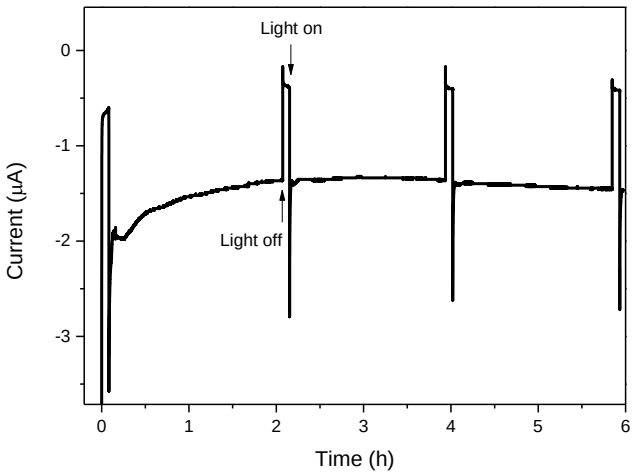

Figure 6-20: Current density measurement from H_2 evolution experiment at a constant potential of -0.48 V_{AgCl} under constant simulated sunlight illumination (100 mW cm^{-2}).

6.4 Conclusions

This Chapter has explored the synthesis of $PrFeO_3$ (PFO) through a facile sol-gel method and its subsequent fabrication into active photocathodes. At time of writing, there are no current demonstrations of PFO photocathodes for PEC processes within literature, hence this is a very valuable and interesting demonstration. Firstly, PFO particles were synthesised and measured for their ability for photochemical H_2 evolution, which showed relatively low evolution rates of 36 μmol h^{-1} g^{-1}. These PFO particles were then prepared into photocathode films using a doctor blading method onto FTO-ABS glass substrates (PFO-A), which showed very minimal cathodic photocurrent of -2 μA cm^{-2} at -0.98 V_{AgCl}. To improve on this, PFO films were prepared through spray pyrolysis of nitrate precursors directly onto the glass substrate followed by calcination at 500, 600 and 700 °C. These PFO-B films achieved an optimised photocurrent of -130 μA cm^{-2} at -0.48 V_{AgCl} for a 600 °C calcination, compared to -17 and -101 μA cm^{-2} for 500 and 700 °C respectively. Highlighting that a calcination temperature of 600 °C was optimal for a maximised photocurrent and displayed a good stability by maintaining 96 % of its original photocurrent after 1 hour of chopped light illumination.

In addition, it was found that on application of higher calcination temperatures there

were greater efficiencies of charge separation and reductions in recombination due to proposed fewer defects/trap states. This was demonstrated through the calculation of rise times in relation to RC time constants, that were recorded as 1.25, 0.17 and 0.13 s for temperatures 500, 600 and 700 °C respectively. This increased rise time at a calcination of 500 °C, eludes to slower rates of charge extraction and hence increased electron-hole recombination. This is in agreement with the lower IPCE of 1.2 %, compared to 6.6 and 2.7 % at 350 nm (-0.3 V_{AgCl}) for 600 and 700 °C. This increase in temperature was also beneficial in terms of film quality, porosity and crystallinity. Moreover, despite the reduction in photocurrent in the absence of O_2, PEC water reduction was possible producing 0.016 μmol cm^{-2} h^{-1} of H_2 over 6 hours. After surveying the literature this is thought to be the first demonstration of PFO photocathodes for PEC processes, hence there is an extensive body of work that can still done to better understand the electronic properties of this material.

Chapter 7

7 Fabrication of metal-insulator-semiconductor junctions

As part of this Thesis, work was completed during a 3-month research placement at the Helmholtz Center Berlin for Materials and Energy (HZB) commencing in May 2019. All research concepts were developed by Dr. Ibrahim Ahmet under the supervision of Prof. Roel Van De Krol, with the work detailed within this Chapter being completed by myself.

7.1 Introduction

An important aspect of any PEC system is that of the interaction at the semiconductor/electrolyte and the semiconductor/metal interfaces. At these interfaces there is inevitable charge transfer creating space charge regions, and with it band bending within the semiconductor occurs. In the case of the semiconductor/metal interface (MS), band bending occurs so that the work function of the semiconductor matches that of the metal co-catalyst. However, in some cases when there is a direct contact between the semiconductor and the metal, metal-induced gap states can form that result in fermi level pinning and reduction in the Schottky barrier height of the MS junction.[154] This occurs due to the energy bands within the semiconductor aligning to these dense surface states, which become pinned to the fermi level. This results in the Schottky barrier height being independent of the metal's work function, which can result in higher levels of surface recombination and lower photovoltages. In addition, this follows that on the addition of metal co-catalysts, lack of improvement in photocurrent will be observed due to this detrimental fermi level pinning.

One such technique to effectively unpin the fermi level is through introducing an insulator layer to form a metal-insulator-semiconductor (MIS) junction. The role of this insulating layer is to be able to create a Schottky contact between the insulator and the high work function metal, that allows the tunnelling of charges from the semiconductor through this passivation layer to the metal on the surface. This can result in the band bending that is required to increase the Schottky barrier and with it photovoltage.[155] High quality insulating layers can be deposited through atomic layer deposition which is a thin film deposition process which involves the exposure of

precursors in alternation onto a substrate to grow a thin film. This is done by first exposing the substrate to the first precursor which reacts in a self-limiting manner until all available surface sites have been used, which is then followed by a vacuum step to remove any unreacted precursors. The substrate is then exposed to the second precursor which reacts with the first on the surface of the substrate which produces the desired material, followed by a vacuum step once more. This is then repeated to grow a film in a very controlled manner where growth rate per cycle can be determined to allow for the growth of a desired thickness of material through controlling the number of growth cycles during deposition.

Al_2O_3 has been used as a successful insulator layer on n-Si for water oxidation. This photoanode consisting of n-Si/SiO_x/Al_2O_3/Pt/Ni (Figure 7-1) demonstrated a high photovoltage (V_{ph} = ~ 500 mV) and stability for solar water splitting when compared to the absence of Al_2O_3. This was achieved using a thin Al_2O_3 layer prepared through atomic layer deposition (ALD) to act to unpin the fermi level of n-Si, whilst using a high work function metal (Pt) and water oxidation catalyst (Ni), which both also contribute to increased stability.[156] Further research from the same group investigated the effects of using different work function metals on the effective barrier height and photovoltage. It was found that there was a strong positive correlation between increasing metal work function and photovoltage, with Pt providing the best results thus highlighting the importance of the choice of metal used.[157] In addition to Al_2O_3, SnO_2 can also be used as an effective insulator layer and has been used previously for photocathodes.[158] Hence, it would be of interest to use SnO_2 to create a novel MIS junction with an active photoanode such as $BiVO_4$. Previous work conducted at HZB focuses on $BiVO_4$ films for solar water oxidation[27,159,160], hence this semiconductor was chosen to be used as part of this proposed MIS junction with SnO_2 and Pt.

The main aims and objectives of this work was to firstly develop and optimise an ALD process to deposit SnO_2 on a home-built system using a tetrakis(dimethylaminno) tin (TDMASn) precursor, with either a water or O_2 plasma oxidiser. Experimental conditions are needed to be considered with this process, such as that of precursor exposure time, deposition temperature and choice of oxidiser. The optimisation of this ALD process can then be completed upon n-Si wafers, and then subsequently

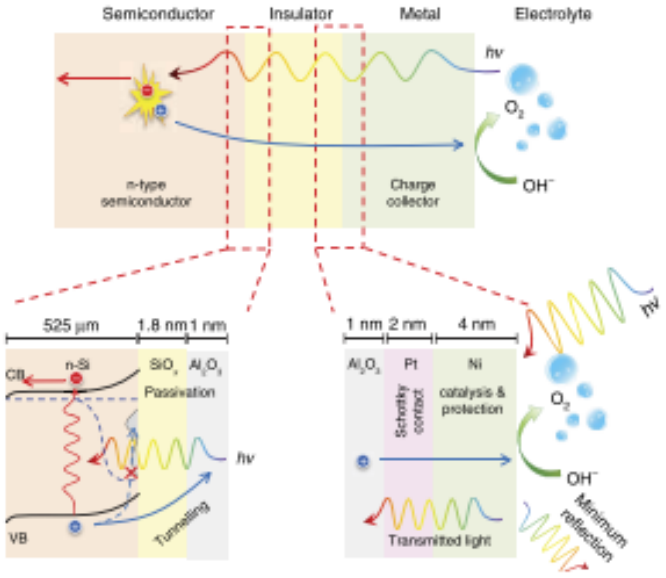

Figure 7-1: Metal-insulator-semiconductor photoanode schematic for arrangement of n-Si/SiO_x/Al_2O_3/Pt/Ni. Reproduced from Ref.[156]

deposited with Pt and Ni by E-beam evaporation. These n-Si/SiO_x/SnO_2/Pt/Ni architectures can then be used to measure whether a successful MIS junction is formed, and what SnO_2 thickness is optimal. This optimised process can then be applied to $BiVO_4$ photoanodes, in attempt to improve photovoltage, photocurrent and most crucially its electrochemical stability.

7.2 Optimisation of ALD process to fabricate SnO_2

Firstly, optimisation of the ALD process for SnO_2 was done to establish whether there can be a successful deposition of SnO_2 onto a substrate and to determine ideal deposition parameters. A home-built ALD system was used with a reactor temperature ranging from 120 to 200 °C, with alternating exposures of tetrakis(dimethylaminno) tin (TDMASn) and water, which has been previously used to grow SnO_2 by ALD (Method 2.17).[130] Firstly, growth rate per cycle (GPC) was calculated in order to determine the number of cycles required to achieve a desired film thickness. The ångström resolution film thicknesses were determined by *in situ* real-time spectroscopic ellipsometry (RTSE) (J.A. Woollam Co. Inc., M-2000X, 210–1000 nm) directly attached to the ALD reactor. The windows (fused silica) in the optical path were partially protected by a nitrogen flow (99.9999%). The thickness of the native

oxide on the Si wafers were fitted to a model prior to each deposition, following the approach described by Herzinger et al.[133] and consecutive data were fitted to a model for the growth of SnO_2 on a Si wafer with a 0.15 nm native SiO_x and ~1 nm Al_2O_3 seed layer. The growth per cycle (GPC) was calculated by dividing the SnO_2 film thickness by the number of ALD cycles. GPC can be affected by alternating exposure time of precursors, deposition temperature and the type of precursors used. All of which were investigated with an n-type silicon substrate.

The effect of TDMASn exposure time was first investigated to examine the influence on the growth rate of SnO_2. For all n-Si films, an initial layer of Al_2O_3 was deposited using ALD with alternating exposures of trimethyl aluminium (TMA) and H_2O for 10 cycles (1 nm) onto a n-Si wafer. This was done to produce a highly chemically uniform surface to promote nucleation of the subsequent growth of SnO_2 (actual architecture: n-Si/SiO_x/Al_2O_3/SnO_2). Firstly, different TDMASn exposure times of 0.25, 0.5, 1, 2, 4, 8, and 10 s with 30 cycles each were completed onto the same n-Si wafer. The exposure time of H_2O was kept constant at 0.5 s with a reactor temperature of 170 °C. In situ ellipsometry was used to determine film thickness. Figure 7-2 shows film thickness against time for changes in TDMASn exposure time. There are 2 data points per cycle, giving a characteristic zig-zag appearance in the data shown, this is due to the initial measurement being taken after the first exposure resulting in an increased thickness, and the second measurement being taken after vacuum and purging

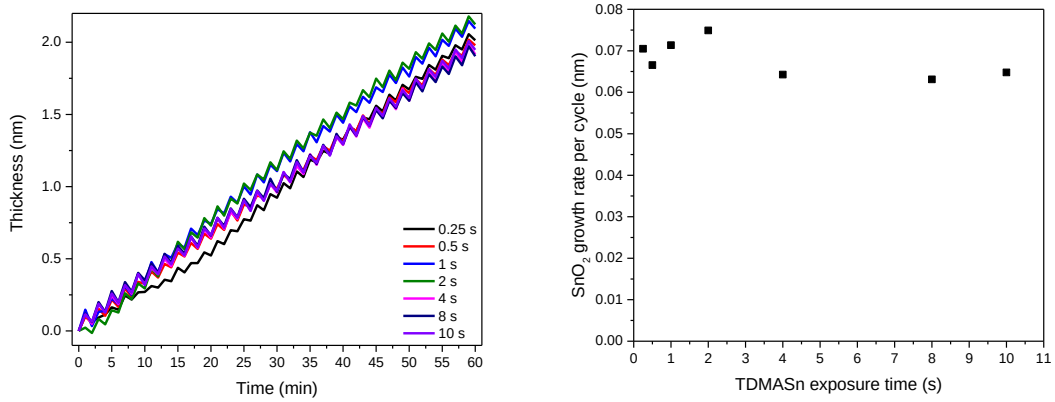

Figure 7-2: Fitted in situ ellipsometry data determining film thickness at every ALD half cycle. Measurements used for investigating the impact of TDMASn exposure times(left) and summary of calculated GPC values (right).

resulting in a lower thickness, hence this observed oscillation. The gradient of these data points can then be used to establish the GPC. There is little fluctuation in GPC between different exposure times, with values of 0.071, 0.067, 0.071, 0.075, 0.064, 0.063, 0.065 nm for 0.25, 0.5, 1, 2, 4, 8, and 10 s respectively. However, it was recommended to avoid higher exposure times as this can result in the boiling of the precursor within the bubbler that can cause damage to the inlet. Hence, it was decided to complete further depositions with a 1 s TDMASn exposure time.

Next, an investigation into the effects of changing the H_2O exposure time on GPC was completed. The exposure time of TDMASn was kept constant at 1 s, with a deposition temperature of 170 °C. Exposure times of 0.1, 0.25, 0.5 and 1 s of H_2O were used, with GPC values of 0.058, 0.050, 0.048, 0.046 nm respectively being achieved (Figure 7-3). Similarly, to alternating TDMASn exposure times, relatively little variation in GPC is seen, hence there wouldn't be any significant changes in the total time needed for deposition. Due to this, all further depositions used an exposure time of 0.5 s for H_2O. It is also vital when exploring ALD experimental parameters to establish the ALD window, which is the temperature range where successful ALD occurs.

To determine the location of the ALD window a range of deposition temperatures were investigated. Exposure times of TDMASn and H_2O of 1 and 0.5 s were used respectively. Deposition temperatures of 120, 140, 155, 170, 185 and 200 °C were used with the deposition of 30 cycles of SnO_2 for each temperature on the same n-Si

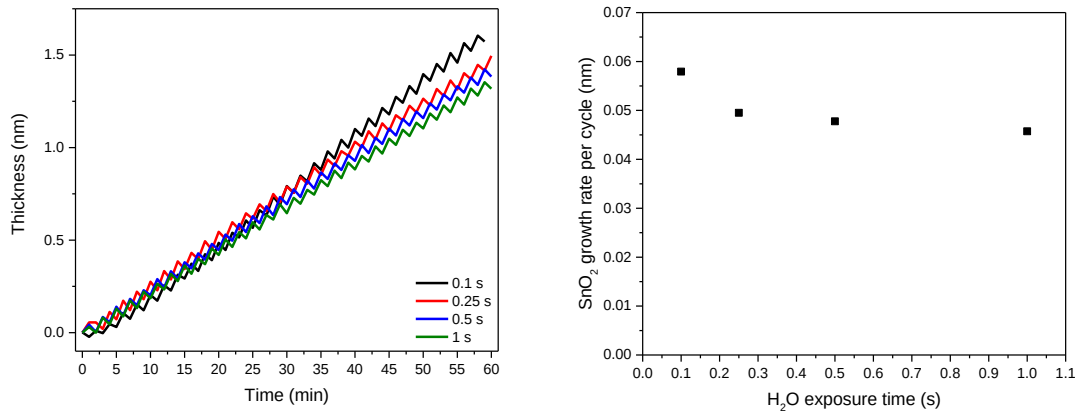

Figure 7-3: Fitted in situ ellipsometry data determining film thickness at every ALD half cycle. Measurements for investigating the impact of H_2O exposure times (left) and summary of calculated GPC values (right).

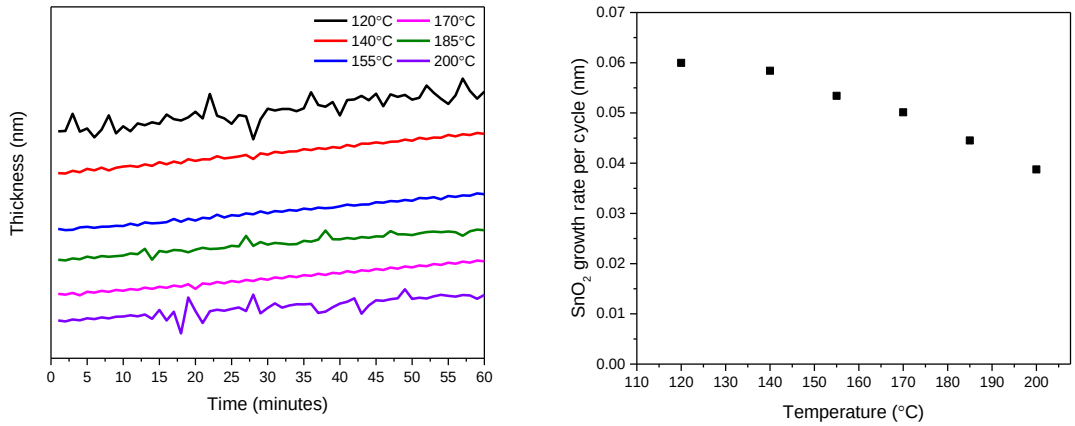

Figure 7-4: Fitted in situ ellipsometry data determining film thickness at every ALD half cycle. Measurements for investigating the impact of reactor temperature (left) and summary of calculated GPC values (right).

wafer. It can be seen in Figure 7-4, many of the ellipsometry data gradients do not display a well-ordered characteristic ALD growth pattern, with numerous anomalous data points. This could be due difficulties in the fitting of the ellipsometry measurements on increasing film thickness for each subsequent change in temperature. Nevertheless, linear fits were calculated to determine the GPC for each temperature. GPC values of 0.060, 0.058, 0.053, 0.050, 0.045 and 0.039 nm were found for temperatures 120, 140, 155, 170, 185 and 200 °C respectively. At lower temperatures there is a slight increase in GPC which can be explained by potential condensation of the precursor within the reactor, resulting in lower control of deposition with reduces ALD character. At higher temperatures of 185 and 200 °C, there is a decrease in GPC that can be attributed desorption of precursors on the substrate surface. It can be postulated therefore that the ALD window for this SnO_2 deposition lies between 150 and 170 °C, however due to the inconsistent appearance of the ellipsometry measurements a more confident determination of the ALD window cannot be made. An additional parameter that can be explored in relation to ALD is the oxygen source. H_2O has been used thus far, but can be substituted for O_2 plasma, which is able to provide higher levels of reactivity.

O_2 plasma can be incorporated into the ALD process for SnO_2, to allow for the oxidation of precursors. Different deposition temperatures of 100, 150, 170 and

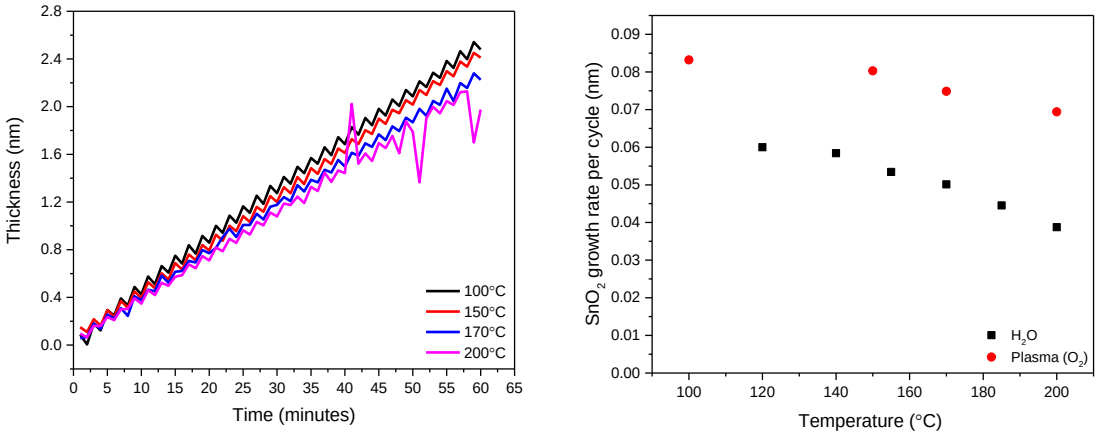

Figure 7-5: Fitted in situ ellipsometry data determining film thickness at every ALD half cycle. Measurements for investigating the impact of reactor temperature for a plasma process (left) and summary of calculated GPC values for different temperatures for H_2O and plasma ALD processes (right).

200 °C were investigated for this plasma method. Figure 7-5 shows that using a plasma O_2 source demonstrates higher GPC values when comparing to the use of H_2O. At a deposition temperature of 170 °C, a H_2O precursor achieved a GPC of 0.050 nm whereas O_2 plasma achieved a GPC of 0.075 nm. With temperatures 100, 150 and 200 °C achieving GPC values of 0.083, 0.080 and 0.069 nm respectively. Some anomalies are present in these GPC trends collected for 200 °C that could be explained due to high film thickness at this measurement. This increased GPC across a range of temperatures can be attributed to the increased reactivity of using plasma as an oxidation source. Similarly, to that reported in previous the section, at lower temperatures there is increased GPC perhaps due to condensation, and a decrease in GPC at higher temperatures due to desorption. It appears at first glance that there will be time saved when utilising this plasma method due to faster growth rates, however each cycle of plasma deposition takes longer to complete. Hence, when calculating the growth rate in terms of nm/min, the H_2O method achieves 0.030 nm/min and the and the plasma method achieves 0.028 nm/min, hence any justification in choosing an O_2 plasma method over H_2O, would have to arise from parameters other than higher GPC. After this optimisation of ALD process, characterisation is required to establish whether SnO_2 was successfully deposited, which can be done through XPS.

7.3 X-ray photoelectron spectroscopy to confirm presence of SnO_2

To confirm the presence of SnO_2 on the n-Si substrate, XPS measurements were completed. Firstly, XPS measurements were undertaken where the n-Si/SiO_x/Al_2O_3/SnO_2 (A) film remained under vacuum, to avoid any exposure to air. In which the (A) denotes the use of the H_2O ALD process and (B) representing a plasma method. This was done by transferring the film directly from the ALD reactor chamber into to the XPS chamber for measurement, whilst remaining under vacuum. Figure 7-6a and b display the XPS spectra obtained for this n-Si/SiO_x/Al_2O_3/SnO_2 (A) film. It can be seen from the Sn 3d spectrum in Figure 7-6a that peaks present at 495.7 and 487.3 eV can be attributed to Sn $3d_{3/2}$ and Sn $3d_{5/2}$ respectively. There is no characteristic shoulder present at approximately 486 eV for Sn $3d_{5/2}$ that would

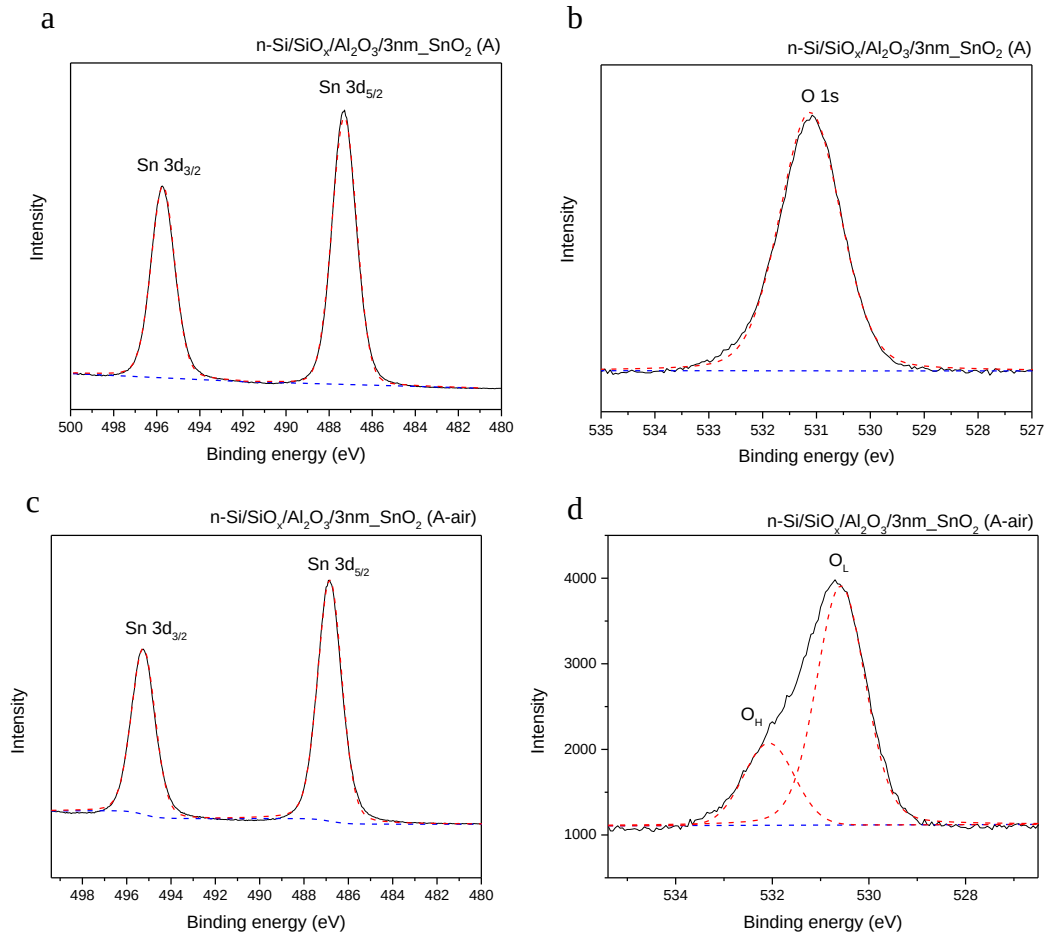

Figure 7-6: XPS measurements of (a, b) n-Si/SiOx/3nm_SnO_2 for a SnO_2 ALD method using H_2O as a precursor when it has not been exposed to air and (b, c) when it has been exposed to air.

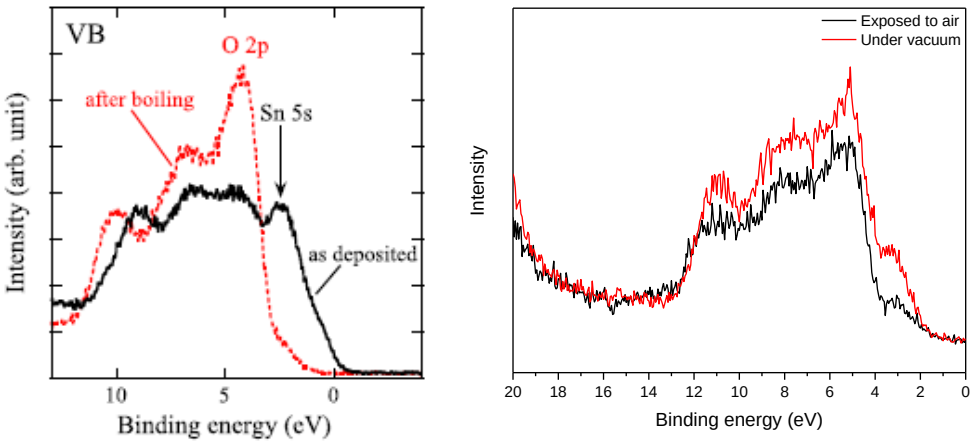

Figure 7-7: XPS valence band measurements for SnO ('as deposited') and SnO_2 ('after boiling') taken from literature[102] (left) and XPS valence measurements for SnO_2 prepared by ALD with a H_2O precursor.

indicate any Sn^{2+} present, hence the fitting can be entirely attributed to Sn^{4+}. This is consistent with SnO_2 being present as opposed to SnO, suggesting that this ALD method is able to successfully prepare pure SnO_2 as required. The O 1s spectrum in Figure 7-6b contains a peak consistent with the presence of bound O at 531.1 eV, further suggesting SnO_2 present. The same XPS measurements were then carried out with these n-Si/SiO_x/Al_2O_3/SnO_2 (A-air) films (Figure 7-6c and d) where they had been exposed to air over a period of a week after deposition. In this case, it is also seen that there is no shoulder peak within the Sn 3d spectrum, suggesting that SnO_2 is still present even after exposure to air. Within the O 1s spectrum there is the appearance of a shoulder at 532.1 eV corresponding to O_H due to chemisorbed hydroxyl oxygen species, which is expected due to the opportunity of water being present from exposure to air.

To further confirm the oxidation state of the Sn present, the XPS valence band spectrum was obtained for each of the vacuum and air exposure conditions (Figure 7-7). These spectra can then be compared to that of SnO_2 and SnO to determine which is present. Both VB spectra for vacuum and air conditions strongly resemble the VB spectrum of SnO_2 as reported within the literature[161]. If Sn^{4+} is present there is a peak at approximately 2 eV attributed to the Sn 5s orbital, whilst if there is Sn^{2+} present then there is a peak at approximately 5.1 eV corresponding to O 2p orbitals. It can be

also seen that when preparing SnO_2 through a H_2O process, there is the appearance of a shoulder at 3.2 eV, that can be explained due to Sn-OH binding. Ultraviolet photoelectron spectroscopy (UPS) measurements were also done to establish energy band alignments for these prepared films (Figure 7-8). UPS works on the same principles as XPS, in that radiation within the Ultraviolet region (10-400 nm) is fired at a sample that causes the ejection of an electron within the sample where in which

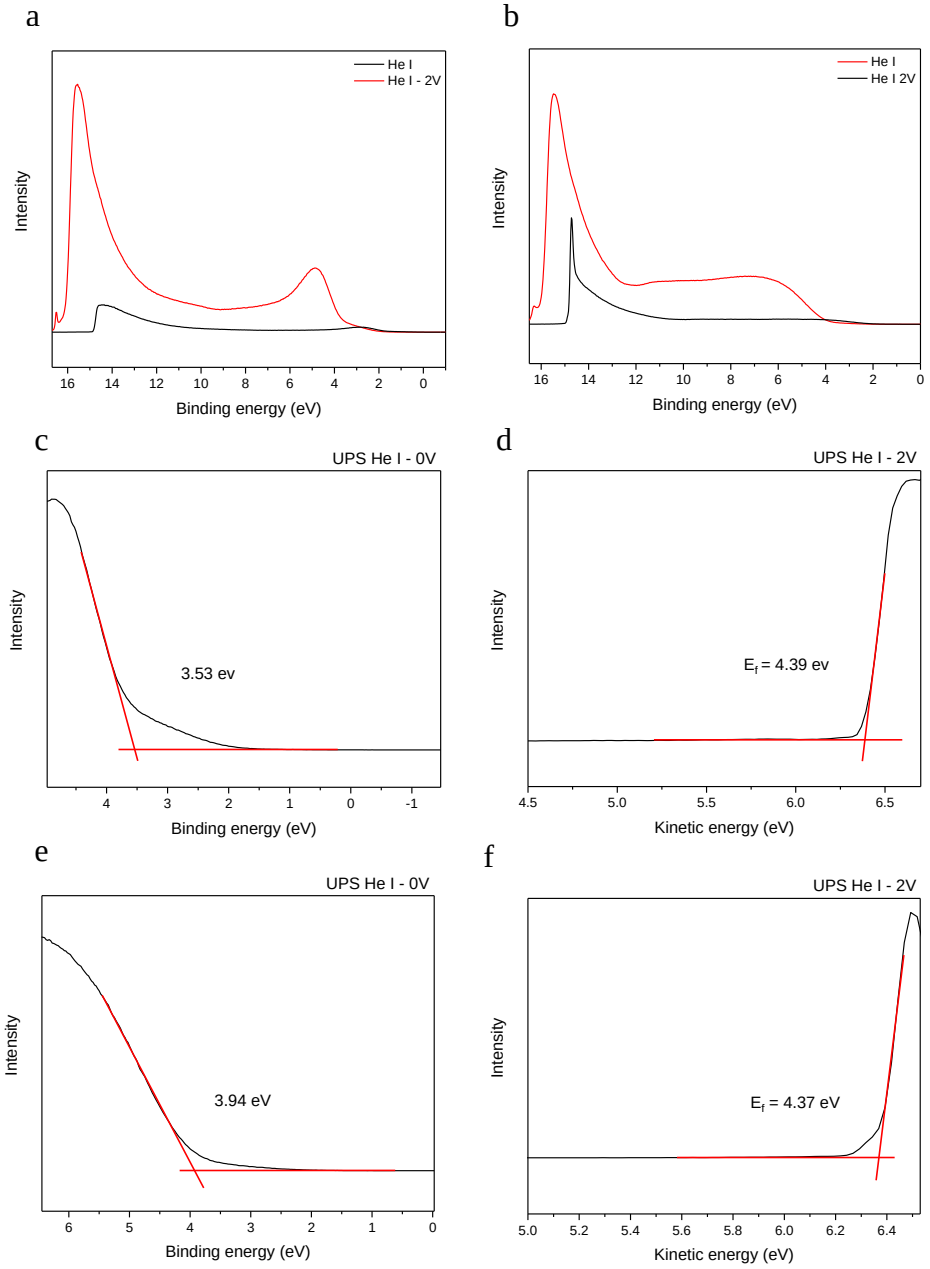

Figure 7-8: UPS measurements of n-Si/SiOx/Al_2O_3/SnO_2 (A) with 0 V applied and 2 V applied for energy band calculations for (a, c and d) vacuum and (b, e and f) air conditions.

the kinetic energy of the electron is measured and related to binding energy by Equation 13. Because UV radiation is of lower energy than X-ray radiation this technique allows for the measurements of lower energy valence band electrons and so properties such as fermi level position and difference in the valance band level and the fermi level can be determined using this technique. The fermi level can then be determined through extrapolating the measurement at the low kinetic energy region and taking away the applied 2 V (vacuum scale). The energy gap between the fermi level and the valence band can be also determined from extrapolating from the UPS spectrum at 0 V at low binding energy. This resulted in fermi levels for the vacuum and air conditions of 4.39 eV and 4.37 eV respectively, and for the energy gaps between the VB and the fermi level are 3.53 and 3.94 eV for vacuum and water exposure respectively (Figure 7-8).

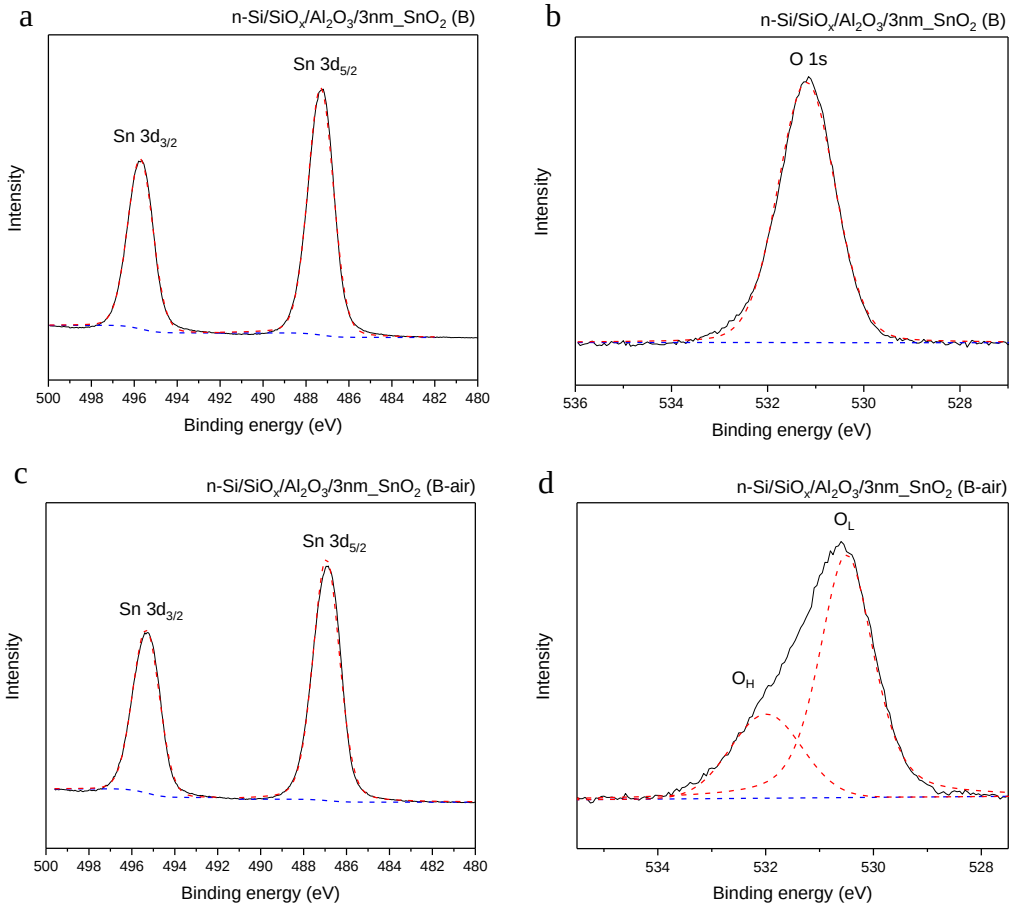

Figure 7-9: XPS measurements of n-Si/SiOx/3nm_SnO_2 for a SnO_2 ALD method using H_2O as a precursor when it has remained (a, b) in vacuum and (c, d) when it has been exposed to air.

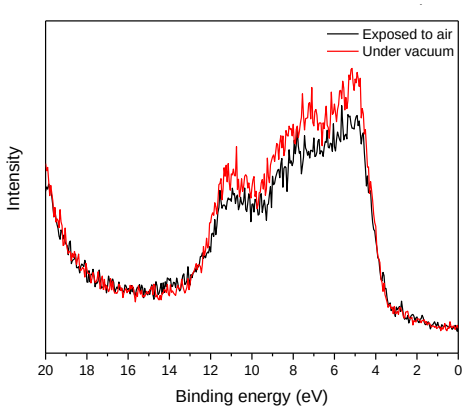

Figure 7-10: XPS valence band measurement of ALD prepared SnO_2 using a plasma precursor.

XPS measurements were also carried out for SnO_2 prepared using a O_2 plasma process. After measuring n-Si/SiO_x/Al_2O_3/SnO_2 (B) under vacuum it can be seen again that there are peaks within the Sn 3d spectra that correspond to Sn $3d_{3/2}$ and Sn $3d_{5/2}$ (495.7 and 487.3 respectively). There is no appearance of a shoulder around 486 eV, suggesting that the contribution to this peak is from Sn^{2+} entirely. As expected, when these films were exposed to air there is the appearance of an O_H attributed shoulder within the O 1s spectrum at 532 eV (Figure 7-9). XPS VB spectra additionally confirms the presence of SnO_2 due to the absence of a characteristic Sn 5s peak at 2 eV, hence it can be claimed that when using O_2 plasma in the ALD deposition of SnO_2 was successful in creating pure SnO_2 (). UPS studies allowed for the calculation of the fermi level to be 4.71 and 4.30 eV for the vacuum and exposure to air conditions respectively. With the position of the E_{VB} at 3.24 and 3.46 eV below the fermi level (Figure 7-11).

Using the UPS measurements obtained and assuming a band gap of 3.9 eV for SnO_2, the band positions can be determined for all of the above prepared films (Figure 7-12). All of which have their band gap incorporating the water oxidation potential which is expected for n-Si. With A-air referring to the use of a H_2O precursor with the sample being exposed to air and B-vac referring to the use of a plasma (O_2) process that has remained under vacuum. Small variations are found between these calculated band diagrams with an anomalous reading for n-Si/SiO_x/Al_2O_3/SnO_2 (A-air), due to the fermi level laying at lower energy than the conductance band (E_{CB}), this could be due to discrepancies of measuring the energy band positions using UPS.

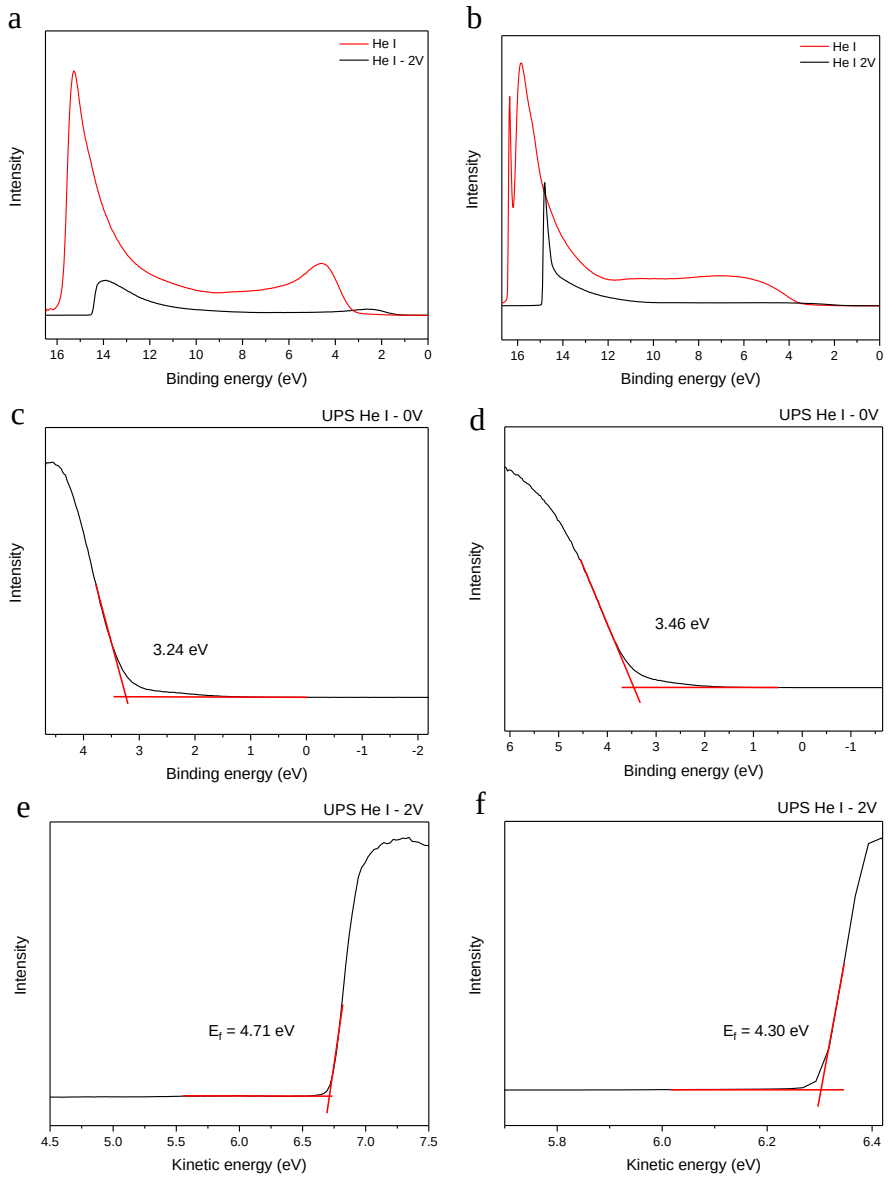

Figure 7-11: UPS measurements of n-Si/SiOx/Al_2O_3/SnO_2 (B) with 0 and 2 V applied for energy band calculations for (a, c and e) vacuum and (b, d and f) air conditions.

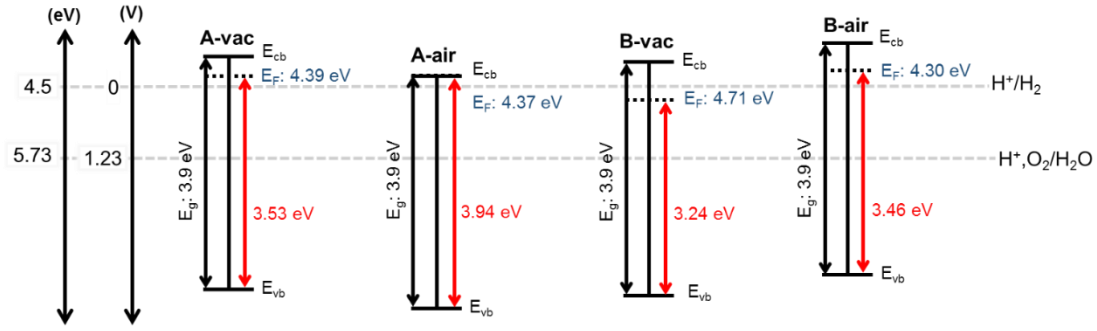

Figure 7-12: UPS calculated band alignments for SnO_2 prepared using ALD with H_2O and plasma (O_2) precursors, when kept under vacuum and when exposed to air.

7.4 n-Si films with a SnO_2 insulating layer

Literature has previously shown Al_2O_3 being used successfully as an insulating layer for water oxidation applications[156]. After being shown that SnO_2 was successfully deposited onto n-Si using an optimised ALD process, these films can then be measured for their PEC activity. The addition of Pt and Ni catalysts was done to demonstrate whether the SnO_2 could successfully form an insulating layer between Si and Pt/Ni to effectively allow for unpinning of the fermi level. Electron beam evaporation was used to sputter 4 nm Pt and 4 nm Ni for both catalysis and protection (Method 2.35). A range of different layer configurations were then measured, n-Si, n-Si/Pt/Ni, n-Si/SnO_2 and n-Si/SnO_2/Pt/Ni to investigate the effects of incorporating this insulating layer of different thicknesses.

7.4.1 Photoelectrochemical measurements

Firstly, n-Si was measured for its PEC activity using chopped simulated sunlight in a 3-electrode system with a Ag/AgCl reference and Pt counter electrode, in a 1 M KPi electrolyte with a 0.5 M Na_2SO_4 hole scavenger (HS) (pH 7) (Method 2.18). A reduced photocurrent was observed after 2 cycles was completed, decreasing from +0.013 mA cm^{-2} to +0.008 mA cm^{-2} at +2.13 V_{RHE} due to inherent instability of Si. No activity could be measured at the water oxidation potential of +1.23 V_{RHE} (Figure 7-13a). Large anodic spikes on light illumination are also observed which is indicative of high levels of electron-hole recombination, supporting the requirement for a protection layer. In order to provide a reference to subsequent addition of an insulating

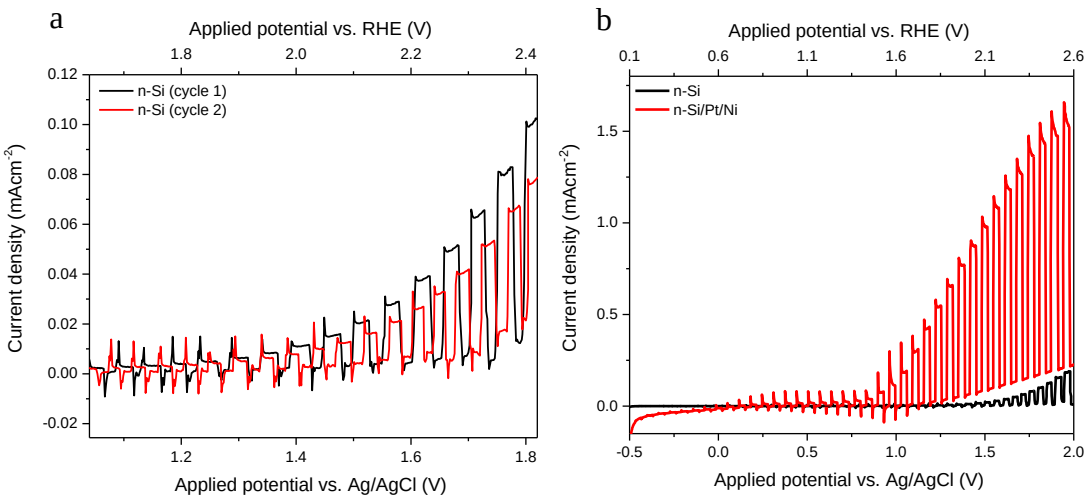

Figure 7-13: Chopped light LSV measurements for (a) n-Si after repeated cycles and (b) comparison between n-Si and n-Si/Pt/Ni.

layer, consecutive 4 nm Pt and Ni layers were deposited by electron beam evaporation onto the n-Si surface, where the thickness was monitored with a calibrate quartz microbalance. Figure 7-13b shows that there is an increase in photocurrent density on the addition of these co-catalysts that can both assist in charge separation and to act as protection layers, with an increase from 0 to +0.014 mA cm^{-2} at +1.23 V_{RHE} being found (0.01 to 0.89 mA cm^{-2} at +2.13 V_{RHE}). A 3 nm SnO_2 layer was then deposited using an ALD plasma process with a TDMASn precursor. In addition to this, 4 nm Pt and 4 nm Ni were then deposited using E-beam evaporation, resulting in an architecture of n-Si/Al_2O_3/3nm_SnO_2/Pt/Ni.

Figure 7-14 shows an increase in photocurrent on the application of this insulating SnO_2 layer. Photocurrent density at +1.23 V_{RHE} increased from +0.01 to +0.11 mA cm^{-2} and at +2.13 V_{RHE} it increased from +0.89 to +4.72 mA cm^{-2}. This enhancement in activity can be attributed to the creation of the intended MIS junction, which has enabled shuttling of electrons to the high work function Pt metal, without the detrimental formation of an ohmic contact caused when n-Si is in direct contact with Pt. In order to optimise this SnO_2 layer, a range of different thicknesses were deposited by ALD.

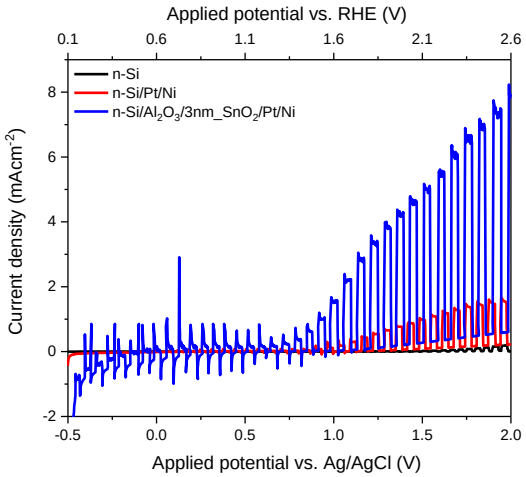

Figure 7-14: Chopped light LSV measurements of bare n-Si and the addition of a 3 nm SnO_2 layer with Pt and Ni.

The thickness of the SnO_2 was increased to 5 nm with Pt/Ni also deposited. This was then compared to n-Si/Pt/Ni. As discussed previously, n-Si/Pt/Ni achieves just +0.014 mA cm^{-2} at +1.23 V_{RHE}, which on the application of 5 nm SnO_2 increases to +0.18 mA cm^{-2} at +1.23 V_{RHE} and +17.7 mA cm^{-2} at +2.13 V_{RHE} (Figure 7-15a). In comparison, applying a 3 nm SnO_2 achieved a photocurrent density of +4.7 mA cm^{-2}, demonstrating that increasing the thickness of SnO_2 is beneficial for activity. This could be due to a thicker SnO_2 layer ensuring that there is full coverage on the n-Si substrate, to achieve the lack of intended direct contact between n-Si and the metals. Additionally, it could be attributed to an increased thickness of SnO_2 improving stability through acting as a protection layer for the n-Si wafer. In any case, a successful MIS junction seems to have been created and allowed for large increases in photocurrent. Measurements were also conducted in 0.1 M KOH (pH 13) which is beneficial for Ni led catalysis, which resulted in a decrease in photocurrent with a comparable on-set potential, which could be due to instability of this system in high pH (Figure 7-15b). The thickness of SnO_2 was increased further to 10 nm, to see whether activity could be enhanced. As expected, the activity recorded increased compared to that without the application of a SnO_2 layer, with a photocurrent recorded of +19.2 mA cm^{-2} at +2.13 V_{RHE} and +0.1 mA cm^{-2} at +1.23 V_{RHE} (Figure 7-16a). Comparing to 3 and 5 nm SnO_2, which achieved lower values of +4.7 and +17.7 mA cm^{-2} respectively, showing that a 10 nm SnO_2 layer appears to be optimum in creating this MIS junction (Figure 7-16b).

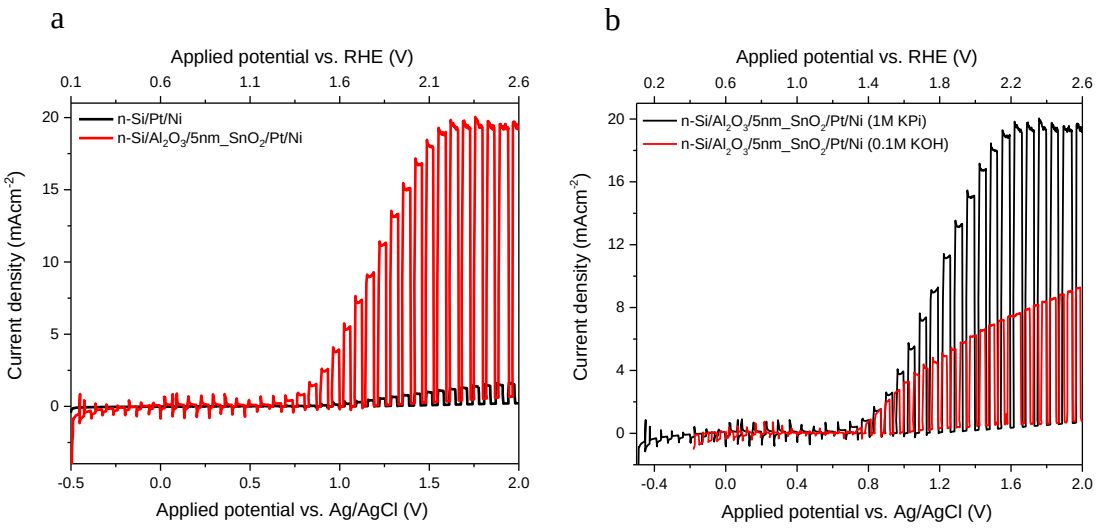

Figure 7-15: Comparison of chopped light LSV measurements of (a) n-Si with 5 nm SnO_2 and Pt/Ni and (b) comaprison between the use of a KPi (pH 7) and KOH (pH 13) electrolyte.

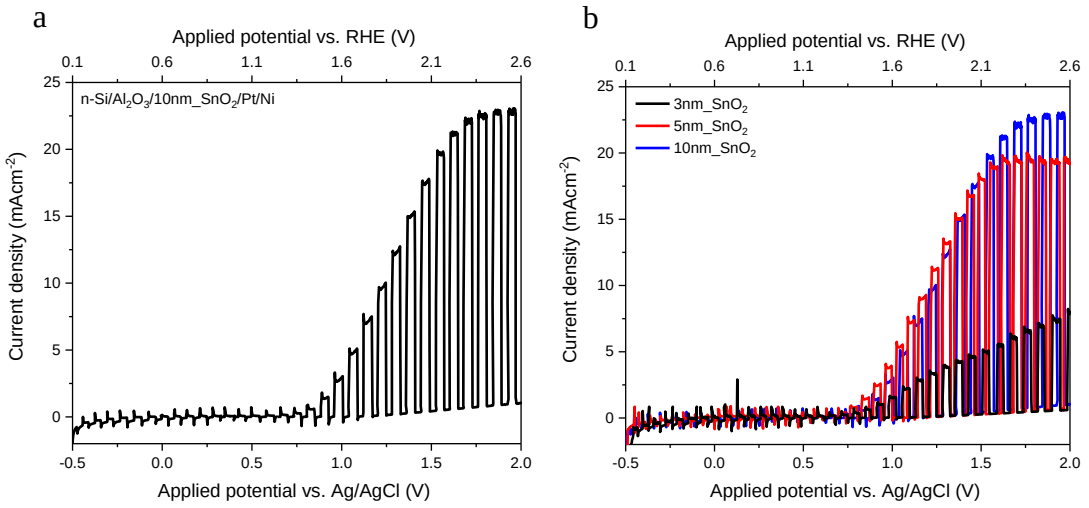

Figure 7-16: Chopped light LSV measurements of (a) n-Si with a 10 nm SnO_2 layer and (b) comparison between SnO_2 layers which were of 3 and 5 nm in thickness.

Overall, it has been demonstrated that incorporating a SnO_2 layer of varying thickness between a n-Si wafer and Pt/Ni catalysts, potentially creates a desired MIS junction. The presence of this insulating layer prevents direct contact between the n-Si and the high work function Pt particles, that can cause trap states and detrimental ohmic contact formation, hindering charge transport. However, when SnO_2 is deposited, this ohmic contact formation is avoided, but instead a Schottky junction can form between n-Si and SnO_2, which assists charge transport. This is demonstrated by the vast

improvements in photocurrent density for n-Si/SnO_2/Pt/Ni films compared to n-Si/Pt/Ni. This technique of creating MIS junctions can then be applied to other n-type semiconductors such as $BiVO_4$, to enhance sensitivity of this photoanode to the addition of high work function metals.

7.5 $BiVO_4$ films with a SnO_2 insulating layer

Next, n-type $BiVO_4$ was used for the creation of MIS junctions. As before, SnO_2 was deposited using an ALD plasma process with a 1s exposure time for TDMASn. SnO_2 was deposited at a thickness of 3, 5, 10 and 20 nm onto FTO-ABS/SnO_2/ $BiVO_4$ films. SnO_2 was previously coated onto the FTO-glass substrate so that an ohmic contact is formed, to prevent the transport of holes to the back contact, with $BiVO_4$ being deposited using spray pyrolysis (completed by Dr. Ibbi Ahmet at HZB). A 4 nm layer of platinum and Ni were deposited onto the SnO_2 layer, and Pt/ Ni were also deposited directly onto $BiVO_4$ without the SnO_2 insulating layer for comparison. To demonstrate the film architectures for these $BiVO_4$ films, they are displayed as schematics in Figure 7-17.

Firstly, SEM micrographs were obtained of $BiVO_4$/5nm_SnO_2 prepared with H_2O (Figure 7-18a and b) and plasma (O_2) method (Figure 7-18c and d). This spray

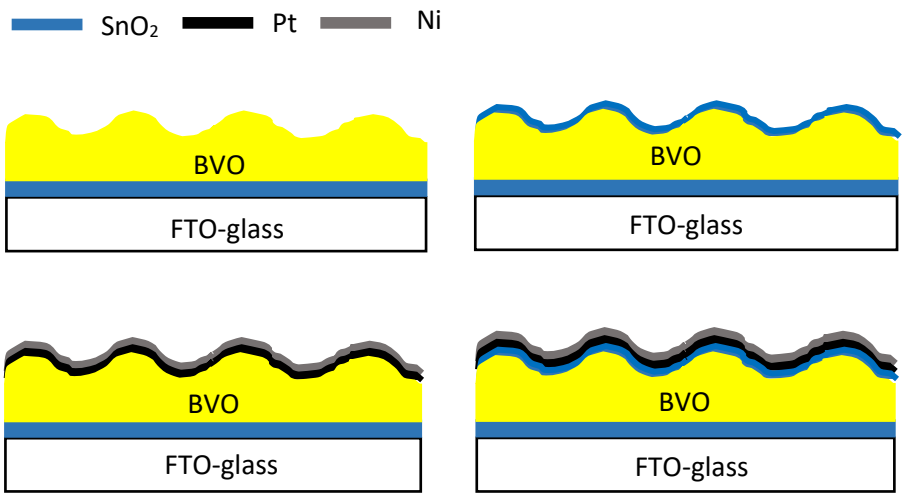

Figure 7-17: Diagrams of fabricated $BiVO_4$ devices, including the prepared architectures FTO-glass/SnO_2/$BiVO_4$, FTO-glass/SnO_2/$BiVO_4$/SnO_2, FTO-glass/SnO_2/$BiVO_4$/SnO_2/Pt/Ni and FTO-glass/SnO_2/ $BiVO_4$/Pt/Ni.

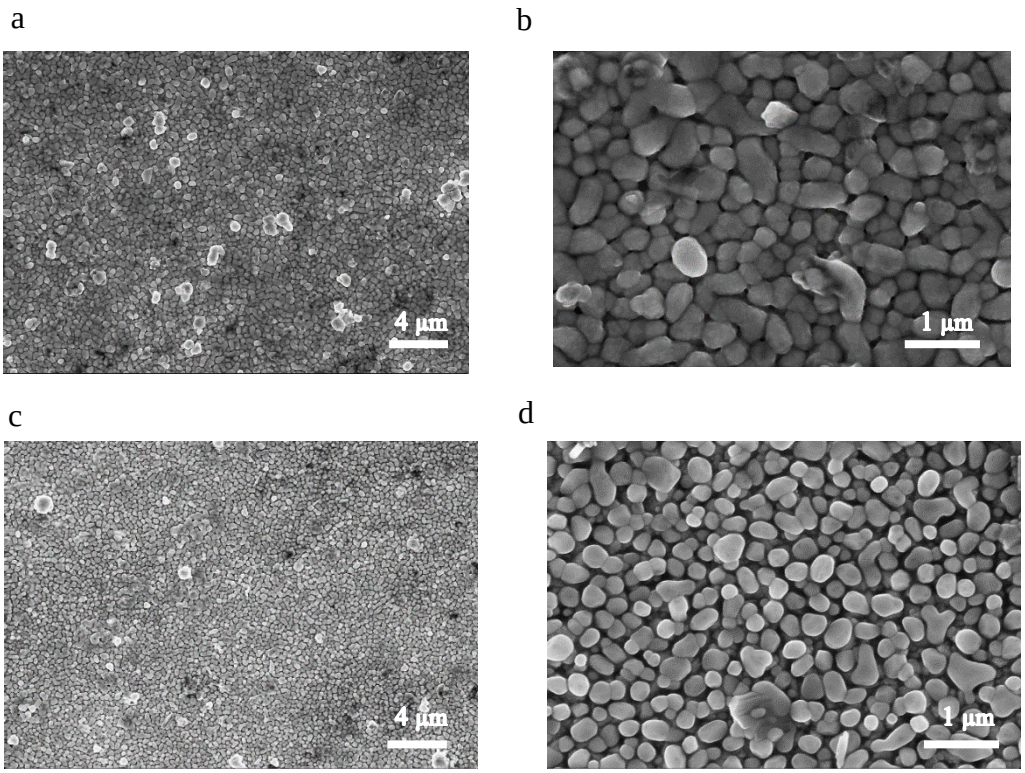

Figure 7-18: FE-SEM micrographs of (a, b) $BiVO_4$/5nm_SnO_2 using a H_2O method and (c, d) $BiVO_4$/5nm_SnO_2 using a plasma (O_2) method.

pyrolysis method used for $BiVO_4$ deposition onto an FTO glass substrate, resulted in a good quality film with high surface coverage. As expected, it would not be possible for the SnO_2 layer to be visible under FE-SEM due to the extremely low thickness, however it is provided a useful insight into the structure of these $BiVO_4$ films. There appears to be a minor change in morphology on higher magnification with the use of a H_2O method compared to a plasma method, with the H_2O method displaying less distinct and slightly larger $BiVO_4$ particles. This could be a result of the different effects from each ALD method, involving interactions with the $BiVO_4$ surface.

7.5.1 Electrochemical measurements

EIS measurements were obtained in order to construct Mott-Schottky plots to determine what effect the addition of SnO_2 has on $BiVO_4$ and to distinguish the electrical properties of the different photoanodes. It can be seen in Figure 7-19 that for all Mott-Schottky plots there is a clear positive slope in the anodic direction for the linear region of the data, characteristic of an n-type semiconductor. It is possible to

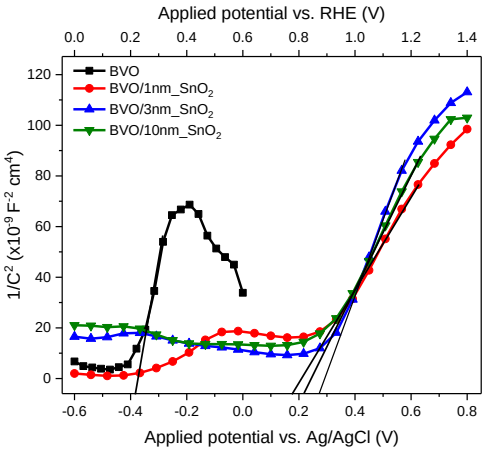

Figure 7-19: Mott-Schottky plots completed at 100 Hz for bare $BiVO_4$ and with 1, 3 and 10 nm SnO_2 deposited. Using electrolyte 0.5 M KPi buffer + 1 mM K_3IrCl_6 + 0.1 mM K_2IrCl_6.

determine the flat band (V_{fb}) potential (i.e the x-axis intercept for the linear portion of the Mott-Schottky plot) from these plots for the bare $BiVO_4$ and the films coated with SnO_2 of different thicknesses. For $BiVO_4$ the V_{fb} = ~ +0.2 V_{RHE}, which corresponds to what is in the literature.[162] For $BiVO_4/SnO_2$ films the V_{fb} is clearly shifts to more anodic potentials to +0.80, +0.90 and +0.86 V_{RHE}, and corresponds closely to literature values for SnO_2 films.[163] An anodic shift in the V_{fb} clearly indicates that there is reduction in fermi level position of the $BiVO_4$ when SnO_2 is added to the surface. This observation provides evidence that the $BiVO_4/SnO_2$ junction results in a reduced barrier height, subsequently the band bending and the depletion region at the $BiVO_4/SnO_2$/electrolyte junction is reduced when compared to the bare $BiVO_4$/electrolyte photoanodes. This is then expected if the SnO_2 fermi level is higher than $BiVO_4$. It is therefore evident that SnO_2 may not act as an ideal surface layer for $BiVO_4$ buried junction and it would be necessary to explore other stable metal oxide with work functions (ϕ) higher than SnO_2, such as V_2O_5 ($\phi \approx 6.8$ eV).[164]

7.5.2 Photoelectrochemical measurements

All prepared $BiVO_4$ architectures were tested in a 3-electrode system with a Ag/AgCl reference electrode, Pt counter and a 1 M KPi electrolyte with 0.5 M Na_2SO_3 HS for films without catalyst (FTO-glass/SnO_2/ $BiVO_4$ and FTO-glass/SnO_2/ $BiVO_4/SnO_2$). High photocurrent densities of +2.9 mA cm^{-2} at +1.23 V_{RHE} were achieved for these

pristine $BiVO_4$ films with HS. On addition of 4 nm Pt and 4 nm Ni, measured without HS (FTO-glass/SnO_2/ $BiVO_4$/Pt/Ni), demonstrated a decreased activity of +0.27 mA cm^{-2} at +1.23 V_{RHE} (Figure 7-20a). In an ideal case, the activity when a catalyst is present, should be comparable with the activity displayed with bare $BiVO_4$ in the presence of a hole scavenger, suggesting that this proposed advantageous device architecture has not formed. Additionally, there is a markable increase in anodic current which can be somewhat indicative of an ohmic junction. This confirms the need of an insulating layer to minimise unfavourable junction interfaces. On the addition of 3 nm SnO_2 layer (with HS) a sharp decrease in photocurrent density was seen to +0.02 mA cm^{-2} at +1.23 V_{RHE} after Pt/Ni were added ($BiVO_4$/SnO_2/Pt/Ni) a photocurrent of +0.007 mA cm^{-2} at +1.23 V_{RHE} was recorded when measured in the absence of HS (Figure 7-20b). The presence of a large increase in current at +1.8 V_{RHE} can be attributed due to Ni oxidation at the surface. This feature is more comparable to resistor behaviour, hence more ohmic in nature. This suggests that an ohmic contact could have formed between the $BiVO_4$ and the SnO_2 resulting in such low activity.

Additionally, it was seen for this 3 nm SnO_2 layer, that there are increases in activity after each cycle within a single measurement and increases further on a second chopped PEC measurement with an additional 2 cycles recorded. Activity increased from +0.02 (cycle 1 measurement 1) to +0.52 mA cm^{-2} (cycle 2 measurement 2) at

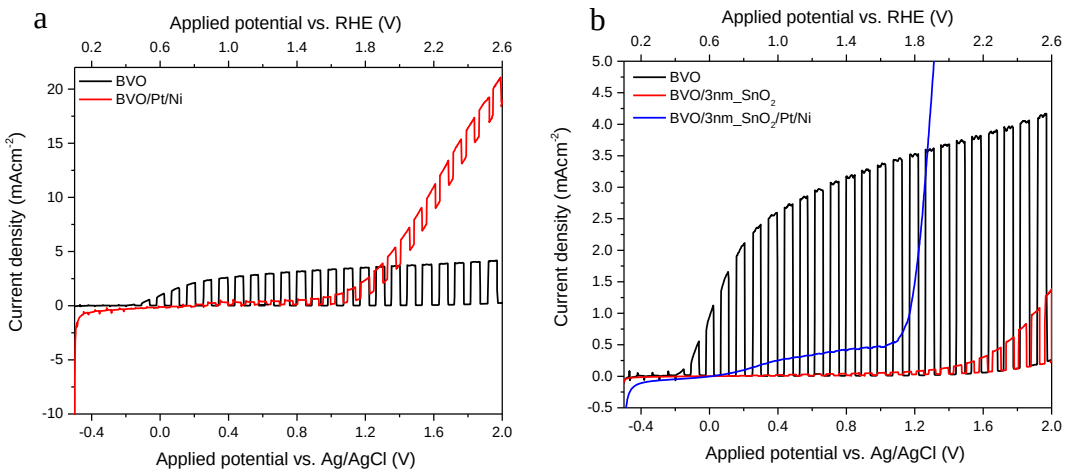

Figure 7-20: Chopped light LSV measurements for (a) $BiVO_4$ films with the addition of Pt/Ni and (b) with the addition of 3 nm SnO_2 and 3 nm SnO_2/Pt/Ni.

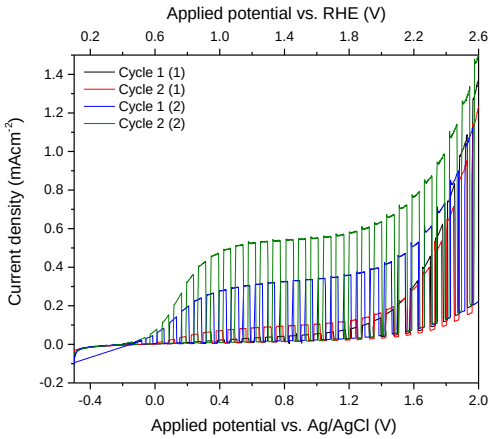

Figure 7-21: Chopped light LSV measurements for two separate data acquisitions with 2 cycles being completed for each, for sample n-Si/ SnO_2/ $BiVO_4$/3nm_SnO_2.

+1.23 V_{RHE} (Figure 7-21) This could be due to degradation of the SnO_2 layer or changes in the SnO_2 surface leading to these increases in photocurrent. Further thicknesses of SnO_2 were tried in order to see if changes in this insulating layer would make any positive impact on the resultant photocurrent. A 5 nm SnO_2 layer was also prepared and the same chopped PEC measurements were undertaken. As before, in the case of a 3 nm SnO_2 layer, there are vast deductions in photocurrent with the addition of this insulating layer and subsequent addition of Pt/Ni, suggesting a failure in producing a favourable MIS junction. $BiVO_4$/5nm_SnO_2 achieves just +0.20 mA

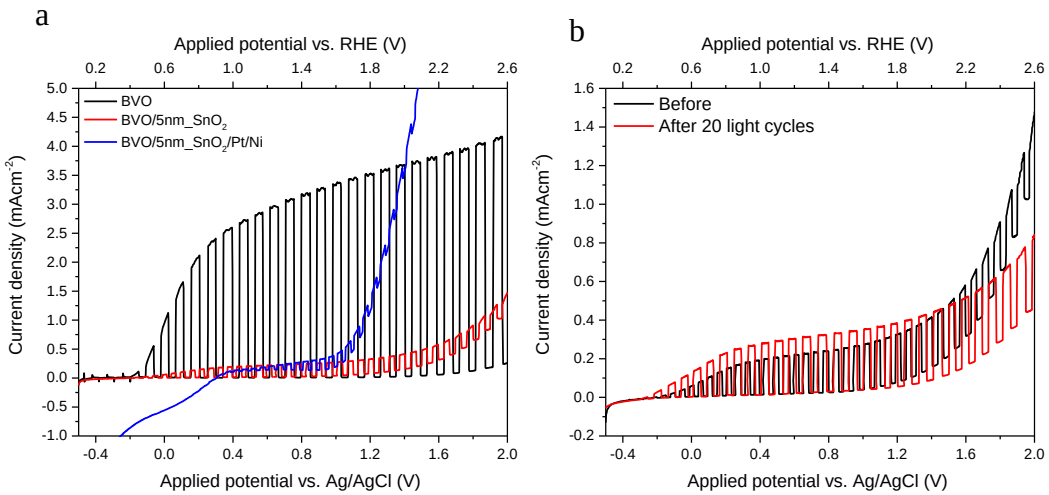

Figure 7-22: Chopped light LSV measurements for (a) $BiVO_4$, $BiVO_4$/5nm_SnO_2 and $BiVO_4$/5nm_SnO_2/Pt/Ni and (b) PEC measurements for $BiVO_4$/5nm_SnO_2 before and after 20 cycles of light illumination.

cm^{-2} at +1.23 V_{RHE} and with the addition of Pt/Ni achieves +0.06 mA cm^{-2} (Figure 7-22a). Again, this seems to suggest a preferential Schottky junction is not being formed at the $BiVO_4/SnO_2$ interface. The SnO_2 perhaps was acting as a detrimental layer of high resistance. To examine whether there are increases in photocurrent after repeated chopped measurements, as seen previously with the 3 nm SnO_2 case, a measurement was taken before and after 20 consecutive cycles of light illumination. It was found that there was a minimal increase from +0.20 to +0.28 mA cm^{-2} at +1.23 V_{RHE}, suggesting that this 5 nm SnO_2 layers is more stable than having a 3 nm SnO_2 layer (Figure 7-22b).

A 10 nm SnO_2 layer was also investigated. Comparable results were obtained displaying identical trends in the effect of the application of this insulating layer and subsequent metal deposition. $BiVO_4$/10nm_SnO_2 achieved just +0.06 mA cm^{-2} and with added Pt/Ni achieving +0.02 mA cm^{-2} at +1.23 V_{RHE} (a). With the SnO_2 potentially acting as a detrimental layer with 10 nm being perhaps too thick to act as a successful insulating layer. Very little difference in activity is seen when repeated measurements were taken suggesting that this SnO_2 is more stable (chop 1 = +0.061 mA cm^{-2} chop 2 = +0.066 mA cm^{-2}) (b). This SnO_2 was increased further still to 20 nm which predictably yielded identical observations. With $BiVO_4$/20nm_SnO_2 achieving just +0.04 mA cm^{-2} and with added Pt/Ni achieving

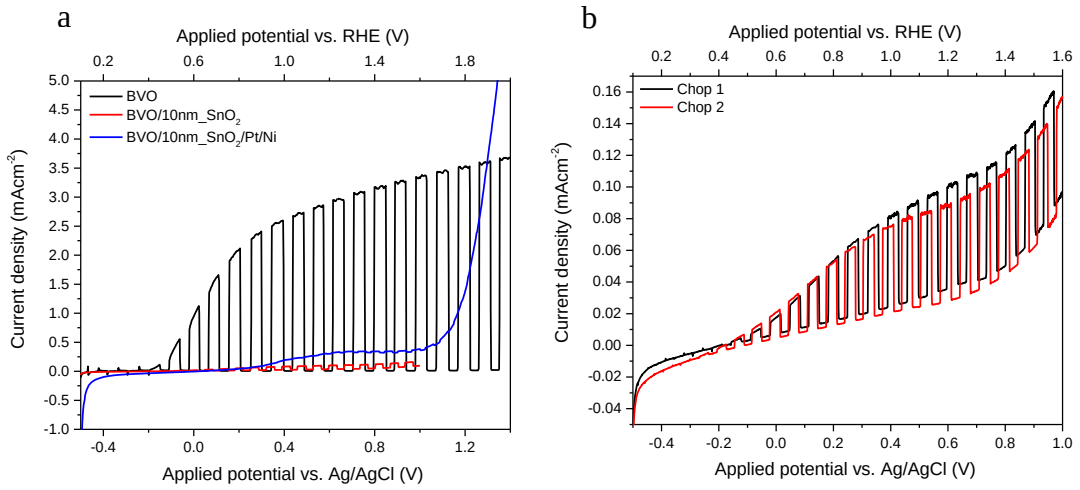

Figure 7-23: Chopped light LSV measurements for (a) $BiVO_4$, $BiVO_4$/10nm_SnO_2 and $BiVO_4$/10nm_SnO_2/Pt/Ni and (b) PEC measurements for $BiVO_4$/10nm_SnO_2 for two different cycles.

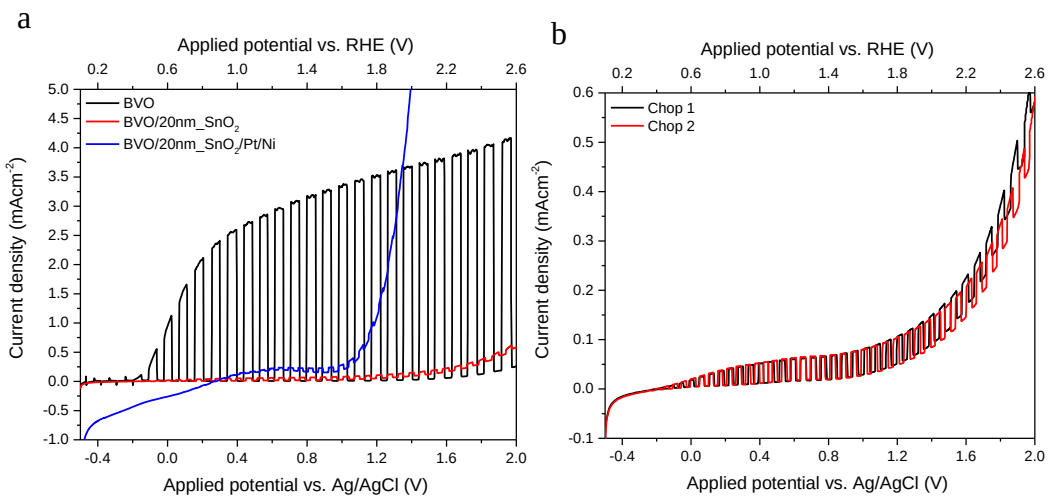

Figure 7-24: Chopped light LSV measurements for (a) $BiVO_4$, $BiVO_4$/20nm_SnO_2 and $BiVO_4$/20nm_SnO_2/Pt/Ni with (b) PEC measurements for $BiVO_4$/20nm_SnO_2 for two different data acquisitions.

+0.03 mA cm^{-2} at +1.23 V_{RHE}. Repeated chopped measurements resulted in negligible changes (+0.045 to +0.046 mA cm^{-2}), suggesting a greater stability compared to a 3 nm SnO_2 layer (Figure 7-24).

In all of the above cases regarding the prepared $BiVO_4$/SnO_2/Pt/Ni films, it was intended that the addition of an insulating SnO_2 layer would allow for the increased interaction of the $BiVO_4$ to the high work function metals, through the unpinning of the $BiVO_4$ fermi level. However, it is clear that this intended junction between the $BiVO_4$ and SnO_2 was not achieved. This would have resulted in higher levels of recombination at the interface due to the accumulation of charges, as they are failing to penetrate the insulating layer to arrive at the Pt/Ni on the surface. The least detrimental thickness of SnO_2 appears to be of 5 nm due to the absence of suggested degradation, with the highest achieved photocurrent of +0.06 mA cm^{-2} compared to +0.007, +0.02 and +0.03 mA cm^{-2} for 3, 10 and 20 nm SnO_2 respectively. With increasing thickness, it can be postulated that the SnO_2 layer will become more resistive due to its insulating properties, which will hinder electrons shuttling through to the surface.

7.6 $BiVO_4$ films with a NiO layer and a SnO_2 insulating layer

It can be suggested that a further layer is required between the $BiVO_4$ and SnO_2 to create the required Schottky junction, which can be done by using NiO, which is known to create this desirable junction. Firstly, XPS was performed to confirm the successful deposition of NiO onto $BiVO_4$. As seen in Figure 7-25, the presence of $BiVO_4$ was seen from the Bi 4f spectrum (Bi $4f_{5/2}$ at 164.1 eV, Bi $4f_{7/2}$ at 158.9 eV) and the O 1s/V 2p spectra (O 1s at 529.6 eV, V $2p_{1/2}$ at 524.1 eV and V $2p_{3/2}$ at 516.5 eV). The successful deposition of NiO can be seen from the Ni 2p spectra where the peak at 872.9 eV and can be attributed to Ni $2p_{1/2}$ (with a satellite peak at 880.2 eV) and the peak at 855.2 eV can be assigned to Ni $2p_{3/2}$ (with a satellite peak at 861.4 eV).

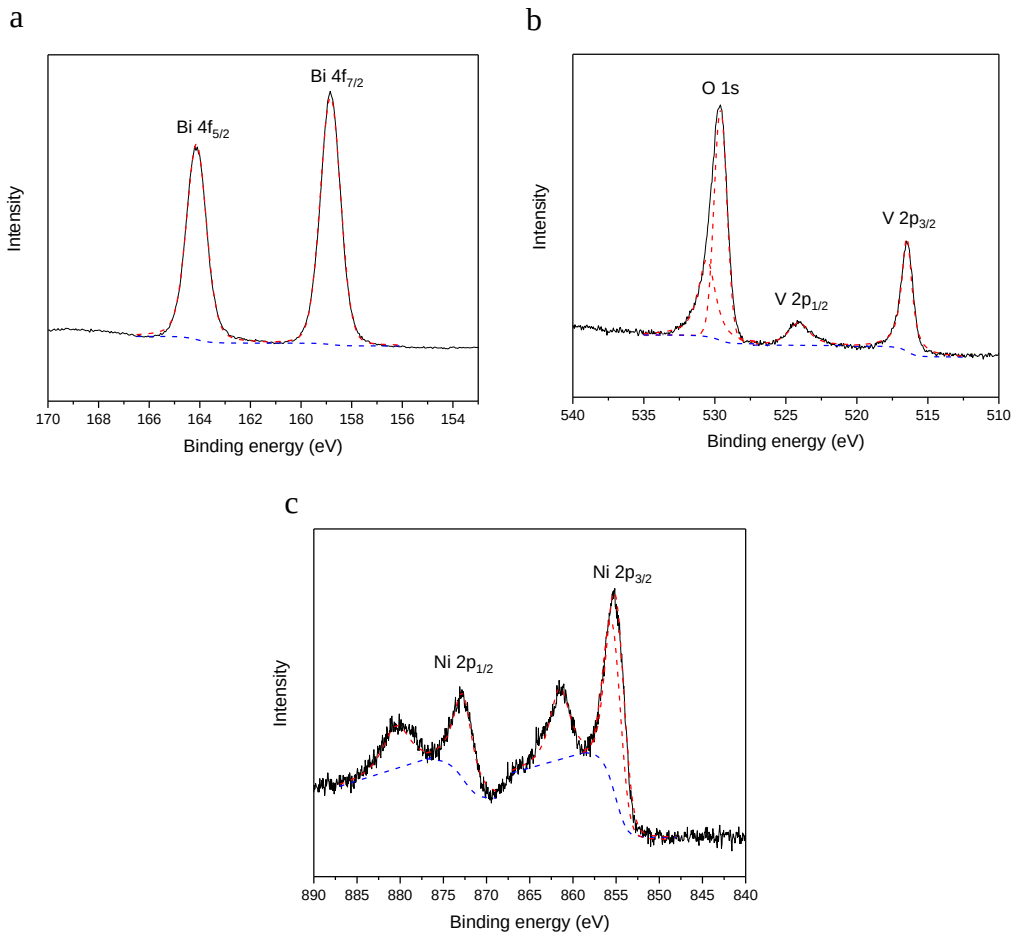

Figure 7-25: XPS spectra of (a) Bi 4f, (b) V 2p and O 1s and (c) Ni 2p for $BiVO_4$/NiO to confirm presence of NiO.

7.6.1 Photoelectrochemical measurements

NiO was deposited on $BiVO_4$ by ALD, with a $Ni(MeC(NtBu)_2)_2$ precursor with O_2 plasma at a thickness of 1 nm, in attempt to create the preferred Schottky junction. PEC measurements were completed for $BiVO_4$/1nm_NiO/5nm_SnO_2 (a) which showed decreases in photocurrent compared to $BiVO_4$/5nm_SnO_2 from +0.20 to +0.012 mA cm^{-2} at +1.23 V_{RHE}, however after repeated measurements of up to 4 times, there was a remarkable increase in activity to +1.35 mA cm^{-2} (b). This could be suggestive of the NiO being beneficial in providing a more favourable junction between the $BiVO_4$ and the SnO_2, to allow charges to pass through the insulating layer more successfully. However, this could also be explained due to potential degradation of the SnO_2 layer, as postulated before when increases in activity were seen on repeated cycling. In addition, there is an increase in dark current around +1.2 V_{RHE}, that could be attributed to Ni oxidation, nevertheless it is clear that the addition of SnO_2 is impeding charge transport ultimately leading to the disappointing photocurrents recorded.

To further probe this interaction, UPS measurements were done to determine the band alignments of $BiVO_4$, NiO and SnO_2 (Figure 7-27). Before measurements were taken of bare $BiVO_4$, it was plasma treated for 1 minute to clean the surface. It can be seen that there are some anomalies present in terms of the calculated fermi levels in

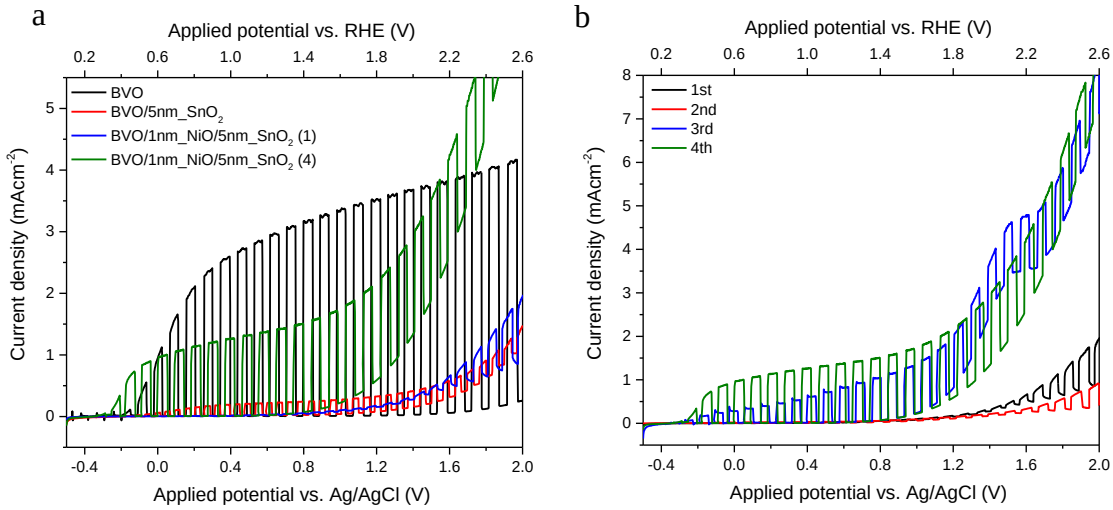

Figure 7-26: Chopped light LSV measurements for (a) $BiVO_4$/1nm_NiO/5nm_SnO_2 comparison and (b) the effect of repeated PEC measurements of up to 4 times.

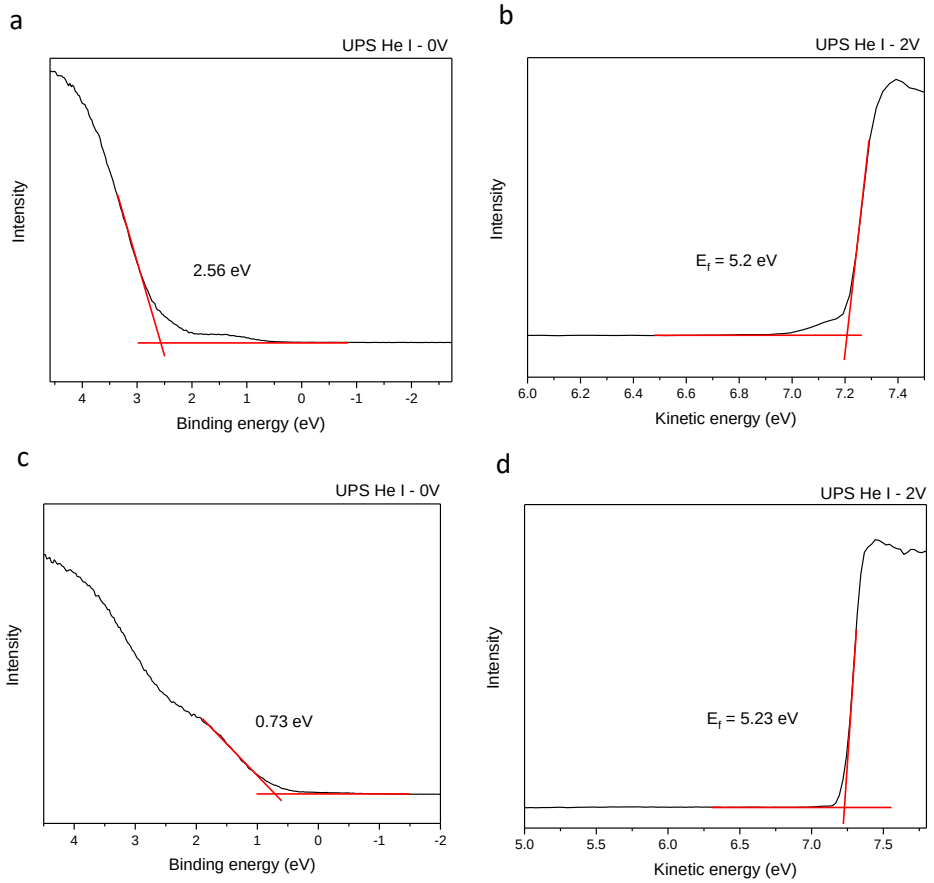

Figure 7-27: UPS measurements of (a, b) $BiVO_4$ (plasma treated) and (c, d) $BiVO_4$/1nm_NiO with 0 V applied and 2 V applied for energy band calculations.

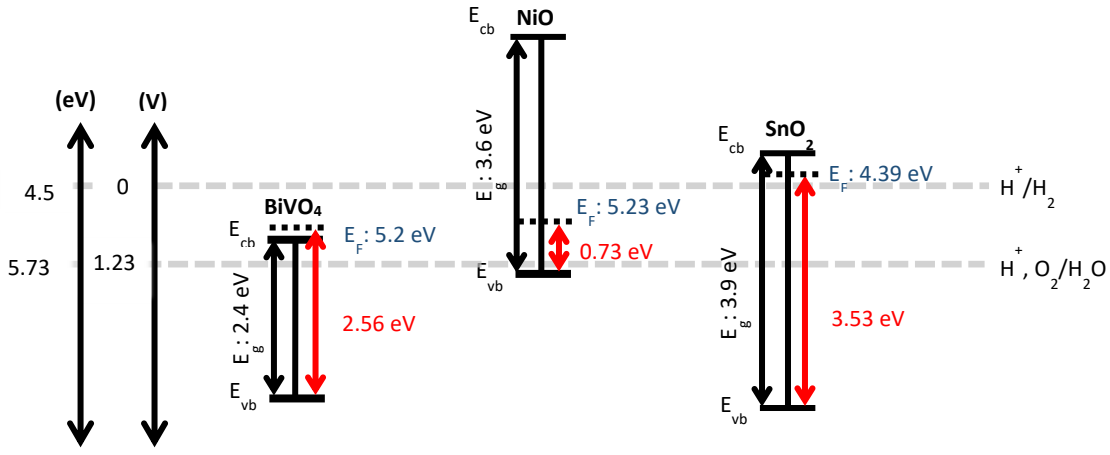

Figure 7-28: UPS calculated energy band diagrams for $BiVO_4$, NiO and SnO_2 completed under vacuum and with no exposure to air.

reference to the conductance band for $BiVO_4$, but in any case both the fermi level of NiO and SnO_2 according to these calculated energy levels are in non-ideal positions for Schottky junction formation (Figure 7-28). There is a clear need for further evaluation of the most suitable material to create a Schottky contact with $BiVO_4$ to allow for creation of a successful MIS junction.

Due to these depressed photocurrents achieved on the addition of a SnO_2 insulating layer, it was investigated whether the introduction of an annealing step would have a positive effect. Previously prepared $BiVO_4/SnO_2$ and $BiVO_4/SnO_2$/Pt/Ni films with 3 and 10 nm SnO_2 layers, were annealed at 450 °C for 2 hours and then PEC measurements were taken. Firstly, when film $BiVO_4$/3nm_SnO_2 was subjected to an annealing step there is a dramatic increase in photocurrent from +0.51 to +1.62 mA

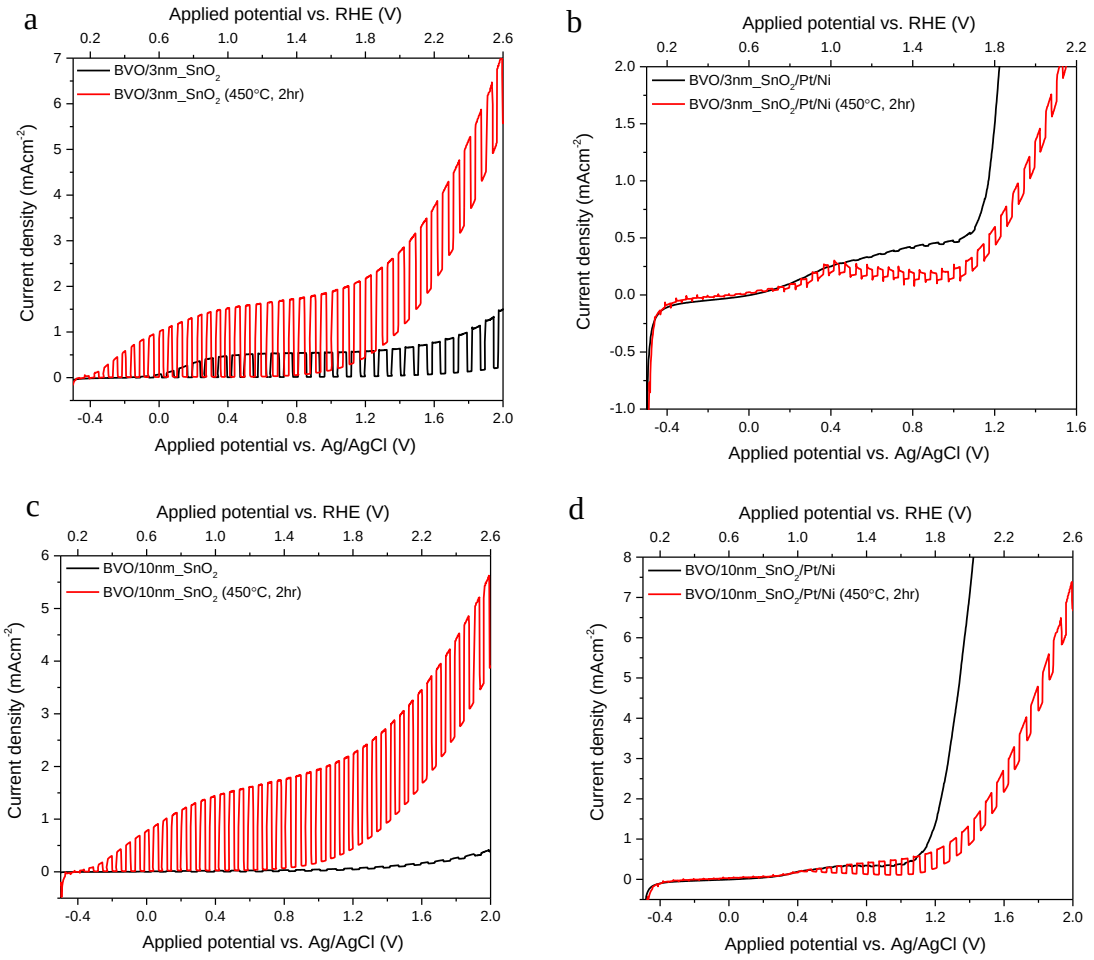

Figure 7-29: Chopped light LSV measurements for BVO/SnO_2 films before and after annealing for BVO films with an (a, b) 3 nm SnO_2 and (c, d) 10 nm SnO_2.

cm^{-2} at +1.23 V_{RHE} (Figure 7-29a) there is also a slight improvement in photocurrent when $BiVO_4$/3nm_SnO_2/Pt/Ni was annealed, increasing to +0.05 from +0.007 mA cm^{-2} (Figure 7-29b). This could be due to decreasing defect states with high temperature annealing, allowing for a better contact between the $BiVO_4$ and subsequent layers to create more efficient junctions. The same positive effect is seen when annealing $BiVO_4$/10nm_SnO_2 films, where an increase from +0.03 to +1.57 mA cm^{-2} at +1.23 V_{RHE} which is a much larger increase in activity than seen with a 3 nm thick SnO_2 layer (Figure 7-29c). Additionally, there is increased photocurrent seen for films with Pt/Ni, increasing from +0.01 to +0.17 mA cm^{-2} (Figure 7-29d). Again, introducing an annealing step improved the photocurrent of this photoanode, potentially due to decreases in defect states.

7.7 Conclusions and future work

In this work we have been able to demonstrate an ALD process to prepare SnO_2 films on n-Si and $BiVO_4$ with thicknesses ranging from 3 to 20 nm. This process was optimised in terms of precursor exposure time (TDMASn and H_2O), deposition temperature and changing of precursors (Plasma, O_2). From this, GPC was calculated on changing conditions through the use of in situ ellipsometry measurements. It was found that the optimal conditions for this ALD process was using an exposure time of 1 s for TDMASn and 0.5 s for H_2O, with a reactor temperature of 170 °C which provided a GPC of between 0.05 and 0.071 nm/cycle. It was found that using a plasma (O_2) precursor resulted in higher GPC, which was as expected due the higher reactivity for oxidation, achieving 0.08 nm/cycle. However, although there was an increase in GPC for a plasma process, there was no increase in growth in relation to time, with a rate of 0.028 nm/min whilst using H_2O precursor results in a rate of 0.03 nm/min. It can be concluded that there is no apparent benefit of using a plasma-based process in terms of time saved, nevertheless there could be benefits in terms of morphology of the SnO_2.

This developed SnO_2 ALD process was then used to deposit SnO_2 onto n-Si and $BiVO_4$ of varying thicknesses (3, 5 and 10 nm), in order to create a MIS junctions. It was found, that applying a SnO_2 layer onto n-Si, enhanced the photocurrents and

improved the n-Si photoanode. Bare n-Si demonstrated an unreadable photocurrent at +1.23 V_{RHE} and +0.01 mA cm^{-2} at +2.13 V_{RHE}. On the addition of Pt/Ni (n-Si/SiO_x/Pt/Ni) the photocurrent density increased to +0.89 mA cm^{-2} at +2.13 V_{RHE} due to the protection and catalysis that Pt/Ni provides. On the addition of a 3 nm SnO_2 layer between the n-Si and Pt/Ni (n-Si/SiO_x/Al_2O_3/3nm_SnO_2/Pt/Ni), photocurrent density increased further to +4.72 mA cm^{-2} at +2.13 $V_{RHE.}$ Additionally, with a 5 nm SnO_2 layer +17.7 mA cm^{-2} at +2.13 V_{RHE} was achieved. Finally, with the application of a 10 nm SnO_2 layer, the highest photocurrent of +19.2 mA cm^{-2} at +2.13 V_{RHE} was recorded. The introduction of SnO_2 has drastically improved photocurrent with increasing thickness of SnO_2 being beneficial. It can therefore be postulated that the intended MIS junction has been formed, which has unpinned the n-Si fermi level and allowed for the creation of a Schottky junction and charge tunnelling to the surface metals. Further work can be done to assess the effects of different metals on the Schottky barrier height, and thus the achievable photovoltage due to changes in metal work function, which can be probed using both PEC analysis and solid-state *j-v* measurements under illumination.

The deposition of a SnO_2 onto $BiVO_4$ photoanodes was also done with the intention to create a similar beneficial MIS junction. When applying Pt/Ni directly onto $BiVO_4$, without an insulating layer, there was an activity of +0.27 mA cm^{-2} measured without a hole scavenger (HS), compared with bare $BiVO_4$ that achieved +2.94 mA cm^{-2} +1.23 V_{RHE} (with HS). This decrease of photocurrent can be attributed to the potential formation of an ohmic contact between the $BiVO_4$ and the Pt/Ni caused by fermi level pinning, which demonstrated the need for insulation. When 3 nm of SnO_2 was applied there was a sharp decrease in activity to +0.02 mA cm^{-2} in the presence of HS, which suggests a strong insulation of charges and a potential ohmic contact between the $BiVO_4$ and the SnO_2. A further decrease in photocurrent was seen on the addition of Pt/Ni (+0.007 mA cm^{-2}, no HS) suggesting that the creation of a Schottky junction between the $BiVO_4$ and SnO_2 was unsuccessful in this case. An explanation of this could be due to unfavourable band positions determined from UPS analysis, displaying a higher fermi level position for SnO_2 compared to $BiVO_4$, which would result in an ohmic contact being formed. Also, it can be postulated that due to the surface roughness of $BiVO_4$, and due to the assumed higher coverage of Pt, that detrimental shunting could be occurring, all of which contributing to the reductions in

photocurrent observed. It is apparent that further probing into the interaction between $BiVO_4$ and SnO_2 is needed to better understand how to create a successful MIS junction for $BiVO_4$, so that enhancements in photoanodic activity can be achieved and improved electrolyte stability of $BiVO_4$ is realised.

Chapter 8

8 Thesis Conclusions

The primary research aim of this Thesis was to explore the photoelectrochemical (PEC) properties of perovskite oxide compounds through the application of different film fabrication methods. The synthesis of lanthanum iron oxide ($LaFeO_3$) and praseodymium iron oxide ($PrFeO_3$) was completed, with their subsequent fabrication into photocathodes being successfully demonstrated. Chapter 2 outlined the synthesis of $LaFeO_3$ (LFO) nanoparticles by a facile sol-gel synthesis, exploring the use of different calcination temperatures. These LFO nanoparticles were shown to be active for photocatalytic water reduction, with higher calcination temperatures of 600 and 700 °C providing the best activity through demonstrating increased H_2 generation. Calcination temperature was shown to have implications for particle size and surface area of LFO, with higher temperatures resulting in larger particles and lower surface area, thus highlighting the importance of its consideration. However, a lack of confidence in the photocatalytic measurements obtained was apparent due to major observed difficulties with particle dispersion.

As well as confirming the ability of LFO particles for photocatalytic processes, such as water reduction, PEC activity was also explored in depth. Chapter 3 outlined various strategies for the fabrication of LFO photocathodes to be measured for their activity within PEC cells. Firstly, a doctor blading method was employed (LFO-A), involving the dispersion of LFO particles in solution with subsequent deposition onto a fluorine-doped tin oxide coated aluminoborosilicate (FTO-ABS) glass substrate. Field-emission scanning electron microscopy (FE-SEM) was used to obtain micrographs of these films and revealed that this method resulted in poor film quality in terms of coverage and uniformity on the substrate, which drastically limited achievable photocurrent. Improvements were made through prior milling and sonication of the LFO particles with deposition being completed through a spray pyrolysis method (LFO-B), which actively reduced particle sizes and increased photocurrent. It was proposed that deposition of pre-calcined LFO may limit the quality of the contact between the particles and the FTO, hence the deposition of metal oxide precursors directly onto the glass substrate using spray pyrolysis, with a

subsequent high temperature heating step was undertaken (LFO-C). This allowed for the formation of LFO directly upon the FTO surface, which was proposed to allow for better contact and greater stability of LFO film. Not only was the photocurrent increased to more than double that seen previously, there were noticeable increases in substrate coverage, uniformity and stability.

Ultimately within Chapter 3, the highest achieving films in terms of PEC activity, was when a sacrificial polymer template was used in conjunction with a spin coating fabrication method and 600 °C annealing. Two different polymer templates were explored, a graft co-polymer poly(vinyl chloride)-g-poly(oxyethylene methacrylate) (PVC-g-POEM) and a polymeric surfactant polyethylene glycol *tert*-octylphenyl ether (Triton X-100) named LFO-D and LFO-E respectively. Combining these templates with LFO nitrate-based precursors assisted in directing particle growth and reducing particle sintering, through creating micelle structures with the precursors. These solutions were then spin coated onto FTO-ABS glass substrates and heated to high temperatures to remove the polymer template and form LFO of high surface coverage and uniformity. With this, visible increases in film quality were seen in both cases, accompanied by vast enhancements in photocurrent, surface area, charge separation, conversion efficiency and stability. Despite showing competition of photogenerated electrons for oxygen reduction over water reduction, a demonstration was made for successful PEC water reduction for LFO-E films. It was also found that an in situ hydrothermal synthesis method for LFO film fabrication (LFO-F), resulted in the growth of high surface area LFO spindles of interesting morphology onto the FTO surface, giving rise to comparably high photocurrent to templating methods. This good performance was attributed to increased light scattering and surface area of these LFO-F films promoting enhanced charge generation. Overall, it was observed that changes in fabrication method can have vast influences on film quality and ultimate activity for PEC processes, that have not been currently explored in such depth for LFO photocathodes.

An additional research aim was to investigate techniques such as the addition of co-catalysts, heterojunctions and blocking layers to enhance photocurrent for prepared LFO films. Chapter 4 detailed the successful deposition of platinum onto templated

LFO-D films using PEC deposition, that can allow for increases in activity through improved charge transfer. However, an increase of the maximum photocurrent already obtained for these LFO-D films was not achieved, due to issues associated with high film thickness of LFO-D films not being compatible with electron transport to the LFO/Pt interface. It was also briefly examined whether a heterojunction could be formed between LFO and CuO, where an increase in stability was found for CuO when LFO was added, however due to time constraints this was not investigated fully. Finally, it was additionally explored whether the addition of an interfacial blocking layer or a hole transport layer could be applied in order to prevent recombination at the FTO surface and improve charge separation. This was explored for hydrothermally grown LFO-F films, by depositing an initial polymer templated layer to act as a blocking layer to prevent electron-hole recombination on the FTO surface, prior to the hydrothermal LFO growth. Small increases in photocurrent were observed on the application of this blocking layer, however further electrochemical impedance spectroscopic (EIS) measurements are required to establish whether an increase in charge separation was achieved. It is apparent that future work is required to explore these techniques in greater detail, so that impressive enhancements of photocurrent can be achieved, especially in terms of selectivity towards HER.

Further to the investigation of LFO for photocatalytic and PEC processes, $PrFeO_3$ (PFO) was also synthesised and explored in Chapter 5. PFO particles were synthesised using a sol-gel method with different calcination conditions and displayed activity for photocatalytic water reduction. PFO photocathodes were then fabricated using a spray pyrolysis method with nitrate-based precursors (PFO-B). Various annealing temperatures or 500, 600 and 700 °C for PFO formation were investigated with the highest photocurrent being achieved for PFO-B films calcined at 600 °C, which also displayed good stability over 1 hour. It was also found that on increasing calcination temperature there were greater levels of porosity as seen under FE-SEM, and greater efficiencies of charge transport and conversion. Although a lower calcination temperature of 500 °C provided a greater electrochemically active surface area, it was observed that there was a lack of crystallinity and poor charge transport properties, due to proposed defect/trap states. As seen in Chapter 3 with LFO photocathodes, a reduction of photocurrent is seen when O_2 is removed from the electrolyte, highlighting that photocurrent cannot be entirely attributed to HER. Despite this, PEC

water reduction was still possible with H_2 being measured from continuous light illumination and a constant applied potential of a PFO-B film. This fabrication of PFO photocathodes with subsequent examination for PEC processes is thought to be the first demonstration of its kind.

Finally, in Chapter 6, metal-insulator-semiconductor (MIS) junctions were explored as part of a short research project at the Helmholtz center Berlin for Energy and Materials (HZB). It was found that the application of an insulating SnO_2 layer prepared by an optimised atomic layer deposition method on n-type silicon was effective in enhancing stability and photocurrent of n-Si. This allowed for the creation of a proposed Schottky junction between SnO_2 and the deposited Pt/Ni, where it was found that a thicker SnO_2 layer of 10 nm was advantageous. In addition, it was attempted to create an MIS junction with $BiVO_4$ (BVO) photoanodes, however, an increase in photocurrent was not achieved and hence this favourable junction was not created. Further work would be required to investigate this to establish the cause of this failure in MIS junction formation for BVO photoanodes.

Overall, this Thesis has demonstrated the ability of perovskite oxides, such as $LaFeO_3$ and $PrFeO_3$ to be effective photocathodes. This work is both valuable and relevant to the research community due to the advancements made into this reported awareness of the effects of film fabrication technique on film quality and ultimate activity. With this, improvements in photocurrent for LFO photocathodes were made when compared to many published literature values (~10 µA cm^{-2}). Here, an optimised maximum photocurrent of -161 µA cm^{-2} was recorded with a high potential onset of +1.4 V_{RHE} for cathodic photocurrent on polymer templating and spin coating. This photocurrent is comparable to the highest achieved in the literature for pristine LFO photocathodes and demonstrates improved onset potential compared to other p-type materials. This Thesis also demonstrated the fabrication of PFO photocathodes that were shown to be active for PEC water reduction. This is of very high interest due to the limited investigations of PFO for photocatalytic processes, as well as no known demonstration of PFO photocathodes for PEC processes prior to this work. Future work that could be carried out by the scientific community in relation to PFO photocathodes is to investigate further film fabrication, dopants and co-catalysts.

Chapter 9

9 References

1 J. K. Casper, *Greenhouse gases : worldwide impacts*, Facts On File, 2010.

2 United Nations, *Framework Convention on Climate Change Adoption of the Paris Agreement*, Paris, 2015.

3 Committee on Climate Change, *Climate Change Act 2008*, Statute Law Database, 2008.

4 T. Ackermann, *Renew. Sustain. Energy Rev.*, 2000, **4**, 315–374.

5 M. M. Abu-Khader, *Prog. Nucl. Energy*, 2009, **51**, 225–235.

6 C. Baker, *Energy Policy*, 1991, **19**, 792–797.

7 G. K. Singh, *Energy*, 2013, **53**, 1–13.

8 S. Mekhilef, R. Saidur and A. Safari, *Renew. Sustain. Energy Rev.*, 2011, **15**, 1777–1790.

9 R. van de Krol and M. Grätzel, *Photoelectro - chemical Hydrogen Production*, Springer, 2012.

10 M. R. Pai, a M. Banerjee, a K. Tripathi and S. R. Bharadwaj, *Fundamentals and Applications of the Photocatalytic Water Splitting Reaction*, Elsevier Inc., 2012.

11 S. Ahmed and M. Krumpelt, *Int. J. Hydrogen Energy*, 2001, **26**, 291–301.

12 T. Hisatomi, J. Kubota and K. Domen, *Chem. Soc. Rev.*, 2014, **43**, 7520–7535.

13 Z. Wang, C. Li and K. Domen, *Chem. Soc. Rev.*, 2019, **48**, 2109–2125.

14 Q. Wang, T. Hisatomi, Q. Jia, H. Tokudome, M. Zhong, C. Wang, Z. Pan, T. Takata, M. Nakabayashi, N. Shibata, Y. Li, I. D. Sharp, A. Kudo, T. Yamada and K. Domen, *Nat. Mater.*, 2016, **15**, 611–615.

15 M. Winter and R. J. Brodd, *Chem. Rev.*, 2004, **104**, 4245–4269.

16 L. F. Brown, *Int. J. Hydrogen Energy*, 2001, **26**, 381–397.

17 L. Jörissen, *Angew. Chemie Int. Ed.*, 2011, **50**, 9787–9787.

18 C. Xiang, K. M. Papadantonakis and N. S. Lewis, *Mater. Horiz.*, 2016, **3**, 169–173.

19 K. Ellmer, *Nat. Photonics*, 2012, 6, 809–817.

20 K. Bädeker, *Ann. Phys.*, 1907, **327**, 749–766.

21 Z. Y. Banyamin, P. J. Kelly, G. West and J. Boardman, *Coatings*, 2014, **4**, 732–746.

22 S. Yu, L. Li, X. Lyu and W. Zhang, *Sci. Rep.*, 2016, **6**, 20399.

23 J. Montero, J. Herrero and C. Guillén, *Sol. Energy Mater. Sol. Cells*, 2010, **94**, 612–616.

24 C. Wang, T. Hisatomi, T. Minegishi, Q. Wang, M. Zhong, M. Katayama, J. Kubota and K. Domen, *J. Phys. Chem. C*, 2016, **120**, 15758–15764.

25 Q. Chen, G. Fan, H. Fu, Z. Li and Z. Zou, *Adv. Phys. X*, 2018, **3**, 863–884.

26 X. Chen and W. Shangguan, *Front. Energy*, 2013, **7**, 111–118.

27 I. Y. Ahmet, Y. Ma, J. W. Jang, T. Henschel, B. Stannowski, T. Lopes, A. Vilanova, A. Mendes, F. F. Abdi and R. Van De Krol, *Sustain. Energy Fuels*, 2019, **3**, 2366–2379.

28 B. A. Pinaud, J. D. Benck, L. C. Seitz, A. J. Forman, Z. Chen, T. G. Deutsch, B. D. James, K. N. Baum, G. N. Baum, S. Ardo, H. Wang, E. Miller and T. F. Jaramillo, *Energy Environ. Sci.*, 2013, **6**, 1983–2002.

29 L. C. Seitz, Z. Chen, A. J. Forman, B. A. Pinaud, J. D. Benck and T. F. Jaramillo, *ChemSusChem*, 2014, **7**, 1372–1385.

30 A. Fujishima and K. Honda, *Nature*, 1972, **238**, 37–38.

31 J. Jitputti, S. Pavasupree, Y. Suzuki and S. Yoshikawa, *J. Solid State Chem.*, 2007, **180**, 1743–1749.

32 L. Piispanen, M Hupa, *Appl. Surf. Sci.*, 2011, **258**, 1126–1131.

33 M. a Lazar, S. Varghese and S. S. Nair, *Catalysts*, 2012, **2**, 572–601.

34 Y. Yang, S. Niu, D. Han, T. Liu, G. Wang and Y. Li, *Adv. Energy Mater.*, 2017, **1700555**, 1–26.

35 A. G. Tamirat, J. Rick, A. A. Dubale, W.-N. Su and B.-J. Hwang, *Nanoscale Horiz.*, 2016, **1**, 243–267.

36 G. G. Bessegato, T. T. Guaraldo and M. V. B. Zanoni, in *Modern Electrochemical Methods in Nano, Surface and Corrosion Science*, 2014, pp. 271–319.

37 J. Y. Kim, G. Magesh, D. H. Youn, J. W. Jang, J. Kubota, K. Domen and J. S. Lee, *Sci. Rep.*, 2013, **3**, 2681.

38 R. Liu, Y. Lin, L.-Y. Chou, S. W. Sheehan, W. He, F. Zhang, H. J. M. Hou and D. Wang, *Angew. Chemie Int. Ed.*, 2011, **50**, 499–502.

39 Q. Jia, A. Iwase and A. Kudo, *Chem. Sci.*, 2014, **5**, 1513.

40 F. F. Abdi and R. Van De Krol, *J. Phys. Chem. C*, 2012, **116**, 9398–9404.

41 J. Luo, L. Steier, M. K. Son, M. Schreier, M. T. Mayer and M. Grätzel, *Nano Lett.*, 2016, **16**, 1848–1857.

42 A. Paracchino, V. Laporte, K. Sivula, M. Grätzel and E. Thimsen, *Nat. Mater.*, 2011, **10**, 456–461.

43 W. Niu, T. Moehl, W. Cui, R. Wick-Joliat, L. Zhu and S. D. Tilley, *Adv. Energy Mater.*, 2018, **8**, 1–8.

44 W. Yang, J. H. Kim, O. S. Hutter, L. J. Phillips, J. Tan, J. Park, H. Lee, J. D. Major, J. S. Lee and J. Moon, *Nat. Commun.*, , DOI:10.1038/s41467-020-14704-3.

45 Y. X. Yu, L. Pan, M. K. Son, M. T. Mayer, W. De Zhang, A. Hagfeldt, J. Luo and M. Grätzel, *ACS Energy Lett.*, 2018, **3**, 760–766.

46 S. Masudy-Panah, R. Siavash Moakhar, C. Sheng Chua, H. Ru Tan, T. It Wong, D. Chi and G. Kumar Dalapati, *ACS Appl. Mater. Interfaces*, 2016, **8**, 1206–1213.

47 A. A. Dubale, C. J. Pan, A. G. Tamirat, H. M. Chen, W. N. Su, C. H. Chen, J. Rick, D. W. Ayele, B. A. Aragaw, J. F. Lee, Y. W. Yang and B. J. Hwang, *J. Mater. Chem. A*, 2015, **3**, 12482–12499.

48 Y. Yang, D. Xu, Q. Wu and P. Diao, *Sci. Rep.*, 2016, **6**, 35158.

49 L. Pan, J. H. Kim, M. T. Mayer, M. K. Son, A. Ummadisingu, J. S. Lee, A. Hagfeldt, J. Luo and M. Grätzel, *Nat. Catal.*, 2018, **1**, 412–420.

50 W. Wang, M. O. Tade and Z. Shao, *Chem. Soc. Rev.*, 2015, **44**, 5371–5408.

51 K. Zhang, J. Sunarso, Z. Shao, W. Zhou, C. Sun, S. Wang and S. Liu, *RSC Adv.*, 2011, **1**, 1661.

52 G. E. Eperon, V. M. Burlakov, P. Docampo, A. Goriely and H. J. Snaith, *Adv. Funct. Mater.*, 2014, **24**, 151–157.

53 J. M. Ball, M. M. Lee, A. Hey and H. J. Snaith, *Energy Environ. Sci.*, 2013, **6**, 1739.

54 P. P. Boix, S. Agarwala, T. M. Koh, N. Mathews and S. G. Mhaisalkar, *J. Phys. Chem. Lett.*, 2015, **6**, 898–907.

55 M. Crespo-Quesada, L. M. Pazos-Outón, J. Warnan, M. F. Kuehnel, R. H. Friend and E. Reisner, *Nat. Commun.*, 2016, **7**, 6–12.

56 L. Gao, *Chem. Commun*, 2018, **54**, 11459–11462.

57 I. Poli, J. Baker, U. Hintermair, T. M. Watson, M. Regue, S. Eslava, S. Kumar, E. V Sackville and P. J. Cameron, *Nat. Commun.*, 2019, **10**, 1–10.

58 P. Kanhere and Z. Chen, *Molecules*, 2014, **19**, 19995–20022.

59 K. Iwashina and A. Kudo, *J. Am. Chem. Soc.*, 2011, **133**, 13272–13275.

60 K. Maeda, *ACS Appl. Mater. Interfaces*, 2014, **6**, 2167–2173.

61 H. Zhang, G. Chen, Y. Li and Y. Teng, *Int. J. Hydrogen Energy*, 2010, **35**, 2713–2716.

62 P. Kanhere, J. Zheng and Z. Chen, *Int. J. Hydrogen Energy*, 2012, **37**, 4889–4896.

63 S. J. A. Moniz, C. S. Blackman, P. Southern, P. M. Weaver, J. Tang and C. J. Carmalt, *Nanoscale*, 2015, **7**, 16343–53.

64 S. Mohan, B. Subramanian, I. Bhaumik, P. K. Gupta and S. N. Jaisankar, *RSC Adv.*, 2014, **4**, 16871–16878.

65 Y.-N. Feng, H.-C. Wang, Y.-D. Luo, Y. Shen and Y.-H. Lin, *J. Appl. Phys.*, 2013, **113**, 146101.

66 P. Yilmaz, D. Yeo, H. Chang, L. Loh and S. Dunn, *Nanotechnology*, 2016, **27**, 345402.

67 H.-M. Xu, H. Wang, J. Shi, Y. Lin and C. Nan, *Nanomaterials*, 2016, **6**, 215.

68 C. Ederer and N. A. Spaldin, *Phys. Rev. B - Condens. Matter Mater. Phys.*, 2005, 71, 224103.

69 S. Thirumalairajan, K. Girija, B. Valmor, R. Mastelaro and N. Ponpandian, *New J. Chem.*, 2014, **38**, 5480–5490.

70 S. Li, L. Jing, W. Fu, L. Yang, B. Xin and H. Fu, *Mater. Res. Bull.*, 2007, **42**, 203–212.

71 S. N. Tijare, M. V. Joshi, P. S. Padole, P. a. Mangrulkar, S. S. Rayalu and N. K. Labhsetwar, *Int. J. Hydrogen Energy*, 2012, **37**, 10451–10456.

72 P. Shen, J. C. Lofaro, W. R. Woerner, M. G. White, D. Su and A. Orlov, *Chem. Eng. J.*, 2013, **223**, 200–208.

73 S. N. Tijare, S. Bakardjieva, J. Subrt, M. V Joshi, S. S. Rayalu, S. Hishita and N. Labhsetwar, *J. Chem. Sci*, 2014, **126**, 517–525.

74 M. I. Díez-García, V. Celorrio, L. Calvillo, D. Tiwari, R. Gómez and D. J. Fermín, *Electrochim. Acta*, 2017, **246**, 365–371.

75 J. Choi, H. Park and M. R. Hoffmann, *J. Phys. Chem. C*, 2010, **114**, 783–792.

76 S. Islam, S. Nagpure, D. Kim and S. Rankin, *Inorganics*, 2017, **5**, 15.

77 E. Wang, P. Zhang, Y. Chen, Z. Liu, T. He and Y. Cao, *J. Mater. Chem.*, 2012, **22**, 14443–14449.

78 J. T.-W. Wang, Z. Wang, S. Pathak, W. Zhang, D. W. deQuilettes, F. Wisnivesky-Rocca-

Rivarola, J. Huang, P. K. Nayak, J. B. Patel, H. A. Mohd Yusof, Y. Vaynzof, R. Zhu, I. Ramirez, J. Zhang, C. Ducati, C. Grovenor, M. B. Johnston, D. S. Ginger, R. J. Nicholas and H. J. Snaith, *Energy Environ. Sci.*, 2016, **9**, 2892–2901.

79 Q. Peng, B. Shan, Y. Wen and R. Chen, *Int. J. Hydrogen Energy*, 2015, **40**, 15423–15431.

80 J. Ting, B. J. Kennedy, Z. Zhang, M. Avdeev, B. Johannessen and L.-Y. Jang, *Chem. Mater*, 2010, **22**, 1640–1646.

81 G. P. Wheeler, V. U. Baltazar, T. J. Smart, A. Radmilovic, Y. Ping and K.-S. Choi, *Chem. Mater.*, 2019, **31**, 5890–5899.

82 C. Jiang, A. Savio, J. A. Moniz, A. Wang, T. Zhang and J. Tang, *Chem. Soc. Rev. Chem. Soc. Rev*, 2017, **46**, 4645–4660.

83 M. Reza Gholipour, C.-T. Dinh, F. Béland and T.-O. Do, *Nanoscale*, 2015, **7**, 8187–8208.

84 A. Galińska and J. Walendziewski, *Energy & Fuels*, 2005, **19**, 1143–1147.

85 S. N. Tijare, M. V Joshi, P. S. Padole, P. A. Mangrulkar, S. S. Rayalu and N. K. Labhsetwar, *Int. J. Hydrogen Energy*, 2012, **37**, 10451–10456.

86 P. V. Kamat and J. Bisquert, *J. Phys. Chem. C*, 2013, 117, 14873–14875.

87 S. Bai, L. Yang, C. Wang, Y. Lin, J. Lu, J. Jiang and Y. Xiong, *Angew. Chemie Int. Ed.*, 2015, **54**, 14810–14814.

88 H. S. Han, S. Shin, J. H. Noh, I. S. Cho and K. S. Hong, *JOM*, 2014, **66**, 664–669.

89 K. Sivula, F. Le Formal and M. Gr, *Chem. Mater*, 2009, **21**, 2862–2867.

90 ‡ and Craig A. Grimes Jinzhan Su,† Liejin Guo,*,† Ningzhong Bao, *Nano Lett.*, 2011, **11**, 1928–1933.

91 Q. Xiang, B. Cheng and J. Yu, *Angew. Chemie - Int. Ed.*, 2015, **54**, 11350–11366.

92 F. Meng, J. Li, S. K. Cushing, J. Bright, M. Zhi, J. D. Rowley, Z. Hong, A. Manivannan, A. D. Bristow and N. Wu, *ACS Catal.*, 2013, **3**, 746–751.

93 X. Ren, H. Yang, S. Gen, J. Zhou, T. Yang, X. Zhang, Z. Cheng and S. Sun, *Nanoscale*, 2015, **8**, 752–756.

94 H. M. El-Bery, Y. Matsushita and A. Abdel-moneim, *Appl. Surf. Sci.*, 2017, **423**, 185–196.

95 X. An, K. Li and J. Tang, *ChemSusChem*, 2014, **7**, 1086.

96 D. Zhou, T. Zhou, Y. Tian, X. Zhu and Y. Tu, *J. Nanomater.*, 2017, **2018**, 1–15.

97 Y. Wei, X. Chang, T. Wang, C. Li and J. Gong, *Small*, 2017, **13**, 1–7.

98 V. Celorrio, K. Bradley, O. J. Weber, S. R. Hall and D. J. Fermín, *ChemElectroChem*, 2014, **1**, 1667–1671.

99 X. Sun, D. Tiwari and D. J. Fermin, *J. Electrochem. Soc.*, 2019, **166**, H764–H768.

100 S. H. Ahn, J. Zhao, J. H. Kim and X. Zheng, *Electrochim. Acta*, 2017, **244**, 184–191.

101 H. Fei, Y. Yang, D. L. Rogow, X. Fan and S. R. J. Oliver, *ACS Appl. Mater. Interfaces*, 2010, **2**, 974–979.

102 A. M. El Sayed and W. M. Morsi, *J. Mater. Sci.*, 2014, **49**, 5378–5387.

103 T. Grewe and H. Tüysüz, *ChemNanoMat*, 2016, **2**, 273–280.

104 J. T. Park, S. H. Ahn, D. K. Roh, C. S. Lee and J. H. Kim, *ChemSusChem*, 2014, **7**, 2037–2047.

105 D. K. Roh, S. J. Kim, H. Jeon and J. H. Kim, *ACS Appl. Mater. Interfaces*, 2013, **5**, 6615–6621.

106 D. J. Kim, J. K. Kim, J. H. Lee, H. H. Cho, Y.-S. Bae and J. H. Kim, *J. Mater. Chem. A*, 2016, **4**, 12497–12503.

107 S. Xu, C. H. Zhou, Y. Yang, H. Hu, B. Sebo, B. L. Chen, Q. D. Tai and X. Zhao, *Energy and Fuels*, 2011, **25**, 1168–1172.

108 M. I. Díez-García and R. Gómez, *ChemSusChem*, 2017, **10**, 2457–2463.

109 S. Eslava, A. Reynal, V. G. Rocha, S. Barg and E. Saiz, *J. Mater. Chem.*, 2016, **4**, 7200–7206.

110 M. Scafetta, A. Cordi, J. Rondinelli and S. May, *J. Phys. Condens. Matter*, 2014, **26**, 505502.

111 R. D. Kumar and R. Jayavel, *J. Mater. Sci. Mater. Electron.*, 2014, **25**, 3953–3961.

112 Y. Wang, J. Zhu, L. Zhang, X. Yang, L. Lu and X. Wang, *Mater. Lett.*, 2006, **60**, 1767–1770.

113 K. M. Parida, K. H. Reddy, S. Martha, D. P. Das and N. Biswal, *Int. J. Hydrogen Energy*, 2010, **35**, 12161–12168.

114 R. Hu, C. Li, X. Wang, Y. Sun, H. Jia, H. Su and Y. Zhang, *Catal. Commun.*, 2012, **29**, 35–39.

115 K. Peng, L. Fu, H. Yang and J. Ouyang, *Sci. Rep.*, 2016, **6**, 19723.

116 S. Acharya, S. Mansingh and K. M. Parida, *Inorg. Chem. Front.*, 2017, **4**, 1022–1032.

117 J. Wang, Z. Wang, P. Qu, Q. Xu, J. Zheng, S. Jia, J. Chen and Z. Zhu, *Int. J. Hydrogen Energy*, 2018, **43**, 7388–7396.

118 G. Singh, A. Elikkottil and B. Pesala, *Int. J. Hydrogen Energy*, 2018, **44**, 578–586.

119 G. S. Pawar, A. Elikkottil, S. Seetha, K. S. Reddy, B. Pesala, A. A. Tahir and T. K. Mallick, *ACS Appl. Energy Mater.*, 2018, **1**, 3449–3456.

120 P. Wang, Y. He, Y. Mi, J. Zhu, F. Zhang, Y. Liu, Y. Yang, M. Chen and D. Cao, *RSC Adv.*, 2019, **9**, 26780–26786.

121 G. P. Wheeler and K. S. Choi, *ACS Energy Lett.*, 2017, **2**, 2378–2382.

122 T. Wang and K. Chang, *Chem. Commun.*, 2015, **51**, 3630–3633.

123 G. S. Pawar and A. A. Tahir, *Sci. Rep.*, 2018, **8**, 1–9.

124 J. Yang, R. Hu, W. Meng and Y. Du, *Chem. Commun.*, 2016, **52**, 2620–2623.

125 Y. Soltanabadi, M. Jourshabani and Z. Shariatinia, *Sep. Purif. Technol.*, 2018, **202**, 227–241.

126 X. Sun, D. Tiwari and D. J. Fermin, *J. Electrochem. Soc.*, 2019, **166**, H764–H768.

127 Y. Chen, D. Wang, H. Qin, H. Zhang, Z. Zhang, G. Zhou, C. Gao and J. Hu, *J. Rare Earths*, 2019, **37**, 80–87.

128 H. Huang, L. Lv, F. Xu and J. Liao, *Microchim. Acta*, 2017, **184**, 4141–4149.

129 P. Tang, X. Xie, H. Chen, C. Lv and Y. Ding, *Ferroelectrics*, 2019, **546**, 181–187.

130 J. W. Elam, D. A. Baker, A. J. Hryn, A. B. F. Martinson, M. J. Pellin and J. T. Hupp, *J. Vac. Sci. Technol. A Vacuum, Surfaces, Film.*, 2008, **26**, 244–252.

131 B. K. Kang, G. S. Han, J. H. Baek, D. G. Lee, Y. H. Song, S. Bin Kwon, I. S. Cho, H. S. Jung and D. H. Yoon, *Adv. Mater. Interfaces*, 2017, **4**, 1–8.

132 Q. Zhang, V. Celorrio, K. Bradley, F. Eisner, D. Cherns, W. Yan and D. J. Fermín, *J. Phys.*

Chem. C, 2014, **118**, 18207–18213.

133 C. M. Herzinger, B. Johs, W. A. McGahan, J. A. Woollam and W. Paulson, *J. Appl. Phys.*, 1998, **83**, 3323–3336.

134 A. Hankin, F. E. Bedoya-Lora, J. C. Alexander, A. Regoutz and G. H. Kelsall, *J. Mater. Chem. A*, 2019, **7**, 26162–26176.

135 C. Glynn and C. O'Dwyer, *Adv. Mater. Interfaces*, 2017, **4**, 1600610.

136 V. Celorrio, L. Calvillo, C. A. M. van den Bosch, G. Granozzi, A. Aguadero, A. E. Russell and D. J. Fermín, *ChemElectroChem*, 2018, **5**, 3044–3051.

137 G. P. A. Gobaille-Shaw, V. Celorrio, L. Calvillo, L. J. Morris, G. Granozzi and D. J. Fermín, *ChemElectroChem*, 2018, **5**, 1922–1927.

138 M. I. Díez-García and R. Gómez, *ChemSusChem*, 2017, **10**, 2457–2463.

139 J. a. Gómez-Cuaspud, E. Vera-López, J. B. Carda-Castelló and E. Barrachina-Albert, *React. Kinet. Mech. Catal.*, 2017, **120**, 167–179.

140 S. Thirumalairajan, K. Girija, N. Y. Hebalkar, D. Mangalaraj, C. Viswanathan and N. Ponpandian, *RSC Adv.*, 2013, **3**, 7549–7561.

141 M. S. Prévot, N. Guijarro and K. Sivula, *ChemSusChem*, 2015, **8**, 1359–1367.

142 F. H. Taylor, J. Buckeridge and C. R. A. Catlow, *Chem. Mater.*, 2016, **28**, 8210–8220.

143 B. Zhang, L. He, T. Yao, W. Fan, X. Zhang, S. Wen, J. Shi and C. Li, *ChemSusChem*, 2019, **12**, 1026–1032.

144 T. M. Ng, M. T. Weller, G. P. Kissling, L. M. Peter, P. Dale, F. Babbe, J. De Wild, B. Wenger, H. J. Snaith and D. Lane, *J. Mater. Chem. A*, 2017, **5**, 1192–1200.

145 G. Ma, J. Liu, T. Hisatomi, T. Minegishi, Y. Moriya, M. Iwase, H. Nishiyama, M. Katayama, T. Yamada and K. Domen, *Chem. Commun. Chem. Commun*, 2015, **4302**, 4302–4305.

146 S. A. Domínguez-Domínguez Joaquín Arias-Pardilla AE ngel Berenguer-Murcia AE Emilia Morallón AE Diego Cazorla-Amorós, *J. Appl. Electrochem.*, 2008, **38**, 259–268.

147 H. Zhang, F. Jiang, R. Zhou, Y. Du and P. Yang, *Int. J. Hydrogen Energy*, 2011, **36**, 15052–15059.

148 H. Xing, L. E, Z. Guo, D. Zhao, X. Li and Z. Liu, *Inorg. Chem. Front.*, 2019, **6**, 2488–2499.

149 K. Persson, Materials Data on PrFeO3 (SG:62) by Materials Project, https://www.osti.gov/dataexplorer/biblio/1276430-materials-data-res2-sg-materials-project.

150 V. Celorrio, L. Calvillo, G. Granozzi, A. E. Russell and D. J. Fermin, *Top. Catal.*, 2018, **61**, 154–161.

151 V. Celorrio, L. Calvillo, E. Dann, G. Granozzi, A. Aguadero, D. Kramer, A. E. Russell and D. J. Fermín, *Catal. Sci. Technol.*, 2016, **6**, 7231–7238.

152 V. Celorrio, E. Dann, L. Calvillo, D. J. Morgan, S. R. Hall and D. J. Fermin, *ChemElectroChem*, 2016, **3**, 283–291.

153 B. V. Prasad, G. N. Rao, J. W. Chen and D. S. Babu, *Solid State Sci.*, 2012, **14**, 225–228.

154 W. Mönch, *J. Appl. Phys.*, 2012, **111**, 1–8.

155 A. Agrawal, J. Lin, M. Barth, R. White, B. Zheng, S. Chopra, S. Gupta, K. Wang, J. Gelatos, S. E. Mohney and S. Datta, *Appl. Phys. Lett.*, 2014, **104**, 8–12.

156 I. A. Digdaya, G. W. P. Adhyaksa, B. J. Trześniewski, E. C. Garnett and W. A. Smith, *Nat. Commun.*, 2017, **8**, 1–8.

157 I. A. Digdaya, B. J. Trześniewski, G. W. P. Adhyaksa, E. C. Garnett and W. A. Smith, *J. Phys. Chem. C*, 2018, **122**, 5462–5471.

158 J. Azevedo, S. D. Tilley, M. Schreier, M. Stefik, C. Sousa, J. P. Araújo, A. Mendes, M. Grätzel and M. T. Mayer, *Nano Energy*, 2016, **24**, 10–16.

159 R. Irani, I. Y. Ahmet, J.-W. Jang, S. P. Berglund, P. Plate, C. Höhn, R. Böttger, S. W. Schmitt, C. Dubourdieu, S. Lardhi, L. Cavallo, M. Harb, P. Bogdanoff, R. van de Krol and F. F. Abdi, *Sol. RRL*, 2019, **1900290**, 1–11.

160 F. F. Abdi, D. E. Starr, I. Y. Ahmet and R. van de Krol, *Chempluschem*, 2018, **83**, 941–946.

161 K. Nose, A. Y. Suzuki, N. Oda, M. Kamiko and Y. Mitsuda, *Appl. Phys. Lett.*, 2014, **104**, 2–6.

162 J. Resasco, H. Zhang, N. Kornienko, N. Becknell, H. Lee, J. Guo, A. L. Briseno and P. Yang, *ACS Cent. Sci.*, 2016, **2**, 80–88.

163 L. Kavan, L. Steier and M. Gratzel, *J. Phys. Chem. C*, 2017, **121**, 342–350.

164 M. T. Greiner, L. Chai, M. G. Helander, W. M. Tang and Z. H. Lu, *Adv. Funct. Mater.*, 2012, **22**, 4557–4568.